# OVERHAULING SOUND DIFFUSION IN AUDITORIA USING DEEP-SUBWAVELENGTH ACOUSTIC METAMATERIALS

by ERIC BALLESTERO

A thesis submitted in fulfilment of the requirements for the degree of

Doctorate of Philosophy (Ph.D.)

at

London South Bank University,

School of Architecture & Built Environment

EST 1892 **LSBU**

June 2021 – Examination Version

I declare that this thesis has been composed solely by myself and that it has not been submitted, in whole or in part, in any previous application for a degree. Except where stated otherwise by reference or acknowledgement, the work presented herein is entirely my own.

*London, June 2021*

Eric Ballestero

*Page left intentionally blank*

Life is an unfoldment, and the further we travel the more truth we can comprehend. To understand the things that are at our door is the best preparation for understanding those that lie beyond.

— Hypatia of Alexandria


In memory of Bob Peters; for his outstanding teaching, genuine love for science and history, and for his kind support in getting me to learn more about acoustics.

*Page left intentionally blank*

# ABSTRACT

THE REDUCED amount of space available in critical listening environments, such as orchestra pits, rehearsal rooms or even recording studios, often impairs the installation of helpful, but sizeable, acoustic treatments on their boundaries. This can be a problem as such acoustic treatments, mainly used for sound absorption and diffusion, are key for controlling the physical aspects of sound propagation in the environment. This research thus proposes to study experimentally and numerically a cutting-edge metamaterial-inspired approach designed to provide ultra-thin and adaptable alternatives to traditional acoustic treatments, with a particular focus on sound diffusion, and how these can be integrated in practical computational frameworks. These novel deep-subwavelength acoustic metamaterials, termed metadiffusers, allow for efficient sound diffusion within dimensions $1/10^{\text{th}}$ to $1/20^{\text{th}}$ thinner than ordinary sound diffusers. Moreover, the optimization potential of metadiffusers brings a vast panel of variable configurations depending on the situation requirements. Results presented throughout this thesis outline several of these configurations with experimental and/or numerical validations in free-field scattering scenarios as well as numerical room acoustic applications. Very good agreement is found all through between the analytical and experimental/numerical scattering and diffusion datasets, thus demonstrating the outstanding and versatile potential of metadiffusers to be applied in many critical listening environments where space is at a premium, such as orchestra pits or recording studios.

*Page left intentionally blank*

## PUBLICATIONS

Some of the information gathered in this thesis can be found in the following publications:

### *Journals & Bulletins*

* Ballestero, E., Jiménez, N., Groby, J.-P., Dance, S., Aygun, H. and Romero-García, V.,"Experimental validation of deep-subwavelength diffusion by acoustic metadiffusers". In: *Applied Physics Letters*, 115.8 (2019), p. 081901. DOI: 10.1063 /1.5114877. URL: https://doi.org/10.1063/1.5114877.

* Romero-García, V., Pagneux, V., Groby, J., Jimenez, N., Ballestero, E.,"Métamatériaux pour l'acoustique audible : Absorption parfaite et diffusion sublongueur d'onde". In: *Acoustique et Techniques*, 94/95:33-39. (2020). URL: http://hdl. handle.net/10251/164477.

* Ballestero, E., Jiménez, N., Groby, J.-P., Dance, S., Aygun, H. and Romero-García, V.,"Metadiffusers for Quasi-Perfect and Broadband Sound Diffusion". In Submission to: *Applied Physics Letters*, 119.4 (2021), p. 044101. DOI: 10.1063/5.0053413. URL: https://doi.org/10.1063/5.0053413.

* Ballestero, E., Hamilton. B., Jiménez, N., V., Groby, J.-P., Romero-García, V., Aygun, H., and Dance, S.,"Scattering Evaluation of Equivalent Surface Impedances of Acoustic Metamaterials in Large FDTD Volumes Using RLC Circuit Modelling". In Submission to: *MDPI Applied Sciences*, 11(17) (2021), p. 8084. DOI: 10.3390/app11178084.
URL: https://doi.org/10.3390/app11178084.

### *Conference Proceedings*

∗ Ballestero, E., Shearer, D., Aygun, H., and Dance, S.,"Acoustic Conditions in Orchestra Pits: Are Metadiffusers a Potential Solution?". In: *Auditorium Acoustics*, Hamburg, Germany, (2018).

∗ Ballestero, E., Shearer, D., Aygun, H., and Dance, S.,"Acoustic Diffusers and Metadiffusers in Orchestra Pits: the Good, the Bad, and the Loony". In: *$1^{st}$ Symposium on Acoustic Metamaterials*, Xátiva, Spain, (2018).

∗ Ballestero, E., Jiménez, N., Groby, J.-P., Dance, S., Aygun, H. and Romero-García, V.,"3D-Printed Quadratic Residue Metadiffuser – Design and Measurements of an Optimized Deep-Subwavelength Sound Diffuser ". In: *$23^{rd}$ International Congress on Acoustics*, Aachen, Germany, (2019).

∗ Ballestero, E., Jiménez, N., Groby, J.-P., Dance, S., Aygun, H. and Romero-García, V.,"Deep-Subwavelength Materials for Controlling Sound Diffusion: Experimental Validation of Metadiffusers". In: *Meta 2019*, Lisbon, Portugal, (2019).

∗ Ballestero, E., Jiménez, N., Groby, J.-P., Dance, S., Aygun, H. and Romero-García, V.,"Experimental Validation of a 3D-Printed Quadratic Residue Metadiffuser". In: *$2^{nd}$ Symposium on Acoustic Metamaterials*, Ischia, Italy, (2019).

∗ Ballestero, E., Jiménez, N., Groby, J.-P., Dance, S., Aygun, H. and Romero-García, V.,"Measuring Scattering Properties of a 3D-Printed Quadratic Residue Metadiffuser ". In: *COST-DENORMS Final Event & Dissemination*, Coimbra, Portugal, (2020).

∗ Jiménez, N., Cox, T.J., Requena-Plens, J.M., Ballestero, E., Groby, J.-P., Romero-García, V.,"Beyond Schroeder diffusers using acoustic metasurfaces". In: *Tecniacústica 2020: 50º Congreso Español de Acústica. XI Congreso Ibérico de Acústica*, Faro, Portugal, (2020).

## ACKNOWLEDGEMENTS

First and foremost, I would like to acknowledge my supervisory team who guided me throughout the entirety of this endeavour. More precisely, I am grateful for Prof. Dance's unwavering support and enthusiasm, Dr. Aygun's critical feedback and encouraging words, and Dr. Romero-García's keen eye for details and active endorsement. Additionally, I wish to thank external collaborators Dr. Jiménez, Dr. Groby, and Dr. Hamilton, for their invaluable teachings and kind attention which have been critical in my development as a researcher. A particular mention goes to Dr. Shearer for years of daily positive interactions and assistance in many tasks. Further acknowledgements go the Royal Opera House Sound & Performance Group for their patronage and positive feedback in this project.

Many thanks go to my partner, Caroline, for her love but also her patience for putting up with me and my aspirations for many years. I would also like to thank my friends and family for their unconditional support, with a special mention to Thibault and Thomas for their active involvement and help. Thanks also go to the many university technicians that have contributed in the progress of this research.

Finally, I would like to acknowledge and dedicate this thesis to my former mentors in acoustics Gérard Martin, Prof. Catherine Semidor and late Prof. Bob Peters, without whom I might not have taken such path in life.

To all the people above, I am thankful for not only achieving doctoral studies, but to be able to walk on a journey that always inspired me.

*Page left intentionally blank*

*Page left intentionally blank*

# CONTENTS

## GLOSSARY

In order of appearance.

| | | |
|---|---|---|
| $\rho$ | Total density | $\text{kg.m}^{-3}$ |
| $\rho_0$ | Ambient density | $\text{kg.m}^{-3}$ |
| $\delta\rho$ | Excess density | $\text{kg.m}^{-3}$ |
| $\upsilon$ | Particle velocity | $\text{m.s}^{-1}$ |
| $p$ | acoustic pressure | Pa |
| $P$ | Total pressure | Pa |
| $p_0$ | Ambient pressure | Pa |
| $\kappa$ | Bulk modulus | Pa |
| $c_0$ | Ambient speed of sound | $\text{m.s}^{-1}$ |
| $c$ | Speed of sound | $\text{m.s}^{-1}$ |
| $u$ | Physical scalar | |
| $t$ | Time variable | s |
| $x$ | Cartesian $x$ axis | m |
| $y$ | Cartesian $y$ axis | m |
| $z$ | Cartesian $z$ axis | m |
| $Z_0$ | Specific acoustic impedance of air | $\text{Pa.s.m}^{-1}$ |
| $\widetilde{Z}$ | Volume impedance (2D) | $\text{Pa.s.m}^{-2}$ |
| $\mathcal{P}$ | Volume Pressure (2D) | $\text{Pa.m}^{-1}$ |
| $\mathcal{V}$ | Volume Velocity (2D) | $\text{m}^{-2}\text{.s}$ |
| $e$ | Euler number | |
| $i$ | Imaginary unit | |
| $\omega$ | Radial frequency | $\text{rad.s}^{-1}$ |
| $\pi$ | Pi | |

| | | |
|---|---|---:|
| $f$ | Frequency | Hz |
| $\lambda$ | wavelength | m$^{-1}$ |
| $k$ | Wavenumber | rad.m$^{-1}$ |
| $\mathcal{F}$ | Fourier transform operator | |
| $c_p$ | Phase speed of sound | m.s$^{-1}$ |
| $\alpha_{att}$ | Acoustic attenuation coefficient | m$^{-1}$ |
| $\alpha_s$ | Spatial acoustic attenuation coefficient | m$^{-1}$ |
| $\alpha_t$ | Temporal acoustic attenuation coefficient | m$^{-1}$ |
| $\delta_{visc}^{BL}$ | Viscous acoustic boundary layer | m |
| $\nu$ | Kinematic viscosity coefficient | m$^2$.s$^{-1}$ |
| $\mu$ | Shear viscosity coefficient | Pa.s$^{-1}$ |
| $T$ | Temperature | °C |
| $\delta_{therm}^{BL}$ | Thermal acoustic boundary layer | m |
| $\vartheta$ | Heat conduction coefficient | W.m$^{-2}$.K$^{-1}$ |
| Pr | Prandtl number | |
| $C_p$ | Specific heat at constant pressure | J.kg$^{-1}$.K$^{-1}$ |
| $C_v$ | Specific heat at constant volume | J.kg$^{-1}$.K$^{-1}$ |
| $\gamma$ | Ratio of specific heats | °C/cm |
| $K$ | Thermal conductivity | W.m$^{-1}$.K$^{-1}$ |
| $\delta_\tau$ | Excess temperature | °C |
| $\mathcal{M}$ | Propagation constant | |
| $\rho_e$ | Effective density | kg.m$^{-3}$ |
| $\kappa_e$ | Effective bulk modulus | Pa |
| $r_c$ | Radius of cylinder | m |
| $J_n$ | Bessel function of the first kind of order $n$ | |
| $G_\rho$ | Stinson density boundary layer function | m$^{-1}$ |
| $G_\kappa$ | Stinson compressibility boundary layer function | m$^{-1}$ |

| | | |
|---|---|---|
| $a_m$ | Duct cross-section dimension | m |
| $b_m$ | Duct cross-section dimension | m |
| $\alpha_m$ | Duct cross-section coefficient | |
| $\beta_m$ | Duct cross-section coefficient | |
| $h$ | Height of slit | m |
| $L$ | Length of slit | m |
| $p_i$ | Incident pressure | Pa |
| $p_r$ | Reflected pressure | Pa |
| $R$ | Reflection coefficient | |
| $\psi$ | Incident wave angle | rad |
| $Y$ | Acoustic admittance | S |
| $\alpha$ | Absorption coefficient | Sabin |
| $U$ | Scalar field | |
| $G$ | Green's function | |
| $G_K$ | Kirchhoff Green's function | |
| $\mathbf{r}$ | Coordinate vector $\mathbf{r} = |\mathbf{r}_1 - \mathbf{r_0}|$ | $\mathbf{r}x, y, z$ |
| $\mathbf{r}_0$ | Coordinate vector at the source | $\mathbf{r}x_0, y_0, z_0$ |
| $\mathbf{r}_1$ | Coordinate vector at evaluation point | $\mathbf{r}x_1, y_1, z_1$ |
| $H_0$ | Source location at $\mathbf{r}_0$ | |
| $H_1$ | Point location at $\mathbf{r}_1$ | |
| $\Sigma$ | Aperture area (2D) | m |
| $G_{S1}$ | First Rayleigh Green's function | |
| $G_{S2}$ | Second Rayleigh Green's function | |
| $\delta_\psi$ | Directional diffusion coefficient | |
| $I_s$ | Scattered sound intensity | $\mathrm{W.m}^{-2}$ |
| $p_s$ | Scattered sound pressure | Pa |
| $\theta$ | Elevation angle | rad |
| $\phi$ | Azimuth angle | rad |

| | | |
|---|---|---|
| $\delta_{flat}$ | Flat reflector directional diffusion coefficient | |
| $\delta_{n,\psi}$ | Normalized directional diffusion coefficient | |
| **T** | Total transfer matrix | |
| **M** | Transfer matrix | |
| $\cdot_w$ | (underscript) Quantity related to a well | |
| $\cdot_s$ | (underscript) Quantity related to a slit | |
| $\cdot_{HR}$ | (underscript) Quantity related to a Helmholtz resonator | |
| $\cdot_n$ | (underscript) Quantity related to a Helmholtz resonator neck | |
| $\cdot_c$ | (underscript) Quantity related to a Helmholtz resonator cavity | |
| $\Delta l$ | end correction to free space | |
| $\lambda_B$ | Bragg wavelength | m |
| $F$ | Force | N |
| $F_s$ | Restoring force | N |
| $F_s$ | Motion force | N |
| $a$ | Acceleration | m.s$^{-2}$ |
| $K_s$ | Stiffness coefficient | N.m$^{-1}$ |
| $M$ | Mass | kg |
| $V$ | Volume | m$^3$ |
| $w$ | width | m |
| $l$ | length | m |
| $\psi_B$ | Bloch wave function | |
| $M_r$ | Number of HRs | |
| $f_{Bragg}$ | Bragg frequency | Hz |
| $\epsilon$ | Cost function | |
| $\Gamma$ | Geometry parameters matrix | |

| | | |
|---|---|---|
| $D$ | Slit width | m |
| $c_{in}$ | Inequality optimization constraint | |
| $c_{eq}$ | Equality optimization constraint | |
| $b_l$ | Lower optimization boundaries | m |
| $b_u$ | Upper optimization boundaries | m |
| $\psi_n$ | Basis function | |
| $a_x$ | Periodicity in the $x$-axis | m |
| $\beta_q$ | Secondary far-field diffraction lobes | rad |
| $C$ | Courant number | |
| $\delta_t$ | Time stepping | s |
| $\delta_x$ | Space stepping | m |
| $\Delta_f$ | Frequency range | Hz |
| $\mathcal{D}$ | Diffuseness coefficient | |
| $\mathcal{D}_{e/l}$ | Early-to-late diffuseness coefficient | |
| $\mathcal{D}_e$ | Early diffuseness coefficient | |
| $\tau_e$ | Average time of early reflections | s |
| mfp | Mean free path | m |

# LIST OF FIGURES

# ACRONYMS

AES   Audio Engineering Society

BEM   Boundary Element Method

DOA   direction of arrival

CFL   Courant-Friedrichs-Lewy

FEM   Finite Element Method

FDTD   Finite Difference Time-Domain

FFT   Fast Fourier Transform

FDM   Fused Deposition Method

GPU   Graphics Processing Unit

HR    Helmholtz Resonator

IBCs   Impedance Boundary Conditions

IDWM   Interpolated Digital Waveguide Mesh

ISO    International Standard Organization

IWB   Interpolated Wideband

NDE   Non-Destructive Evaluation

MLS   Maximum Length Sequence

PDE   Partial Differential Equation

PML   Perfectly-Matched Layer

PPW   Points Per Wavelength

PRD   Primitive Root Diffuser

PRM  Primitive Root Metadiffuser

PRS  Primitive Root Sequence

PWE  Plane Wave Expansion

QPD  Quasi-Perfect Diffusion

QRD  Quadratic Residue Diffuser

QRS  Quadratic Residue Sequence

QRM  Quadratic Residue Metadiffuser

QWR  Quarter-Wavelength Resonator

RLC  Resistor-Inductor-Capacitor

SDM  Spatial Decomposition Method

SRL  Standard Rectilinear

TPD  Ternary Phase Diffuser

TPM  Ternary Phase Metadiffuser

TPS  Ternary Phase Sequence

TMM  Transfer Matrix Method

*Page left intentionally blank*

# INTRODUCTION

THE context of the herein research lies at the crossroads between multiple acoustic topics, such as room acoustics, physical acoustics, and to some extent, psychoacoustics. Due to the interconnectivity of these scientific fields, the following chapter is intended to give the rationale behind the multidisciplinary research aim and clarify the context in which the research arose.

## 1.1 AIM, RATIONALE & OBJECTIVES

The aim of this research is to design and implement deep-subwavelength acoustic metamaterials, i.e., acoustic structures with a size much smaller than the targeted wavelengths, that can outshine traditional acoustic treatments in auditoria where space is at a premium.

Auditoria are rooms primarily focused towards a critical listening of musical content, sometimes accompanied by visual performances. They generally come in the form of theatres, opera houses, rehearsal rooms and concert halls, but can also extend to any place, big or small, where the listening of sound is of interest. In many occasions, these rooms often benefit from acoustic treatments for controlling the propagation of sound and thus enhance the listening experience to its best. These can often be divided in two main categories, each targeting a specific acoustic phenomenon, viz., treatments for sound absorption or sound diffusion. The former aims at absorbing acoustic energy from the room whereas the latter controls the directions of acoustic waves being reflected.

Whilst these acoustic treatments have been extensively studied and implemented in countless rooms, there are cases however where they can prove difficult to install, especially in environments with critical space limitations. This is due to the sizeable nature of typical acoustic treatments, which often rely on the structure

thickness to increase their acoustic performance. Relatively small auditoria such as orchestra pits in opera houses, some rehearsal rooms, or even sound recording and monitoring studios are typical examples of environments where space is at a premium, and where traditional acoustic treatments come with the additional compromise of acoustic quality versus space availability. In order to ensure the acoustic quality of these rooms, it is therefore important to look at potential alternatives minimizing the amount of space being traded whilst keeping a competitive acoustic performance. The work presented in this thesis explores such path through the use of deep-subwavelength acoustic diffusers, termed *metadiffusers*, for controlling the distribution of early sound reflections in such constrained environments within ultra-thin dimensions.

The knowledge gap that this thesis intends to cover is (i) to expand the lack of information about metadiffusers, as these structures are relatively new, through further analytical optimization insights, experimental measurements and numerical scattering validations, and (ii) to provide with a numerical framework and data for adding such structures into large FDTD computational environments that are typical of room acoustic studies.

In order to achieve the above-mentioned goal, the following set of objectives is proposed to ensure a robust scientific approach throughout this research.

Objectives of the thesis:

- to bring a deep understanding of the theory of acoustic scattering and sound diffusion;

- to present a study of the acoustic performance of traditional sound diffusers;

- to provide an analytical framework for computing acoustic scattering;

- to explore numerical tools and methods available to consolidate analytical scattering predictions;

- to set-up an experimental apparatus for comparing previous scattering predictions with physical scattering data;

- to lay down a numerical framework for simulating scattering prediction data into larger real-world situations;

- to evaluate the objective impact of metadiffusers on the acoustic field in modelled situations; and lastly

- to evaluate the subjective impact of sound diffusion in a practical situation.

## 1.2 LITERATURE REVIEW, HYPOTHESIS & RESEARCH QUESTION

The following subsection provides a literature review going from the musical context of opera house acoustics to the physical breakthroughs of acoustic meta-materials, and how these can be engineered as suitable alternatives when traditional acoustic treatments reach their limit. Although the herein research context arose from technical difficulties for controlling sound in the orchestra pit of the Royal Opera House (ROH), Covent Garden, London, most of the arguments made through this review can be applicable to any similar scenario where space to install traditional acoustic treatments is limited.

The present research began in December 2017, when the ROH decided to engage a PhD research programme with London South Bank University (LSBU) for tackling a rising issue, common to almost all opera houses: the overwhelming loudness in orchestra pits. The orchestra pit of an opera house consists in a deep, hollow cavity, placed between the stage and the audience (see Fig. 1.1). This peculiar



SECTION                    ORCHESTRA / FIRST TIER PLAN
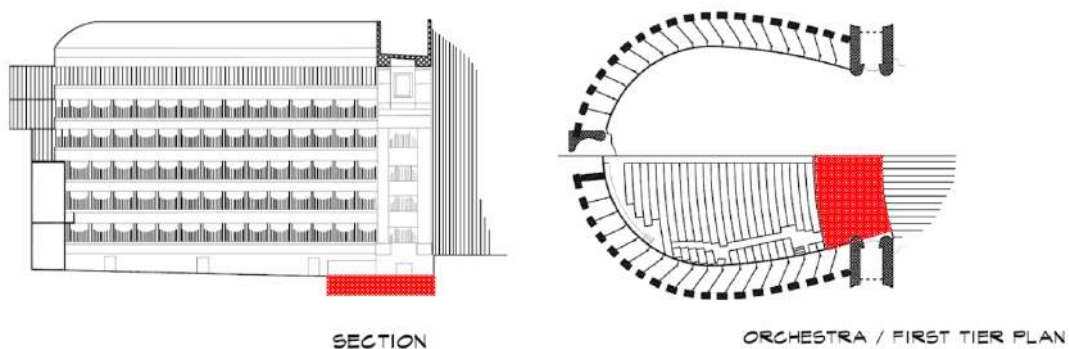
Figure 1.1: Teatro alla Scala, Milano, Italy, from [1]. The red colouring highlights the orchestra pit area.

placement helps reduce the sound coming from the orchestra to the audience in order to prioritize the singers' voices, as well as visually hiding it for aesthetic purposes [1]. The orchestral layout within the pit, i.e., how the different musical groups are arranged around the conductor, often varies with the chosen *repertoire.* The operatic range of productions is usually varied, including ballets, operas, and symphonic concerts, all of which can host from small orchestral configurations (50-60 musicians) to bigger ones (100+ musicians) [2]. These configurations change once or twice a day to allow for planned rehearsals and evening plays. There exists many different kinds of orchestra pits, varied in shape and dimensions. Some of them are partially covered by an overhang under which a portion of the orchestra sits. The intrinsic shape, volume and boundaries of orchestra pits will affect how sound is perceived in both the pit and the main auditorium [3]. Whilst audience may *generally* be satisfied by the overall orchestral sound levels, musicians in the pit often complain about the loudness of such performing environment [4–6]; a rather logical statement when 60 to 100 musicians are closely packed inside an open box.

It must be noted here that the use of the word *loudness* is highly polysemic. It may refer to sound intensity (physics) [7], relative isophonic level (physiology) [8], high neural stress (neurology) [9], annoyance (psychology) [10], or even all of the above as loudness has been hypothesised to be a multidimensional descriptor related to the perceived magnitude of sound [11]. Such polyvalency can be illustrated by the following example, where a pleasant but strong sound can sometimes be perceived as being less loud than a disagreeable but quieter one. This seems to indicate that the context of sound generation can highly affect how loud it is perceived, and that loudness in musical contexts can therefore hardly be compared to that of industrial noise settings.

High sound levels in orchestra pits, and loudness to some extent, are likely inevitable. This is mostly due to the presence of several tens of musical instruments playing at the same time, which can also be partially enhanced by louder musical instruments and more dramatic repertoires. In such context, reducing loudness can be more a matter of limiting the amount of psychological overload than pure sound

reduction, as it can seem impractical to drastically reduce the sound levels inside the pit. This could lead to reduced orchestral sound levels in the pit and audience as well as potentially affecting the feeling of musical balance and force musicians to play louder. This dilemma might be the reason why no standardised solutions have been generally implemented for this peculiar performing environment [12, 13], for which only a scarce amount of work has been conducted over the past 40 years [1, 2].

The majority of acoustical research in orchestra pits aimed to gather information or state the issues rising in such performing environments, mainly focusing on hearing loss due to dangerous sound levels [14–18] and with only a few dealing with the pure physical interactions between sound and the enclosure's boundaries [19–23].

Pioneering works led to a better understanding of acoustic propagation in orchestra pits; they helped establishing optimum and reliable physical descriptors, such as Support, Ensemble and Room Feedback [4, 13, 22, 24, 25]. From them it is known that the pit acts as a coupled space with respect to the main auditorium, illustrated with the double slope decay curve in energy decay measurements [3, 13]. The early part of the experienced acoustic field in the pit should thus be regulated by the local acoustic conditions of the enclosure. Insightful work from J. Meyer [12] focused on the troublesome acoustic conditions in the under-stage area that could give birth to strong vertical standing waves in the low frequency bands, eventually affecting the listening and performing capacities of back row musicians; usually the timpani, double bass and percussions. Guidance about possible acoustic treatments in orchestra pits was given by T. J. Cox and P. D'Antonio [26, 27], where they proposed that low- to mid-frequency absorption should be used to critically control instrument-borne high levels [25] and diffusion used to improve ensemble conditions [28, 29], as excessive sound levels and poor ensemble conditions were found to be the two main defaults of orchestra pits [3, 4, 13, 14, 22, 28, 29].

For the purpose of this research, a particular interest will be given to sound diffusion as it can help reduce the intensity of sounds reaching musicians within spe-

cific time windows due to the spatio-temporal dispersion of sound [26]. This could positively affect their acoustic environment without adding too much acoustic absorption, which could unbalance operatic performance conditions. Some previous experiments explore the temporal distribution aspects of sound in pits, doing so by (i) dividing the orchestra pit in different blocks with absorptive and diffusive acoustical panels [30], (ii) installing an electroacoustic reinforcement system to slightly delay the generated sound differently for several orchestral groups [3, 13], or (iii) adding diffusion to scatter sound with diffusers built inside the walls [26, 28]. Most of these experiments yielded positive results towards either increasing performing parameters or slightly reducing the sound intensity in the pit, but were rejected due to orchestral considerations. The latter fact is illustrated by Paoletti *et al.* who stated that even though a convenient acoustic solution could be thought of [in orchestra pits], it would likely be not installed or tested for either human, artistic or economic reasons [31]. In the first two cases, it appears that musicians very much disliked the proposed configurations as it would break their musical balance and ensemble feeling while playing in the pit. Music being a critical part of opera, acoustic measures cannot therefore be of intrusive nature. However, the aforementioned strategy with built-in diffusers seems to have been generally well received by the musician community [26, 32]. An example of such configuration can be seen in Fig. 1.2. Following such strategy, one can thus control the distribution of early sound reflections arriving at the musicians through the use of acoustic diffusers so as to better distribute the sound energy through time and try to increase their feeling of ensemble playing and musical balance.

Sound diffusers are locally reacting surfaces that spread reflected waves into many directions, reducing the strength of the undesired specular reflections and audible echoes, whilst sound energy is preserved in space [26]. In some cases, the spreading of sound energy can be achieved through the diffraction and/or specular reflections generated by the geometrical nature of the constituting elements present at the surface of the diffuser, such as triangles and/or spheres. In other cases, the scattering of sound can be achieved through a specific topological distribution of the acoustic impedance along the surface, leading to a spatially-dependent profile

Figure 1.2: Two views of the pit at Nicholas Music Center, Rutgers University. (Architects: Bhavnani & King Architects, NY; photos from RPG Diffusor Systems Inc. found in [26].)

of the reflection coefficient along the surface. The latter locally reacting surfaces are thus often termed as phase grating diffusers, or Schröeder diffusers [33, 34] in honour to the pioneering works of M.R. Schröeder in the 1970's. Usually, Schröeder diffusers make use of quarter-wavelength resonators, such as wells, as illustrated in Fig. 1.3, in order to achieve a phase grating on the impinging sound wave, where a maximum phase shift of the reflection coefficient occurs at $L = c_0/4f$, where $f$ is the frequency of the wave, $L$ is the depth of the slit, and $c_0$ is the speed of sound in air. By combining many such QWRs of different sizes, sound diffusers with specific goals can be designed, i.e., break specular reflections or homogenize them [35]. The spatially dependent reflections of a sound diffuser are generally tailored to the surface's impedance design, which usually follows numerical sequences taken from Number Theory [36–38] that posses, or tend to have, a uniform spatial Fourier transform of their reflection coefficient at multiples of the design frequency [26, 39], thus leading to an even scattering of sound.

However, whilst the strategy of using built-in diffusers on the walls seems to be valid, it possesses a significant drawback that can make it impractical to implement in some situations. The drawback of typical sound diffusers is that they can be relatively bulky due to their quarter-wavelength scale, usually between 10 cm to 50 cm deep depending on the frequency range being addressed. This would imply the integration of sound diffusers in the pit during its construction, or to refurbish entirely the pit and thus close any scheduled performance for a considerable time,

Figure 1.3: Example sound diffuser using quarter-wavelength resonators, or wells.

which would have serious economic implications. The sheer size of the acoustic structures also make it difficult to add them *a posteriori* as they would take a significant portion of the inner pit space; the space between musicians being already at a premium. At the ROH, a rule of thumb for any added wall elements is that they should not exceed 10 cm at most, with lesser dimensions greatly welcomed. Although typical sound diffusers could be made within these dimension constraints, this would result in a significant performance drop in acoustic diffusion. Built-in Schröeder diffusers are thus difficult to incorporate into most of the existing orchestra pits across the world. Nonetheless, a hypothesis based on the previous elements can be made.

> *Hypothesis:* Acoustic diffusers disposed along the boundaries of auditoria can spatially and temporally disperse the sounds perceived by performing musicians and thus help reduce the perceived loudness.

The space constraints in orchestra pits, or any similarly space-limited critical listening environment, help establish a direction of research, i.e., to evaluate non-standard acoustic solutions in order to achieve efficient acoustic diffusion within a range of 10 cm or less. In other words, knowing that most standard acoustic treatments work optimally on a quarter-wavelength scale, an even lower subwavelength scale must be achieved in order to answer to the following research question.

> *Research question:* Are there any thinner alternative structures to traditional acoustic diffusers and how could these be implemented in practical situations?

As hinted by the tittle of this work, a potential answer to such question lies under the study of metamaterials. These are composite structures engineered in such a way that they can manipulate waves in a variety of ways (conventional and less conventional) within much smaller structural dimensions than the targeted wavelengths, i.e., to deep-subwavelength extents compared to the more traditional quarter-wavelength or subwavelength approaches. As such, ultra-thin acoustic metamaterials designed around a sound diffusion context will form the core of this research and will be studied under different perspectives.

## 1.3 OUTLINE OF THE THESIS

The present thesis aims to answer the aforementioned research question by exploring the several aspects revolving around the main topic of sound diffusion and acoustic metamaterials, and how these can be designed for overhauling sound diffusion in small auditoria. In order to do so, the thesis unfolds according to the following structure:

CHAPTER 2 presents a general theoretical overview of different wave physics phenomena essential for understanding the mechanisms involved in sound diffusers and acoustic metamaterials, such as wave propagation fundamentals, dispersion relation, dissipative effects introduced by acoustic boundary layers and wave diffraction/scattering theory.

CHAPTER 3 explains what traditional sound diffusers are and how their acoustic characteristics can be quantified. This chapter also provides design insights with respect to some of the sound diffuser types that can be commonly encountered. Lastly, the intrinsic and contextual limitations of such structures are highlighted, paving the way to the use of acoustic metamaterials.

CHAPTER 4 introduces the origin and concept of metamaterials as periodic locally-resonant structures. Furthermore, this chapter provides an analytical model for describing the physical behaviour of sound waves propagating in such medium, emphasizing on the apparition of strong dispersion, band-gaps and subsonic propagation speed. These elements are all critical elements in the de-

sign of highly optimizable deep-subwavelength sound diffusers, a.k.a, metadiffusers.

CHAPTER 5 brings a mix of experimental and numerical validations of some metadiffuser designs, some of which were reported for the first time. It includes experimental acoustic scattering measurements of a 3D-printed Quadratic Residue metadiffuser, numerical simulations of Quasi-Perfect metadiffusers and a cross-optimization study of broadband metadiffusers.

CHAPTER 6 discusses the potential drawbacks of modelling compact structures such as metadiffusers into large Finite-Difference Time-Domain numerical schemes used for simulating the acoustics of a room where the implementation of deep-subwavelength metamaterials would be of beneficial use. This problematic allows to establish a numerical solution based on an RLC-circuit filter optimization for approximating the acoustical characteristics of highly resonant structures, such as metamaterials, in large volumes.

CHAPTER 7 provides a summary of the results developed throughout this research and expounds on future works.

# WAVE PHYSICS & ACOUSTIC SCATTERING

IN order to fully understand how effectively some surfaces can scatter or absorb sound, it is important to first grasp the principles of sound propagation and how the latter behaves when interacting with physical boundaries. In this chapter, emphasis will be given to the description of propagating acoustic waves further leading to useful formulations characterizing sound scattering and diffusion; two core aspects at the centre of this work.

## 2.1 FUNDAMENTALS OF PHYSICAL ACOUSTICS

The following section outlines the fundamental aspects of wave theory required to formulate a wave propagation equation and thus to define the intrinsic propagation characteristic parameters of the latter.

### 2.1.1 *Thermodynamic Assumptions & Conservation Laws*

For simplicity, only one-dimensional (1D) acoustic wave propagation in a duct (a waveguide) will be considered. The 1D conservation equations used to describe such propagation of sound depend of a set of basic thermodynamic assumptions, which are generally respected for the transport of acoustic energy through a fluid such as air. Here, the underlying assumptions are:

1. The control volume of the fluid is fixed in space, i.e., the volume of fluid being moved is constant throughout the continuum geometry;

2. The flow of the disturbance is in one dimension;

3. Body forces are not significant, i.e., forces that act throughout the whole volume of a body, such as gravity, are not considered;

4. The fluid is inviscid, i.e., viscous effects are not accounted for and the only significant force applied is pressure; and

5. The fluid is approximated as being lossless, or non-dissipative.

Should these assumptions hold true, the 1D conservation equations – Equation of Continuity (Eq. 2.1), Momentum (Eq. 2.2) and State (Eq. 2.3) – write as

$$\frac{\partial \rho}{\partial t} + \frac{\partial}{\partial x}(\rho v) = 0, \tag{2.1}$$

$$\rho\left(\frac{\partial v}{\partial t} + v \cdot \frac{\partial v}{\partial x}\right) + \frac{\partial p}{\partial x} = 0, \tag{2.2}$$

$$p = c_0^2 \delta\rho \left[1 + \frac{B}{2!A}\frac{\delta\rho}{\rho_0} + \frac{C}{3!A}\left(\frac{\delta\rho}{\rho_0}\right)^2 + \ldots\right], \tag{2.3}$$

where $\rho$, $\rho_0$ and $\delta\rho \equiv \rho - \rho_0$ represent the total density, ambient density and excess density of the medium, respectively, $v$ is the fluid particle velocity vector, $p = P - p_0$ denotes the excess acoustic pressure made by the wave pressure $P$ over the ambient pressure $p_0$, and $c_0$ is the ambient speed of sound. $A$, $B$ and $C$ are coefficients based on the nature of the fluid (gas or liquid) obtained from a Taylor series expansion of $\delta\rho/\rho_0$. The coefficient $A$ is better known as the adiabatic bulk modulus of the fluid later referenced as $\kappa$.

This set of non-linear equations can be linearly approximated by a small-signal approach where the physical variables related to the wave disturbance of the medium, $p$, $v$, and $\delta\rho$, are considered much smaller than their static quantities, i.e., $|\delta\rho| \ll \rho_0$, $|p| \ll \rho_0 c_0^2$, and $|v| \ll c_0$. This approximation generally remains valid even for the loudest sounds humans usually experience and thus excludes high pressure shock waves, for example. If approximated this way, the conservation equations simplify to the following linearised format:

$$\frac{\partial \rho}{\partial t} + \frac{\partial}{\partial x}(\rho_0 v) = 0, \tag{2.4}$$

$$\rho_0 \frac{\partial v}{\partial t} + \frac{\partial p}{\partial x} = 0, \tag{2.5}$$

$$p = c_0^2 \delta\rho. \tag{2.6}$$

This set of equations will form the basis for the propagation of 1D sound waves in a waveguide. These will respectively be amended as further examples of viscid and

12

dissipative media will be considered in order to illustrate the impact of viscous and thermal effects on the wave being propagated. The linear conservation equations also allow the derivation of the linear wave equation.

### 2.1.2 *The Wave Equation & Wave Characteristics*

The wave equation is a second order Partial Differential Equation (PDE) describing the propagation of disturbances in a medium in one or more directions at a certain speed, which can be formulated as

$$c^2 \nabla^2 u - \frac{\partial^2 u}{\partial t^2} = 0, \tag{2.7}$$

where $\nabla^2$ is a Laplacian defined in Cartesian coordinates as $\nabla^2(\cdot) = \nabla(\nabla(\cdot)) = \partial/\partial_x^2(\cdot) + \partial/\partial_y^2(\cdot) + \partial/\partial_z^2(\cdot)$, $u$ is a physical scalar property associated with the disturbance of the signal, $c$ represents the speed at which the wave travels, and $x, y, z$ and $t$ are the Cartesian spatial coordinates and time, respectively.

As the wave equation is a PDE, various solutions can be found to be suitable for energy propagation. There is however a set of solutions commonly agreed upon representing the 1D propagation of a wave through space, described in the form of a linear superposition of two waves, $f(\xi)$ and $g(\eta)$, such that

$$\xi = x - ct, \tag{2.8}$$

$$\eta = x + ct, \tag{2.9}$$

$$u(\xi, \eta) = f(\xi) + g(\eta) = f(x - ct) + g(x + ct), \tag{2.10}$$

or

$$u(\xi, \eta) = f\left(t - \frac{x}{c}\right) + g\left(t + \frac{x}{c}\right). \tag{2.11}$$

Equation 2.10, usually known as d'Alembert's formula, shows that solutions of the 1D wave equation are sums of a right (forward) and left (backward) travelling wave functions, $f(\xi)$ and $g(\eta)$ respectively. Due to the linearity of the wave equation, it thus implies that at any moment $t$ any point of space $x$ follows the theorem of superposition. An advantage with d'Alembert's formulation is that it

can cover many solution types of the wave equation, such as $u = A \sin a(x - ct)$, $u = A \cos a(x - ct)$, $u = A e^{\pm ia(x-ct)}$, $u = A \ln a(x - ct)$, $u = A(x - ct)^n$ or even $u = \delta(x - a)$. Basically, d'Alembert's formulation encompasses any wave function that can be expressed as a Laurent series of the type

$$u(x, t) = \sum_{n=-\infty}^{\infty} a_n (x - ct)^n. \tag{2.12}$$

Taking a solution of the type $u(x, t) = f(x - ct)$ for describing the propagation of a 1D progressive wave, and assuming that the second backward propagative term is null (thus assuming just a forward $+x$ direction travelling wave), the derivation of $u$ along time and space allows to write the relation between the two derivatives as

$$\frac{\partial u}{\partial t} = -c \frac{\partial u}{\partial x}. \tag{2.13}$$

By reordering the linearised Momentum equation in Eq. 2.5, and injecting Eq. 2.13 for $u = v$ into the latter, the Momentum equation becomes

$$\frac{\partial p}{\partial x} = \rho_0 c_0 \frac{\partial v}{\partial x}, \tag{2.14}$$

The pressure can thus be expressed in simple terms by integrating over $x$:

$$p = \rho_0 c_0 v \quad \text{or} \quad p = Z_0 v, \tag{2.15}$$

where $Z_0 = \rho_0 c_0 = (p/v)|_{+x}$ is the specific acoustic impedance of the medium defined for a $+x$ propagative wave.

The concept of impedance is paramount for describing the acoustic characteristics of a medium, as it is a quantity that describes the resistivity of a medium with respect to the acoustic disturbance propagating through it, i.e., it *impedes* the flow of energy. In the general case of fluid media of undefined section or geometry (i.e., unbounded), the characteristic acoustic impedance can be defined as above by using a point-like definition of the particle velocity. However, in the case of plane wave propagation in a bounded system of finite width, such as a duct, it may be useful to use a flow formulation of the particle velocity, or volume velocity. For any wave with constant pressure over a specified area, e.g., a plane wave in a duct of
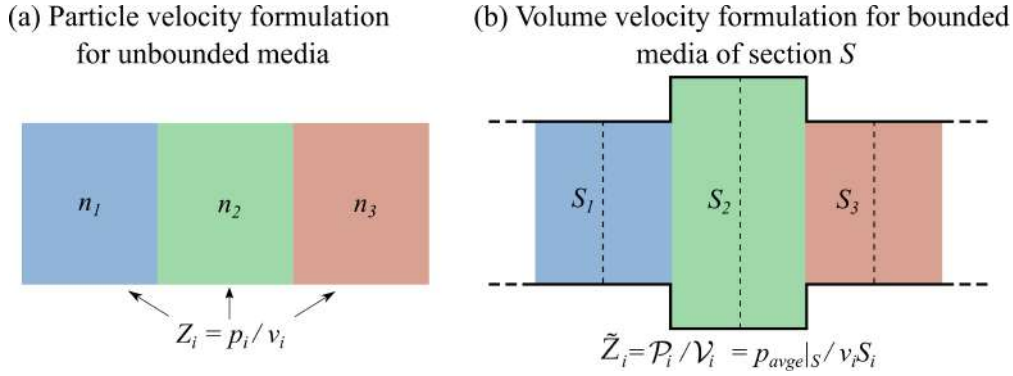
Figure 2.1: Schematic diagram displaying the formulation of the acoustic impedance in (a) an unbounded media and (b) a bounded media of cross-section area $S$.

cross-sectional area $S$, the acoustic impedance, $\tilde{Z}$, is here defined as the ratio of the pressure averaged over that surface, $\mathcal{P}$, to the volume velocity, $\mathcal{V} = Sv$, such that

$$\tilde{Z} = \mathcal{P}/\mathcal{V} = Z/S, \tag{2.16}$$

where the $\tilde{\ }$ upper-script denotes the use of volume velocity rather than particle velocity.

The notion of particle flow is a convenient tool at disposition when describing the propagation of sound waves in waveguides of different cross-section. Due to the reflections thus generated at the boundaries between the different section elements, the particle flow formulation of the characteristic impedance allows to generalize the state of the acoustical variables for a waveguide of given cross-section area. This formulation will indeed be useful for describing further acoustical notions in Chaps. 3 and 4.

### 2.1.3 *Fourier Transforms & the Helmholtz Equation*

Generally, the use of time harmonic signals in wave physics, such as cosines or sines, is preferred due to their convenient form and ease of operation when dealing with derivatives and complex numbers. This stems from Euler's formula which establishes a fundamental relationship between trigonometric functions and a complex exponential function, written as

$$e^{ix} = \cos x + i \sin x, \tag{2.17}$$

where $e$ is the Euler number and $i = \sqrt{-1}$ is the imaginary unit. This formulation is described as a "jewel" for mathematics, physics and engineering alike by R. Feynman who depicted it as the most remarkable formula in mathematics [40]. This way, a harmonic wave of radial frequency $\omega = 2\pi f$, and wavenumber $k = \omega/c$, cannot only be described by a trigonometric function, say $u(x,t) = A\cos(\omega t - kx)$, but can also be expressed in exponential terms, e.g., $u(x,t) = Ae^{i(\omega t - kx)}$.

However, not all waves are steady state monochromatic (i.e., of single wavelength) but some may be transient and broadband to a relative degree. In the case of a waveform with multiple frequencies, the equally powerful Fourier transform pairs devised a century after Euler's formula take the full advantage of the latter in order to define that any complex wave can be constructed as a sum of harmonic waves. More specifically, the Fourier transform pairs offer the ability to change one's perspective of the wave, observing it either in the time domain or in the frequency domain. Given a time domain signal $u(x,t)$, the frequency domain equivalent, $\hat{u}(x,\omega)$ ($\hat{\phantom{u}}$ denoting the frequency transformed signal), can be obtained by

$$\hat{u}(x,\omega) = \mathcal{F}[u(x,t)] = \int_{-\infty}^{\infty} u(x,t)e^{-i\omega t}\mathrm{d}t, \tag{2.18}$$

where $\mathcal{F}$ denotes the Fourier transform defined by the integration operation. Conversely, a return to the time domain can be achieved by the inverse Fourier transform as

$$u(x,t) = \mathcal{F}^{-1}[\hat{u}(x,\omega)] = \frac{1}{2\pi}\int_{-\infty}^{\infty} \hat{u}(x,\omega)e^{i\omega t}\mathrm{d}\omega. \tag{2.19}$$

In the same logic, the wave equation can also be transformed from its time-domain formulation to a frequency-domain one, either via direct Fourier (or Laplace) transform or by assuming a time-harmonic wave function $\phi$ of amplitude $\Phi$, such as $\phi = \Phi e^{i\omega t}$. Then, one obtains

$$\nabla^2 \phi + k^2 \phi = 0, \quad \text{or} \quad \left(\nabla^2 + k^2\right)\phi = 0, \tag{2.20}$$

resulting in the Helmholtz equation, where $\nabla^2$ is a Laplacian, $k$ is the wavenumber and $\phi$ is a derivable wave function. This is a second order PDE representing a time-independent form of the wave equation.

$$a_n \cos(nx) + b_n \sin(nx)$$
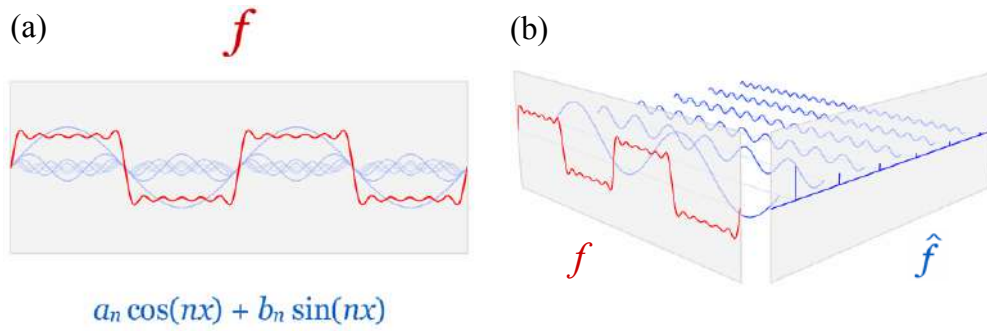
Figure 2.2: (a) Wave signal composed by a multitude of frequencies. (b) Decomposition of the total wave signal into individual wave constituents. [from Wikipedia [41], CC]

The application of Fourier transforms does not strictly stop at time-frequency transformations but can also be used to describe wave radiation from a surface based on its complex valued reflection coefficient, a fact that will be further explored in this chapter (see Sec. 2.3.3). Furthermore, Fourier transforms are generally easier to compute because of (i) the fast and efficient Fast Fourier Transform (FFT) algorithms widely available, and (ii) the lower dimensionality of the Helmholtz equation (3 dimensions) compared to the wave equation (4 dimensions). Due to the critical nature of Fourier Transforms, their application has become a paramount topic in the study of wave physics, owing to J. Fourier an as remarkable contribution to science than that of L. Euler. In F. Hunt's words [42]: "Blessed be Fourier!".

## 2.2 DISSIPATIVE EFFECTS IN FLUID MEDIA

This section emphasizes on the description of dissipative processes in fluid media as well as the resulting dispersion relation representing how different propagating wavelengths are affected by the medium's effective parameters.

### 2.2.1 *Wave Dispersion & Dispersion Relation*

At the beginning of this chapter, a simple 1D wave equation framework was stated under many ideal thermodynamic assumptions concerning the medium. A

general solution to this wave equation was shown through d'Alembert formulation in Eq. 2.11, illustrating the principle of linear wave superposition. Additionally, Fourier transform pairs were used to state that any periodic signal can be decomposed into a sum of its harmonic constituents. Therefore, a space and time propagating signal, $p(x,t)$, being the sum of discrete harmonic frequencies, can also be considered a solution of the wave equation. This travelling wave signal can be termed as a wave packet, or wave train, defined by its disturbance "envelope", i.e., the spatial sum of its frequency constituents. If such time-harmonic solution was plugged into the wave equation (Eq. 2.7), the speed of each of the propagating wavelengths would be defined as

$$c_p = \frac{\omega}{k},\tag{2.21}$$

where $c_p$ is the phase velocity of waves inside the packet, each with a wavenumber $k$ and an angular frequency $\omega$. This ratio of angular frequency over wavenumber is commonly referred to as the *dispersion relation* of the disturbance within the medium. In wave physics, *dispersion* is the phenomenon where the phase velocity of the propagating wave is dependent of its frequency. In the simplified 1D case above (Eq. 2.21), the dispersion relation indicates that the speed of sound is constant for every wavenumber, or frequency, and that no dispersion is happening inside the medium. In this case, the group velocity, $v_g$, of the entire packet is the same as the phase velocity, i.e., $v_g \equiv \partial\omega/\partial k = c_p$. Such a medium is thus termed as being non-dispersive and wave packets travelling through it will maintain a constant shape as all the constituting frequencies will remain at the same relative speed between each other.

However, in the case of dispersion, where the frequency components that make up the wavelet have different speeds, the relative phase between the components would change over distance, therefore adding to a distinct wavelet shape with a different propagative speed than its frequency components. Although such phenomenon is commonly disregarded in many ideal aspects of acoustic wave propagation in air – due to the infinitesimal amount of dispersion present in most cases – it is however a fundamental concept that is likely to arise with the addition of any detailed physical phenomema, such as dissipative effects that affect wave energy
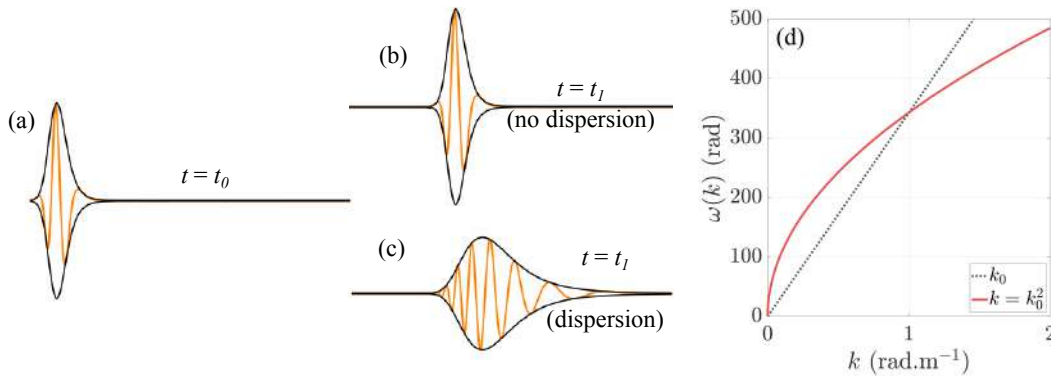
Figure 2.3: (a) Wave packet at $t = t_0$. (b) Wave packet at $t = t_1$ in a non-dispersive medium. (c) Wave packet at $t = t_1$ in a dispersive medium with a changed envelope. (d) Dispersion relation of the two media, where the dispersive medium has $k = k_0^2$. [(a,b,c) modified from Wikipedia [43], CC]

transportation and absorption in the medium. These effects generally come in the form of viscosity, heat conduction or relaxation, and can be found in free-field wave propagation as well as near media boundaries. As it will be explained further along in this work, the inclusion of such dissipative effects can lead to strong dispersion in particular cases.

Under the ideal set of thermodynamic assumptions aforementioned, the dispersion relation is found to be constant for all frequencies. Such relation describes the wavenumber $k$ as a function of the angular frequency $\omega$, i.e., $k = k(\omega)$, which has real and imaginary parts:

$$k = \beta - i\alpha_{\text{att}}, \tag{2.22}$$

where $\alpha_{\text{att}}$ is the attenuation coefficient and $\beta$ (real part of $k$) is related to the phase speed by $c_p = \omega/\beta$ through the Kramers-Kronig relation [44, pp. 122-127]. The latter describes the frequency dependence of wave propagation and attenuation in a medium by linking the real and imaginary parts of a complex function. This can be shown by substituting Eq. 2.22 in a time harmonic solution, yielding

$$u = u_0 e^{-\alpha_s x} e^{i(\omega t - \beta x)} = u_0 e^{-\alpha_s x} e^{i\omega\left(t - \frac{x}{\omega/\beta}\right)}, \tag{2.23}$$

where the first negative exponential term indicates a reduction of the wave amplitude with respect to distance and the second imaginary exponential term represents the phase change of the wave through time and distance. Due to the decay of sound

19

with respect to distance, $\alpha_s$ represents here the *spatial* attenuation coefficient, in opposition to the *temporal* attenuation coefficient that can be found in time based problems where one wants to know how rapidly sound decays with time. In order to express the temporal attenuation coefficient, one must then take an initial value wave field defined in space at a time $t = 0$ through the following solution:

$$u = u_0 e^{ik(x-ct)}. \tag{2.24}$$

In this case, the wavenumber $k$ is regarded as real valued and $c$ can be determined from the previous dispersion relation $c_p = \omega/\beta$ with $\beta = k + i\alpha_{\text{att}}$. Here, $\alpha_{\text{att}}$ will be replaced by $\alpha_t$, the temporal attenuation coefficient, in order to avoid confusion between the two types of attenuation coefficients. Thus, the expression for $u$ becomes

$$u = u_0 e^{-\alpha_t t} e^{i(\omega t - \beta x)}. \tag{2.25}$$

where, in the same manner as before, the fist exponential term shows the attenuation of acoustic energy through time, whilst the second represents the phase change. Thanks to Eq. 2.23 and Eq. 2.25, the speed of sound $c$ can be divided into real and imaginary components similarly to Eq. 2.22:

$$c = c_p - i\frac{\alpha_t}{k}. \tag{2.26}$$

### 2.2.2 *Overview of Viscothermal Acoustic Boundary Layers*

One of the most important dissipative effects encountered throughout this work is that of visco-thermal losses (and dispersion) generated by the presence of boundary layers, which arise when a wave travels very close to, or over a surface. In such context, the presence of a boundary exerts a frictional shear force in the form of drag, or resistance, over the fluid which locally strengthens its viscous properties. Simultaneously, the interface of the two media, fluid and surface boundary, opens the way for heat conduction to take place between the two whenever temperature differences are to exist.

The following section summarizes knowledge of standard (free-field) viscous, thermal and viscothermal dissipative processes in viscid fluids. For the sake of clarity, more extensive details concerning the forms of the respective propagation

equations and dispersion relations of each dissipative process can be found in Appendix A.

Unlike previously, let's consider the 1D propagation of time-harmonic plane waves in a *viscid* fluid bounded by two surfaces, much like an infinite duct. In the mainstream, centred around the main axis (away from the boundaries), the amplitude of the particle oscillations is nominal but will be decreased the closer to the boundaries as these will make the fluid adhere to them. A transition zone can therefore be stipulated where the values of particle displacement go from nominal in the mainstream to minimal (down to zero) at the boundaries. This transition region is called the *acoustic boundary layer* – not to be confused with the ordinary viscous boundary layer that develops over distance on a surface due to a steady fluid flow on it. In an inviscid fluid, the flow would be frictionless and the acoustic boundary layer non-existent. In viscid scenarios, the thickness of the viscous acoustic boundary layer can be defined [45] by

$$\delta_{visc}^{BL} = \sqrt{\frac{2\mu}{\omega\rho_0}} = \sqrt{\frac{2\nu}{\omega}}, \tag{2.27}$$

which is the distance from the wall required for the particle velocity amplitude to increase from zero to $1/\upsilon$ of its mainstream value, and where $\nu = \mu/\rho_0$ is the kinematic viscosity coefficient and $\mu$ the shear viscosity coefficient. This distance is frequency-dependent and is usually quite small, e.g., 0.2 mm at 100 Hz. However, as illustrated further in this work, the distance can become non-negligible in relatively narrow scenarios, thus affecting the absorption and dispersion of propagating acoustic waves.

A thermal acoustic boundary layer simultaneously coexists with the viscous one. In the mainstream, compressions and rarefactions take place adiabatically (with no heat transfer) whereas close to the surfaces the flow tends to be isothermal (where its remains at constant temperature, balancing any discrepancies). As the surface can be considered as an infinite heat source (or sink), adjacent fluid particles tend to stay at the same temperature where any deviations are quickly quenched by heat flow from the wall to the fluid. The thermal acoustic boundary layer is thus
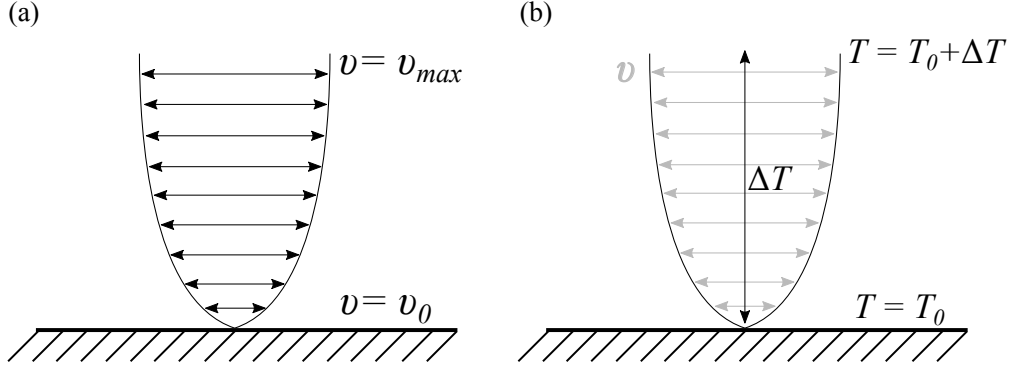
Figure 2.4: (a) Viscous boundary layer for oscillating particle velocity $v$. (b) Thermal boundary layer for temperature $T$. (close up at the boundary)

the region near the surface where the thermal character of the flow changes from adiabatic to isothermal. The thickness of such region is

$$\delta_{therm}^{BL} = \sqrt{\frac{2\vartheta}{\omega\rho_0 C_p}} = \sqrt{\frac{2\mu}{\omega\rho_0 \mathrm{Pr}}} = \frac{\delta_{visc}^{BL}}{\sqrt{\mathrm{Pr}}}, \tag{2.28}$$

where $\vartheta$ is the heat conduction coefficient, $\mathrm{Pr} = \mu C_p / K$ is the dimensionless Prandtl number used to characterise the importance of viscosity with respect to heat conduction, $C_p$ is the specific heat at constant pressure (related to the specific heat at constant volume, $C_v$, by the the ratio of specific heats $\gamma = C_p / C_v$) and $K$ is the thermal conductivity.

The two types of acoustic boundary layers can be combined into a single viscothermal wave equation in order to account for both processes by deriving and combining the momentum and energy equations of both models (see App. A). From this, effective propagation parameters, such as the density and bulk modulus, can be determined in order to further examine the acoustic properties of the medium, e.g., determine wavenumbers and dispersion relations. However, such fundamental formulation can be quite cumbersome to work with, and thus approximate models have been developed to achieve similar goals.

### 2.2.3 *Complex Density & Compressibility in Narrow Tubes*

In 1991, M. Stinson published a paper [46] on plane wave sound propagation in narrow and wide circular tubes, as well as a generalization of the theory for tubes

of arbitrary cross-sectional shape. There, he reviews the general Kirchhoff theory of sound propagation in circular tubes, for which analytical approximations were given by Zwikker and Kosten [47]. By assuming (i) a constant pressure over the tube's cross-section, and (ii) that excess density and pressure where comparable in magnitude to their respective equilibrium values, the latter approximations would allow to separate complex density and compressibility parameters into much simpler forms, for both narrow and wide tubes in low and high frequency regimes. The intermediary frequency range was later covered by Stinson's approach, which would also extend Zwikker and Kosten approximations to tubes of arbitrary cross-sectional shape rather than just circular ones.

The following part of this section will focus on the physical developments of Stinson's paper. For ease of read, most mathematical derivations are here omitted in exchange for a better emphasis on the conceptual steps and on the important resulting equations.

Starting with Kirchhoff's general theory of sound propagation in a circular tube of radius $r_c$ containing an ideal gas of viscosity $\mu$ and thermal conductivity $K$, a system of equations relating the pressure $P$, the temperature $T$, the density $\rho$ and the particle velocity $\vec{v}$ can be determined by the linearized Navier-Stokes force equation [39, Chap. 10], the mass continuity equation (Eq. A.1 in App. A) and the thermally conducting wave equation (Eq. A.14 in App. A). Considering $\vec{v}$ to be composed of radial and axial unit vector basis $\hat{r}$ and $\hat{z}$, respectively, i.e., $\vec{v} = q\hat{r} + u\hat{z}$, a set of solutions for $u$ (axial velocity component), $q$ (radial velocity component), $\delta\tau$ (excess temperature), $p$ (excess pressure) and $\delta\rho$ (excess density) can be expressed. Yet, the formulation for these solutions is quite cumbersome as it still relies on differential operators, which are not only explicitly termed in most solutions but also redundantly found within in $u$ and $q$ through a propagation constant $\mathcal{M}$. Even by integrating such formulations over the cross-section of the circular tube so that most differential terms disappear along the axial direction, the resulting system of equations can still be difficult to apply.

A simplified expression of the above system of equations can be made by assuming a set of approximations: (i) that pressure is constant along the cross-section

of the tube, and (ii) that excess pressure and density are of similar magnitude than equilibrium values. This way the complexity of the wave propagation constant $\mathcal{M}$ can be significantly simplified, as well as enabling a separation of viscous and thermal effects. Applying such approximations yields much simpler average velocity $\langle u \rangle$ and excess density $\langle \delta\rho \rangle$ formulations, through which similarly simple complex density and compressibility equations can be defined, For a *cylindrical* duct of radius $r_c$, the latter can be written as

$$\rho_e(\omega) = \rho_0 \left[ 1 - \frac{2}{r_c G_\rho(\omega)} \frac{J_1(r_c G_\rho(\omega))}{J_0(r_c G_\rho(\omega))} \right]^{-1}, \tag{2.29}$$

$$\kappa_e(\omega) = \kappa_0 \left[ 1 - \frac{2(\gamma - 1)}{r_c G_\kappa(\omega)} \frac{J_1(r_c G_\kappa(\omega))}{J_0(r_c G_\kappa(\omega))} \right]^{-1}, \tag{2.30}$$

where $r_c$ is the radius of the cylindrical duct, $J_n$ is the Bessel function of the first kind and order $n$, and with $G_\rho(\omega) = \sqrt{i\omega\rho_0/\eta}$ and $G_\kappa(\omega) = \sqrt{i\omega\rho_0 \mathrm{Pr}/\eta}$. Of course, such formulation is only valid for cylinders, and accuracy in predictions will decrease the higher the frequency inside the circular tube, with a limit at the cut-off angular frequency $\omega < 1.84 c_0/r_c$. Higher frequencies in the duct might lead to strong higher-order modes thus invalidating the plane wave approximation.

For arbitrary cross-sectional shapes, and assuming the propagation constant $\mathcal{M}$ to be very small compared to $G_\rho(\omega)$ and $G_\kappa(\omega)$, the complex density and compressibility functions take much general formulations which are dependent on the type of acoustic wave solution that is being propagated.

For a *rectangular* cross-section, the complex density and compressibility are defined as

$$\rho_e(\omega) = \rho_0 \frac{(a/2)^2 (b/2)^2}{4 G_\rho^2(\omega) \sum\limits_{m \in \mathbb{N}} \sum\limits_{n \in \mathbb{N}} \left[ \alpha_m^2 \beta_n^2 (\alpha_m^2 + \beta_n^2 - G_\rho^2(\omega)) \right]^{-1}}, \tag{2.31}$$

$$\kappa_e(\omega) = \kappa_0 \frac{1}{\gamma + \frac{4(\gamma-1)G_\kappa^2(\omega)}{(a/2)^2(b/2)^2} \sum\limits_{m \in \mathbb{N}} \sum\limits_{n \in \mathbb{N}} [\alpha_m^2 \beta_n^2 (\alpha_m^2 + \beta_n^2 - G_\kappa^2(\omega))]^{-1}}, \tag{2.32}$$

where $a$ and $b$ are the dimensions of the rectangular cross-section, $\alpha_m = (2m + 1)\pi/a$ and $\beta_m = (2n + 1)\pi/b$.

In the case of a *narrow slit* of width $h$ and length $l \gg h$, which will be of

great interest further along in this work, the complex density and compressibility functions can be simply written as

$$\rho_e(\omega) = \rho_0 \left[ 1 - \frac{\tanh(\frac{h}{2}G_\rho(\omega))}{\frac{h}{2}G_\rho(\omega)} \right]^{-1}, \tag{2.33}$$

$$\kappa_e(\omega) = \kappa_0 \left[ 1 + (\gamma - 1)\frac{\tanh(\frac{h}{2}G_\kappa(\omega))}{\frac{h}{2}G_\kappa(\omega)} \right]^{-1}. \tag{2.34}$$

The inclusion of vicsothermal acoustic boundary layers in a waveguide can lead to significant losses, mostly depending of the dimensions of the duct with respect to the size of the boundary layers. Moreover, the presence of acoustic boundary layers can induce strong dispersion, further inducing changes on the propagation speed of the wave disturbance. Such effects shall be explored later in the thesis as they can play a major role in metamaterial design strategies.

## 2.3 ACOUSTIC SCATTERING OF LOCALLY-REACTING SURFACES

Wave scattering can lead to many types of practical applications, such as tomographic reconstruction techniques used in atmospheric science [48], oceanography [49] or biomedical imaging [50]. Scattering is also at the core of sound (and light) diffusion. To better understand the nature behind this phenomena, the next section emphasizes on the principles of sound reflection before dwelling on the different theories of wave diffraction.

### 2.3.1 *Principles of Sound Reflection*

The interaction of an acoustic wave with an assumed infinitely large surface of any kind results in three main acoustic effects, known as sound absorption, transmission and reflection. Considering a plane wave incident at an angle $\psi$ to a perfectly rigid boundary at $y = 0$, as illustrated in Fig 2.5, the incident and reflected pressures, $p_i$ and $p_r$ are given by

$$p_i = A_i e^{i(\omega t + kx\cos\psi + ky\sin\psi)}, \tag{2.35}$$

$$p_r = A_r e^{i(\omega t + kx\cos\theta - ky\sin\theta)}, \tag{2.36}$$

where $A_i$ and $A_r$ are the magnitudes of the incident and reflected waves, respectively. Here, the transmission and absorption phenomena are neglected as the boundary is assumed to be infinitely rigid. This implies a Neumann boundary condition of the type

$$\frac{\partial p}{\partial y}\bigg|_{y=0}, \tag{2.37}$$

where $p = p_i + p_r$ from Snell-Descartes law of reflection. The ratio of reflected over incident pressures defines the acoustic reflection coefficient as

$$R = \frac{p_r}{p_i}, \tag{2.38}$$

which characterises the magnitude and phase of the sound waves being reflected by the surface. In the case of oblique incidence (normal incidence being a simplified case), the reflection coefficient can also be written as:

$$R = \frac{\frac{Z}{\rho_0 c_0}\cos(\psi) - 1}{\frac{Z}{\rho_0 c_0}\cos(\psi) + 1}, \tag{2.39}$$

$$\frac{Z}{\rho_0 c_0}\cos(\psi) = \frac{1 + R}{1 - R}, \tag{2.40}$$

where $Z/\rho_0 c_0 = Z/Z_0$ is the normalized specific acoustic impedance. The admittance of the surface, Y, is defined as the reciprocal of the impedance, i.e.,

$$\text{Y} = \frac{1}{Z}. \tag{2.41}$$

As the real and imaginary terms of the surface impedance (viz., resistance and reactance) provide information about the energy losses and the phase changes of the wave being reflected, the acoustic impedance or its equivalent surface reflection
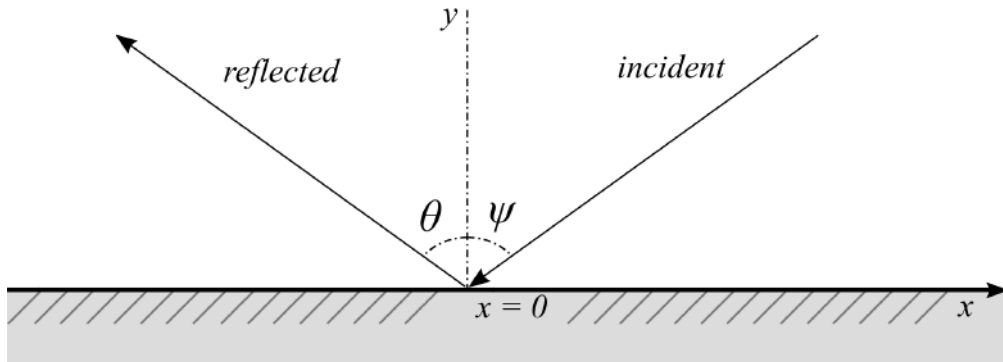


Figure 2.5: Schematic decomposition of an incident sound wave propagating in a medium hitting a rigid boundary at $y = 0$ and at an angle $\psi$.

coefficient can therefore give more insight into the absorbing properties of the surface than the absorption coefficient of a surface alone, defined as

$$\alpha = 1 - |R^2|, \tag{2.42}$$

where $|R^2|$ is the magnitude of the complex reflection coefficient, therefore resulting in a loss of complex-valued information. This is why a lot of importance is usually given to reflection and transmission coefficients, or acoustic impedances, as they allow to exhibit complex-valued information about the change of acoustic propagation at the boundary between different media.

### 2.3.2 *Theories of Wave Diffraction*

In the previous subsection, sound reflection was treated as a purely specular phenomenon, i.e., the wavelength of the impinging acoustic wave was assumed to be relatively small compared to the boundary it is being reflected from. The rest of this chapter will emphasize on another aspect of sound reflection, that is diffraction. Diffraction appears where sound waves interact with objects of similar size than their wavelength. Due to the wave nature of the propagation, such scenario usually involves the ability of sound waves to re-radiate from the blocking object, go around it and spread further. This phenomenon implies that secondary sound sources located at the boundaries of the obstacle can potentially add to each other, due to the principle of superposition, which in turn can cause areas of destructive or constructive interferences. The interference born from this superposition can thus create complex radiation patterns, the shape of which can be crucial for controlling the propagation of sound.

#### 2.3.2.1 *Helhmholtz-Kirchhoff Diffraction*

The methods for predicting the amount of energy radiated from a diffracting object are many and generally depend on the degree of mathematical acumen used to describe the physical phenomena at play. The most common starting point for predicting the diffracted energy pattern is through the use of the *Huygens-Fresnel* diffraction principle, which states that each point on a wavefront can be considered

the source of a new spherical wave and where the back-propagating portion of each secondary wave is dropped. This concept of virtual secondary spreads forms the basis of diffraction theory, and can be found again in most mathematical statements that derive from the general theory of *Kirchhoff* diffraction. The latter makes use of the known Helmholtz wave equation, and applies to it the knowledge of Green's integral theorem. Being a variant of the more general divergence theorem, Green's theorem relates the surface integral of a field to its volume integral. More precisely, it relates the scalar field $U$ (e.g., scalar field distribution of a solution of the wave equation over the region $U$, such as a pressure field expressed as $p(\mathbf{r}) = e^{ik\mathbf{r}}/\mathbf{r}$) and a Green's function $G$ in a volume $V$ to those of an enclosing surface $S$ (see Fig. 2.6), expressed as

$$\iiint_V \left( U \nabla^2 G - G \nabla^2 U \right) \mathrm{d}V = \iint_S \left( U \frac{\partial G}{\partial n} - G \frac{\partial U}{\partial n} \right) \mathrm{d}S, \tag{2.43}$$

where $n$ is the unit vector locally normal to the surface $S$ pointing inward to the volume. As this function is not continuous on $H_0$ (source position), the latter must be excluded by an additional portion of the surface of integration $S'$ that separates point $H_0$ from the volume $V$. The boundary conditions are normally specified in terms of the values of the function $U$ and its normal derivative $\partial U/\partial n$ on the boundary. If $U$ and $G$ both satisfy the Helmholtz equation and have continuous first and second partial derivatives on the surface of integration, then the volume integral on the left side of Eq. 2.43 vanishes, where the surface integrals over $S$ and $S'$ can be re-arranged into

$$\iint_{S'} \left( U \frac{\partial G}{\partial n'} - G \frac{\partial U}{\partial n'} \right) \mathrm{d}S' = -\iint_S \left( U \frac{\partial G}{\partial n} - G \frac{\partial U}{\partial n} \right) \mathrm{d}S. \tag{2.44}$$

The Kirchhoff Green's function $G_K$ has the form of a spherical wave evaluated at $\mathbf{r_1} = \{x_1, y_1, z_1\}$ generated from point $H_0$ excluded from $V$ by the sphere of radius $\mathbf{r_0} = \{x_0, y_0, z_0\}$, so that

$$G_K = \frac{e^{ik\mathbf{r}}}{\mathbf{r}} \rightarrow \frac{\partial G_K}{\partial n} = \left( ik - \frac{1}{\mathbf{r}} \right) \frac{e^{ik\mathbf{r}}}{\mathbf{r}} \cos(\mathbf{n}, \mathbf{r}), \tag{2.45}$$

where $\mathbf{r} = |\mathbf{r_1} - \mathbf{r_0}|$ is the radius difference between the surface $S$ and $S'$. Considering the limiting case of $S'$ vanishingly collapsing on $H_0$ yields the *Helmholtz-Kirchhoff* (H-K) integral theorem which gives the field $U$ at the location $\mathbf{r}$ as

$$U(\mathbf{r}) = \frac{1}{4\pi} \iint_S \left[ \frac{e^{ik\mathbf{r}}}{\mathbf{r}} \frac{\partial U}{\partial n} - U \frac{\partial}{\partial n} \left( \frac{e^{ik\mathbf{r}}}{\mathbf{r}} \right) \right] \mathrm{d}S. \tag{2.46}$$
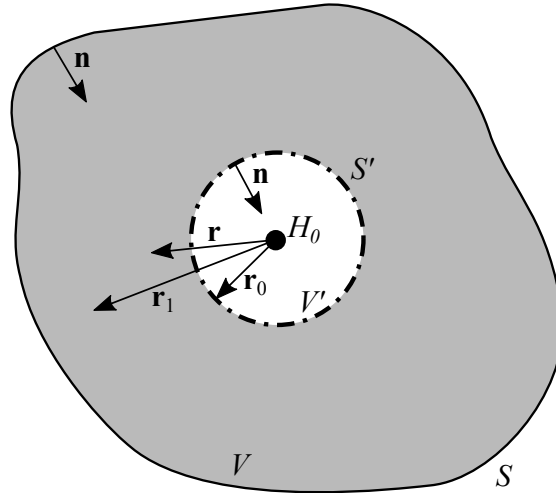
Figure 2.6: Visual representation of the Helmholtz-Kirchhoff integral theorem through Green's theorem, where a volume $V$ is enclosed by a surface $S$.

The latter equation allows for the field $U$ at any point $\mathbf{r}$ to be expressed in terms of its boundary values on any closed surface surrounding that point. It holds true when (i) the scalar theory is used (which makes it more applicable in acoustics than optics), (ii) $U$ satisfies the Helmholtz equation, and (iii) $U$ has first and second partial derivatives on and within $S$.

### 2.3.2.2 *Fresnel-Kirchhoff Diffraction*

The Helmholtz-Kirchhoff integral is a general formulation which needs to be further derived depending on the diffraction scenario. Let's take the more precise case of an observation point $H_0$ and an aperture $\Sigma$ located within a planar screen $S_1$ as shown in Fig. 2.7. The diffraction integral can here be evaluated as a sum of integrals over three portions of a closed surface that include the aperture $\Sigma$, the blocking area $S_1$ surrounding the aperture, and the portion of the propagating sphere $S_2$ with radius $D$. In that case, two types of conditions can be assumed to simplify the Helmholtz-Kirchhoff diffraction integral, viz., the Sommerfeld radiation condition and the Kirchhoff boundary conditions.
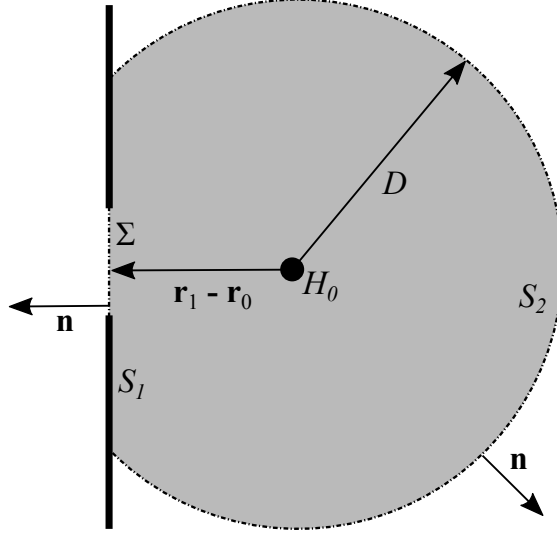
Figure 2.7: Visual representation of the Fresnel-Kirchhoff diffraction through an aperture in a screen.

First, the Sommerfeld radiation condition simplifies the contribution of any potentially diffracting secondary source outside the aperture $\Sigma$ on the surface $S_2$ to the point where it is neglected, expressed in terms of the following limit

$$\lim_{D \to +\infty} D \left( \frac{\partial U}{\partial n} - ikU \right) = 0. \tag{2.47}$$

Practically, this means that the waves being radiated outside the aperture $\Sigma$, i.e. from $S_1$, vanish at least as fast as the original propagating spherical wave, thus excluding their contribution to the quickly expanding surface $S_2$.

On the other hand, the Kirchhoff – or sometimes Cauchy – boundary conditions are used to define the values of $U$ and its derivative $\partial U / \partial n$ over the surrounding area $S_1$. These can be applied if

1. Across the transparent portion of the screen $\Sigma$, both the field and its derivative are exactly the same as they would be in the absence of the screen; and

2. In the surface region outside the screen aperture $\Sigma$, namely $S_1$, both the field and its derivative are zero, i.e., $U$ and $\partial U / \partial n$ are discontinuous at the boundary of the aperture.

Although these conditions may seem unrealistic due to the fact that if the integral solution of $U$ and $\partial U / \partial n$ is zero on a finite surface then its field value is zero

anywhere, the underlying results can still be considered quite correct with respect to experimental measurements despite the lack of physical consistency. The advantage of formulating such conditions is that it greatly helps simplify the diffraction problem from a sum of three integrals over different surfaces to just one, leaving only the integral over the open aperture $\Sigma$.

If it is also assumed that the aperture is illuminated by a spherical wave of unit-amplitude centred on $H_0$, i.e., $U = e^{ik\mathbf{r}}/\mathbf{r}$ , then the *Fresnel–Kirchhoff* (F-K) diffraction integral is obtained:

$$U(\mathbf{r}) = \frac{1}{4\pi} \iint_\Sigma \frac{e^{ik\mathbf{r}}}{\mathbf{r}} \left( \frac{\partial U}{\partial n} + ikU \cos(\mathbf{n}, \mathbf{r}) \right) d\Sigma. \tag{2.48}$$

On top of the previous assumptions, the latter diffraction integral holds true when (i) a single point source radiation is considered, and (ii) the point $P_0$ is several wavelengths away from $\Sigma$, i.e., $\lambda \ll \mathbf{r}$. The last assumption opens the way for alternate versions of the Fresnel–Kirchhoff diffraction integral where the size of the wavelength $\lambda$ over the aperture size, but also with respect to the observing point, is considered in different cases; bringing the notions of near- and far-field diffraction.
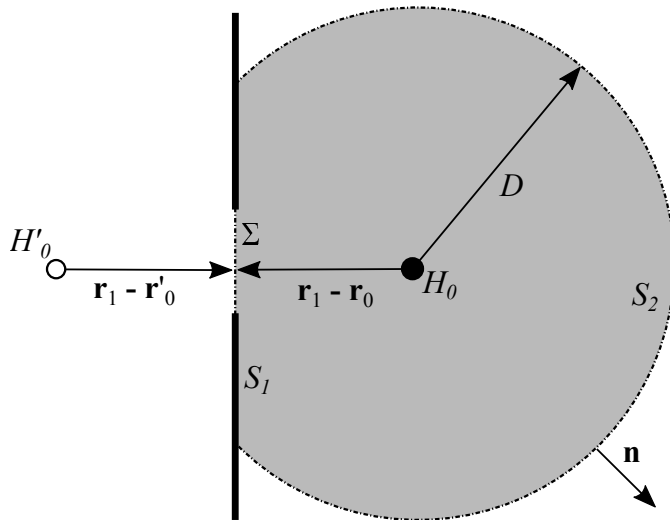


Figure 2.8: Visual representation of the Rayleigh-Sommerfeld diffraction through an aperture in a screen.

### 2.3.2.3 *Rayleigh-Sommerfeld Diffraction*

The apparent inconsistency of Kirchhoff boundary conditions was corrected by Sommerfeld when choosing alternative Green's functions. In the first Sommerfeld case, the Green's function vanishes at the boundary as

$$G_{S1} = \frac{e^{ik\mathbf{r}}}{\mathbf{r}} - \frac{e^{ik\mathbf{r}'}}{\mathbf{r}'} \rightarrow G_{S1}|_{\Sigma} = 0, \tag{2.49}$$

where primed superscripts refer to the mirror image of $H_0$ on the opposite side of the screen. Replacing this new Green's function, equivalent of a Dirichlet boundary condition, into the H-K equation (Eq. 2.46), and simplifying it, yields

$$U(\mathbf{r}) = \frac{1}{4\pi} \iint_{S_1} \left( -U \frac{\partial G_{S1}}{\partial n} \right) dS_1, \tag{2.50}$$

which is one of the *Rayleigh-Sommerfeld* diffraction integrals, here referred as the first. This expression has the advantage of not necessarily needing to specify a value for the derivative of $U$ on $S_1$ since the knowledge of the field $U$ suffices in itself. That way, if one sets $U = 0$ on the portion $S_1$, the field $U$ would remain the same across the aperture as in the absence of screen, thus bypassing the inconsistencies of Kirchhoff boundary conditions. Alternatively, the second Sommerfeld case employs a Green's function which has its derivative vanish as

$$G_{S2} = \frac{e^{ik\mathbf{r}}}{\mathbf{r}} + \frac{e^{ik\mathbf{r}'}}{\mathbf{r}'} \rightarrow \frac{\partial G_{S2}}{\partial n}\bigg|_{\Sigma} = 0, \tag{2.51}$$

where $G_{S2}$ now equates to a Neumann boundary condition. This results in the second *Rayleigh-Sommerfeld* diffraction integral

$$U(\mathbf{r}) = \frac{-ik}{2\pi} \iint_{\Sigma} U(H_1) \frac{e^{ik\mathbf{r}}}{\mathbf{r}} \cos(\mathbf{n}, \mathbf{r}) d\Sigma, \tag{2.52}$$

or

$$U(\mathbf{r}) = \iint_{\Sigma} h(H_0, H_1) U(H_1) d\Sigma, \tag{2.53}$$

where

$$h(H_0, H_1) = \frac{-ik}{2\pi} \frac{e^{ik\mathbf{r}}}{\mathbf{r}} \cos(\mathbf{n}, \mathbf{r}). \tag{2.54}$$

Here, $h(H_0, H_1)$ is a weighting factor that is applied to the field $U(\mathbf{r})$ across the aperture $\Sigma$. The Rayleigh-Sommerfeld diffraction integrals in Eq. 2.50 and Eq. 2.52 show that the field is a superposition of spherical waves (factor $e^{ik\mathbf{r}}/\mathbf{r}$) starting

from each point in the aperture, each with an appropriate amplitude and obliquity factor – an illustration of the Huygens-Fresnel principle previously mentioned.

The Rayleigh-Sommerfeld and Fresnel-Kirchhoff diffraction integrals are very similar, with a difference in their obliquity factor. Assuming a relatively large distance **r** or axial placement in the Rayleigh-Sommerfeld integral, the ubiquity factor reduces to unity and brings both integrals to the same formulation. Being more complete, the Rayleigh-Sommerfeld integral is thus commonly defined as a formulation better suited for near-field situations. Depending on how far the field is then to be estimated, further approximations to the Fresnel-Kirchhoff integral can lead to more simple formulations of the diffraction, using either Fresnel (simplified near-field) or Fraunhofer (far-field) integrals.

#### 2.3.2.4  *Fresnel & Fraunhofer Diffraction*

In the case of the Fresnel diffraction integral, Eq. 2.48 is approximated for small aperture sizes with respect to the wavelength ($a \ll \lambda$, where $a$ is the size of the aperture). Assuming now a 3D Cartesian coordinate system, where the aperture lies in the $(x_0, y_0)$ plane, illuminated from the left by a monochromatic wave $U$, the field can be calculated in the plane of observation $(x_1, y_1)$, parallel to $(x_0, y_0)$
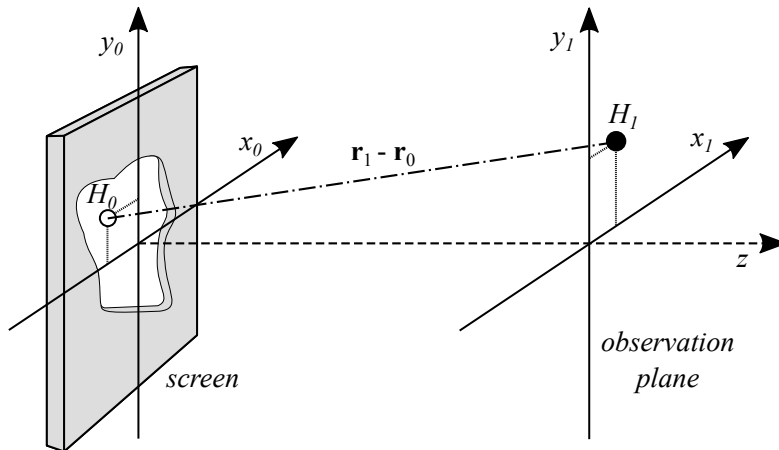


Figure 2.9: Visual representation of the Fresnel and Fraunhofer diffraction through an aperture in a screen.

but a distance $z$ to the right (see Fig. 2.9). Starting with the Rayleigh-Sommerfeld integral, the field in the point $H_1$ can be described as

$$U(\mathbf{r}) = \iint_\Sigma h(x_0, y_0, x_1, y_1) U(x_0, y_0) \mathrm{d}x_0 \mathrm{d}y_0, \tag{2.55}$$

with

$$h(x_0, y_0, x_1, y_1) = \frac{-ik}{2\pi} \frac{e^{ik\mathbf{r}}}{\mathbf{r}} \cos(\mathbf{n}, \mathbf{r}), \tag{2.56}$$

and

$$\mathbf{r} \equiv | \mathbf{r} - \mathbf{r_0} | = \sqrt{z^2 + (x_0 - x_1)^2 + (y_0 - y_1)^2}. \tag{2.57}$$

Assuming a paraxial situation, where the axial distance $z$ is much larger than the transverse dimensions $x$ and $y$, then the ubiquity factor can be approximated to unity, i.e., $\cos(\mathbf{n}, \mathbf{r}) \approx 1$, and the distance $\mathbf{r}$ in the denominator replaced by $z$ (and not in the exponential term as it is highly sensitive to variations), leading to

$$h(x_0, y_0, x_1, y_1) \approx \frac{-ik}{2\pi z} e^{ik\mathbf{r}}. \tag{2.58}$$

Furthermore, the exponential term can be developed into a binomial expansion, retaining only the first two terms, where

$$\mathbf{r} \equiv | \mathbf{r} - \mathbf{r_0} | \approx z \left[ \frac{1}{2} \left( \frac{x_0 - x_1}{z} \right)^2 + \frac{1}{2} \left( \frac{y_0 - y_1}{z} \right)^2 \right], \tag{2.59}$$

resulting in

$$h(x_0, y_0, x_1, y_1) \approx \frac{-ike^{ikz}}{2\pi z} e^{\frac{ik}{2z}[(x_0 - x_1)^2 + (y_0 - y_1)^2]}. \tag{2.60}$$

The entire $(x_0, y_0)$ plane can be integrated if the field value outside the aperture $\Sigma$ is defined as $U(x_0, y_0)|_{S_1} \equiv 0$. This yields the *Fresnel* diffraction integral

$$U(x_1, y_1) = \frac{-ike^{ikz}}{2\pi z} \iint_{-\infty}^{+\infty} U(x_0, y_0) e^{\frac{ik}{2z}[(x_0 - x_1)^2 + (y_0 - y_1)^2]} \mathrm{d}x_0 \mathrm{d}y_0, \tag{2.61}$$

or

$$U(x_1, y_1) = \frac{-ike^{ikz}}{2\pi z} e^{-\frac{ik}{2z}[x_1^2 + y_1^2]} \iint_{-\infty}^{+\infty} U(x_0, y_0) e^{-\frac{ik}{2z}[x_0^2 + y_0^2]} e^{i\frac{2\pi}{\lambda z}[x_0 x_1 + y_0 y_1]} \mathrm{d}x_0 \mathrm{d}y_0. \tag{2.62}$$

This expression is valid close to the aperture, on a paraxial assumption, but not as valid as the R-S formulation due to the simplifications. This is why the Fresnel integral is often called a near-field approximation.

When taking a distance $z$ even larger, so that

$$z \gg \frac{k(x_0^2 + y_0^2)_{\max}}{2}, \tag{2.63}$$

then a further simplification of Eq. 2.62 can be made where the quadratic phase term can also be neglected, resulting in the *Fraunhofer* diffraction integral

$$U(x_1, y_1) = \frac{-ike^{ikz}}{2\pi z}e^{-\frac{ik}{2z}[x_1^2+y_1^2]}\iint_{-\infty}^{+\infty} U(x_0, y_0)e^{i\frac{2\pi}{\lambda z}[x_0 x_1 + y_0 y_1]}\mathrm{d}x_0\mathrm{d}y_0. \quad (2.64)$$

Both the Fresnel and Fraunhofer diffraction integrals intuitively show that the field in the observation plane $U(x_1, y_1)$ is a 2-dimensional Fourier transform of the field in the object plane $U(x_0, y_0)$. Indeed, the Fraunhofer integral in Eq. 2.64 can be seen to share much similarity with the expression of a 2-dimensional Fourier transform of the field in the $(x, y)$ domain into the $(f_x, f_y)$ domain, such as

$$\mathcal{F}\{g(x, y)\} = \iint_{-\infty}^{+\infty} g(x, y)e^{i2\pi(f_x x + f_y y)}\mathrm{d}x\mathrm{d}y. \quad (2.65)$$

Rewriting the Fraunhofer integral in terms of the latter 2D Fourier transform gives

$$U(x_1, y_1) = \frac{-ike^{ikz}}{2\pi z}e^{\frac{ik}{2z}[x_1^2+y_1^2]}\mathcal{F}\{U(x_0, y_0)\}_{f_x=x/\lambda z, f_y=y/\lambda z}, \quad (2.66)$$

where $\mathcal{F}$ denotes the Fourier transform. The spherical-divergence factor $e^{ikz}/z$ can usually be dropped as it does not contribute to the directivity pattern of the diffraction field. This results in only an amplitude factor (the first exponential) accompanying the Fourier transform. The implications of such relation for obtaining the scattering patterns of complex locally-reacting fields are discussed in the next and last subsection of this chapter.

### 2.3.3 *Wave Scattering from Locally-Reacting Surfaces*

At the end of the previous subsection, it has been shown that through some approximations the diffraction pattern of waves going through an aperture has the same form as a spatial Fourier transform of the source field. In more practical scenarios, the aperture assumed heretofore can take many forms. It can be an open aperture with full wave transmission from one side of the screen to the other, but it can also be partially-opaque (transmitting some frequencies more than others), or even fully reflective and thus sending the wave on the opposite direction. The diffraction surface can also have non-uniform wave properties, i.e., transmission or reflection properties that vary in the $(x_0, y_0)$ domain. These types of diffracting surfaces, called *locally-reacting* due to the local reactions at normal incidence at

each point, will be the ones of most concern in this work as they can effectively lead to a *grating* (or spatial dispersion) of the amplitude and phase of the diffracted wave. Therefore, the previous notation of the field $U(x_0, y_0)$ comes in handy for describing the wave properties of the diffracting surface. When considering a transmission problem of a partially opaque screen aperture, the field $U(x_0, y_0)$ can be characterized by its *transmission coefficient*

$$T(x_0, y_0) = \frac{U(x_0, y_0)_+}{U(x_0, y_0)_-}, \tag{2.67}$$

where $U(x_0, y_0)_+$ and $U(x_0, y_0)_-$ are the wave functions immediately before and after the aperture, respectively. Conversely, if a reflection problem is considered, then the field can be described by its *reflection coefficient* (also defined in Eq. 2.38)

$$R(x_0, y_0) = \frac{U(x_0, y_0)_r}{U(x_0, y_0)_i}, \tag{2.68}$$

where $U(x_0, y_0)_i$ and $U(x_0, y_0)_r$ are the incident and reflected wave functions at the boundary of the surface, respectively. Such functions are generally complex, and thus fit well within the scope of spatial Fourier transforms. If $\arg(T(x_0, y_0)) \neq 0$, the grating modifies the phase of the wave, whereas if $|T(x_0, y_0)| \neq constant$, then the grating modifies the magnitude of the wave. A similar analysis can also be made with $R(x_0, y_0)$.

The above integral formulations are thus powerful tools as they can help determine the diffracted wave field over a surface by simply specifying its spatially-dependent transmission or reflection properties. In a reflection problem, where a
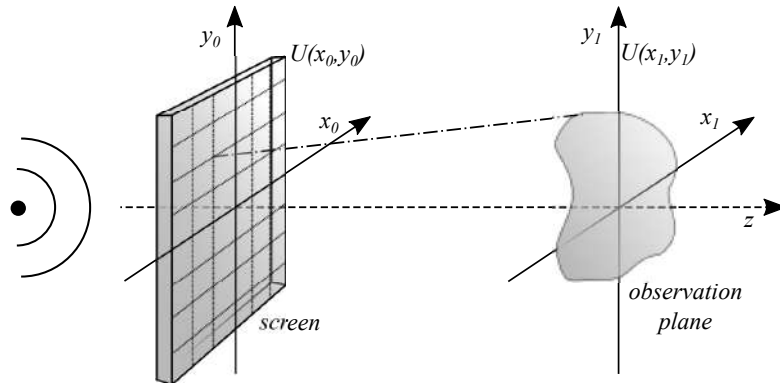


Figure 2.10: Visual representation of the Fresnel/Fraunhofer diffraction through a locally-reacting screen.

near-field scattered acoustic field $p_s(\mathbf{r})$ is defined at a point $\mathbf{r}_1 = \mathbf{r}(x_1, y_1, z_1)$ scattered by a surface centred at $\mathbf{r}_0 = \mathbf{r}(x, y, z = 0)$, the Rayleigh-Sommerfeld integral can therefore be re-written as

$$p_s(\mathbf{r}) = \frac{-ik}{2\pi} \iint_{S_0} p_0(\mathbf{r_0}) R(\mathbf{r_0}) \frac{e^{ik\mathbf{r}}}{\mathbf{r}} dS_0, \qquad (2.69)$$

where $\mathbf{r} = \mid \mathbf{r}_1 - \mathbf{r_0} \mid$, $p_0(\mathbf{r_0})$ is the incident pressure field on $S_0$ and $R(\mathbf{r_0})$ is the spatially dependent reflection coefficient of the locally-reacting surface $S_0$.

Moving to the far-field, a transition is made between Cartesian and spherical coordinates, where now $\mathbf{r} = \mathbf{r}(\phi, \theta, r)$, with $0 < \phi < 2\pi$ defining the azimuth, $0 < \theta < \pi$ defining the elevation, and $r \approx \mathbf{r} = \mid \mathbf{r}_1 - \mathbf{r_0} \mid$ approximating the distance of any point to the plane of the surface. By operating a second order Taylor expansion on $\mathbf{r}$ (as in Eq. 2.59), it yields

$$\mid \mathbf{r}_1 - \mathbf{r_0} \mid \approx r - \frac{x}{r} x_0 - \frac{y}{r} y_0 \approx r - \cos(\phi)\sin(\theta)x_0 - \sin(\phi)\sin(\theta)y_0. \qquad (2.70)$$

Introducing the above approximations to Eq. 2.69, the Fraunhofer approximation of the scattered far-field can similarly be described as

$$p_s(\phi, \theta) = -i\frac{k}{2\pi}\frac{e^{ikr}}{r} \iint_{S_0} p_0(x_0, y_0) R(x_0, y_0) e^{-i(k_x x_0 + k_y y_0)} dS_0, \qquad (2.71)$$

where the transversal components of the wavevector in the $x$ and $y$ directions are given by $k_x = k\cos(\phi)\sin(\theta)$ and $k_y = k\sin(\phi)\sin(\theta)$, respectively.

This chapter provides the fundamental equations that will be applied in the remainder of this thesis. The integral formulations in Eqs. 2.69 and 2.71 mark the importance of the surface reflection coefficient over the resulting scattered energy. Thus, in order to design efficient scatterers, an emphasis should be given to the nature of the surface reflection coefficient and how it can be modified.

---

The equations presented in this chapter can be found in the following references:

[39] A.D. Pierce. *Acoustics: An Introduction to Its Physical Principles and Applications*. McGraw-Hill series in mechanical engineering. McGraw-Hill Book Company, 1981.

[40] R.P. Feynman, R.B. Leighton, and M.L. Sands. *The Feynman Lectures of Physics*. Addison-Wesley world student series. Addison-Wesley Publishing Company, 1963.

[44]  W.C. Elmore, M.A. Heald. *Physics of waves.* Dover, 1969.

[46]  M.R. Stinson. "The propagation of plane sound waves in narrow and wide circular tubes, and generalization to uniform tubes of arbitrary cross-sectional shape". In: *J. Acoust. Soc. Am.* 89.2 (1991), pp. 550-558.

[45]  D.T. Blackstock, *Fundamentals of Physical Acoustics.* A Wiley-Interscience publication, 2000.

[51]  O.K. Ersoy, *Diffraction, Fourier Optics and Imaging.* Wiley Series in Pure and Applied Optics. John Wiley & Sons, Ltd, 2007.

[52]  K. Iizuka, *Elements in Photonics. Volume 1: Free Space and Special Media.* Wiley Series in Pure and Applied Optics. John Wiley & Sons, Ltd, 2002.

# TRADITIONAL SOUND DIFFUSERS

ACOUSTIC scattering occurs when a travelling sound wave encounters an obstacle or inhomogeneity in its path, e.g., an aperture, a solid object, or a change of medium density. This encounter results in sound breaking into secondary waves propagating in a variety of directions. The phenomenon behind each secondary wave spread is better known as wave diffraction. Although scattering and diffraction are often used interchangeably, the former tends to be a more global consequence of the latter. Knowing the magnitude and phase of such scattered waves can be crucial in scenarios where wave propagation control is desired.

Potential places where sound diffusers are in demand are mostly places linked to musical performance and practice, such as concert halls, opera houses, recital halls and recording studios. Other acoustic scattering applications can cover topics such as 3D imaging in Non-Destructive Evaluation (NDE) techniques (echocardiography/holograms) or acoustic cloaking in human technologies (radar/sonar) and in the animal world (acoustic camouflage). In general, scattering can be observed in a dazzling number of physical phenomena, with one so obvious and continuously present that we might forget all about it: the blue hue in the sky (Rayleigh scattering). However exciting all these topics can be, they will here be ruled out in favour of the former musical context.

This chapter will proceed to explain what sound diffusers are, how acoustic scattering from a surface can be quantified and how it can be reduced to a sound diffusion coefficient. Furthermore, light will be given to a few of the most popular traditional sound diffusers. Finally, the limitations of such structures will be addressed and recent developments of modern solutions will be presented; ultimately introducing the concept of acoustic metamaterials.

## 3.1 ACOUSTIC SCATTERING & SOUND DIFFUSION

This section discusses the nature of sound diffusers, how their acoustic scattering properties can be characterized, and ultimately, how the latter can be experimentally measured.

### 3.1.1 *What Are Sound Diffusers & What Are They Used For?*

In acoustics, diffusers are used for breaking specular reflections and distributing sound energy in space. The latter can be achieved through a specific spatial distribution of the reflection coefficient, or the surface impedance, along the scattering plane. This spatial profile of the reflection coefficient, with spatially-dependent values of magnitude and phase, will ultimately lead to a particular scattering pattern. Remembering that scattering patterns can be considered as spatial Fourier transforms of the reflection coefficient, one can then deduct the paramount importance of determining the right sequence of reflection coefficient values along the surface in order to break the sound in any desired way. Sound diffusers aim to achieve this goal by affecting the phase (and sometimes the magnitude) of the reflected sound through the implementation of locally-resonant elements across the surface. This scheme benefits from the incorporation of different resonant elements which posses each a certain frequency-dependent phase behaviour, hence making the latter a prime choice for the task at hand, i.e., scattering sound.

Investigations on acoustic diffusers date from the early 1970s and first appeared as a physical sub-field deriving from the more general topic of Fourier optics – as many analogies can be made between light waves and sound waves. The question on which shape (i.e., the sequential profile of the varying reflection coefficient) would be required for a surface to optimally scatter acoustic waves was investigated by M.R. Schröeder in 1975. The research culminated in his renown seminal paper [33] proposing the use of number theory sequences in sound diffuser designs, such as the binary Maximum Length Sequence (MLS). A few years after that, he also proposed designs based on integer sequences such as the Quadratic Residue
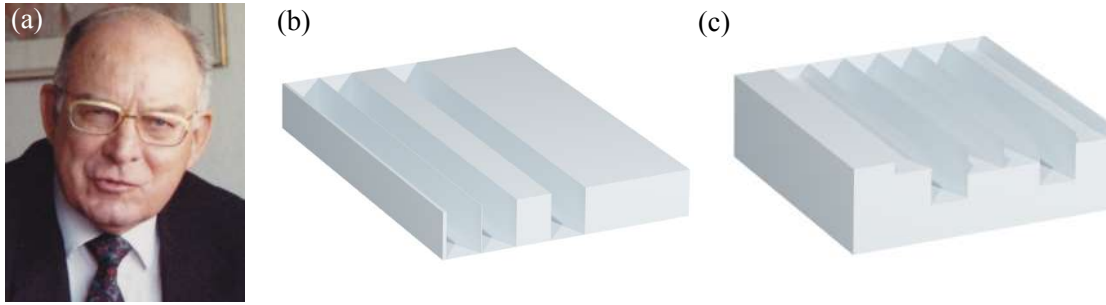
Figure 3.1: (a) Picture of M.R Schröeder (from Wikipedia [60] CC, 1993). Illustration of (b) an MLS sound diffuser and (c) a QRS sound diffuser. (see Sec. 3.2.2)

Sequence (QRS) and the Primitive Root Sequence (PRS). These sequences would allow particular distributions of the reflection coefficient along the surface, thus allowing a mathematical construction of scattering structures. Additionally, these can be designed through relatively simple means, involving elementary equations and small regular cavities, or wells.

Grounded by his previous work on the acoustical effects of small regular resonators in concert halls, the proposition of using number sequences and quarter-wavelength resonators in diffuser design led to the modern foundations of phase grating sound diffusers, which are sometimes referred to as Schröeder diffusers in honour to his pioneering works. Examples of such diffusers are illustrated in Fig. 3.1. Schröeder's work was followed by decades of investigations focusing primarily on (i) characterising sound scattered fields and finding insightful qualitative objective descriptors [53, 54], (ii) studying the subjective effects of sound scattering fields on human perception, mostly in music [28, 55, 56], and (iii) exploring new design paradigms for sound diffusers in order to adapt to ever-changing contextual needs [37, 57–59]. The work presented in this thesis can be thought as an example of the latter.

### 3.1.2 *Coefficients of Sound Scattering Fields*

Now that light has been shed on the nature and use of sound diffusers, other insights are required in order to characterize the scattering properties of these structures and quantify them for further objective evaluations. Across many fields and applications, two major aspects of sound scattering commonly rose to the main-

stream for determining the ability of diffusers to effectively break sound waves in a specific way. There are the so called *scattering coefficient* and *diffusion coefficient*, which slightly differ one from another despite the close meaning of both words. The former rates the ability of the surface to scatter sound in a non-specular way whilst the latter rates the uniformity of the scattered sound distribution [61, 62]. The scattering coefficient can be seen as a good descriptor in a context where strong echoes have to be diminished. The diffusion coefficient stands out for where sound reflections have to be evenly distributed in space. In this work, most diffuser devices will be compared through the use of the diffusion coefficient.

As the scattered sound from a surface depends on its ubiquity angle, the diffusion coefficient also depends on the angle of incidence of the impinging wave. The directional diffusion coefficient [62], $\delta_\psi$, produced when a sound diffuser is radiated by a plane wave at the incident angle $\psi = (\theta', \phi')$ can be estimated from the hemispherical distribution

$$\delta_\psi = \frac{\left[ \iint_S I_s(\theta, \phi) \mathrm{d}S \right]^2 - \iint_S I_s^2(\theta, \phi) \mathrm{d}S}{\iint_S I_s^2(\theta, \phi) \mathrm{d}S}, \tag{3.1}$$

where $I_s(\theta, \phi) \propto |p_s(\theta, \phi)|^2$ is proportional to the scattered intensity. Note here the use of superscripted primes when defining $\psi$ for separating incident angles from reflected angles. The integration of Eq. 3.1 is performed over a hemispherical surface ($-\pi/2 \leq \phi \leq \pi/2$ and $\theta = 2\pi$) where $\mathrm{d}S = \mathrm{d}\theta\mathrm{d}\phi$. This coefficient can be normalized to that of a plane reflector, $\delta_{flat}$, so as to eliminate the diffracting effect caused by the finite size of the structure (i.e., when considering a finite system), resulting in

$$\delta_{n,\psi} = \frac{\delta_\psi - \delta_{flat}}{1 - \delta_{flat}}. \tag{3.2}$$

This normalization allows to characterize purely the diffusion properties of the surface compared to that of a flat plane reflector. A normalized diffusion coefficient $\delta_{n,\psi} \equiv 0$ thus results in as much scattering than a flat surface would provide. The other case of $\delta_{n,\psi} \equiv 1$ conversely indicates a perfectly uniform scattering, i.e., a spherical distribution.

In the quest of uniform scattering, it is known from Chap. 2 that the sound field around a scattering object can be described as a spatial Fourier transform
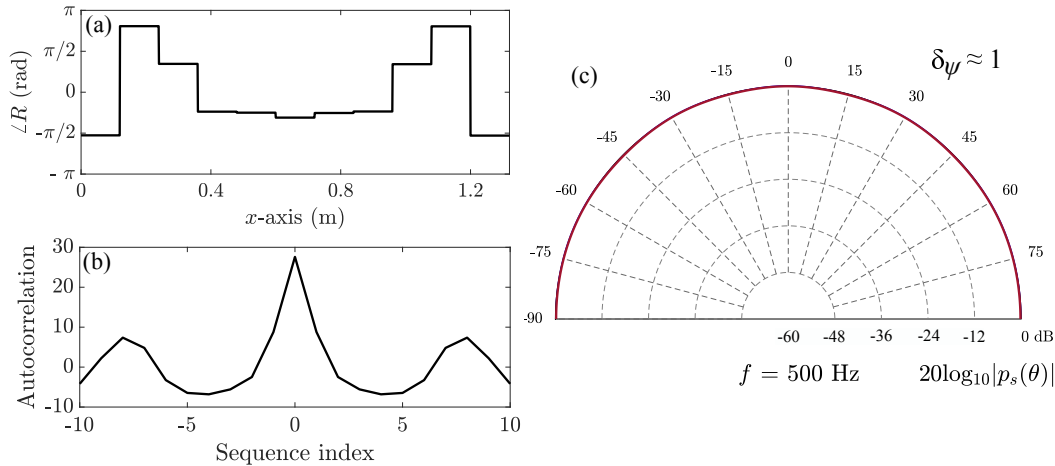
Figure 3.2: (a) Arbitrary phase of a reflection coefficient $R(x)$ designed to produce omnidirectional scattering at $f = 500$ Hz. (b) Autocorrelation of $R(x)$. (c) Far-field scattered sound pressure produced over $R(x)$.

of its surface reflection coefficient. Then, a more detailed way of establishing the quality of the scattering surface may reside in estimating the quality of the auto-correlation function of said reflection coefficient. This relation is explored through the Wiener–Khinchine theorem, which states that the autocorrelation function of a sequence has a spectral decomposition given by the power spectrum of that process, i.e., that the Fourier transform of an autocorrelation function gives the power spectrum. This relation can also be applied to sound diffusers in order to build devices with efficient diffusion coefficient values. Consequently, from this point of view, a good sound diffuser is one which has a delta function in the autocorrelation of the reflection coefficient, as this will lead to a flat power spectrum with respect to $kx$ and $ky$ when performing a spatial Fourier transform; thus providing an even scattered energy distribution or a constant scattered amplitude in space. An example of such process is illustrated in Fig. 3.2 where an arbitrary phase of a reflection coefficient $R(x)$ along the $x$-axis (assuming a 1-dimensional structure) is shown next to its autocorrelation function. It can be observed that the delta-like autocorrelation leads to an even distribution of the scattered sound energy, thus achieving a diffusion coefficient of almost unity.

### 3.1.3 *Measuring Polar Scattering Distributions – ISO 17497-2*

There are a few ways to measure the resulting scattered sound that is being reflected back from a surface. In general, the process requires thoroughness in details and must take place in a perfectly controlled environment so to minimize any potential interferences that might appear during the measurements. Proper measurement guidance on such topic was not inscribed in any official standard until the beginning of the 21$^{st}$ century. Until then, unofficial methods for measuring acoustic scattering were investigated instead, such as the Mommertz-Vorlander method [63]. Years later, these investigations lead to the Audio Engineering Society (AES) to publish the standard AES-4id-2001 "Characterization and measurement of surface scattering uniformity" [64]. The latter was adapted a few years after by the International Standard Organization (ISO), which published in 2004 and 2012 the standard ISO 17497-2 "Measurement of the directional diffusion coefficient in a free field" [62]. The first one provides guidance on determining the random-incidence scattering coefficient in a reverberation chamber, whereas the second helps establishing the directional diffusion coefficient in an anechoic room. As previously mentioned, a particular attention will be given to the latter coefficient throughout this work.

ISO 17497-2 stipulates the required conceptual framework chain for determining the uniformity of the scattered field. First, the experiment must take place in a controlled free-field environment, i.e., an anechoic chamber. Ideally, the surface sample would be placed at the centre of the room, facing in the up direction, whilst a speaker is placed as far as possible facing the surface, e.g., axially on top of the surface if one considers a normal incidence case. With this set-up where a loudspeaker radiates a chosen signal, such as an exponential sine sweep (eSweep) or a Maximum Length Sequence (MLS) in order to obtain an impulse response, the sound pressure being scattered by the surface can then be measured by evenly sampling the hemispherical space around said surface. Depending on the sampling resolution, this task can be a tedious one. If one considers a 5° resolution between spherical points (commonly agreed minimal resolution), this process can lead to

72 and 36 sampling points in azimuth ($\phi$) and elevation ($\theta$) planes, respectively, resulting in 2486 measurement positions ((36-1)x(72-1)+1); and just one incident angle. Thankfully, the process can be made easier with multi-channel acquisition cards and/or the programming of robotic devices for rotating the sampled surface and measuring at required intervals. A conceptual framework chain of ISO-17497-2 is shown in Fig. 3.3.

Although this process can yield scattering information about the surface, there still can be a few processes interfering with the desired results. One of these can be identified to be related to the slight energy response of the room, which even being anechoic would still provide a minimal acoustic signature through the thin metallic structural elements that may help the installation of the measurement set-up. In order to remove such effect, the overall measurement framework must be repeated at least twice, once with no sample present, referred to as the background response, and a second time with the scattering surface present. When such data is gathered, the response of the background can then be subtracted from the one with the sample, which will also help cancel the influence of the direct sound into the receivers, thus resulting only in the scattered response from the surface. This process can be observed in Fig. 3.3(b) where the two insets represent the measured and background impulse responses, the subtraction of which results in the main impulse response displayed. Needless to say that such operations are very sensitive to time information and that both measurements must be as synchronous as possible. Lastly, if one aims to normalize the directional diffusion coefficient that was obtained, a third measurement must be conducted within the same conditions as the previous two, measuring the scattering properties of a flat plane reflector of same dimensions as the first scattering surface.

## 3.2 TRADITIONAL PHASE-GRATING DIFFUSERS

This subsection gives more emphasis on the mathematical methods used to describe sound diffusers and explain the physical processes that come from analytical formulations.
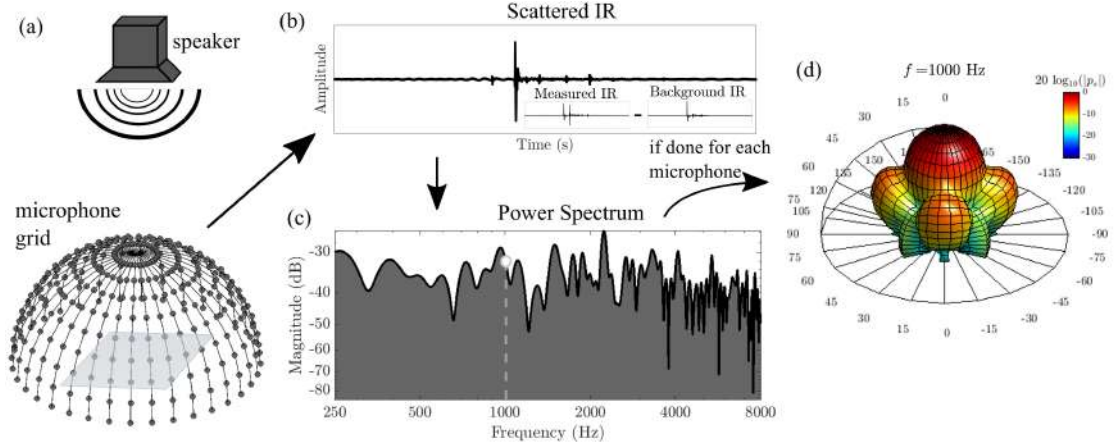
Figure 3.3: Measurement framework of ISO 17497-2. (a) Speaker sending a signal over a surface sampled by a hemispherical distribution of microphones. (b) Resultant scattered impulse response (IR). (c) Power spectrum of the scattered IR. (d) Hemispherical scattered sound pressure distribution.

### 3.2.1 *Reflection Coefficient of Phase-Grating Diffusers*

Phase-grating, or Schröeder diffusers, are generally composed of a sequence of wells with different depths. In order to understand the strategic importance of the sequences commonly used for these devices, the physical modelling of sound propagating in a well will here be discussed first. This will help determine the reflection coefficient at the surface of the cavity; a crucial step for controlling the sequence distribution of the reflection coefficient and thus the scattering of sound.

A well can be considered as an open-closed tube of rectangular cross-section. Assuming a plane wave propagation inside a rigid well, this simple configuration allows a maximum phase shift of the reflection coefficient at $L = c_0/4f$, where $f$ is the frequency shift, $L$ is the depth of the slit, and $c_0$ is the speed of sound in air. The $1/4$ factor of the wavelength $\lambda = c/f$ results in a common use of the term Quarter-Wavelength Resonator (QWR) for referring to such type of acoustic resonators.

One way to obtain the reflection coefficient at the top of each QWR, $R_{QWR}$, is through the use of the Transfer Matrix Method (TMM) which relates the sound pressures, $P$, and normal acoustic flow velocities, $\mathcal{V}$, at both extremities of the resonator. A general overview of the TMM for a open-closed tube is given here,

where a more detailed description of this analytical method can be found in Chap. 4. The transfer matrix of the $n$-th well, $\mathbf{T}^n$, of length $L$ and height $h$, extending from $y = 0$ to $y = L$ is written as

$$\begin{bmatrix} P^n \\ \mathcal{V}^n \end{bmatrix}_{y=0} = \mathbf{T}^n \begin{bmatrix} P^n \\ \mathcal{V}^n \end{bmatrix}_{y=L} = \begin{bmatrix} T_{11}^n & T_{12}^n \\ T_{21}^n & T_{22}^n \end{bmatrix} \begin{bmatrix} P^n \\ \mathcal{V}^n \end{bmatrix}_{y=L}. \tag{3.3}$$

The transmission matrix $\mathbf{T}^n$ can further be expressed as

$$\mathbf{T}^n = \begin{bmatrix} T_{11}^n & T_{12}^n \\ T_{21}^n & T_{22}^n \end{bmatrix} = \mathbf{M}_{\Delta l_{QWR}}^n \mathbf{M}_{QWR}, \tag{3.4}$$

where $\mathbf{M}_{QWR}^n$ and $\mathbf{M}_{\Delta l_{QWR}}^n$ are the transmission matrix and the radiation correction matrix for the $n$-th QWR, respectively. The transmission matrix of a QWR can be expressed as that of an isotropic homogeneous material, $\mathbf{M}_{QWR}^n$, of unit length $L$, which results in

$$\mathbf{M}_{QWR}^n = \begin{bmatrix} \cos(k_w^n L) & -iZ_w^n \sin(k_w^n\ L) \\ \frac{-i}{Z_w^n}\sin(k_w^n L) & \cos(k_w^n L) \end{bmatrix}, \tag{3.5}$$

where $Z_w^n = \sqrt{\kappa_w^n \rho_w^n}/S_w$ is the characteristic impedance of the well, $\kappa_w$ the effective bulk modulus in the well, $\rho_w$ the density of the air in the well, and $S_w = h^n$ the section of the well. The radiation correction from the top of the well to the free space, $\mathbf{M}_{\Delta l_{QWR}}^n$, can be written as

$$\mathbf{M}_{\Delta l_{QWR}}^n = \begin{bmatrix} 1 & Z_{\Delta l_{QWR}}^n \\ 0 & 1 \end{bmatrix}, \tag{3.6}$$

with $Z_{\Delta l_{QWR}}^n = i\omega \Delta l_{QWR}^n \rho_0 / \phi_t^n S_w$ being the characteristic radiation impedance of the $n$-th slit, $S_0 = S_w$ the unit cross-section, $\rho_0$ the air density and $\Delta l_{QWR}$ the end correction of the well, which can be expressed as

$$\Delta l_{QWR} = h^n \sigma^n \sum_{m=1}^{\infty} \frac{\sin^2(m\pi\sigma^n)}{(m\pi\sigma^n)^3}, \tag{3.7}$$

with $\sigma^n$ being the superficial porosity.

The reflection coefficient of the $n$-th rigid QWR, $R_{QWR}^n$, can ultimately be calculated using the matrix elements as

$$R_{QWR}^n = \frac{T_{11}^n - Z_0 T_{21}^n}{T_{11}^n + Z_0 T_{21}^n}, \tag{3.8}$$
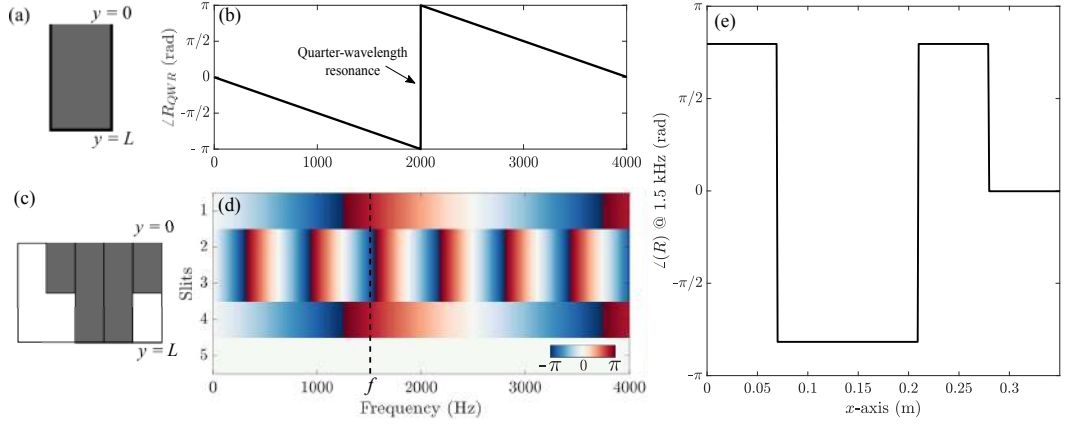
Figure 3.4: (a) A QWR of depth $L = 4$ cm. (b) Phase of the reflection coefficient $R(x)$ along frequency. (c) A series of $N = 5$ QWRs of different depths. (d) Phase of the reflection coefficient $R(x)$ along the $N$ slits. (e) Distribution of $R(x)$ at $f = 1.5$ kHz.

where $Z_0 = \rho_0 c_0 / S_o$ is the specific impedance of air. Alternatively, the effective surface impedance of each slit can be expressed as

$$Z_{QWR}^n = Z_0 \frac{1 + R_{slit}^n}{1 - R_{slit}^n}. \tag{3.9}$$

This expression of the reflection coefficient holds true given the assumptions of plane wave propagation and isotropic homogeneous medium distribution in the well. As shown in Chap. 2, viscothermal losses from the boundary layers can be accounted through the effective propagation parameters $\kappa_e$ and $\rho_e$, which can then be input into the TMM well as $\kappa_w$ and $\rho_w$.

Alternatively, the impedance of a QWR can be obtained by the simple relation $Z_{QWR} = -i Z_0 \cot(kL)$, from which the reflection coefficient can then be calculated. It is a simpler approach than the TMM but should give fairly similar results under the assumptions of plane wave propagation and that no viscothermal losses are accounted.

Based on this modelling theory, the phase response of a slit can be obtained and plotted, as shown in Fig. 3.4. Assuming a depth $L = 4$ cm, one can observe that the phase shift of the slit indeed occurs at a frequency which wavelength is four times that of the slit depth, illustrating the concept of quarter-wavelength resonance. Furthermore, if many slits of different heights were grouped one next to the other, this would result in a succession of reflection coefficients of same

overall phase shape (triangular in this case) but with different resonant frequencies. When considering a monochromatic impinging wave, this will lead to a grating of the reflection coefficient across the surface estimated at $y = 0$. Using previously established knowledge, one can then plot the scattered pressure of the surface according to any scattering integral.

### 3.2.2 *Number Theory Sequences Used For Sound Scattering*

Now that the reflection coefficients of rigid QWRs have been derived in the TMM one can focus towards the various ways of creating particular phase grating sequences in order to achieve specific scattering distributions. As discussed previously, the properties of the reflection coefficient distribution must show interesting autocorrelation values. Mathematical sequences devised through Number Theory can help reach such goal. Number Theory is a branch of mathematics based on the study of integers and integer-valued functions. Considered a key aspect of mathematics and science since ancient times, Number Theory is prominently used today in may fields and applications, ranging from statistics and topology to computation, signal processing and communication technologies. For instance, some of the arithmetic sequences discussed below are also widely used in antennae signal communication.

### 3.2.2.1 *Maximum Length Sequences*

A MLS is a type of pseudorandom binary sequence. That means that it only utilizes ones and zeros and combines them in a way that seems *almost* random. Emphasis on the 'pseudo' part comes from the fact that (i) such sequences are deterministically constructed, and (ii) that a great number of integers is required in order to avoid repeated patterns of number sequences. In more practical terms, the set of values is finite, and randomness thus depends on the length of the sequence. If the sequence is relatively short, then it is likely that some pattern (consecutive set of ones or zeros) may be repeated thus impairing its randomness. The irregularity of the sequence also depends on the way it is constructed. An MLS is generated using maximal linear feedback shift registers, which cause a

periodic loop over every possible sequence value to affect the binary value of the $n$-th integer (or bit) in the sequence by shifting its value with that of the shift register. Mathematically, an MLS can be represented by the recursive formulation

$$s(n+m) = s(n) \oplus s(n+m-1), \tag{3.10}$$

where $n$ is a bit in the initial vector sequence $s(n)$ of length $N$, $m$ is the order of the shift register and $\oplus$ is a XOR operator (modulo-2 sum). For instance, an MLS of length $N = 7$ with a shift register order $m = 3$ results in the sequence $\{1,1,1,0,1,0,0\}$. The initial vector sequence cannot be entirely composed of zeros as this would freeze the loop without providing any new '1' element in the resulting sequence.

An advantage of the MLS process is that it is deterministic in the making but results in a pseudo-random sequence with interesting properties. One of the most important is that the MLS is spectrally flat except at DC (0 Hz), which is a relevant characteristic not only in our present case, but in other signal-based operations such as impulse response capture, signal multiplexing or imaging. For the randomness in the sequence to be high, a large length sequence $N$ must be considered. The more irregular and longer the sequence, the more its autocorrelation value would tend to a delta function, ultimately leading to a Kronecker delta

$$\delta_{ij} = \begin{cases} 1, & \text{if } i = j, \\ 0, & \text{if } i \neq j. \end{cases} \tag{3.11}$$

In practice, sound diffusers based on MLS cannot be infinitely long and thus a finite sequence length must be chosen. This, alongside the width of the slits, are the two major factors in determining the overall width of the diffuser. Due to the binary nature of the MLS, the diffuser would then result in an alternation of spatial blocks where ones would correspond to a flat surface and zeros to a well cavity of depth $L = \lambda_0/4$, where $\lambda_0$ is the wavelength of the design frequency. An example of an MLS diffuser based on the above $N = 7$ sequence is likewise illustrated in Fig. 3.5. One can observe that the scattering at the design frequency is symmetric and is attenuated by $10\log(N+1)$ dB in the normal axis but otherwise radiates high amplitudes of energy in non-specular directions, thus providing a relatively even scattering. If more sequence bits would be introduced then a more uniform

Figure 3.5: (a) Phase of the reflection coefficient $R_{MLS}$ along the $x$-axis of a $N = 7$ MLS diffuser of depth $L = 3$ cm. (b) Far-field scattered sound pressure against frequency. (c) Normalized diffusion coefficients $\delta_{0,n}$ of an MLS diffuser unit and 3 repetitions. (d) Far-field scattered sound pressure at $f = 2833$ Hz.

scattering would be seen.

On another note, diffuser sequences such as the one that is displayed in Fig. 3.5. can often be repeated periodically in order to cover more surface. Due to the scattering nature of one period, the repetition of multiples generates another layer of scattering between period units, resulting again in constructive and destructive interferences between them. This leads to directions in space where sound is attenuated and others where the scattered sound intensity is maximal. These highs and lows in the scattering distribution caused by the periodicity of a structure are commonly referred to as diffraction-grating lobes. In MLS designs, many repetitions lead to diffraction-grating lobes with even energy, to the exception of the zeroth order one, which is attenuated by $10\log(N + 1)$. Also, when the depth of the well becomes $L = \lambda/2$, the wells re-radiate sound in phase with the sound reflected from the flat surface elements, causing the diffuser to virtually behave like a flat reflector. This can be seen in Fig. 3.5 by a drop in the diffusion coefficient around 6 kHz; also visible in the phase of the reflection coefficient by the coincident white band (0 rad) around the same frequency. This frequency at which a diffuser

sub-units coincidently radiate sound in phase is called the critical frequency. Because of the similar depth between wells caused by the binary nature of sequence, MLS diffusers thus have a limited bandwidth within which they can be effective (approximatively one octave).

### 3.2.2.2 *Quadratic Residue Sequences*

In order to bypass the lack of diffusion bandwidth generated by MLS diffusers, the Quadratic Residue sequence (QRS) became commonly used, which combines efficient diffusion and extended bandwidth. The QRS can be determined as

$$s(n) = n^2 \mathrm{mod} N, \tag{3.12}$$

where 'mod' is the least non-negative remainder of the prime number $N$. The depth $L$ of each well can then be determined by

$$L(n) = \frac{s(n)\lambda_0}{2N}, \tag{3.13}$$

where $\lambda_0$ is the wavelength of the design frequency. The results of an example of an $N = 5$ Quadratic Residue Diffuser (QRD) is displayed in Fig. 3.6. The broader
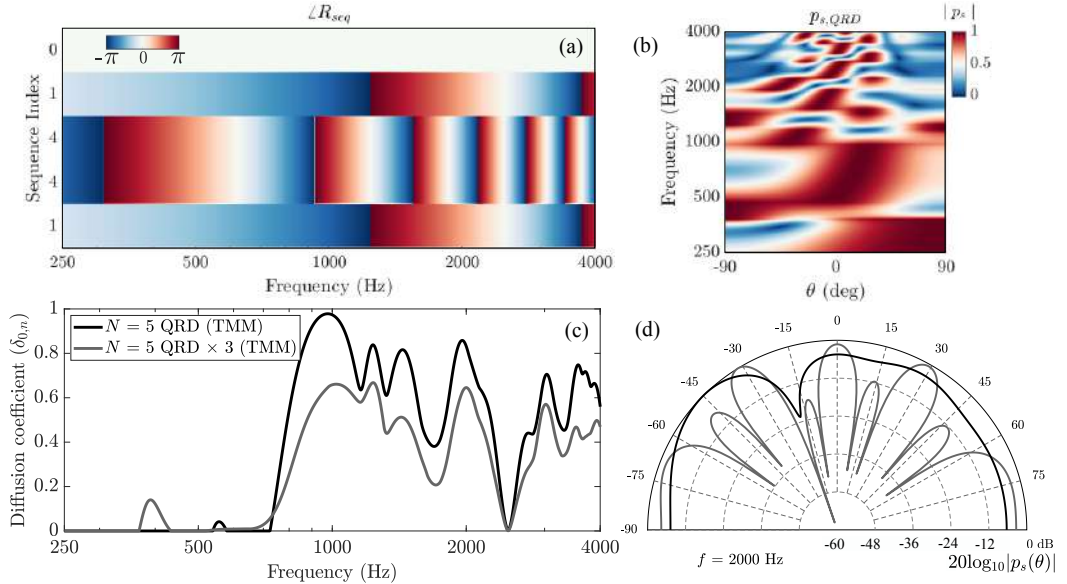


Figure 3.6: (a) Phase of the reflection coefficient $R_{QRD}$ along the $x$-axis of a $N = 5$ QRD. (b) Far-field scattered sound pressure against frequency. (c) Normalized diffusion coefficients $\delta_{0,n}$ of a single QRD diffuser unit and 3 repetitions. (d) Far-field scattered sound pressure at $f = 2000$ Hz.

bandwidth of QRDs is enhanced by the various slit depths postponing the critical frequency up to $f_c = N f_0$, where $f_0$ is the design frequency. Asides the broader bandwidth covered by such sequences, QRDs benefit in that the diffraction lobes generated by multiple diffuser repetitions yield the same energy. These two aspects of QRDs, broader bandwidth and even diffraction lobes, have resulted in the quick success of the sequence amongst the acoustic community.

### 3.2.2.3  *Primitive Root Sequences*

The Primitive Root sequence (PRS) is quite different in scope than the previous sequences, in that it aims to reduce the energy reflected in the specular direction, producing notches in the scattering distributions at discrete frequencies. The formulation of the PRS can seem familiar with the QRS:

$$s(n) = r^n \mathrm{mod} N, \tag{3.14}$$

where $N$ is an odd prime and $r$ is the primitive root of $N$. The way the sequence of a Primitive Root Diffuser (PRD) is built results in $N - 1$ wells per period. Similarly to the QRD, the PRD provides a relatively broad sound diffusion bandwidth and displays even diffraction lobes when repeated – a feature made possible due to the modulo operator. The ability of a PRD to reduce specular reflections improves as the prime number $N$ increases.

### 3.2.2.4  *Ternary Sequences*

A Ternary Phase Sequence (TPS) is made with three variations of bits, in contrast to the binary nature of the MLS. A ternary sequence is thus composed of 1's, 0's, and -1's. Here, the meaning of each value has to be reviewed. 1's and -1's correspond to the binary values obtained out of an MLS, where the zeros of the MLS have now been changed to -1s. This change is operated to give more physical sense to the sequence, as 1's reflect the sound waves without phase shifts and -1's reflect them in opposite phase (at the design frequency). Thus the 0 elements introduced in a ternary sequence physically refer to sound absorption, therefore introducing the main advantage of these hybrid sequences: scattering sound but reducing the
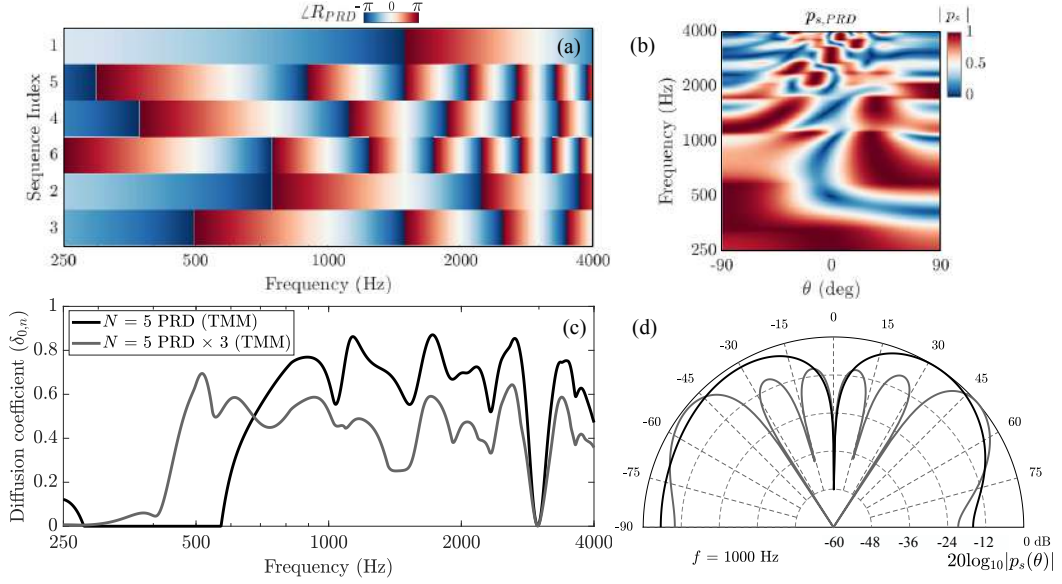
Figure 3.7: (a) Phase of the reflection coefficient $R_{PRD}$ along the $x$-axis of a $N = 6$ PRD. (b) Far-field scattered sound pressure against frequency. (c) Normalized diffusion coefficients $\delta_{0,n}$ of a single PRD diffuser unit and 3 repetitions. (d) Far-field scattered sound pressure at $f = 1000$ Hz.

energy conveyed in certain directions.

However, the way ternary sequences are usually generated in optical applications does not grant effective scattering as they aim to maximize the power carried by a signal. This results in a low amount of 0's in the sequences, disrupting the balance of bit elements that would be required for efficient sound scattering. T. Cox and P. D'Antonio devised a way for designing ternary sequences that is better suited to sound diffuser applications [37]. It mainly consists in balancing again the sequence bits in order to aim for a high sequence autocorrelation and nominal absorption values. To achieve such goal, two MLS of length $= 2^m - 1$ must be formed, under the constraint that the order of the sequences $m \neq 0 \mod 4$. Then, the MLSs need to have suitable cross-correlation properties. This can be done by forming the first MLS and sample it at a different sample rate to generate the second complimentary sequence. A sample rate $\Delta n = 2^k + 1$ can be chosen, where $k$ is an integer. Additionally, a parameter $e = \gcd(m, k)$ can also be defined, where 'gcd' is the greatest common divisor. For this parameter to lead to a correct distribution
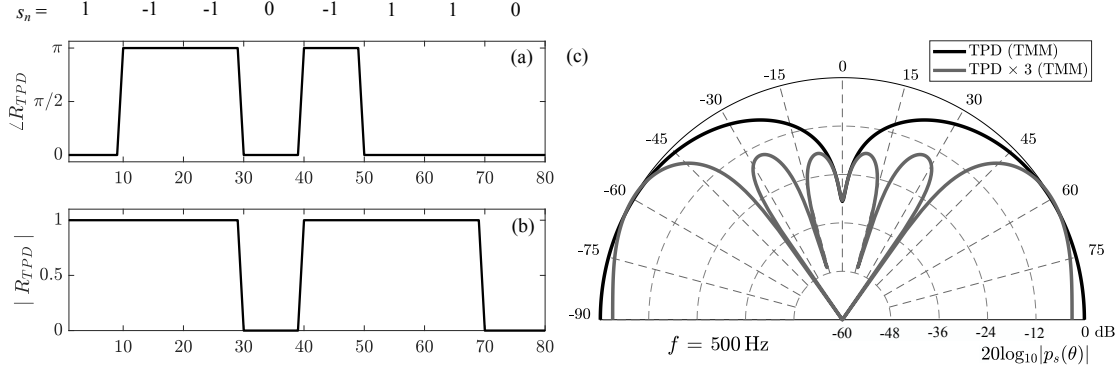
Figure 3.8: (a) Phase of the $R_{TPD}$ along the $x$-axis. (b) Magnitude of $R_{TPD}$ along the $x$-axis. (d) Far-field scattered sound pressure at $f = 500$ Hz.

of cross-correlation values, $m/e$ must be chosen as odd. Then, the two MLSs can have a cross-correlation $S_{ab}(\tau)$ displaying three values,

$$
S_{ab}(\tau) = \begin{cases} -1 + 2^{(m+e)/2}, & \text{occurring} \quad 2^{m-e-1} + 2^{(m+e)/2} \quad \text{times,} \\ -1, & \text{occurring} \quad 2^m - 2^{m-e} - 1 \quad \text{times,} \\ -1 - 2^{(m+e)/2}, & \text{occurring} \quad 2^{m-e-1} - 2^{(m+e)/2} \quad \text{times.} \end{cases} \tag{3.15}
$$

This will give the total number of 1's and $-1$'s in the sequence by $\approx N(1 - 2^{-e})$, i.e., the amount of reflective surface. In the high frequency regime, when $\lambda < d$, the absorption coefficient of the diffuser can be defined as $\alpha = 1 - 2^{-e}$. If a ternary diffuser is designed so that $\alpha \approx 0.5$, this implies that $e = 1$, meaning that the order of the MLS, $m$, must be odd.

The ternary sequence $c_n$ can ultimately be formed by

$$
c_n = 2^{-(m+e)/2}(S_{ab}(\tau) + 1). \tag{3.16}
$$

Figure 3.8 illustrates the phase and magnitude of the reflection coefficient of a $N = 8$ Ternary Phase Diffuser (TPD) along the $x$-axis. It can be observed that the reflection coefficient profile displays sound absorption for the 0 index bits due to a complete reduction in the magnitude with no phase shift. Alternatively, phase inversion is provided by -1 elements with no change to the reflect sound magnitude and in-phase reflection is provided for 1 elements with no change in both phase and magnitude. The scattering pattern of the TPD illustrates a reduction in the specular reflections whilst maximising scattering at other angles.

### 3.2.2.5 *Alternative Sequences*

Besides the above-mentioned sequences, many other can be found across the literature. Quadriphase sequences have been studied [37] for counteracting the lack of diffusion at multiples of the design frequency of ternary diffusers, although the complexity of the sequence design requires deeper mathematical considerations. Index sequences making use of polyphase Legendre sequences were explored by Schröeder [65] and were found to have similar properties to PRS. Furthermore, usage of the Zadoff-Chu sequence [66], providing a perfect delta in the autocorrelation function, has also been investigated. Despite it's apparent appeal, its practical implementation in sound diffusers resulted in similar behaviour to that of the QRS. However, new computational paradigms making use of optimization algorithms have been devised to improve the scattering of sound diffusers [67]. These would try to optimize (e.g., minimize) a function given a cost function and search for a sequence (monophase or polyphase) that leads to the desired scattering distribution whilst agreeing with any constraints. The rise of computer technology has made this approach a viable one, and it will be explored later on this work.

### 3.2.3 *Sequence Periodicity & Modulation*

The inter-scattering of periodic repetitions of a scattering structure gives rise to diffraction lobes, i.e., focused zones of high scattered sound energy with pseudo-null values between them. Such diffraction lobes have been illustrated in each of the previous diffusers, in which cases most sequences aimed towards generating lobes with even energy. Diffuser repetitions can be generally encountered in situations where a balance needs to be struck between diffuser area coverage and manufacturing constraints. On the one hand, large diffusers (large unit width) of several meters long can be too large to efficiently transport and mount. On the other hand, small diffusers (small unit width) often come with poor diffusion properties. This is one of the main reasons why small to medium-sized diffusers are generally put together in arrays. Yet, repetitions of diffuser sequences can generate even diffraction lobes, resulting in a somewhat even distribution.

However, two main disadvantages can clearly be observed from the use of repe-

titions. Firstly, the greater the number of diffuser repetitions of fixed periodicity width, the greater the Q factor of the grating lobes. This progressively leads to a decrease of the overall directional diffusion coefficient as it is an autocorrelation of the scattered sound pressure in space. Yet, a too small number of repetitions leads to largely spaced diffraction lobes, making clear near-null areas where sound is almost entirely cancelled. Secondly, such diffraction grating can cause a comb-filtering of the reflected sound due to the superposition of different phases, affecting the frequency content of the original sound and potentially altering the sensation of pitch (colouration phenomenon).

This set of drawbacks makes the design of some diffusers quite paradoxical, such as the QRD, which is said to provide even diffraction lobes when repeated, yet these lead to more uneven scattering.

In order to overcome such negative effects, sequence periodicity can be modulated and made aperiodic in the same way the bits of each sequence are put together to obtain efficient sound diffusers. This technique is called sequence modulation and can yield impressive results, albeit at the cost of space.

By defining a new sequence composed of $j$ diffusers each with $N$ individual slits, then a sequence can be thought of such that some diffuser units reflect sound in a different phase than some others. Again, like all the previous ones, the sequence needs to have good autocorrelation properties. A good example in this case would be to use a Barker sequence [26, 68]; an aperiodic binary sequence whose Fourier transform is the flattest possible for a binary sequence. The advantage of using Barker sequences instead of MLS or Zadoff-Chu sequences is that they don't require a large amount of integers to exhibit good autocorrelation values, with a maximum length $j = 13$. This is a welcome feature in the present case of diffuser repetitions as they are usually repeated only a few times. A Barker modulation can thus help enhance the scattered distribution of the diffuser array despite the larger area being covered.

Considering the case of $j = 3$ repetitions of a QRD, the respective Barker sequence gives $\{+1, +1, -1\}$. In this sequence and in the present context, $+1$ can refer to a normal QRD and $-1$ to a QRD unit in opposition of phase ($\pm 180°$). This
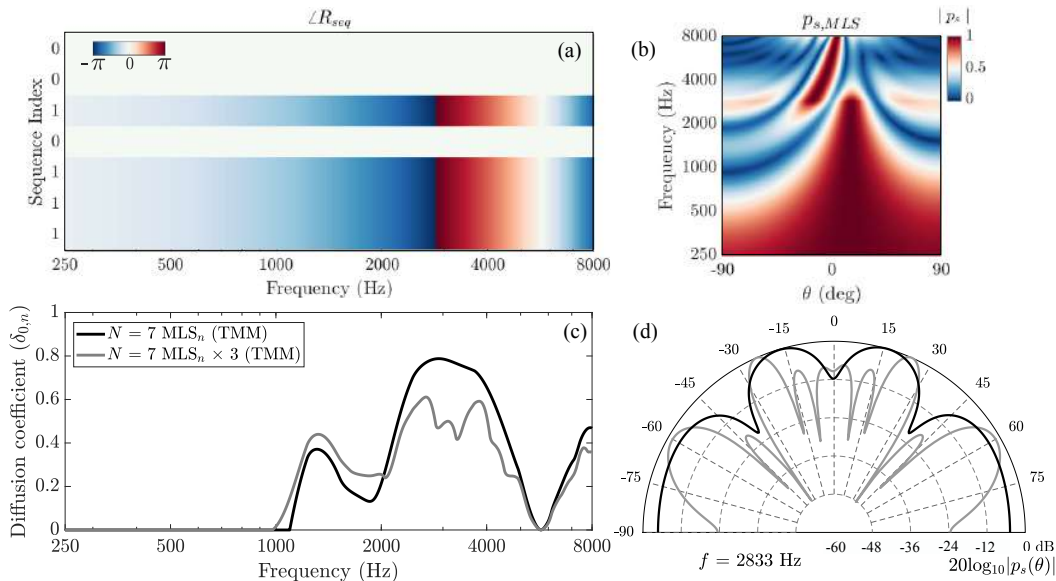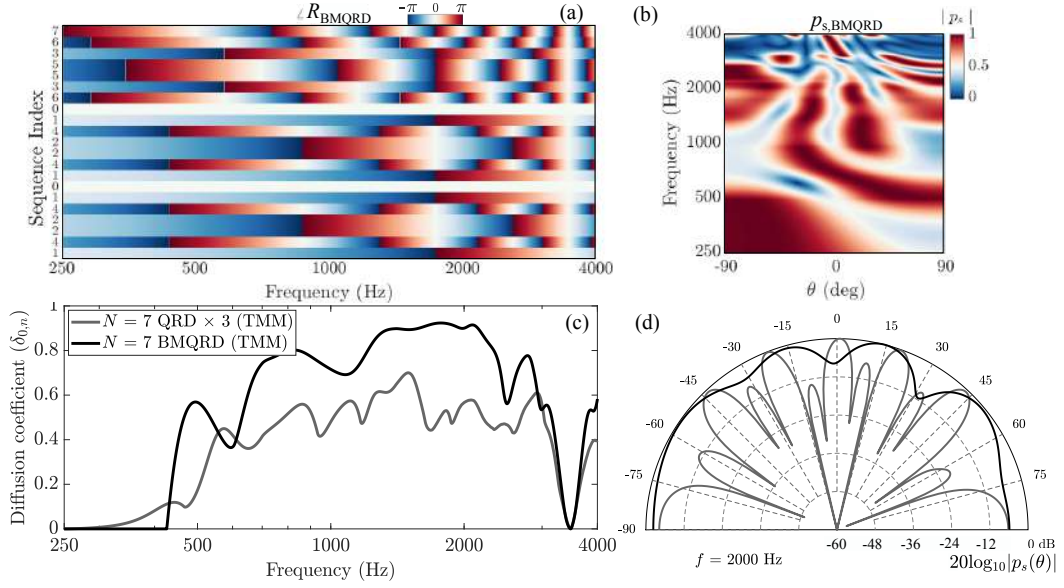
Figure 3.9: (a) Phase of the reflection coefficient $R_{BMQRD}$ along the $x$-axis of a $N = 15$ BMQRD diffuser of varying depth. (b) Far-field scattered sound pressure against frequency. (c) Normalized diffusion coefficients $\delta_{0,n}$ of a BMQRD diffuser unit and 3 QRD repetitions. (d) Far-field scattered sound pressure at $f = 2000$ Hz.

phase shift can be obtained by 'pushing down' the diffuser unit deeper so that the individual wells become longer, therefore adding to the phase change. The amount of distance required to do so can be calculated by subtracting the integer depth value of individual wells by the overall number of bits, $N$, of the diffuser. An illustration of such scheme is displayed in Fig. 3.9, where it can clearly be seen that the scattering obtained from the Barker-modulated QRD has significantly improved compared to that of the normal QRD repetitions.

The improvements in sound diffusion yielded by a Barker modulation can have a critical impact in mitigating the adverse effects of diffuser periodicity. However, one major disadvantage of such scheme resides in the added depth of the overall diffuser structure. As an example, QRDs have already a nominal depth $L = \lambda_0/2$ (depth of the deepest well). Depending on the desired design frequency, a QRD can get relatively bulky if aimed towards mid to low frequencies, e.g., 27 cm depth at $f_0 = 500$ Hz. Adding extra depth to such diffuser design can become quite impractical depending on the contextual space limitations. Here, the Barker modulated-QRD

in Fig. 3.9 has a depth $L \approx 40$ cm, which increases significantly the size and weight of the sound diffusing structure.

## 3.3 LIMITATIONS OF TRADITIONAL SOUND DIFFUSERS

This final section discusses the limitations of traditional sound diffusers, emphasizing on design theory assumptions, on the practical considerations of typical quarter-wavelength sound diffusers, as well as on the novel strategies that were lately reported to bypass such issues.

### 3.3.1 *Design Methodology Considerations*

The design methodology used in this chapter to describe the surface reflection coefficient and the scattered field of a sound diffuser composed of an array of QWRs of varying depth relies on subtle assumptions which can sometimes be easily overlooked or forgot in the design process.

First, one of the main assumptions used in the TMM is that of plane wave propagation in the wells, which is considered true only if the wavelength of the impinging wave is bigger than the width of the slit, i.e., $\lambda \gg h$, where $h$ is the well width. Should the wavelength start to diminish to the point where it is not longer larger than the well, higher order modes (e.g., transversal) might start to appear and lead to different results.

Secondly, no visco-thermal losses made by the acoustic boundary layers inside the slits were accounted for. This still holds true until the slit width is at least 2 cm wide, with 4 cm commonly assumed to be a safe minimal width. Below such dimensions, visco-thermal losses due to boundary layers will start to have an impact and would thus need to be considered, as is the case of acoustic metamaterials.

Another assumption is that of locally-reacting wells, meaning that the state of acoustic pressure and particle velocity is assumed to be the same over the boundary of the open cavity, leading to a homogeneous surface impedance (and reflection coefficient) across the opening. In practical terms, points close to the

center of a cavity act slightly differently than those close to the boundaries with the neighbouring wells. In a similar thought, the radiation of each well into its close neighbours is also neglected, e.g., evanescent waves along the surface. These practical assumptions can often explain certain variations between analytical modelling and measurements and/or simulations. However, consistent results can still be obtained despite these simplifications.

One last major assumption used throughout the previous examples remains in the choice of the scattering integral being used. As a reminder of Chap. 2, every integral (F-K, R-S, Fresnel, Fraunhofer) comes with a set of field simplifications (e.g., small signal approximation, single point source radiation, far-field, etc.) which depending on the situation at hand can become sufficiently important as to be significant. The results presented in this work will nevertheless consider these underlying assumptions to be true.

### 3.3.2 *Quarter-Wavelength Bulkiness & Space Inhibition*

Briefly mentioned in Sec. 3.2.3, most diffuser designs making use of QWRs can result in bulky structures in the mid- to low frequency regimes. This is inherently due to the acoustic resonance mechanism at play in open-closed tubes which is set



Figure 3.10: Queen Elizabeth Hall, Southbank Centre, London. Deep sound diffusers are installed behind the stage. [photo from Ramboll UK Ltd.]

to a quarter of the design wavelength. In a QRD, the deepest slit has a dimension set to $L = \lambda_0/2$ (half a wavelength) in order to be truly effective at a frequency twice as high. For example, with a design frequency of $f_0 = 500$ Hz a QRD would thus turn out into a structure 27 cm deep; working optimally at 1 kHz. Another QRD designed for $f_0 = 250$ Hz, working best at 500 Hz, would result in a structure 56 cm deep. Such bulky diffusers can sometimes be seen in concert halls, as illustrated in Fig. 3.10. Other quarter-wavelength sound diffusing strategies would also have similar size constraints. Furthermore, the depth, and therefore volume of the structure, have both a major impact on its weight, which would also vary according to the density of the manufacturing material. In summary, the larger the diffuser the heavier it also gets. Consequently, depending on the range of frequencies being covered, it can be quite challenging sometimes to fit a sound diffuser into a practical environment, even more so in places where space and mass are already at a premium.

Critical musical environments that might require acoustic diffusion but also have strong limitations with regards to space are primarily recital rooms, orchestra pits in opera houses and recording studios. The space limitations in such environments come from (i) building constraints which limit the amount of workable space, (ii) logistical constraints which are made by the equipment required in the room, such as pianos, drum kits, electronics, or the amount of people to fit, and (iii) acoustical constraints which are in charge to find a balance between acoustic quality and the aforementioned limitations. For example, some recording studios often shorten even more the available space by building a room within a room for optimal sound isolation/insulation purposes, where the remaining space is generally further reduced to fit the required technical equipment. In the case of orchestra pits and some recital rooms, the sheer amount of musicians, chairs, stands, and instruments being present in the environment is the major logistical constraint, where musicians get a little more or a little less than 1.5 m$^2$ each on average [69, 70]. In both situations, space from the walls is thus a precious commodity. Within this context, it has been a growing challenge to design acoustic diffusers that can be contained into ever small practical dimensions.

### 3.3.3 *Late Developments in Modern Sound Diffusers*

In the quest for minimising the size of sound diffusers, the most crucial aspect to study comes down to lowering the resonant frequency of the quarter-wavelength diffuser units, as achieving a lower resonant frequency within existing diffuser dimensions is equivalent to achieve good diffusion at usual frequencies within smaller dimensions. Following such goal, many strategies have been tried. T. Cox *et al.* [34] proposed folding strategies that minimize space by bending QWRs between and underneath their neighbours, thus extending their length and boosting low frequency diffusion. Similar attempts in lowering the resonant frequency were made by J. Hunecke *et al.* [71] who introduced a QWR model closed by perforated or micro-perforated sheets on top of it. P. D'Antonio [38] commercialised optimised sound diffusers made of slotted panels incorporating two-dimensional Helmholtz resonators (HRs) instead of QWRs. By using HRs, the resonance frequency of each slit can be down-shifted, thus extending the bandwidth at which efficient sound diffusion can occur.

This idea of using HRs instead of QWRs has recently been revisited by using the rising concept of metamaterials, which are "composite structures whose wave functionalities arise as the collective manifestations of its locally resonant constituent units" [72]. For example, a block of wood would have physical properties (e.g., density, bulk modulus) dictated by its chemical/atomic composition whereas a metamaterial would gain its physical properties by its structure or arrangement rather than the material it is actually made of. A basic example of an acoustic metamaterial could simply consist of an array of HRs loaded inside a waveguide, achieving deeper subwavelength features due to the coupling of the HRs with the tube [73]. In that sense a HR is a unit cell of the metamaterial.

Considering that Schröeder diffusers are already a sort of structure with locally resonant units (sequence of QWRs), it indeed seems that such sound diffusers already fit the wide definition of metamaterials. However, the notion of Schröeder diffusers can be imagined as an early precursor of modern acoustic metamaterials, where the resonant nature of its constituents can now be enhanced manifold, allowing the design of structures presenting efficient sound diffusion properties within

much deeper subwavelength dimensions.

In 2017, Zhu *et al.* [74] revisited the problem of sound diffuser bulkiness by designing an ultra-thin QRD using a planar array of HRs focused on the low frequency range. These innovative diffusers do not have porous absorbent inside the HRs, in opposition to Ref. [38] above, but rather rely on the tuning of thermoviscous losses to work to deeper frequency regimes. Also, such diffusers only work optimally in a particular frequency range for a particular design and do not present adaptable geometry. Right before the beginning of this work, N. Jiménez *et al.* published in July 2017 a scientific article [75] discussing new state-of-the-art sound diffusers, called *metadiffusers*. More specifically, they developed adaptable metamaterial-inspired sound diffusers optimized on a deep-subwavelength regime which could display efficient sound diffusion performance within dimensions $1/10^{\text{th}}$ to $1/20^{\text{th}}$ thinner than ordinary sound diffusers, with some being as small as 2 cm; making an ideal candidate for the topic of this research as (i) space is critical resource, and (ii) they can be optimized to fit a multitude of custom designs.

The concept of metadiffusers relies heavily on the previously illustrated resonating mechanism inherent to acoustic metamaterials. As such, metadiffusers are rigidly backed slotted panels where each slit is loaded by an array of HRs (see scaled scheme in Fig. 3.11). As it will be seen in the next Chapter, this causes the quarter-wavelength resonance of the slit to be shifted into deep-subwavelength extents, therefore strongly reducing the effective thickness of the panel [76–78]. The geometry variables of metadiffusers are very flexible and can be determined following an optimization procedure. Therefore, many designs were proposed in Ref. [75] were based on numerical sequences that already exist for traditional diffusers, e.g., Quadratic Residue, Primary Root and Ternary Phase sequences. Some others metadiffuser schemes which do not follow any particular sequence but aim to maximise sound diffusion and/or sound absorption will also be discussed in this work [79].

The research by N. Jiménez *et al.* opens the way for compact sound diffuser designs for musical listening rooms where space is limited, such as orchestra pits
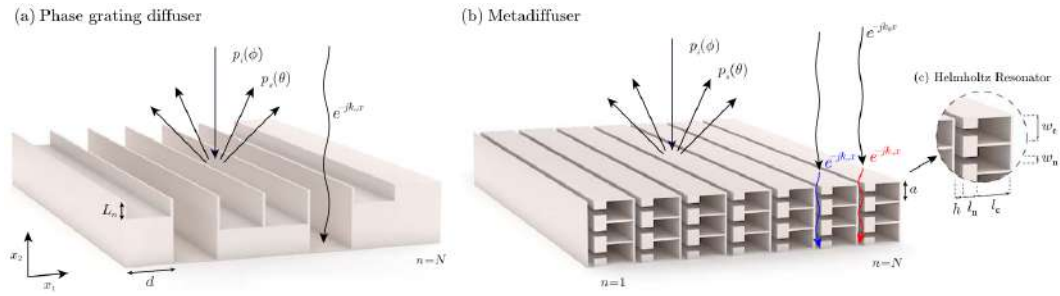
Figure 3.11: (a) Scheme of a Schröeder diffuser composed by $N = 7$ wells. (b) Conceptual scheme of a metadiffuser composed of $N = 7$ deep-subwavelength slits, each of them loaded by $M = 3$ HRs. (c) Detail of a slit of the metadiffuser showing the geometrical parameters of the cavity of a HR ($w_c$ and $l_c$) and its neck ($w_n$ and $l_n$). (After Jiménez *et al.* [75])

and recording studios. This significant change in dimensions holds great potential as such metasurfaces can fit well within strict space limitations. Although some metadiffuser designs were already thought off by the start of the present research, plenty of room is still left for further experimental and numerical validations as well as for exploring new paths for controlling sound diffusion using such structures.

The equations presented in this chapter can be found in the following references:

[26] T. J. Cox, and P. D'Antonio. *Acoustic Absorbers and Diffusers: Theory, Design and Application.* Crc Press, 2009.

[37] T. J. Cox, J.A.S. Angus, and P. D'Antonio. *Ternary and quadriphase sequence diffusers.* The Journal of the Acoustical Society of America 119:310-319, 2006.

[53] T. J. Cox, and P. D'Antonio. *Schroeder Diffusers: A Review.* Building Acoustics 10:1-32, 2003.

[62] ISO 17497-2. *Acoustics – Sound-scattering properties of surfaces – Part 2: Measurement of the directional diffusion coefficient in a free field.* International Standards Organisation, 2012.

[80] N. Jiménez, J-P. Groby and V. Romero-García. *Sound Waves in Metamaterials and Porous Media. Chapter 1. The transfer matrix method in acoustics: Modelling one-dimensional acoustic systems, phononic crystals and acoustic metamaterials.* Springer, 2021,

# 4

## ACOUSTIC METAMATERIALS: LOCALLY-RESONANT STRUCTURES

PHASE grating diffusers, or Schröeder diffusers, are acoustic devices designed to disperse sound in space and time. Such diffusers usually make use of Quarter-Wavelength Resonators (QWR) in the form of wells which possess a resonant frequency $f_0 = c/4L$, where $c$ is the speed of sound and $L$ is the depth of the resonator. However, it has been pointed out that diffusers based on such resonators can often result in bulky structures for mid- to low frequency regimes. Reducing the depth required to manipulate the reflection coefficient of the resonant units has thus been a growing endeavour. Modern advances in the field of wave control materials and structures made over the recent years lead to the application of cutting-edge strategies, such as metamaterials, for down-shifting the resonant frequency of sound diffusers to deep-subwavelength extents.

Most of this chapter will discuss the origin and implications of metamaterials in acoustics, and how these structures affect the constitutive wave propagation parameters (viz., density and bulk modulus) at local and global scales. Further along, some core concepts of metamaterials will be discussed, leading to an upgrade of the previously established Transfer Matrix Method (TMM) that was used for determining the acoustic propagation in a QWR. The new formulation will be applied to a waveguide backed with a periodic array of Helmholtz resonators (Helmholtz Resonator (HR)) and will account for viscothermal losses made by acoustic boundary layers as well as radiation corrections for the resonating unit cells.

Finally, light will be shed on metamaterial-inspired deep-subwavelength sound diffusers known as *metadiffusers* – the cornerstone of this work. Details on how they are designed and how they work will be laid out, leading to a comparison with their traditional counterparts.

## 4.1 RESONANT UNIT CELLS – THE CORE OF METAMATERIALS

This section introduces the concept of metamaterials and outlines the analytical modelling of a simple acoustic metamaterial and its constituent units in the form of Helmholtz resonators (HRs).

### 4.1.1 *The Broad Horizons of Acoustic Metamaterials*

The first conceptual works on metamaterials – although they were not named as such until later – date back to the late 1980s. By then, most academic discussions on the topic dwelt on issues rising from quantum mechanics, more precisely on the study of periodically arranged atomic lattices which would form high transmission energy bands along with bandgaps with no transmission at all [81–83]. Due to the analogous wave formulations between quantum mechanics, optics and acoustics, these studies sprung the advent of photonic and phononic crystals [84–86], which are periodic structures affecting the motion of light waves or sound waves, respectively. In order to be effective, these must however be of the order of the relevant wavelength, resulting in relatively sizeable structures in audible acoustic applications.

The emergence of metamaterials in the first decade of the 21$^{st}$ century addressed dimension issues but also introduced new functionalities not found previously in ordinary materials. Metamaterials could be be defined as "structured composites whose wave functionalities arise as the collective manifestations of its locally resonant constituent units" [72]. Due to the resonant nature of its constituents, the relevant wavelength at the resonant frequency can be orders of magnitude lower than the physical dimension of the resonant unit; making subwavelength and deep-subwavelength features common to most metamaterials. These structures also possess the ability to manipulate waves in such way that no naturally occurring material has been found to do (e.g., negative or near zero density and bulk modulus in acoustics). This brings a second broader definition, which from the Greek "*meta*" (beyond) and the Latin "*materia*" (matter, material), a metamaterial is any engineered composite that has physical properties that are not found in naturally

66

**Phononic Crystals** (a)

- wavelength: $\lambda \sim \lambda_B = 2a$

- Bragg interferences

- identical unit cells (lattice)
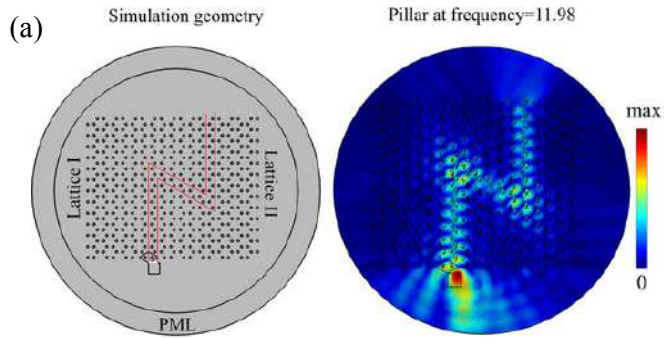
**Acoustic Metamaterials** (b)

- deep-subwavelength: $\lambda \gg \lambda_B$

- local resonances

- different unit cells
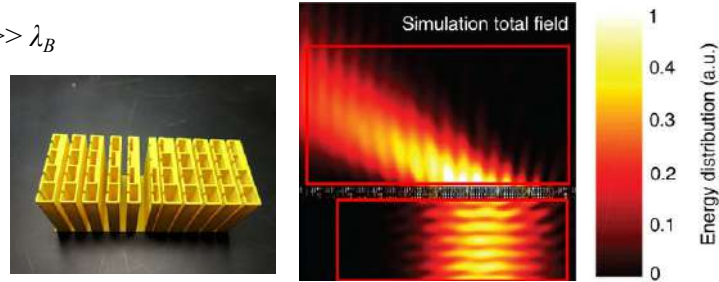


Figure 4.1: Conceptual comparison between phononic crystals and acoustic metamaterials. (a) Example of a phononic crystal bending sound made of a periodic lattice of identical unit cells (from [87]). (b) Acoustic metamaterial refracting sound made of periodic non-identical resonating unit cells (from [88]).

occurring materials. Although the academic community is yet to entirely agree on a set definition for metamaterials, one of these two definitions is often stated, where an emphasis is regularly made on the fact that theses structures are (i) engineered with a specific purpose, and (ii) that they are composites, meaning that they can be made of multiple elements different in nature (which may contrast with photonic/phononic crystals). Figure 4.1 shows a comparison between a phononic crystal and an acoustic metamaterial. One of the major differences between these two types of structures is that of their typical working spatial scales. Phononic crystals work around scales of the order of the unit cell $\lambda \sim \lambda_B = 2a$, where $\lambda_B$ is the Bragg wavelength (bandgap centre wavelength) defined as twice the size of the unit cell $a$, whereas acoustic metamaterials work at orders of magnitude below, i.e., $\lambda \gg \lambda_B$. The latter is due to the resonating nature of the unit cell, which does not necessarily needs to be identically repeated.

Generally, metamaterials (and crystals) are used to control, direct, or manipulate waves in their respective media. In acoustics, controlling sound waves is made by manipulating the effective propagation parameters of the wave equation such as density, $\rho$, and the bulk modulus, $\kappa$, which are related together by the Newton-Laplace formulation for the speed of sound where $c = \sqrt{\rho/\kappa}$. More specifically, metamaterials can display negative values of the effective propagation parameters [72], a feature that is not commonly found in nature and that can be of crucial impact in design strategies. By affecting such fundamental parameters, acoustic metamaterials can be engineered to transmit, reflect, trap, or amplify mechanical waves at certain frequencies in gas, liquid or solid media. As such, acoustic metamaterials come in a variety of shapes for many wave control applications, going from cloaking [89] to trapping [77, 78] and imaging [48], with scales ranging from ultrasonic [50] to seismic wavelengths [90].

Based on the previous definitions, a basic example of an acoustic metamaterial can be made by considering a series of resonators lined within a waveguide, e.g., a duct. Before studying the effective implications of periodicity in such case, priority should be given to define the acoustic properties of the locally-resonant unit cells, and how they come into play within an overall mathematical description of a periodic system.

### 4.1.2 *Locally-Resonant Elements in Waveguides*

Assuming plane waves propagating inside a waveguide of rectangular or cylindrical shape, such as a duct, the change in acoustic pressures and normal particle velocities from one end of the duct to the other can be described through a two-port transmission line. The TMM outlined in Sec. 3.2.1 is a good mathematical tool that can be used to describe such transmission line by a matrix formulation of its constituting elements.

First, in the case of a 1D plane wave propagating in a homogeneous isotropic
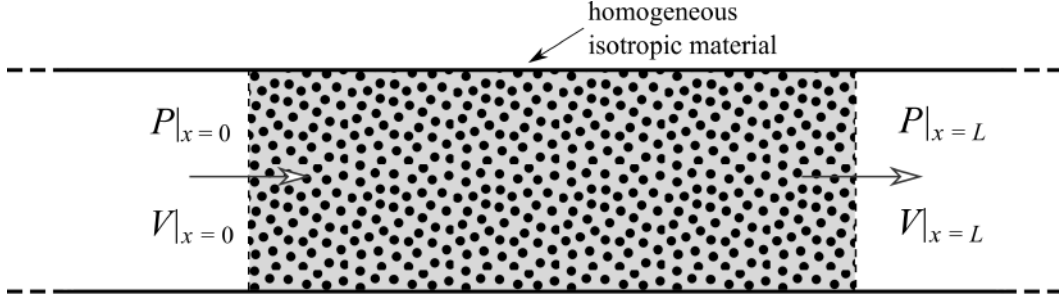
Figure 4.2: Two-port representation of a homogeneous isotropic material bounded within a waveguide of length $L$.

material bounded between two rigid boundaries (see Fig. 4.2), the transfer matrix $\mathbf{T}$ characterizing the material between $x = 0$ and $x = L$ can be written as

$$
\begin{bmatrix} P \\ \mathcal{V} \end{bmatrix}_{x=0} = \mathbf{T} \begin{bmatrix} P \\ \mathcal{V} \end{bmatrix}_{x=L} ,
\tag{4.1}
$$

with

$$
\mathbf{T} = \begin{bmatrix} \cos kL & -i\tilde{Z}\sin kL \\ -i\sin kL/\tilde{Z} & \cos kL \end{bmatrix} ,
\tag{4.2}
$$

where $\tilde{Z} = Z/S$ is the flow formulation ($\mathcal{V} = vS$) of the characteristic impedance of the medium over the section $S$, $k$ is the wavenumber, and $L$ is the length of the material along the $x$ direction. This formulation considers continuity of pressure and flow along the main propagation direction. Yet, some elements can be added within the transmission line which can induce pressure or flow drops in other directions, which is usually the case with locally resonant elements.

Assuming now that a resonating element of lateral dimension $\Delta x$ is much smaller than the wavelength of the propagating wave, the element can then be considered as a punctual resonator. The transfer matrix of this infinitesimal element can be defined in a similar way as Eq. 4.1, but where the transmission matrix $\mathbf{T}$ depends on how the locally-resonating element is loaded within the duct.

### 4.1.2.1 *Side-branch (parallel) elements*

One of the ways a locally-resonant element can be implemented to a waveguide is by loading it to one of its boundaries, as shown in Fig. 4.3. The loaded element can be of variable nature, i.e., an open or closed duct, a HR, or any complex-
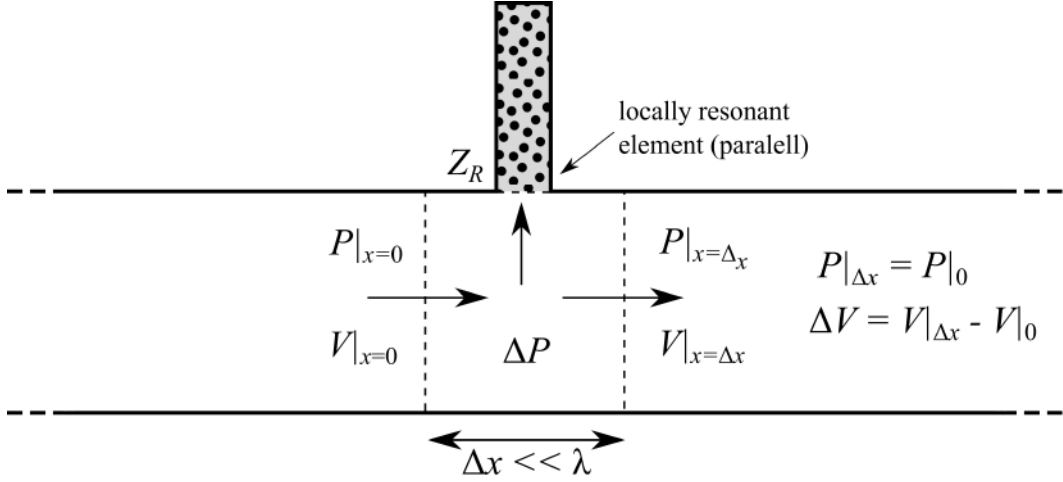
Figure 4.3: Two-port representation of a side-branch locally-resonating element loaded in parallel in a waveguide. The resonator introduces a flow drop while pressure is continuous.

shaped dead-end cavity. On the one hand, the pressure remains constant along the element, i.e.,

$$\Delta P = P|_{\Delta x} - P|_0 = 0, \quad \text{or} \quad P|_0 = P|_{\Delta x}. \tag{4.3}$$

On the other hand, a flow drop at the side-branch resonator implies

$$\Delta \mathcal{V} = \mathcal{V}|_{\Delta x} - \mathcal{V}|_0 = \frac{P|_0}{\tilde{Z}_R}, \tag{4.4}$$

where $\tilde{Z}_R$ the characteristic impedance of the resonator.

The equations relating pressure and flow at both sides of the loaded element can then be expressed as

$$P|_{\Delta x} = P|_0, \tag{4.5}$$

$$\mathcal{V}|_{\Delta x} = \mathcal{V}|_0 + \frac{P|_0}{\tilde{Z}_R}, \tag{4.6}$$

which can be re-written in matrix form to give the transmission matrix of the *parallel* connected element, $\mathbf{T}_p$, as

$$\mathbf{T}_p = \begin{bmatrix} 1 & 0 \\ 1/\tilde{Z}_R & 1 \end{bmatrix}. \tag{4.7}$$

### 4.1.2.2 *In-line (series) elements*

In contrast to the side-branch (parallel) resonator, an in-line locally-resonant element is implemented in series within the waveguide, i.e., across its section, as
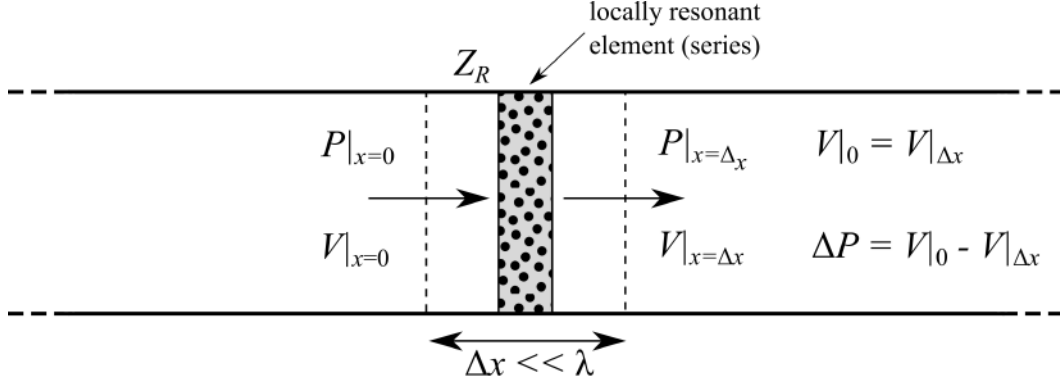
Figure 4.4: Two-port representation of an in-line locally-resonating element loaded in series in a waveguide. The resonator introduces a pressure drop while flow is continuous.

shown in Fig. 4.4. This element can be either a membrane, a plate, or even a section of air stuck between two other elements. In such situation, the flow is continuous across the resonating element, resulting in

$$\Delta \mathcal{V} = 0, \quad \text{or} \quad \mathcal{V}|_{\Delta x} = \mathcal{V}|_0. \tag{4.8}$$

However, the punctual resonator now implies a pressure drop expressed as

$$\Delta P = P|_{\Delta x} - P|_0 = \tilde{Z}_R \mathcal{V}|_0. \tag{4.9}$$

This leads to the equations relating pressures and particle flows at both sides:

$$P|_{\Delta x} = P|_0 - \tilde{Z}_R \mathcal{V}|_0, \tag{4.10}$$

$$\mathcal{V}|_{\Delta x} = \mathcal{V}|_0. \tag{4.11}$$

In a similar approach as for the parallel resonators, the matrix form relating these two equations allows to obtain the transmission matrix of *series* elements, $\mathbf{T}_s$, as

$$\mathbf{T}_s = \begin{bmatrix} 1 & \tilde{Z}_R \\ 0 & 1 \end{bmatrix}. \tag{4.12}$$

Although QWRs discussed in Sec.3.2.1 (i.e., wells) can be a type of locally-resonant element fitted along a waveguide, the implementation of HRs can further enhance the physical properties of the system and shall thus be discussed in more details.

### 4.1.3 *A Helmholtz Resonator (HR) Overview*

This section will emphasize on the physics of HRs, on the expression of their acoustic impedance and how they can be integrated within a periodical system.

#### 4.1.3.1 *Simple Undamped Harmonic Oscillator*

In order to be effective, a metamaterial needs to possess unit cells with interesting physical properties. In acoustics this often translates in a unit cell that displays complex relative motions between its constituent components, i.e., one that displays an inertial response that differs from one of a rigid body. A classical example of such unit cell comes in the form of a Helmholtz resonator (HR), which is constituted by a cavity enclosing a volume opened to the outside by a lump element, called the neck, often of rectangular or cylindrical shape (see Fig. 4.5). This resonating device is well known in literature as an ideal analogous example of a mass loaded on a spring (i.e., simple harmonic oscillator), where the volume of
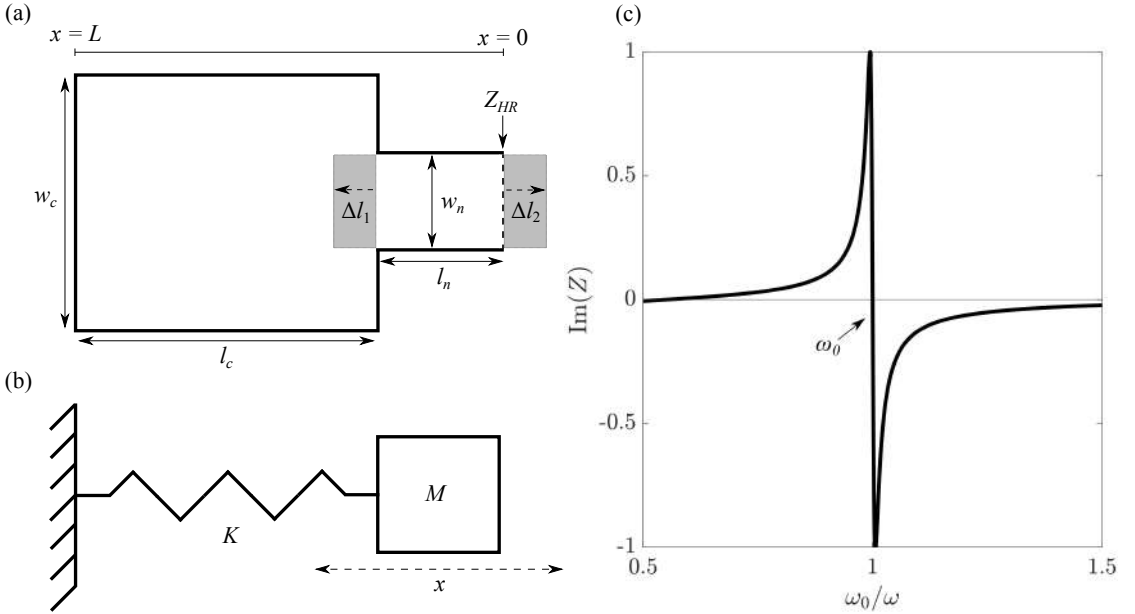


Figure 4.5: (a) Representation of a HR in function of its geometrical variables, with neck length corrections $\Delta l_1$ and $\Delta l_2$. (b) Equivalent mechanical diagram of a simple harmonic oscillator of stiffness $K_s$ and mass $M$ subject to displacement $x$. (c) imaginary part of the oscillator's impedance plotted as function of angular frequency $\omega$.

air inside the cavity of the HR can be viewed as a spring and the one in the neck as a mass. This is due to the fact that the volume of air inside the neck, $V_n = l_n w_n$ in 2D, is pushed in and out of the resonator, and thus respectively compresses and expands the cavity volume, $V_c = l_c w_c$, when an external force is applied, such as that of a sound wave.

When considering such simple analogy, one falls into the ideal situation for which Hooke's law applies, where the restoring force of the spring, $F_s$, can be related to its displacement from its equilibrium position, $x$, and its stiffness coefficient, $K_s$, by the relation $F_s = -Kx$. The sum of the system's balancing forces, $F$, made of the interaction of a mass and a spring can then be viewed as

$$F = F_m - F_s, \tag{4.13}$$

$$\text{or} \quad F = Ma + K_s x, \tag{4.14}$$

where $F_m = Ma$ is the force of the mass given by Newton's second law of motion, and $a$ is the acceleration of the mass $M$.

The mass $M$ of the volume $V_n$ can be defined as $M = V_n \rho$. The acceleration $a$ can also be easily determined by operating a second order derivative over the displacement $x$, i.e., $a = d^2x/dt^2$. Concerning the restoring force of the spring, i.e., the cavity, one can consider that the volume of air in the neck moves out bodily by a small amount $\xi$, which leads the volume $V_c$ to suffer an expansion $\chi = S_n \xi$ or a dilatation $\zeta = S_n \xi / V_c$. Yet, when a fluid is subjected to an incremental hydrostatic pressure $\delta_p$, the said fluid suffers a decrease in volume specified by the volume strain, or dilatation, which according to Hooke's law allows to write the pressure change as $\delta_p = -\kappa \zeta$, where $\kappa = \gamma P$ is the adiabatic bulk modulus, $\gamma$ is the ratio of specific heats and $P$ is the total pressure. Then, the restoring force on the plug of air can thus be written as

$$F_s = S\delta_p = -\frac{\gamma P S_n^2}{V_c} \xi, \tag{4.15}$$

showing that the 'spring constant' of the air in the cavity is $\gamma P S_n^2 / V_c$. Then Eq. 4.14 can be re-written as

$$F = V_n \rho \frac{d^2\xi}{dt^2} + \frac{\gamma P S_n^2}{V_c} \xi. \tag{4.16}$$

By defining the latter expression for a simple harmonic oscillator, one can find its resonant frequency in the form of

$$f_0 = \frac{c}{2\pi}\sqrt{\frac{S_n}{l_n V_c}}.$$ (4.17)

The resonant frequency of a HR of abritrary dimensions is shown in Fig. 4.5, where the imaginary part of the impedance diverges around $\omega_0 = 2\pi f_0$ due to the increased acceleration of the body of air around the neck. Therefore the inertia of the HR acquires a frequency dispersion which can significantly deviate from its equilibrium position and can take negative values in a narrow frequency region that is shaded gray. A careful look onto Eq. 4.17 shows that the HR resonates at frequencies which wavelengths are much larger than its dimensions. A more in-depth discussion to this subwavelenth mechanism is given in Sec. 4.3.3 which compares it that obtained with QWRs. One can also see that the resonant frequency can be affected by the effective parameters $\rho$ and $\kappa$ through the Newton-Laplace formulation of the speed of sound, which in turn can be greatly affected by visctothermal acoustic boundary layers as noted in Sec. 2.2.3.

#### 4.1.3.2   *The Characteristic Impedance of a HR & Neck Length Corrections*

The characteristic impedance provides information about the entire medium considered and is therefore a crucial physical descriptor required for characterizing the propagation of a wave through that medium. In the case of a HR, the latter can be made by an assembly of two rectangular (or cylindrical) tubes of different cross-section. The transfer matrix $\mathbf{T}_{HR}$ for the whole resonator can then be written as a product of the two individual transfer matrices for the neck, $\mathbf{T}_n$, and for the cavity, $\mathbf{T}_c$, leading to

$$\mathbf{T}_{HR} = \mathbf{T}_n \mathbf{T}_c,$$ (4.18)

$$\mathbf{T}_{HR} = \begin{bmatrix} \cos k_n l_n & -i\tilde{Z}_n \sin k_n l_n \\ -i\sin k_n l_n/\tilde{Z}_n & \cos k_n l_n \end{bmatrix} \begin{bmatrix} \cos k_c l_c & -i\tilde{Z}_c \sin k_c l_c \\ -i\sin k_c l_c/\tilde{Z}_c & \cos k_c l_c. \end{bmatrix},$$ (4.19)

where $l_n$, $l_c$, are the lengths of the the neck and cavity, respectively, and $\tilde{Z}_n = \sqrt{\kappa_n \rho_n}/S_n$, $\tilde{Z}_c = \sqrt{\kappa_c \rho_c}/S_c$ their respective characteristic impedances. Applying

rigid boundary conditions at the end of the HR (i.e., at the bottom of the cavity), the characteristic acoustic impedance of the HR can be derived as

$$\tilde{Z}_{HR} = i\tilde{Z}_n \frac{\tilde{Z}_c/\tilde{Z}_n - \tan k_n l_n \tan k_c l_c}{\tilde{Z}_c/\tilde{Z}_n \tan k_n l_n + \tan k_c l_c}. \tag{4.20}$$

This formulation of the acoustic impedance of a HR doesn't take into account the neck length corrections yet. These corrections are used to model more precisely the effective length of the neck by slightly extending the regions at both sides of the neck being subject to the back-and-forths of the mass of air thus moved. The first length correction, $\Delta l_1$, is due to the pressure radiation at the discontinuity between the neck and the cavity of the HR, whilst the second, $\Delta l_2$ comes from the radiation at the discontinuity between the neck and the open area. The total length correction, $\Delta l$, results from the addition of the two correction lengths, $\Delta l = \Delta l_1 + \Delta l_2$, where $\Delta l_2$ depends on the space surrounding the opening of the neck. The following neck length corrections will consider a HR loaded in parallel to the waveguide, resulting in [46]

$$\Delta l_1 = 0.82 \left[ 1 - 1.35 \frac{w_n}{w_c} + 0.31 \left( \frac{w_n}{w_c} \right)^3 \right] w_n, \tag{4.21}$$

$$\Delta l_2 = 0.82 \left[ 1 - 0.235 \frac{w_n}{w_s} - 1.32 \left( \frac{w_n}{w_s} \right)^2 + 1.54 \left( \frac{w_n}{w_s} \right)^3 - 0.86 \left( \frac{w_n}{w_s} \right)^4 \right] w_n, \tag{4.22}$$

where $w_n$, $w_c$ and $w_s$ are the widths of the neck, cavity and the waveguide outside the surrounding area of the neck of the HR, respectively.

Accounting for the total length correction in the acoustic impedance of a HR loaded in a duct results in an upgrade of Eq. 4.20 which can be now be expressed as

$$\tilde{Z}_{HR} = i\tilde{Z}_n \frac{\cos k_n l_n \cos k_c l_c - \frac{k_n \Delta l \tilde{Z}_n}{\tilde{Z}_c} \cos k_n l_n \sin k_c l_c - \frac{\tilde{Z}_n}{\tilde{Z}_c} \sin k_n l_n \sin k_c l_c}{\sin k_n l_n \cos k_c l_c - \frac{k_n \Delta l \tilde{Z}_n}{\tilde{Z}_c} \sin k_n l_n \sin k_c l_c - \frac{\tilde{Z}_n}{\tilde{Z}_c} \cos k_n l_n \sin k_c l_c}. \tag{4.23}$$

## 4.2 1D LOCALLY-RESONANT PERIODIC SYSTEMS

Having defined the physical mechanisms at play in a single resonant unit cell, it is now of interest to discuss the physical implications of periodicity, i.e., joining together several identical resonant unit cells.
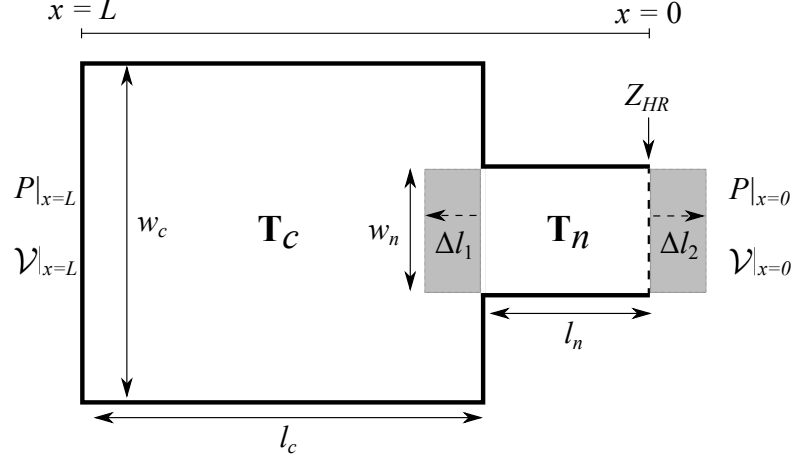
Figure 4.6: Diagram representing the transfer matrix system of a HR in function of its constituting transmission matrices, $\mathbf{T}_n$ (neck), $\mathbf{T}_c$ (cavity), and neck length corrections.

### 4.2.1 *Physical Implications of Periodic Structures*

A structure is periodic if its material properties repeat in space. Considering the latter case of a HR, multiple repetitions of this unit cell evenly spaced along one or more dimensions would lead to a periodic locally-resonant structure. The periodic nature of some structures gives rise to interesting physical phenomena that would not appear otherwise, such as high dispersion and band gaps that nullify wave propagation. Most of the knowledge in this field revolves around the topic of solid state physics, which studies the large-scale properties of materials in function of their atomic-scale properties, i.e., atomic arrangement. The similarity of the wave functions between quantum mechanics, optics and acoustics allows the mathematics describing periodicity to remain the same from atomic-scale to large-scale scenario.

Periodicity can appear under many viewpoints. Yet, a system is said to be periodic when there is symmetry of operations, i.e., when the pattern between unit cells inside a *lattice* (or grid) stays the same despite the application of any transformation, such as a translation, rotation, reflection, or all at once. *Crystal structure* is a term often used to describe a said ordered arrangement (lattice) of identical unit cells, hence the existence of photonic or phononic *crystals* in optics and acoustics.

There are many types of periodic structures with as many different goals, spanning from diffraction gratings made of simple unit cells to labyrinthine waveguides with complex and variable unit cells. However, these structures possess some similarities that derive purely from their periodic nature. One of the most important laws applicable to wave fields inside periodic structures is the Bloch-Floquet theorem.

The Bloch-Floquet theorem stipulates that waves inside a periodic structure are analogous to plane waves modulated by an envelope (or periodic) function, as shown in Fig. 4.7. In such case, it is the envelop function which takes the same periodicity as the structure where the wave field is propagating. Mathematically, the latter can be expressed as

$$\psi_B(\mathbf{r}) = e^{i\mathbf{k}\cdot\mathbf{r}}u(\mathbf{r}), \tag{4.24}$$

where $\mathbf{r}$ is the position, $e^{i\mathbf{k}\cdot\mathbf{r}}$ is a plane wave function, $u(\mathbf{r})$ is the periodic function and $\psi_B(\mathbf{r})$ is the resultant Bloch wave function in the periodic system, which is simply a product of the latter two functions. The Bloch-Floquet formulation of the wave field inside a periodic structure is not only crystal clear but also very efficient. F. Bloch was maybe the first one to be surprised by the simplicity of this discovery:

> *By straight Fourier analysis I found to my delight that the wave differed from the plane wave of free electrons only by a periodic modulation. This was so simple that I did not think it could be much of a discovery, but when I showed it to Heisenberg, he said right away;"That's it!".*

> – F. Bloch, July, 1928
> (from the book edited by Hoddeson *et al.* [91]).

The major implication of this theorem is that due to the periodicity of $u(\mathbf{r})$, one can apply a discrete Fourier transform over it, leading to a mathematical simplification describing the overall wave field. Thanks to this, waves propagating (or non-propagating) inside a periodic structure can be determined following several methods. One of them is called the Plane Wave Expansion (PWE), which by means of Fourier expansion series and an eigen formulation of the wave equation
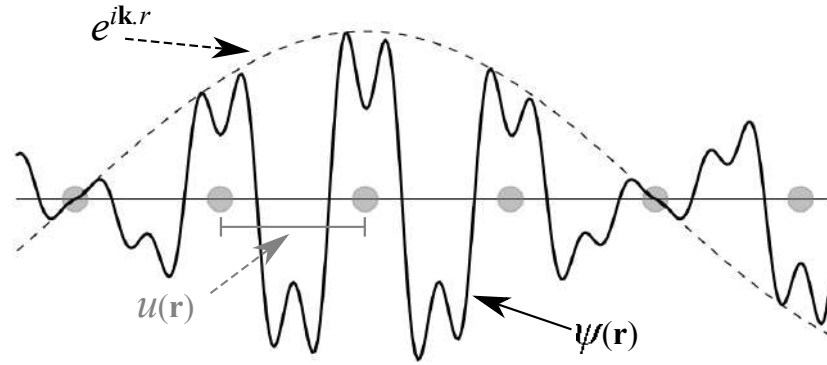
Figure 4.7: Diagram representing the real part of a 1D Bloch wave passing through a periodic medium made of several scatterers. [from Wikipedia [92], CC]

ultimately leads to the dispersion relation and band gap nature of the structure for each of propagating eigenvector directions. However, the PWE will not be used in this work as an application of the Bloch-Floquet theorem into the TMM will be shown instead in the next section.

The other important physical phenomenon that rises in periodic structures is that of Bragg scattering, sometimes referred to as Bragg diffraction or Bragg condition. The latter refers to the ability of a crystalline structure to specularly radiate scattered energy for specific wavelengths and incident directions. This is due to the constructive and destructive interferences arising from the scattering of the multitude of elements comprised inside a crystal lattice. Similarly to Snell-Descartes law, Bragg's law relates the incident angles of the wavevectors and their wave-
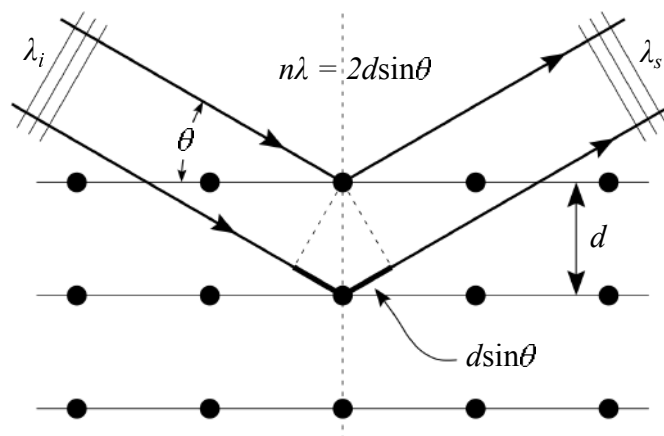


Figure 4.8: Diagram representing the Bragg scattering of a wave interacting with a periodic medium. [from Wikipedia [93], CC]

length with the spacing of the lattice's unit cells. This relation can be expressed as

$$n\lambda = 2d\sin\theta, \tag{4.25}$$

where $n$ is a positive integer known as the order of the corresponding reflection, $\lambda$ is the wavelength of the incident wave, $d$ is the distance between unit cells, and $\theta$ is the normal glancing angle made between the impinging wave and the unit cells.

A major consequence of Bragg diffraction is that for certain frequency ranges the crystal will be reflecting waves in phase and thus will not allow any energy to be effectively transmitted throughout the structure, therefore creating a band-gap (or stop band) with no effective wave propagation. The width of such band-gap depends on the periodicity of the structure, the filling fraction of unit cells, and the propagation speed inside the periodic medium.

### 4.2.2 *A Waveguide Loaded With Multiple Helmholtz Resonators*

Now that the resonant mechanisms of a unit cell and the major physical implications of periodic structures have been outlined, a case study of a 1D locally-resonant periodic system can be made where both of these concepts are put together. The dispersion relation and band-gap of such structure can be then be obtained by using the previously established TMM.

The system thus considered consists of a tube of circular or rectangular cross-section within which a series of HRs are loaded along its length (see Fig. 4.9). One HR and its neighbouring opening area in the tube can be translated here as a unit cell of lattice constant $a$, integrated as a parallel resonant branch to the main tube. Accordingly, the HRs can be described as punctual scatterers by the transmission matrix $\mathbf{M}_{HR}$ as

$$\mathbf{M}_{HR} = \begin{bmatrix} 1 & 0 \\ 1/\tilde{Z}_{HR} & 1 \end{bmatrix}, \tag{4.26}$$

where $\tilde{Z}_{HR}$ is the characteristic impedance of the HR, as explained in Sec. 4.1.3.2. Due to the periodicity of the system, the physical characteristics of the entire structure can be obtained by the local study of a unit cell, a strategy made possible

79

thanks to the Bloch-Floquet theorem. For such periodic system, the pressures and normal flow velocities from both ends of the unit cell can satisfy said theorem provided that

$$
\begin{bmatrix} P \\ \mathcal{V} \end{bmatrix}_{x=0} = \mathbf{T}_{uc} \begin{bmatrix} P \\ \mathcal{V} \end{bmatrix}_{x=a} = \begin{bmatrix} T_{11} & T_{12} \\ T_{21} & T_{22} \end{bmatrix} \begin{bmatrix} e^{-ik_ea}P \\ e^{-ik_ea}\mathcal{V} \end{bmatrix}_{x=a}, \tag{4.27}
$$

where $P$ and $\mathcal{V}$ are the pressures and flow velocities, $k_e$ is the effective wavenumber propagating in the periodic medium. The transmission matrix of the unit cell, $\mathbf{T}_{uc}$, takes the form of a lump of a slit transmission matrix, $\mathbf{M}_s$, multiplied by that of the scattering matrix of the HR, $\mathbf{M}_{HR}$, such that

$$
\mathbf{T}_{uc} = \mathbf{M}_s \mathbf{M}_{HR} \mathbf{M}_s \tag{4.28}
$$

$$
\mathbf{T}_{uc} = \begin{bmatrix} \cos k_e \frac{a}{2} & -i\tilde{Z}_s \sin k_e \frac{a}{2} \\ -i\sin k_e \frac{a}{2}/\tilde{Z}_s & \cos k_e \frac{a}{2} \end{bmatrix} \begin{bmatrix} 1 & 0 \\ \frac{1}{\tilde{Z}_{HR}} & 1 \end{bmatrix} \begin{bmatrix} \cos k_e \frac{a}{2} & -i\tilde{Z}_s \sin k_e \frac{a}{2} \\ -i\sin k_e \frac{a}{2}/\tilde{Z}_s & \cos k_e \frac{a}{2} \end{bmatrix}. \tag{4.29}
$$

Equation 4.27 can thus be rearranged to obtain

$$
\left( \begin{bmatrix} T_{11} & T_{12} \\ T_{21} & T_{22} \end{bmatrix} - \begin{bmatrix} e^{ik_ea} & 0 \\ 0 & e^{ik_ea} \end{bmatrix} \right) \begin{bmatrix} P \\ V \end{bmatrix}_{x=a} = 0. \tag{4.30}
$$

Defining $\Lambda = e^{ik_ea}$, this system only possesses solution if

$$
\left| \begin{bmatrix} T_{11} - \Lambda & T_{12} \\ T_{21} & T_{22} - \Lambda \end{bmatrix} \right| = 0. \tag{4.31}
$$

By using the reciprocity condition in symmetric matrices, i.e., $T_{11}T_{22} - T_{12}T_{21} = 1$, the dispersion relation can be obtained by isolating $\Lambda$ and taking the real part of its Euler notation ($e^{ik_ea} = \cos k_ea - i\sin k_ea$), resulting in

$$
\cos k_ea = \frac{T_{11} + T_{22}}{2} = \frac{\mathrm{Tr}(\mathbf{T}_{uc})}{2}, \tag{4.32}
$$

with $\mathrm{Tr}(\mathbf{T}_{uc})$ being the trace of the matrix $\mathbf{T}_{uc}$, i.e., the sum of its diagonal components. Finally, the effective complex wavenumber and effective acoustic impedance at the entrance of the structure can be obtained from the transfer matrix elements as

$$
k_e = \frac{1}{a}\cos^{-1}\left( \frac{T_{11} + T_{22}}{2} \right), \quad Z_e = \sqrt{\frac{T_{12}}{T_{21}}}. \tag{4.33}
$$
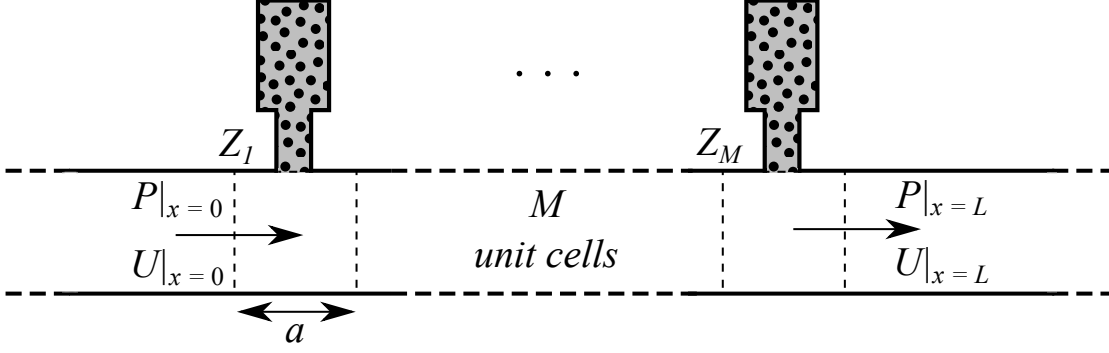
Figure 4.9: Two-port representation of $M$ locally-resonant unit cells of size $a$ loaded in parallel into a waveguide of length $L$.

The above derivation of the dispersion relation holds true for a unit cell within an infinitely periodic medium. Due to periodicity, this dispersion relation and the subsequent propagation sound speed are the same independently of the number of unit cells. However, in order to characterize the transmission and/or reflection coefficients of the periodic structure, one needs to take into account the actual number of unit cells that are being repeated. Thus, in finite periodic systems, the transfer matrix of the whole structure, $\mathbf{T}$, becomes the product of the individual transmission matrices of each constituting unit cell, such that

$$\mathbf{T} = \mathbf{T}_{uc}^{M} = (\mathbf{M}_s \mathbf{M}_{HR} \mathbf{M}_s)^{M} \tag{4.34}$$

where $M_r$ is the number of unit cells in the finite periodic structure. The dispersion relation within this system remains the same as previously, but now that a set number of unit cells is being accounted for, the underlying transmission or reflection coefficients can then reflect the finiteness of the periodic structure.

In a transmission problem, the transmission and reflection coefficients of a periodic structure can be determined from the transfer matrix elements of the finite system of length $L = Ma$, resulting in

$$T = \frac{e^{-ik_e L}(T_{11}T_{22} - T_{12}T_{21})}{T_{11} + T_{12}/Z_0 + Z_0 T_{21} + T_{22}}, \tag{4.35}$$

$$R = \frac{T_{11} + T_{12}/Z_0 - Z_0 T_{21} - T_{22}}{T_{11} + T_{12}/Z_0 + Z_0 T_{21} + T_{22}}. \tag{4.36}$$

### 4.2.3 *Dispersion Relation, Slow Sound & Band-Gap*

Now that the physics of a periodic resonant structure have been described, the resultant dispersion relation and transmission/reflection coefficients of a periodic system can be obtained by computing the transfer matrix **T** for a wide range of frequencies. A first example will consider a tube loaded by a series of identical HRs of arbitrary dimensions and of lattice constant $a_x$. This will allow to draw the dispersion relation inside the periodic medium as well as the phase velocity of the propagating acoustic wave. A second example will consider the same tube loaded with a variable number of unit cells, $M$, allowing to output the reflection, transmission and absorption coefficients of the periodic structure.

The dispersion relation shown in Fig. 4.10(a) shows the real part of the normalised wavenumber propagating in one unit cell, which due to periodicity will remain the same for the entirety of the periodic structure independently of the number of unit cell repetitions. It can be observed that the periodic medium becomes more dispersive as the frequency of the propagating sound wave approaches
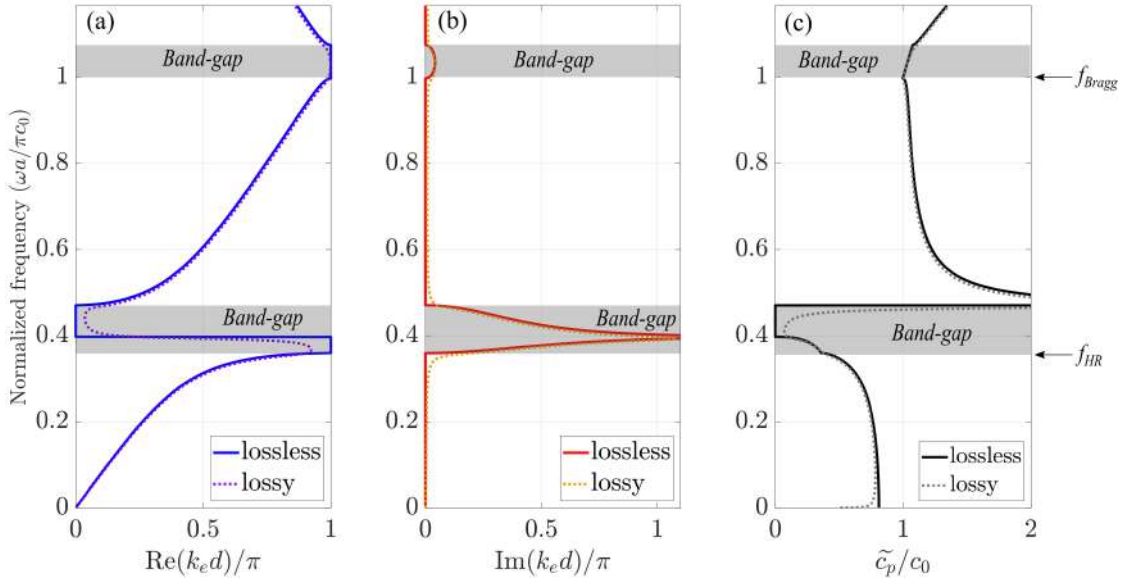


Figure 4.10: (a) Real part of the dispersion relation, $\text{Re}(k_e)$, of an arbitrary locally-resonant unit cell in a periodic medium. (b) Imaginary part of the dispersion relation, $\text{Im}(k_e)$. (c) Phase speed of sound propagation, $\tilde{c}_p$, in the periodic medium.

the resonant frequency of the HR. At low frequencies, the dispersion relation already deviates steadily from that of a homogeneous isotropic medium and reaches an asymptotic peak at the HR resonance, where the real part of the wavenumber remains steady and its imaginary component increases respectively, as shown in Fig. 4.10(b). This is due to the fundamental resonance mechanism of the HR unit cell, which when approaching its resonance frequency has its imaginary part increase. After the peak in $\mathrm{Im}(k_e)$, the real part of the wavenumber vanishes as long as the imaginary part of the wavenumber remains positive. During this regime, the real part of the dispersion relation occurring in the medium is zero, meaning that there is no effective sound propagation. The rising of the imaginary part announces the beginning of the band-gap of the periodic structure and all the frequencies covered by this band-gap are therefore not transmitted. The band-gap will progressively disappear until the imaginary part of the dispersion relation vanishes, after which the dispersion relation will evolve according to other medium characteristics. In this case, $\mathrm{Re}(k_e)$ increases almost linearly to unity until a second imaginary peak appears at the Bragg frequency $f_{Bragg} = \omega a / \pi c_0$, where Bragg scattering happens due to the multiple wave interferences caused by periodicity, thus creating a second band gap.

Alternatively, Fig. 4.10(c) shows the effective phase velocity of sound waves propagating in the periodic medium. The first band-gap can be clearly seen to cover the same frequencies as in Figs. 4.10(a,b), where the propagative phase velocity of sound reaches zero. Before such phenomenon, the phase speed inside the periodic medium can be observed to be below that of free air sound propagation, thus creating a subsonic (slow sound) regime where waves propagate at lower speeds. The extent of how slow the sound propagates is intrinsically dictated by the geometry of the unit cells and the waveguide and can thus be reduced further down than in the present example if needed. This characteristic can be of great use for down-shifting the resonant frequency of a hosting waveguide, such as QWR in further cases. Additionally, the inclusion of viscothermal losses in the periodic medium modifies the dispersion relation where the strongly dispersive flat propagative bands (i.e., ideal dispersion relation) are smoothed to more plausible gradients.

For the continuity of the same example, Fig. 4.11 shows the transmission, reflection and absorption coefficients of the same duct loaded with a variable number $M$ of HRs of arbitrary dimensions – which remain the same as before. In the present transmission context, the absorption coefficient is estimated as $\alpha = 1 - |R|^2 - |T|^2$. In the case of $M = 3$ HR, shown in Fig. 4.11(a), it can be observed that the transmission coefficient drops down to its minimum around the resonant frequency of the HR, where the reflection coefficient conversely reaches its maximum. The frequency range of the decrease in transmission clearly falls around the first band-gap of the metamaterial. In the upper frequency range, the band-gap marked by the Bragg frequency does not exhibit any strong reduction in transmission. This is due to the small number of repeated unit cells as explained below. One thing to note in the propagative band below to the first band-gap is the existence of $M - 1$ peaks of transmission coefficients (or gaps in reflection coefficients), which occur for frequencies $\omega a_x / \pi c_0 < 1$; omitting the peak at 0 Hz. These transmission peaks correspond to the Fabry-Pérot resonances of the finite system, where waves can pass through the system only when they are in resonance with it (i.e., constructively in phase). The further the number $M$ is increased, the more Fabry-Pérot resonance peaks are observed, and the sharper the filtering effect on the band-gap results, ultimately fitting at best the lower and upper band-gap boundaries established by the periodic dispersion relation.

Such effect can be seen in the case of $M = 10$ HRs in Fig. 4.11(b), where the increase of repeated unit cells visibly leads to a significant enhancement of the bang-gap of the structure, where the reflection and transmission coefficients now clearly fall within the lower and upper boundaries of the band-gap dictated by the periodic structure. Moreover, the band-gap associated to the Bragg frequency is now substantially more visible. As mentioned previously, this is due to the increase of unit cells in the medium which approximate the infinite periodicity assumed in Bragg scattering theory.

Figure 4.11 also shows the absorption coefficient for both $M = 3$ and $M = 10$ cases when calculated with and without viscothermal losses. It can be observed that losses do generate absorption peaks before and after the band-gaps, with minimal values inside them. The more the number of unit cell repetitions, the
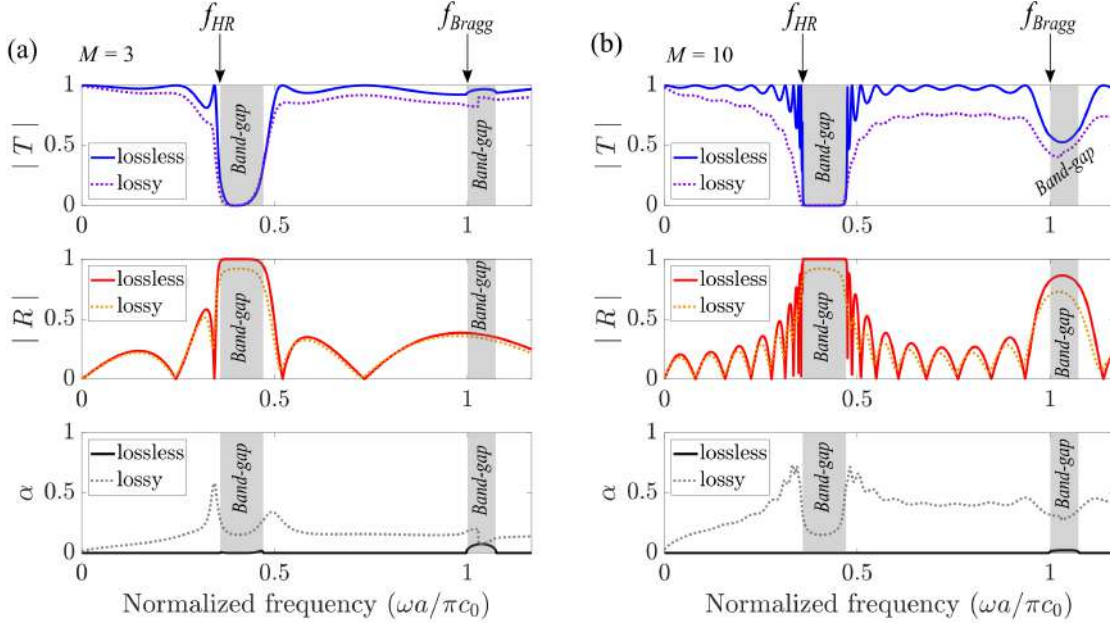
Figure 4.11: Transmission, reflection and absorption coefficients of a 1D locally-resonant periodic system with (a) $M = 3$, and (b) $M = 10$ unit cells.

more absorption is generated due to the rising cross-overs between Fabry-Pérot modes. Also, a higher absorption appears in average over most of the considered spectrum due to the added losses between unit cells.

## 4.3 DEEP-SUBWAVELENGTH SOUND DIFFUSERS (A.K.A. METADIFFUSERS)

In this section, the variable and optimized nature of metadiffusers will be discussed, after which the different types of documented metadiffusers will be covered. Lastly, a comparison between a metadiffuser deep-subwavelength slit and a QWR of same height will be conducted, where a clear emphasis will be made on the phase changes of their respective reflection coefficients.

### 4.3.1 *The Variable & Optimized Nature of Metadiffusers*

Metadiffusers are deep-subwavelength sound diffusers inspired from metamaterial design strategies. As such, they are formed of rigidly backed slotted panels, where each slit is loaded by an array of HRs. As it has been demonstrated previously, this introduces strong dispersion and the effective sound speed inside each
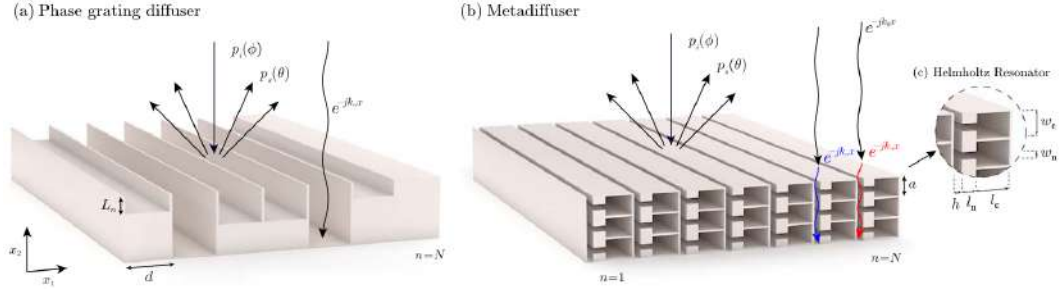
Figure 4.12: (a) Scheme of a Schröeder diffuser (QRD) composed by $N = 7$ wells. (b) Conceptual scheme of a metadiffuser composed of $N = 7$ deep-subwavelength slits, each of them loaded by $M = 3$ HRs. (c) Detail of a slit of the metadiffuser showing the geometrical parameters of the cavity of a HR ($w_c$ and $l_c$) and its neck ($w_n$ and $l_n$). (After *Jiménez et al.* [75])

slit is drastically reduced in the low frequency regime, i.e., at frequencies below the resonant frequency of the HR unit cells. The slowing of sound thus created results in a decrease of the resonant frequency of the entire cavity, allowing resonance to occur within a structural thickness much smaller than the one of a single well (e.g., a QWR).

Figure 4.12 shows the conceptual scheme of a metadiffuser compared to a typical phase-grating sound diffuser. The geometrical dimensions of each slit need to be fined-tuned in order to produce any desired distribution of the surface reflection coefficient. The design strategy behind metadiffusers – loading a slit with a series of HRs – allows great flexibility in geometrical dimensions, where the width of each slit and the lengths and widths of the HRs can be changed to a relatively high degree, only limited by the overall width of the slit made by the sum of both elements. This can result in a plethora of different dispersion relations for each slit thus increasing the potential of geometrical combinations that can be made along the surface. Moreover, the number of HRs in the slits can also be variable depending on the situation. This adaptability rising from the interplay of all these geometrical variables enables a multitude of designs and is a key feature of metadiffusers.

In order to create a metadiffuser, one can use the TMM model in a reflection problem (as in Sec. 3.2.1), which allows to output the reflection coefficient of the system in function of the finite number of unit cells per slit (with $R$ defined as in Eq. 3.8). In such case, the transfer matrix for the $n$-th slit of width $h$ loaded with $M$ identical HRs and separated from the other slits by a distance $d$ can be written as

$$\mathbf{T}^n = \mathbf{M}^n_{\Delta l_{slit}} \left( \mathbf{M}^n_s \mathbf{M}^n_{HR} \mathbf{M}^n_s \right)^M . \tag{4.37}$$

Here, the transmission matrix for each lattice step of the $n$-th slit, $\mathbf{M}_s$, can be described as the one of a homogeneous isotropic medium:

$$\mathbf{M}^n_s = \begin{bmatrix} \cos(k^n_s \frac{a}{2}) & -i\tilde{Z}^n_s \sin(k^n_s \frac{a}{2}) \\ -i\sin(k^n_s \frac{a}{2})/\tilde{Z}^n_s & \cos(k^n_s \frac{a}{2}) \end{bmatrix}, \tag{4.38}$$

where $a$ is the length of the unit cell, $k^n_s$ the wavenumber in the lattice step of the slit, and $\tilde{Z}^n_s = \sqrt{\kappa^n_s \rho^n_s}/S^n_s$ is the characteristic impedance of the slit lattice step of surface $S^n_s = h^n a$. The transmission matrices of the resonators, $\mathbf{M}^n_{HR}$, are introduced as punctual parallel elements of characteristic impedance $\tilde{Z}^n_{HR}$. The transmission matrix for the radiation correction of the $n$-th slit to the free space, $\mathbf{M}^n_{\Delta l_{slit}}$, is implemented as a series element (see Eq. 4.12) with a characteristic radiation impedance $\tilde{Z}^n_{\Delta l_{slit}} = i\omega \Delta l^n_{slit} \rho_0 / \phi^n_t S_0$ where $S_0 = da$ and $\Delta l^n_{slit}$ is the radiation end correction from the slits to the free air. The radiation correction for a periodic distribution of slits can be expressed as [75]

$$\Delta l^n_{slit} = h^n \sigma^n \sum_{n=1}^{\infty} \frac{\sin^2(n\pi\sigma^n)}{(n\pi\sigma^n)^3}, \tag{4.39}$$

where $\sigma^n = h^n/d$ is the superficial porosity. With such information the surface reflection coefficient (in a reflection problem) can be obtained by the cumulation of each slit constituent as

$$R^n = \frac{T^n_{11} - Z_0 T^n_{21}}{T^n_{11} + Z_0 T^n_{21}}, \tag{4.40}$$

which then allows to determine the pattern of the scattered sound pressure made by the panel.

The flexible nature of metadiffusers implies that many phase profiles (of the reflection coefficient along the surface) can be achieved through different geometrical combinations. This means that existing phase profiles – such as QRS, PRS,

etc. – can be matched by a metadiffuser only at certain frequencies given the right geometrical dimensions. In the original publication by N. Jiménez *et al.*[75], it was shown that this could be achieved using an optimization algorithm, e.g., sequential quadratic programming [94] for constrained minimization methods [95]. By doing this, the width of the slit $h$ and the widths and lengths of the necks and cavities of the HRs, $l_n$, $w_n$, $l_c$ and $w_c$ – and the intrinsic viscothermal losses inherent to these – can be fine-tuned in order to reach the target phase profile within certain geometrical constraints, e.g., height of the slit $L$ and number of resonators per slit, $M$.

The optimization problem can be solved via a constrained non-linear minimization [96]. The aim of the latter problem consists in finding a vector, $\Gamma$, that has local minimum to a scalar function $\epsilon(\Gamma)$ subject to constraints on $\Gamma$. In our present context of metadiffusers, $\Gamma$ is matrix containing $N$ vectors (for $N$ slits) each conveying the geometrical variables required to compute the reflection coefficient of a slit, viz., the height of the slit, $L$, the width of the slit, $h$, and the widths and lengths of the necks and cavities of the HRs ($l_n$, $w_n$, $l_c$ and $w_c$). The purpose of the minimization cost function (or objective function), $\epsilon(\Gamma)$, is to tend to zero when the surface reflection coefficient of the metadiffuser is the same as the target diffuser phase profile, i.e.,

$$\epsilon(\Gamma) = R_{meta}(\Gamma) - R_{goal}, \tag{4.41}$$

where $R_{meta}(\Gamma)$ and $R_{goal}$ are the surface reflection coefficients obtained at a particular frequency for the metadiffuser and the target diffuser, respectively. Additionally, $\Gamma$ is subject to constraints with respect to the overall panel height (or slit height), $L$, the overall slit width $D$ determined by the ratio of the panel width, $W$, over the number of slits such that $D = W/N$, as well as low and upper boundaries limiting the search for a local minimum within desired geometrical values. Mathematically, the minimization problem can be expressed as

$$\min_{\Gamma} \epsilon(\Gamma) \begin{cases} c_{in}(\Gamma) \leq 0 \\ c_{eq}(\Gamma) = 0 \\ b_l \leq \Gamma \leq b_u \end{cases} \tag{4.42}$$

where $c_{in}(\Gamma)$ is a constraint inequality and $c_{eq}(\Gamma)$ a constraint equality that return $\Gamma$ matrices, and $b_l$ and $b_u$ are the lower and upper boundary values of $\Gamma$. The inequality constraint $c_{in}(\Gamma)$ can be useful alongside upper and lower boundaries in order to check that the calculated variables do not exceed a certain predefined quantity. On the other hand, the equality constraint $c_{eq}(\Gamma)$ can be used to set a strict condition on some variables. For our present purpose, the lower and upper boundaries, $b_l$ and $b_u$, are enough to constrain our geometry.

With the inclusion of such optimization methods in the design paradigm, metadiffusers that mimic the phase profiles of other sound diffusers can be successfully designed, such as metadiffusers based on QRS, PRS and even hybrid diffusers based on TPS. Besides this equivalent scattering behaviour at some particular frequencies, metadiffusers can also provide significant sound scattering at other frequencies. They also have the advantage to fit within dimensions $1/10^{\text{th}}$ to $1/20^{\text{th}}$ the thickness of traditional sound diffusers. The next section will discuss the particularities of the different types of metadiffuser designs that were documented in the original publication.

### 4.3.2 *Different Types of Metadiffusers*

In the original publication by N. Jiménez *et al.* [75], various types of metadiffusers were reported which targeted phase-profiles of other traditional sound diffusers. In such an approach, the phase of the reflection coefficient of the metadiffusers is not calculated according to a specific number sequence but is here optimised directly to fit the spatially-dependent reflection coefficient of a particular sound diffuser. This is because the sequences and the subsequent design equations determining the depth of the wells discussed in Sec. 3.2.1 only work when the phase of the reflection coefficient behaves in a linear way, e.g., a QWR. Due to the variable nature the metadiffuser slits, the reflection coefficients of each can be highly non-linear, potentially creating great value fluctuations between each slit and thus making the general sequence design equations quite inadequate for such structure. However, the strength of a metadiffuser lies in its incredible flexibility,

which as mentioned previously makes it a fine candidate to optimization methods and can result in an even higher number of potential designs. The following section aims to cover the different types of metadiffusers discussed in the original work of Ref. [75] in order to better introduce the design guidelines required for creating original metadiffusers in the following Chapter.

### 4.3.2.1 *Quadratic Residue Metadiffusers*

The purpose of a Quadratic Residue Metadiffuser (QRM) is to mimic the phase profile of the spatially-dependent reflection coefficient of a QRD at a specific fre-



Figure 4.13: (a) Phase and (b) magnitude of the reflection coefficient of a QRD and the QRM. (c) Far-field polar distribution of the QRD and QRM obtained by TMM. (d) Diffusion coefficient of the QRM optimized at 2000 Hz (marker) and a reference QRD. (e) Absorption coefficient of the QRM, where the grey lines shows the absorption of individual slits $n = 3$ and $n = 5$. (f) Scaled scheme of the QRM with $N = 5$ and $M = 2$.

quency. Assuming a target QRD with $N = 5$ wells, of design frequency $f_0 = 500$ Hz, lateral size $W = ND = 35$ cm and total thickness $L = 27.4$ cm, an equally wide $N = 5$ slits QRM can be designed where each of its slits aims to replicate the phase behaviour of its corresponding well on the QRD. Considering the lateral dimensions of the QRD and QRM, it is best to evaluate the sound scattering of both diffusers at a frequency larger than $\lambda = 0.35$ m ($f >\sim 1000$ Hz) in order to avoid the diffraction regime caused by the finite size of the sample and thus emphasize on the scattering response generated by the series of wells or slits. Thus a frequency $f = 2$ kHz will be taken here.

Figure 4.13 shows the physical characteristics of an optimized QRM and an equivalent QRD which have been both repeated $m = 3$ times using the TMM. As QRDs have the particularity of generating $m$ evenly spaced diffraction lobes in the far-field scattering distribution, multiple repetitions of the QRM should also lead to such effect. It can be seen in Figs. 4.13(a,b) that the distribution of the spatially-dependent reflection coefficients of the two diffusers along the $x$-axis are in excellent agreement. A very small amount of sound absorption from the QRM slits can be seen in the magnitude of its reflection coefficient, slightly deviating from that of the QRD. Figure 4.13(c) shows the far-field scattered sound pressure levels obtained by both diffuser repetitions, where the typical $m = 3$ even diffraction lobes of both structures can be observed to be near identical. This is again supported by the high similarity in surface reflection coefficients, which consequently leads to similar scattering distributions. Figure 4.13(d) shows the normalized diffusion coefficients of both diffusers in function of frequency. It can be observed that the normalized diffusion coefficient at $f = 2$ kHz is the same for both diffusers. On the one hand, the QRD shows better sound diffusion at low frequencies than the QRM (peak at 1 kHz) but presents two notches, one with $\delta_n \approx 0.175$ at around 1.7 kHz and the other with $\delta_n = 0$ at 2.5 kHz. The notch at 2.5 kHz occurs at the critical frequency of the QRD, $f_c = Nf_0$, at which point all wells radiate sound in phase thus limiting the broadband performance of the QRD. On the other hand, the QRM starts to show a good diffusion performance past 1 kHz but remains relatively constant throughout frequency with diffusion

values in the same overall range as those of the QRD. This broadband diffusion behaviour is linked to the number $M$ of HRs inside the slits, the higher number of which produces multiple collective modes that will affect the surface impedance to higher frequencies and thus may help in creating further dispersion. Figure 4.13(e) displays the absorption coefficient of the QRM where the dark grey and light grey lines represent the absorption of the $n = 5$ and $n = 3$ slits and the blue curve shows the absorption averaged over the number of slits, $N$. Due to the strong dispersion relation within the slits, the impact of viscothermal boundary layer losses on the attenuation of sound can be variable depending on the dimensions of the slits and HRs. In this case, the QRM displays a few narrow absorption peaks as a by-product of the optimized geometry; some values of which can reach $\alpha = 0.5$ around some discrete frequencies. Yet, at 2 kHz a minimal absorption of 0.03 is shown. Figure 4.13(f) displays the scaled scheme of the optimized $N = 5$ QRM with $M = 2$ HRs per slit. Despite generating the same scattering at 2 kHz as the QRD of height $L = 27$ cm, the QRM exhibits an overall height $L = 2$ cm almost fourteen times thinner than the QRD.

#### 4.3.2.2 *Primitive Root Metadiffusers*

In a similar approach to the QRM, the Primitive Root Metadiffuser (PRM) aims to replicate the same scattering as a PRD at a specific frequency. Here, an $N = 6$ PRD of height $L = 17.1$ cm is taken as reference for the optimization of an $N = 6$ PRM of height $L = 3.5$ cm. Figures 4.14(a,b) show an excellent agreement between the phases and magnitudes of the two reflection coefficients, leading to congruent far-field scattering distributions as shown in Fig. 4.14(c). As expected from a PRS, both diffusers present a notch in the specular direction in their scattering distributions, i.e., around $\theta = 0°$ at $f = 1$ kHz in this case. The diffusion coefficients of both diffusers outlined in Fig. 4.14(d) show that despite providing the same diffusion as the PRD around a design frequency, the PRM displays a lower broadband diffusion performance. This can be explained by the fact that the PRM is here composed of only one HR per slit, thus reducing the number of collective modes in the slits leading to less fluctuations of the reflection coefficient across the frequency range. The absorption coefficient of the PRM is displayed in Fig. 4.14(e), where

it can be observed that very little absorption occurs in the panel despite the high absorption peak of one slit at around 1.7 kHz. The scaled scheme of the PRM with $M = 1$ resonating unit cell per slit is displayed in Fig. 4.14(f), with a height $L$ almost five times thinner than that of the PRD.

### 4.3.2.3 *Ternary Phase Metadiffusers*

The absorption generated by viscothermal losses within the slits of a metadiffuser can also be used to generate sound diffusion for polyphase sequences, such as the ternary phase sequence, which uses ternary state values of the reflection coefficient,
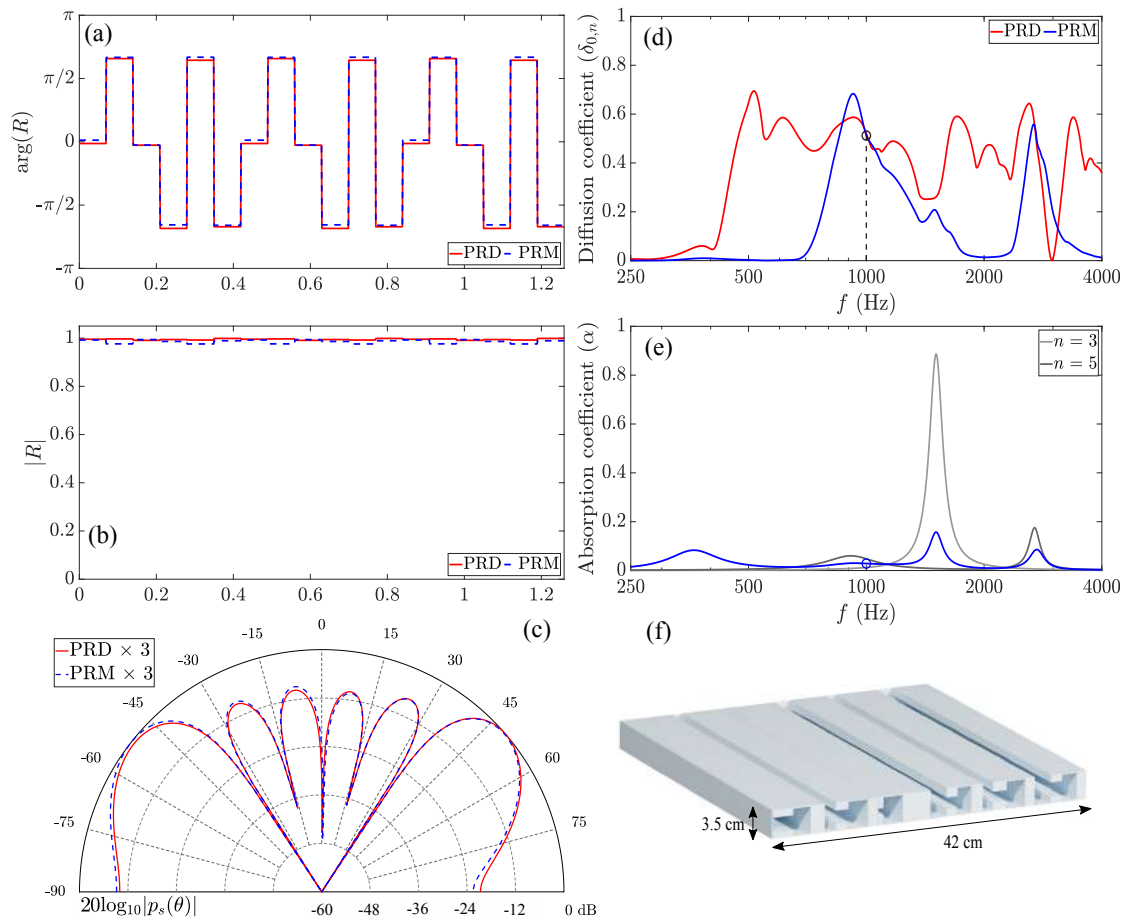


Figure 4.14: (a) Phase and (b) magnitude of the reflection coefficient of a PRD and the PRM. (c) Far-field polar distribution of the PRD and PRM obtained by TMM. (d) Diffusion coefficient of the PRM optimized at 1000 Hz (marker) and a reference PRD. (e) Absorption coefficient of the PRM, where the grey lines shows the absorption of individual slits $n = 4$ and $n = 5$. (f) Scaled scheme of the PRM with $N = 6$ and $M = 1$.

viz., $[1, 0, -1]$, where $[1]$ represents in-phase reflection, $[0]$ is sound absorption, and $[-1]$ is the inverted phase reflection state. A $[0]$ absorption state can be obtained when the reflection coefficient vanishes. In the case of metadiffusers, this can be achieved by matching the impedance of a slit to that of the surrounding air medium at a specific frequency, thus resulting in critical coupling conditions [97, 98]. This strategy leads to a perfect absorption of sound [76] and can be used to design metadiffusers that fit the reflection coefficient profile of a TPD at a target frequency. This idea not only showed excellent results but also holds great potential for broadband applications [99].
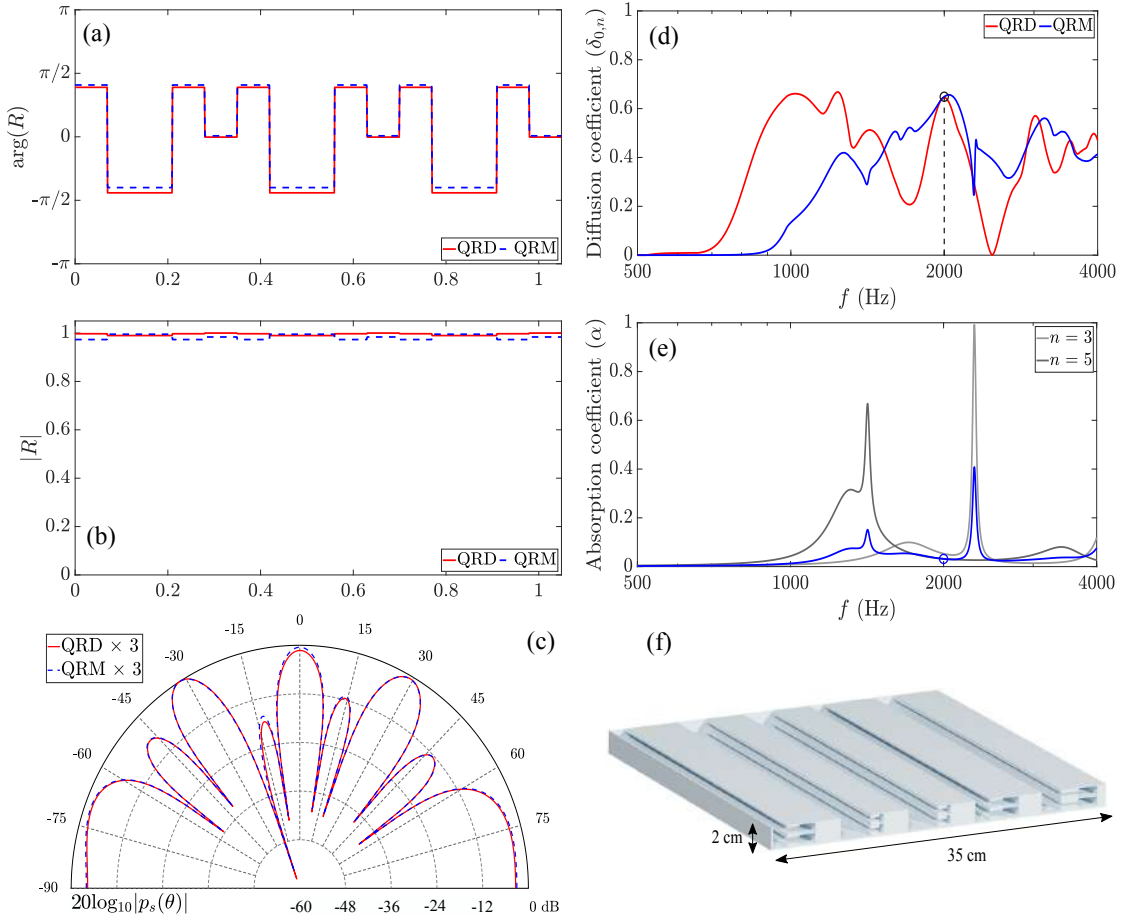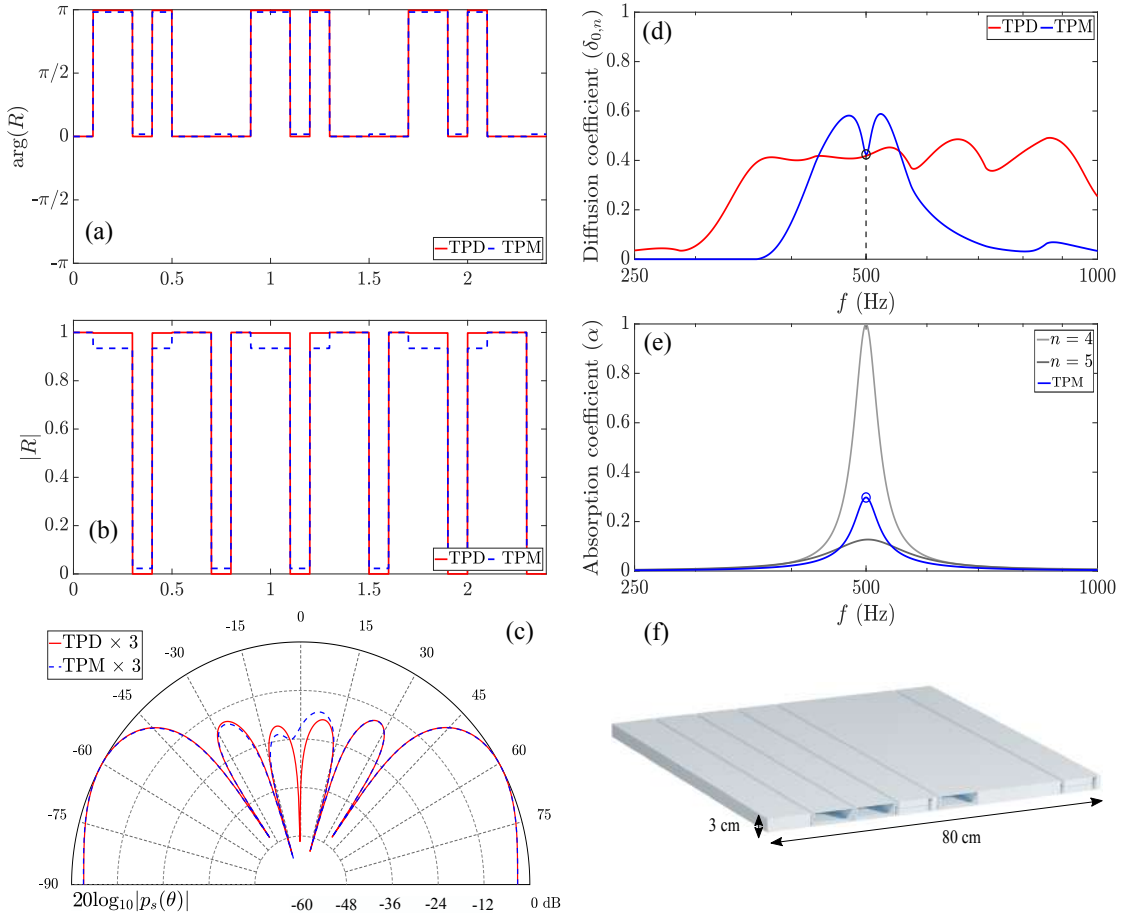


Figure 4.15: (a) Phase and (b) magnitude of the reflection coefficient of a TPD and the TPM. (c) Far-field polar distribution of the TPD and TPM obtained by TMM. (d) Diffusion coefficient of the TPM optimized at 500 Hz (marker) and a reference TPD. (e) Absorption coefficient of the TPM, where the grey lines shows the absorption of individual slits $n = 4$ and $n = 5$. (f) Scaled scheme of the TPM with $N = 8$ and $M = 1$.

Similarly to the two previous metadiffusers, an $N = 8$ Ternary Phase Metadiffuser (TPM) can be optimized to fit the reflection coefficient profile of an $L = 17$ cm TPD following a sequence $s_n = [1, -1, -1, 0, -1, 1, 1, 0]$. The magnitudes and phases of the reflection coefficients displayed in Fig. 4.15(a,b) show an almost perfect agreement at $f = 500$ Hz, with slight differences in the magnitude of the reflection coefficient of the TPM for the slits $n = 2, 3$ and 5. Figure 4.15(c) demonstrates very similar sound scattering distributions between the two diffusers at $f = 500$ Hz, with a small deviation around $\theta \approx 0°$ which might be caused by the slight differences in the phase profile of the reflection coefficient of the TPM. Fig. 4.15(d) displays the normalized diffusion coefficients of both diffusers, presenting the same value at the frequency of 500 Hz. Similarly to the PRM case, the TPM presents a narrow diffusion peak as opposed to that of the TPD, explained by the low number of HRs per slit which fail to produce a higher number of collective modes. The perfect absorption of these slits is illustrated in Fig. 4.15(e), where the absorption coefficient for the last slit reaches unity. The resulting height of the $M = 1$ TPM is shown in Fig. 4.15(f), with a value $L = 3$ cm five times thinner than the original TPD. In the same figure, it can be observed that the slits achieving in-phase reflection – [1] state – are entirely filled of solid material. The fourth and last slits in charge of performing perfect absorption – [0] state – show a similar in-phase reflection of sound but with a magnitude of zero. It is interesting to note that the geometry of the HRs in those slits is quite different than the other ones in that the neck of the HR is very long and thin, which increases significantly the impact of viscothermal boundary layers on the wave propagation.

### 4.3.3 *Deep-Subwavelength vs. Quarterwavelength Resonances*

Lastly, this section compares the resonance mechanisms of a quarter-wavelength resonator (QWR) and a deep-subwavelength resonator (DSWR) in order to illustrate the down-shift of the resonant frequency of the cavity. On the one hand, we consider a cavity of depth $L = 4.28$ cm so that its quarter-wavelength resonance occurs at $f_{QWR} = c/4L \approx 2000$ Hz. The phase of the reflection coefficient of such QWR is displayed in Fig. 4.16(a), with an illustration of the geometry provided

in the inset. It can be observed that the cavity experiences a phase shift of the reflection coefficient at the designed resonant frequency. Elsewhere in the reflection coefficient spectrum, the phase varies linearly with frequency.

On the other hand, the DSWR considers the same cavity height but is loaded by $M = 2$ HRs of arbitrary dimensions throughout the entire cavity height. The phase and geometry of such structure are shown in Fig. 4.16(b). In this plot, the first phase shift of the structure appears at a frequency much lower than the one in the previous case, with a resonant frequency just below 700 Hz. A series of phase shifts can be observed right after due to the coupled resonance of the HRs with the slit as well as higher order modes. As explained in Sec. 4.2.3, the lowering of the phase shift happens because of the change in the dispersion relation induced by the implementation of periodic (finite) locally-resonant unit cells, i.e., HRs. This change in the dispersion relation alters the phase velocity of sound to subsonic values in the low frequency regime, vanishing to zero just before the band-gap. The phase velocity of sound propagating inside the DSWR is plotted in Fig. 4.16(c), where the phase speed inside the QWR approximates that of free air sound propagation. As shown in the figure, the values of $\tilde{c}_p$ in the DSWR reach much lower
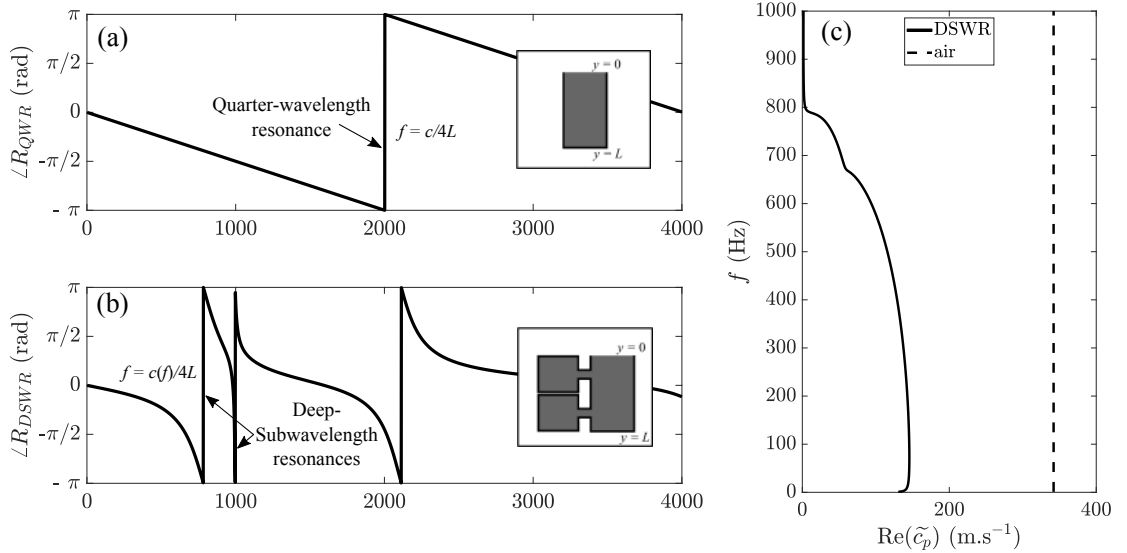


Figure 4.16: Phase of the reflection coefficient of (a) a quarter-wavelength resonator (QWR) of height $L$ and (b) a deep-subwavelength resonator (DSWR) same height $L$ backed with $M = 2$ HRs of arbitrary dimensions. (c) Sound phase velocity of the DSWR compared to that of free air sound propagation.

values compared to that in free air. Due to the dependence of the cavity's resonant frequency on the speed of sound propagation, the latter can be re-written as $f_{DSWR} = c(f)/4L$, where $c(f) \equiv \tilde{c}_p$. Consequently, one can conclude that $f_{DSWR} \ll f_{QWR}$.

Therefore, by adding locally-resonant unit cells to a QWR in the same way a metadiffuser does, the resonant frequency of the cavity can be significantly lowered without changing its depth. In other words, the slow sound produced by the dispersive medium allows to strongly reduces the height of resonant systems to much smaller extents. Also, the presence of two or more HRs allows a much greater flexibility when looking for specific reflection coefficient profiles due to the extensive range of values spanned between neighbouring phase shifts; a useful quality for optimization processes. Such insights will be validated by numerical and experimental methods in the following chapter.

---

The equations presented in this chapter can be found in the following references:

[39] A.D. Pierce. *Acoustics: An Introduction to Its Physical Principles and Applications.* McGraw-Hill series in mechanical engineering. McGraw-Hill Book Company, 1981.

[44] W.C. Elmore, M.A. Heald. *Physics of waves.* Dover, 1969.

[80] N. Jiménez, J-P. Groby and V. Romero-García. *Sound Waves in Metamaterials and Porous Media. Chapter 1. The transfer matrix method in acoustics: Modelling one-dimensional acoustic systems, phononic crystals and acoustic metamaterials.* Springer, 2021,

*Page left intentionally blank*

# EXPERIMENTAL & NUMERICAL EVALUATIONS OF METADIFFUSERS

METADIFFUSERS are compact and modular alternatives to traditional sound diffusers. Due to their metamaterial-inspired origins, metadiffusers rely on a strong dispersion relation inside their slits, which drastically slows the speed of the propagating sound. This allows the resonant mechanism of the constituents Helmholtz Resonators (HR) to occur at lower frequencies, i.e., exhibiting deep-subwavelength properties. Chapter 4 provided the analytical knowledge required to describe the physical mechanisms behind locally-resonant periodic systems and how these were applied to create metadiffusers. This enabled the discussion of metadiffuser designs recently introduced in the literature, for which an analytical and numerical analysis was conducted.

The aim of this chapter is to build on such knowledge and present new original insights into these highly versatile diffusing structures. Firstly, an experimental validation of a Quadratic Residue Metadiffuser (QRM) is presented as an example out of the other designs discussed in the previous chapter, followed by numerical evaluations of Quasi-Perfect Diffusion (QPD) and broadband metadiffuser designs. In order to rightfully compare experimental and/or analytical data with numerical simulations, the framework of the latter is first described.

## 5.1 NUMERICAL ACOUSTIC SCATTERING SIMULATIONS

Most of the numerical simulations presented in this work were conducted using a frequency-domain numerical scheme known as Finite Element Method (FEM). This section will describe the nature and considerations of this numerical scheme, and how it has been used in order to provide acoustic scattering information for custom sound diffusers and metadiffusers of arbitrary dimensions.

### 5.1.1 *Finite Element Method: Scope & Limitations*

In physics, the description of a phenomenon is usually achieved through a general theoretical formulation that models some sort of dynamic system, e.g., pressure and velocity variations in one or more dimensions in acoustics. Such formulation often takes the form of a Partial Differential Equation (PDE). For the majority of cases, it is dauntingly difficult to use these theoretical formulations to describe the state of the variables in the entire domain considered due to the complexity in the mathematical formulation, which usually describes the variables under consideration through partial derivatives at each point of space and time. Instead, approximations to these equations can be made, simplifying the analytical problem based on a set of assumptions.

One useful approximation is that of discretization, where the space and time continuum are discretized into small and finite elements. Writing the differential equations in a discretized state allows a numerical formulation that can be practically used in order to obtain the values of the dependent variables given a certain set of initial conditions. The nature of the numerical scheme then depends on the discretization method being employed. FEM is one of two most common approaches that are used when numerically solving a PDE in the frequency domain, often compared to its boundary equivalent, the Boundary Element Method (BEM). BEM could have been useful for providing scattering (boundary) data but information regarding the inner domain would not be computed as part of this numerical scheme. Of course, other numerical schemes can be designed to work in the time-domain rather than the frequency domain, such as Finite Difference Time-Domain (FDTD). It is worth noting at this point that the schemes of FEM and FDTD will be of most interest in this work. Here, the scope and limitations of the FEM will be presented first whilst the FDTD scheme will be introduced in Chap. 6.

The discretization of a dependent variable in a mathematical model, say $u$, can be approximated to that of a numerical model, $u_h$, by using a linear combination of basis functions. This stems from the fact that every continuous function of some function space can be represented as a linear combination of basis functions, in

the same way that every vector can be represented in vector space by a linear combination of basis vectors. Here, this implies

$$u \approx u_h, \tag{5.1}$$

and

$$u_h = \sum_n u_n \psi_n, \tag{5.2}$$

where $\psi_n$ denotes the basis functions and $u_n$ denotes the coefficients of the functions that approximate $u$ with $u_h$. In a simple 1D scenario where $u$ could represent the temperature $T$ along a rod of length $x$, so that $u = u(T, x)$, the numerical equation Eq. 5.2 allows to approximate the mathematical curve as a series of $n$ continuous small segments, as shown in Fig. 5.1(a). This basis function approximation is said to be a great advantage for FEM as it offers a great freedom in the discritization method. The latter does not have to be necessarily uniform and thus may present clusters of denser discritization allowing for a finer resolution in the gradients of the solution (see Fig. 5.1(b)). Another advantage of FEM is that it is a well developed theory which has been in the making since the 1940's, pioneered by A. Hrennikoff, R. Courant and J. Argyris who led to the first computer applications in science and engineering.

The discretization of space brings the notion of solution convergence towards a limit, which ultimately is what closes the gap between abstract mathematical
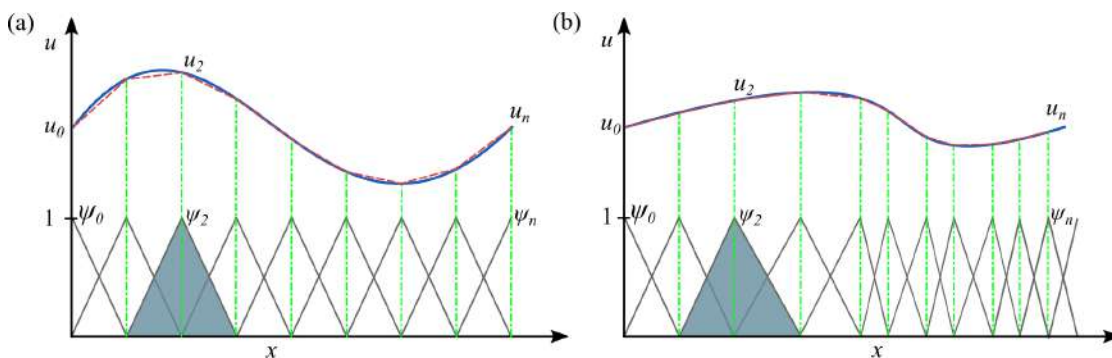


Figure 5.1: (a) The function $u$ (solid blue line) is approximated with $u_h$ (dashed red line), which is a linear combination of basis functions ($\psi_n$ is represented by the solid grey lines). The coefficients are denoted by $u_0$ through $u_n$. (b) Non-uniform distribution of basis functions, i.e., non-uniform discretization.

modelling involving infinities and concrete numerical (or algebraic) modelling involving finiteness. With the latter notion being introduced, it is worth mentioning that the solution of $u_h$ approximates that of the numerical modelling equation only in the limit of an almost infinite number of discritizations, which in turn is another approximation of the fundamentally infinite mathematical model. This emphasizes that numerical solutions are not perfect solutions of a mathematical formulation, but that they are at best as accurate as their numerical model allows to – even with the highest degree of numerical accuracy.

In FEM, the application of a discretization method, such as a Galerkin method, leads to an approximated solution at every discretized point, each with its own basis functions and coefficients. This can then be computed under a matrix form once some initial conditions are set. Consequently, the size of the resultant matrix depends on the meshing of the space, i.e., on how the geometry is discretized, which will also impact the amount of computational load and the size of the computational error. In other words, the coarser the mesh, the less accurate the numerical approximation.

Moreover, in wave physics, the meshing (discretization) of the space is also a crucial factor for determining the resolution of the smallest propagating wavelength. This can be seen as a spatial case of the Nyquist-Shannon sampling theorem, where a minimum number of discretization Points Per Wavelength (PPW) must be used in order to properly represent the wavelength considered and avoid spatial aliasing. However, there is no defined rule for the minimum number of discretization PPW in FEM. It is generally agreed that the more points being used, the closer the approximation will tend to a stable solution. Thus, a minimum guidance of 4 to 6 PPW is typically advised in order to strike a compromise between numerical accuracy and computing load. In practice, this number increases within intricate geometry areas where more discretization is needed in order to faithfully represent the intricacies of wave propagation and thus maintain a good accuracy during the simulation. Of course, a compromise between discretization points or accuracy and computation time would need to be struck for every modelling case.

### 5.1.2 *Numerical Evaluation Framework for Acoustic Scattering*

In this work, a FEM solver integrated within the commercial software COM-SOL Multiphysics 5.3™ [100] was used. The latter provides with a versatile user interface for building geometries in a numerical computation environment. Various physical contexts can be studied through different numerical methods in the frequency and time domains. The reliability of the built-in methods has been tested many times [101, 102] as it is one of the most common commercial software used in industry and academia for numerical physics or multi-physics studies. In the present context of acoustic scattering evaluation, a similar framework to ISO $17497 - 2$ was reproduced.

As illustrated in Fig. 5.2(a), the scattering surface is placed at the centre of a circular (2D) or spherical (3D) domain filled with air, obeying to a linear acoustic propagation equation. The radius of this domain is at least larger than the Rayleigh critical distance, $R_0 = S_{scat}/\lambda_{FEM}$, where $S_{scat}$ is the area of the scattering surface and $\lambda_{FEM}$ is the working wavelength of the FEM simulation – here impinging to the surface at normal incidence. Surrounding this domain, a Perfectly-Matched Layer (PML) of radius $R_{PML} \geq \lambda_{FEM}$ is implemented. A PML is an artificial absorbing layer for wave equations which is supposed to pefectly absorb any incoming wave energy, thus avoiding any reflections at the interface between the non-PML
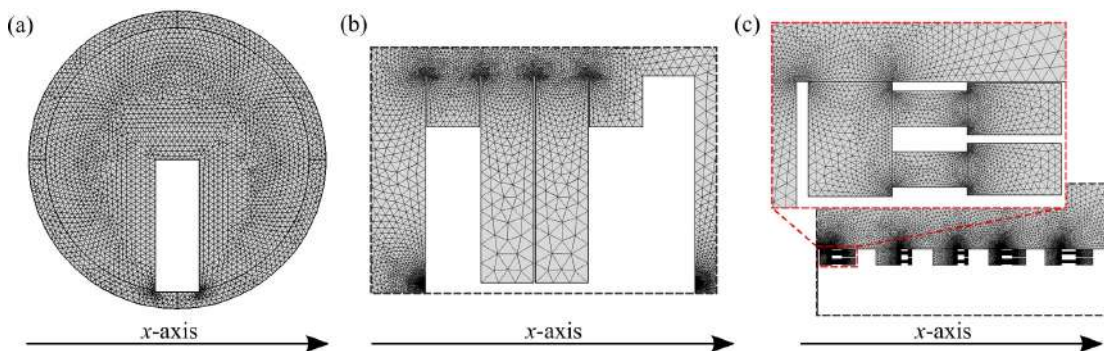


Figure 5.2: 2D FEM meshing setup in COMSOL Multiphysics 5.3™ for (a) a flat reflector, (b) a Quadratic Residue Diffuser (zoom to the surface and wells), and (c) a Quadratic Residue Metadiffuser (zoom to the surface and into the first slit).

and PML domains, thus emulating free-field conditions. The circular or spherical scattered wave-field generated by the surface is captured by a far-field boundary condition at the interface with the PML medium, with a far-field distance much greater than the Rayleigh critical distance. This boundary condition is set in order to fulfil the radiation condition, where no other wave contributions can be made to the scattered wave-field. In the event of closer near-field simulations, the evaluation radius of the far-field boundary condition can be changed to any desired value, limited by the circular/spherical air domain radius around the surface. Ultimately, the scattering surface is mounted on a solid rectangular support that extends up to the far-field boundary condition in order to minimize any potential edge diffraction generated by the finite size of the sample.

The remaining complexity of FEM modelling highly depends on the nature of the scattering object. Figure 5.2 shows different modelling strategies for various scattering surfaces. In the simplest case of a flat panel in Fig. 5.2(a), nothing but a 2D surface with rigid boundary conditions is required. Should the object be a phase-grating diffuser, a similar process is conducted by defining the overall geometry of the sound diffuser with rigid boundary conditions. An example of a QRD is displayed in Fig. 5.2(b). One can observe a more refined mesh in such case due to the smaller geometry elements to model compared to the flat reflector. In the event where such diffuser exhibits thin wells, it might be of interest to create *narrow region* domains for each of the wells in order to account for viscothermal boundary layer losses. The importance of such losses grows as the width of the slit decreases. In general, phase-grating diffusers have wells wide enough so that these mechanisms do not have a significant impact. In the case of a metadiffuser with thin slits and narrow HRs, which purposely take advantage of viscothermal boundary layer processes, a *narrow region* domain has to be applied for every domain section of a slit, viz., HR cavity, HR neck, and slit. As mentioned above, one advantage of FEM is that the meshing of a numerical domain can be non-uniform. This becomes an appreciated feature in order to provide enough sampling resolution in the narrow regions where the intricacies of wave propagation must be well reproduced. This is illustrated in Fig. 5.2(c) where the slits of the metadiffuser are much more densely

discretized than in the wells of the phase-grating diffuser or in the surrounding air domain.

## 5.2 EVALUATION OF A QUADRATIC RESIDUE METADIFFUSER

An experimental validation of the concept of acoustic metadiffusers is reported in this section. The same Quadratic Residue Metadiffuser (QRM) introduced in Sec. 4.3.2 has been 3D-printed and proved to scatter sound according to its design specifications. The diffusion properties of the QRM were characterized experimentally in an ISO-certified anechoic chamber at the Laboratory of Acoustics of the University of Le Mans, France, following the procedure outlined in Sec. 3.1.3, i.e., ISO 17497-2:2012. It has to be noted that the original design was purely two-dimensional; however, in practice, the structure must be bounded and thus becomes finite in the three dimensional space. The experimental results of the QRM and a reference flat rigid reflector are compared with 3D numerical predictions of the finite structures using the above-mentioned FEM evaluation framework, including thermoviscous losses. The experimental scattering results reported herein are in close agreement with simulations and theory, therefore confirming the potential of metadiffusers for controlling sound diffusion at deep-subwavelength scales.

### 5.2.1 *Experimental Setup For ISO 17497-2*

The QRM was manufactured by means of 3D-printing, using a Fused Deposition Method (FDM) of polylactic acid with a Stratasys Fortus 450 MC. The final product can be seen in Fig 5.3(b). The deposition thickness was of the order of 0.5 mm resulting in a minimal corrugation of the 3D-printed flat surfaces, therefore minimizing any porous effects at the boundaries of the material. The 35x35 cm squared panel, of height $L = 2$ cm and side width $D = 35$ cm, is composed of $N = 5$ slits, each loaded with $M = 2$ identical HRs. This QRM mimics the behaviour of a QRD made of $N$ wells and of total thickness of $L = 27.4$ cm designed for a low cut-off frequency of 500 Hz. It must be noted that the design frequency is normally set as the lower frequency limit of the diffuser, but it is not necessarily

the lowest frequency at which the surface produces more scattering than a plane surface, i.e., the ratio between the size of the panel and the wavelength must also be taken into account. In this work, the response was evaluated at $f = 2000$ Hz to avoid the strong diffraction regime of the finite panel due to the small lateral size, due to $\lambda = 0.35$ cm at 1 kHz.

An experimental procedure based on ISO 17497-2:2012 was developed here to determine the sound scattering properties of the metadiffuser. As such, measurements consisted in placing the physical sample (e.g., the QRM or the flat reference panel) at the center of a virtual concentric arc of evenly spaced microphone positions, all within an anechoic environment and keeping unwanted acoustical contributions from the measurement system as minimal as possible (e.g., reflections from the metallic grid on the floor near the surface). A picture of the experimental setup is
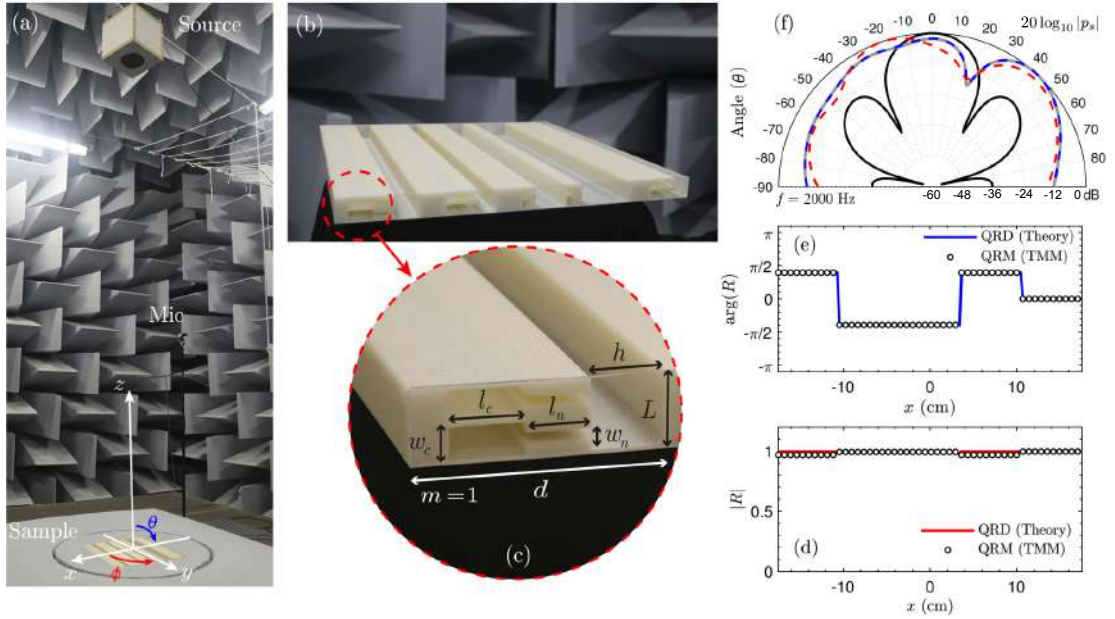


Figure 5.3: (a) Experimental setup and coordinate system. (b) Photograph of the QRM. (c) Details of the first slit ($m = 1$) showing the definition of the geometrical parameters. (d) Phase and (e) magnitude of the spatially dependent reflection coefficient for an ideal QRD (continuous lines) and the tailored QRM (markers). (f) Far-field polar distribution at 2 kHz of an ideal QRD (continuous-blue), QRM obtained theoretically by TMM (circles) and numerically by FEM (dashed red), and a plane reference reflector with the same dimensions (thick black).

shown in Fig. 5.3(a). Microphone positions ranged from $-\pi/2 < \theta < \pi/2$ (elevation) and $0 < \phi < 2\pi$ (azimuth) of 1 m radius around the surface with a position spacing of 6° in the elevation plane ($\theta$) and 20° in the azimuth ($\phi$). The sample was placed on a rotating table, thus allowing a complete hemispherical characterization of the surface scattering by rotating it around the $z$ axis and measuring only in the elevational plane. Measurements were performed for normal incidence by locating the source as far as possible in order to approximate to a plane wave radiation on the sample, here at 2.5 m away from the surface, close to the ceiling. Other angle of incidence could be measured but this approach was not pursued to the technical limitations of source positioning (creation of a railing arc) and measurement time (540 microphone positions for one incident angle). The system was excited using a broadband Maximum Length Sequence (MLS) signal, and impulse responses at each microphone position were obtained by deconvolution. Each impulse response was subtracted from the one obtained from the anechoic background and windowed to extract the scattered sound field. Then, the polar distribution of the scattered field at a specific frequency was obtained after a Fourier transformation of the final impulse responses.

### 5.2.2 *Experimental & Numerical Data Analysis*

The experimental, analytical, and simulated scattered field distributions in the $\phi \pm 90°$ cross section (i.e., across the length of the slits) are shown in Fig. 5.4 for both the QRM and the flat reference panel. Analytical far-field scattering was determined by applying the Fraunhofer integral, which was derived at the end of Chap. 2. Here, we show frequencies ranging from 700 Hz to 3.4 kHz.

On the one hand, the simulated scattered field of the flat panel agrees with the analytical one (continuous-blue and dashed black, respectively). Slight deviations are observed at 2.4 kHz and 3.4 kHz, probably caused by higher order transversal modes in the slits and HRs. The measured scattered field of the flat panel (blue dots) also shows a strong agreement with the simulated and theoretical values, except at grazing angles ($\theta > 60°$) where higher scattering values are observed. This probably occurs because the weak reflected energy from the panel at grazing

angles is comparable to the spurious reflections of the anechoic chamber metallic grid that covers the floor, and is therefore intricately linked to the experimental nature of the data.

On the other hand, the measured scattered field values for the QRM (red circles) are in close agreement with the simulated ones (continuous-red) obtained through FEM. At lower frequencies, e.g., 700 and 1000 Hz, simulated curves for the flat panel and QRM illustrate the fact that the QRM behaves in a similar manner to that of the flat panel, where no additional scattering is being produced, thus illustrating the need to normalize the scattering of a surface to that of a reference to properly estimate the diffusion performance of the diffuser. Above 1500 Hz, a clear difference between flat and QRM surfaces can be observed, with a good agreement between numerical and experimental data. Note that the experimental dip observed at $f = 2000$ Hz around $\theta \approx 0°$ is smoothed in the numerical data, although the latter appears to conserve the overall distribution shape. Despite the good agreement between the different datasets, this punctual difference will have an impact on the resulting directional diffusion coefficient at this frequency as it is an auto-correlation of the angular distribution. A similar analysis can be maintained for the numerical/experimental dips at higher frequencies, although the
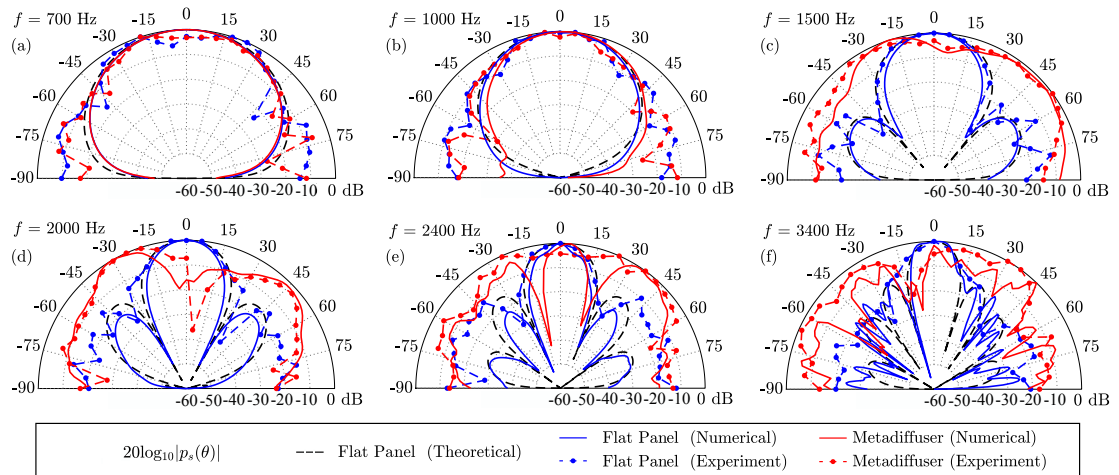


Figure 5.4: Scattered field distribution, $p_s(\theta)$, for normal sound incidence at different frequencies obtained experimentally in the near-field (markers) and numerically for the QRM (blue) and the flat reference panel (red) in the far-field. Theoretical far-field pressure distributions for the flat panel are shown in thick-gray lines.

difference in diffusion coefficient can be expected to be lower due to the multiple dip variations in the polar distributions.

Figure 5.5(a) shows the frequency-dependent directional diffusion coefficients, $\delta_0$, for the QRM and the flat panel, un-normalised and normalised. First, the experimental diffusion coefficient for the flat panel is in close agreement with the analytical one, and as expected, higher diffusion values are achieved in the low frequency regime due to the diffraction of the finite sample. The same phenomenon can be observed for the QRM (blue continuous) in this low frequency regime as it matches the values obtained for the flat panel. This is mainly due to the lack of any slit resonance within the metasurface and is thus illustrated by the normalized diffusion coefficient of the QRM taking values near zero. However, when approaching the frequency $f \approx 1000$ Hz, the dispersion in the slits progressively changes, and the impedance of each deep-subwavelength slit is hence modified. The complex reflection coefficient thus becomes spatially dependent, and following Fraunhofer theory, the scattering distribution starts to change, resulting in higher values of the normalized diffusion coefficient $\delta_0$. Eventually, the spatially dependent reflection coefficient approximates the one of a QRD at $f = 1500$ Hz. At this frequency, the experimental diffusion coefficient takes a value of $\delta_0 = 0.783$, while
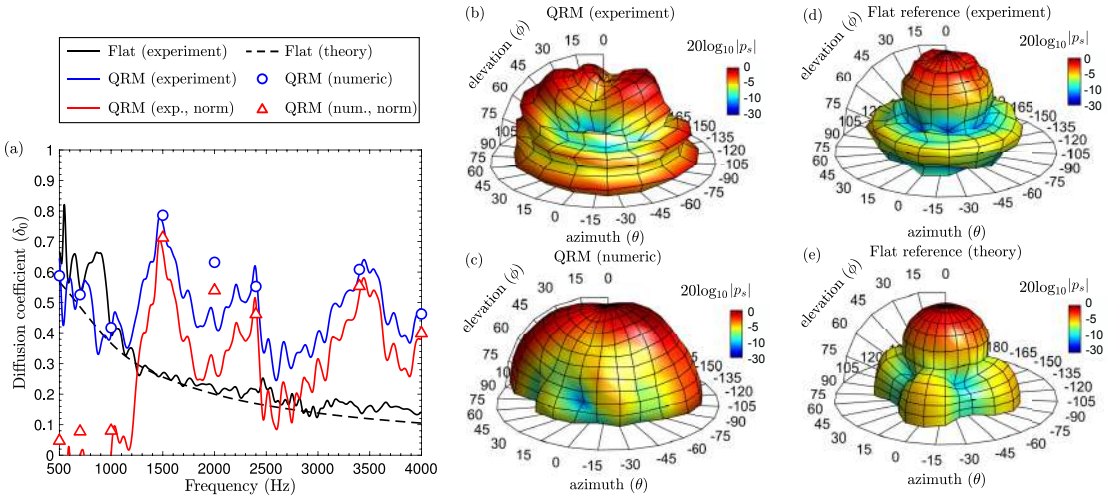


Figure 5.5: (a) Diffusion coefficients of the QRM and a flat reference panel. Scattered field distribution, $p_s(\theta, \phi)$, for the QRM at 1500 Hz (b) measured experimentally and (c) by FEM simulations. (d,e) Corresponding scattered field distribution for the flat reference panel.

the corresponding simulation is placed at a very close value of $\delta_0 = 0.786$. The normalized diffusion coefficient takes a value of $\delta_n = 0.708$ in the experiment and $\delta_n = 0.712$ in the simulation, keeping these values in the range of those reported for classical QRDs. Note that the normalized diffusion coefficient using 1D theory (see Fig. 5.3(f)) is very similar ($\delta_n = 0.69$). However, the latter 1D diffusion value must not be directly compared with the results in Fig. 5.5(a) as oblique and transversal modes along the $y$-direction are not included in the 1D theory. The presence of such modes will affect the impedance of the slits and will thus result in a change of the scattering properties of the surface. Also, as previously mentioned, a dip in the diffusion coefficient at $f = 2000$ Hz can be observed despite the excellent agreement in most of the scattering distribution at that frequency. As previously mentioned, this loss in directional diffusion coefficient is probably due to the dip in the measured scattering distribution at $\theta = \approx 0°$.

The 3D experimental, simulated and theoretical scattering distributions at $f = 1500$ Hz at a distance of 1 m from the sample are shown in Figs. 5.5(b,e). For the QRM, the waves are reflected evenly for the azimuthal plane, $\phi \pm 90°$, corresponding to the cross section of the slits as $R(x, y)$ only shows variations in the $x$-direction. This is an expected behaviour observed in any 1D phase grating diffuser. In contrast, the flat panel mainly scatters waves in the specular direction, with symmetric lobes in the $x$ and $y$ directions. However, both experimental scattering distributions show deviations from theoretical distributions at grazing angles where a constant value of scattered pressure can be observed for all azimuth angles. This could be linked to a default in the experimental setup.

This section experimentally demonstrates the effectiveness of metadiffusers. The scattering distributions observed experimentally using 3D panels are found to be in close agreement with simulated and theoretical designs. A remarkable high diffusion performance is demonstrated by the experimental normalized diffusion coefficient of $\delta_n \approx 0.8$ at $f = 1500$ Hz. This, of course, can be seen to work best for 1D sound diffuser structures with variations of the reflection coefficient profile only in one axis. In the eventual case of 2D sound diffusers, further corrections to the TMM would have to be applied in order to provide a correct estimate of

the 2D reflection coefficient profile. Moreover, some theoretical assumptions regarding higher order modes in high frequency regimes and inter-slit evanescent coupling have been highlighted to be potential suspects for explaining some analytical to numerical/experimental variations. Overall, the large difference in size and mass between the QRM ($L = 3$ cm) and its equivalent QRD ($L = 27.4$ cm) demonstrates the potential and capability of metadiffusers to be applied in many practical situations where classical solutions become too bulky due to a lack of space and/or structure weight.

In the next section, the concept of metadiffusers will be taken a step further, where the variable nature of the these metasurfaces can lead to seemingly impractical or difficult to achieve scattering behaviours with traditional design methods, such as perfect diffusion and highly efficient broadband sound diffusion.

## 5.3 EVALUATION OF QUASI-PERFECT DIFFUSION METADIFFUSERS

Omni-directional radiation of sound, or perfect diffusion, can be impractical or difficult to reach under traditional means. This is due to the considerable size required by, and the lack of tunability, of typical quarter-wavelength scattering strategies necessary for producing the required complexity of the surface acoustic impedance. As such, it can be a challenge to design sound diffusing structures that can display near perfect diffusion performance within slim dimensions.

In the two next sections, a method is given for obtaining quasi-perfect and broadband sound diffusion coefficients using metadiffusers, resulting in structure dimensions much thinner than quarter-wavelength strategies. Whilst reaching perfect diffusion might unveil some discussions on whether or not such value can be perfectly attained, values nearing unity – Quasi-Perfect Diffusion (QPD) – can practically be reached. Throughout the two remaining sections, the relation between the geometry of the metasurface, the bandwidth and the diffusion performance is analytically and numerically studied. For moderate bandwidths, around 1/3 of an octave, the method results in nearly perfect sound diffusion, whilst for a bandwidth of 2.5 octaves an average normalized diffusion coefficient of 0.8 is obtained. The ratio between the wavelength and the size of the unit cell is identified as a limitation

of the performance. This study demonstrates the versatility and effectiveness of metadiffusers to generate diffuse reflections outperforming those of classical sound diffusers.

### 5.3.1 *Designing Metadiffusers for Perfect Diffusion*

Whereas the geometry of the previous metadiffusers was being optimized to produce a reflection coefficient profile fitting a particular numerical sequence at a certain frequency, a different approach to designing metadiffusers for QPD is proposed here: we look for the geometry of the metadiffuser that directly maximizes the normalized diffusion coefficient at the target frequency. The optimization paradigm relies on the same constrained minimization algorithm used in Ref. [75], where the cost function, $\epsilon_{QPD}$, is minimized so that the normalized diffusion coefficient $(0 \leq \delta_{n,\psi}(f) \leq 1)$ would tend to unity at the target frequency, i.e.,

$$\epsilon_{QPD} = 1 - \delta_{n,\psi}(f). \tag{5.3}$$

The total surface of the metadiffuser, of length $D$, is then divided in $N$ unit cells of periodicity $a_x = D/N$. The $j$-th unit cell presents a slit of thickness $L^j$ and width $h^j$ loaded with $M$ resonators which are characterized by the lengths of the neck and cavity, $l_n^j$ and $l_c^j$ respectively, and the widths of the neck and the cavity, $w_n^j$ and $w_c^j$ respectively. In such way, the reflection coefficient presents a profile along $x$ with $N$ different values over the total length of the surface. This profile is then optimized with the previously described methodology. The geometry of the resulting QPD-metadiffuser is shown in Fig. 5.6 and its dimensions can be found in Appendix. B.

### 5.3.2 *Analytical & Numerical Data Analysis*

Figure 5.6 shows the geometry obtained from the optimization of an $N = 11$, $M = 1$, $D = 1.32$ m, and $L = 3$ cm QPD-metadiffuser, as well as the target phase of the reflection coefficient required for QPD at 500 Hz. The spatial Fourier transform of such phase profile provides a constant scattered amplitude in space. A large
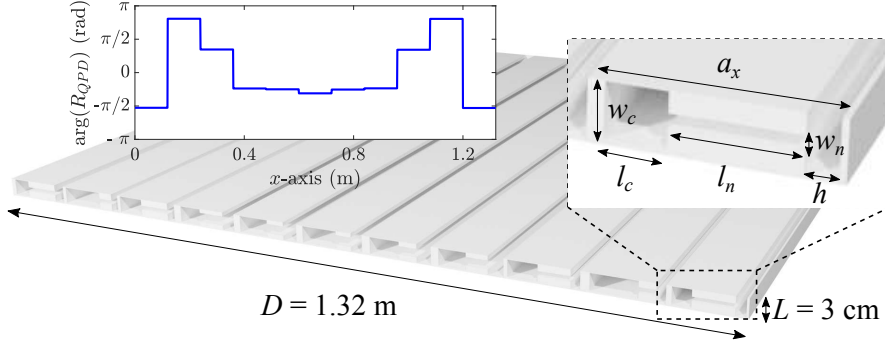
Figure 5.6: Geometry of the $N = 11$ slits Quasi-Perfect Diffusion (QPD) metadiffuser design with $L = 3$ cm, $M = 1$, and $D = 1.32$ m (inset) Target phase of the reflection coefficient at 500 Hz.

panel width $D = 1.32$ m has been taken here in order to avoid the low frequency diffraction regime that would otherwise occur at dimensions close to $\lambda \approx 0.7$ m at 500 Hz. Figure 5.7(a) compares the analytical and numerical normalized diffusion coefficients of two QPD-metadiffusers of same width $D = 1.32$ m, one with $N = 11$ slits aimed for perfect diffusion at 500 Hz and another with $N = 20$ slits tuned at 1.5 kHz. In addition, a similarly optimized $N = 11$ slits quarter-wavelength diffuser (QWD) made for replicating the complex surface impedance required for QPD is displayed alongside the two previous metadiffusers. This enables the comparison of diffusion properties between the equally optimized QPD structures. Figure 5.7(a) shows that the overall shapes of the analytical and numerical curves are in fair agreement along the frequency axis despite some discrete discrepancies. These can be explained by the limitation of analytical assumptions where the evanescent coupling between slits, affecting the local distribution of the acoustic impedance at the surface, is not accounted for. Other assumptions, such as higher order lateral modes for the HRs are not accounted for as well and might explain some high frequency analytical-to-numerical disparities. Nonetheless, the numerical curve for the $N = 11$ QPD displays an excellent normalized diffusion peak value of $\delta_{n,0} = 0.92$ at 500 Hz, which is fairly close to the analytical design value of $\delta_{n,0} = 0.99$. A very good agreement is shown at the second diffusion peak near 2 kHz, probably due to the second resonance mode of the slits. Higher diffusion peaks around 3 kHz seem to have more discrepancies between the different methods but reside within

113
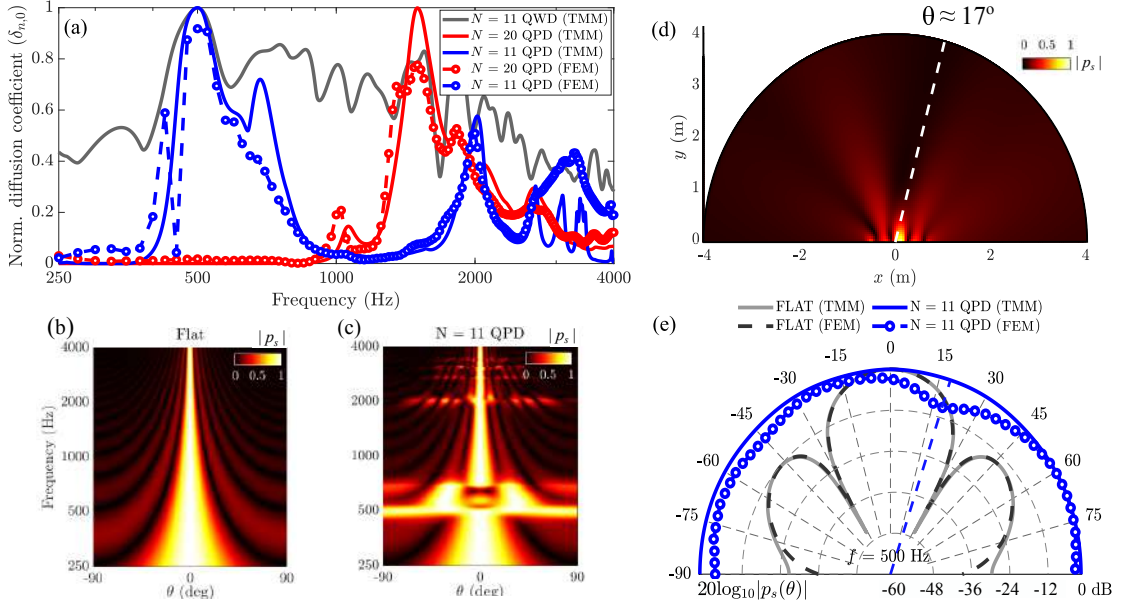
Figure 5.7: (a) Normalized diffusion coefficients of an $N = 11$ slit QPD (blue), an $N = 20$ slit QPD (red), and an optimised $N = 11$ quarter wavelength diffuser (QWD) (grey). (b-c) Far-field scattered sound energy against frequency for a flat surface and $N = 11$ QPD. (d) Near-field of the $N = 11$ QPD obtained through FEM. (e) Far field scattered sound energy at $f = 500$ Hz for the $N = 11$ QPD and flat reference surface of same width.

the same frequency range.

The $N = 11$ QWD shown in Fig. 5.7(a) displays a normalized diffusion coefficient as good as the $N = 11$ QPD-metadiffuser at 500 Hz, i.e., $\delta_{n,0} = 0.99$. However, this performance comes at a steep price in terms of slit depth, resulting in a maximum depth of 81 cm, which is 27 times larger than the $N = 11$ QPD-metadiffuser of 3 cm.

The $N = 20$ metadiffuser tuned for 1.5 kHz shown in Fig. 5.7(a) has been made with a higher number of slits in order to increase the adaptability of the panel and better adapt to the more complex surface impedance that is required to reach QPD in a higher frequency regime for the same panel width. In such case, a numerical normalized diffusion peak value of $\delta_{n,0} = 0.77$ is obtained at 1.5 kHz. Although the analytical reflection coefficient at such frequency produces QPD ($\delta_{n,0} = 0.99$), it appears that the numerical results do not match so well. This is probably due to the effects not considered in the theory that are likely to

arise in high frequency regimes, i.e., higher order modes and evanescent coupling between slits. The numerical amplitude peak at 1.5 kHz could be mitigated by directly optimizing the numerical model for generating omnidirectional scattering. Physically, reaching near-perfect diffusion values at high frequencies ($D/\lambda \gg 1$) can be achieved by increasing the number of slits within the same panel width. This is because the sum of the scattered waves generated by wide slits, radiating as directive pistons, cannot interfere at other directions than in normal and thus fail to efficiently produce uniform scattering. In addition, if the separation between slits is larger than half wavelength, secondary diffraction grating lobes emerge in the far field at angles [26]

$$\beta_q = \sin^{-1}(q\lambda N/D), \tag{5.4}$$

with $q = 1, 2, \ldots$ being the diffraction order. To reach efficient sound diffusion, each slit would thus need to approximate a punctual scatterer and the separation between them should grant the absence of diffraction grating lobes. This suggests a requirement for QPD following the relation

$$ka_x < \pi, \tag{5.5}$$

where $k$ is the wavenumber.

Figure 5.7(b) shows the far-field scattered sound energy against frequency for a flat reflector, where natural diffraction lobes generated by wave interference are illustrated by the increasing number of high and low polar energy distributions along frequency. Alternatively, the QPD of the $N = 11$ metadiffuser is illustrated in Fig. 5.7(c) by a thin and uniform energy band around 500 Hz. Figure 5.7(d) shows the intricacies of the QPD in the near field obtained numerically in which a darker field amplitude area can be seen at $\theta \approx 17°$. This is also illustrated in Fig. 5.7(e) which displays the scattered far-field for the same QPD-metadiffuser, where the magnitude of the normalized scattering obtained numerically at $\theta = 17°$ is $-4$ dB. The numerical polar distribution at other angles is otherwise quite uniform, resulting in high diffusion performance.

Heretofore, two scenarios of QPD-metadiffusers have been discussed, which targeted different frequencies with a specific number of slits. However, metadiffuser optimizations can be further extended to go from single frequency QPD to high broadband sound diffusion.

### 5.4.1  *Designing Metadiffusers for Broadband Sound Diffusion*

Broadband metadiffusers can be designed by modifying the optimization cost function to account for normalized diffusion coefficients held between a low and high cut-off frequency [75], i.e.,

$$\epsilon_{broad} = 1 - \delta_{n,0,avge}(n_f), \tag{5.6}$$

where

$$\delta_{n,0,avge}(n_f) = \int_{f_{low}}^{f_{high}} \delta_{n,0} \mathrm{d}f / n_f \tag{5.7}$$

is the normalized diffusion coefficient averaged over $n_f$ frequency samples. Thus, highly efficient broadband metadiffusers can be designed where the geometry constraints $(N, D, M, L)$ remain the same as in the previous section whilst the rest of the geometry (slits and HRs) would now fit the cost function $\epsilon_{broad}$ for several frequency ranges $\Delta_f = [f_{low} : f_{high}]$. The broadband dimension constraints were chosen to be the same as the QPD case in order to demonstrate the adaptability of the metadiffuser for going from QPD to highly effective broadband diffusion within the same overall structure dimensions. Considering this multitude of variables, Fig. 5.8 emphasizes on the general rate of dependence between the average diffusion coefficient and the number of slits per panel which was obtained over a large population of optimizations with different broadband objectives.

### 5.4.2  *Analytical & Numerical Data Analysis*

Figure 5.8(a) thus illustrates the cross-dependency of the number of slits $N$ and the frequency ranges $\Delta_f$ for optimizing $\delta_{n,0,avge}$ for a metadiffuser of fixed width $D$

= 1.32 m. First, a trend emerges from the positive gradient of the data presented, i.e., the higher the number of slits, the more likely the diffusion coefficient would be efficiently optimized for all the different frequency ranges, with a minimum limit of $N = 3$ slits. This is due to the increased number of slits with which the surface can better adapt to more complex impedance requirements. This can be observed at $N = 3$, where orange-red curves (large frequency ranges) do not reach as high values as the bluer curves (small frequency ranges). However, at $N = 13$, orange-red curves show diffusion values close to the blue curves despite the much larger frequency ranges being covered. These results allow to demonstrate that a high number of narrow slits is indeed required to modulate at best the scattered field. Thus, in a similar way to QPD for which the limit separation distance between slits must be smaller than half the wavelength (i.e., $a_x < \lambda/2$), this would suggests a requirement for obtaining quasi-perfect broadband diffusion to follow the relation of Eq. 5.5, i.e.,

$$ka_x < \pi, \forall k \in 2\pi\Delta_f/c. \tag{5.8}$$
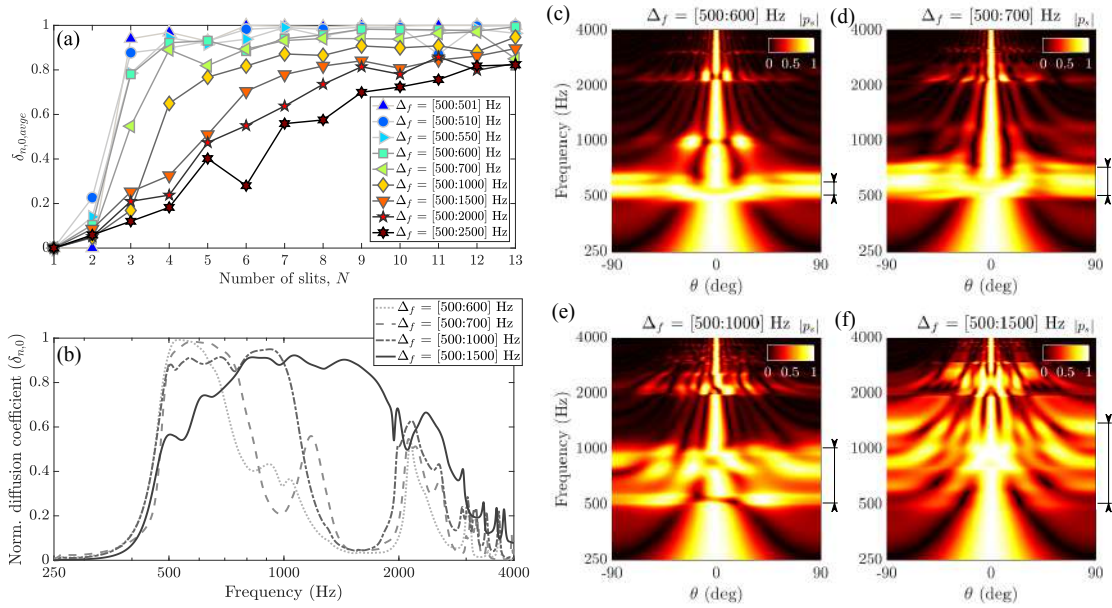


Figure 5.8: (a) Cross-dependency of $\delta_{n,0,avge}$ in function of the number of slits $N$ and frequency ranges $\Delta_f$ for a metadiffuser of fixed width $D = 1.32$ m. (b) Normalized diffusion coefficients of various broadband metadiffuser designs for different $\Delta_f$ frequency ranges. (c-f) Far-field scattered sound energy against frequency for various $\Delta_f$ frequency ranges.

Figure 5.8(b) shows examples of the various normalized diffusion coefficients obtained through different $\Delta_f$ frequency bandwidths tested. In the case of $\Delta_f = [500 : 600]$ Hz, a value $\delta_{n,0,avge} = 0.98$ is achieved. This an extremely high value considering its frequency span over 100 Hz. For the other cases, one can observe that as the frequency range $\Delta_f$ increases, $\delta_{n,0,avge}$ decreases. Yet, the latter still remains at high values, viz., $\delta_{n,0,avge} = 0.96$, 0.90, and 0.84, for ranges $\Delta_f = [500 : 700]$ Hz, $\Delta_f = [500 : 1000]$ Hz and $\Delta_f = [500 : 1500]$ Hz, respectively. In addition, a diffusion peak can be outlined for all the $\Delta_f$ designs. In the case of $\Delta_f = [500 : 1500]$ Hz, this peak provides a continuous decrease of the normalized diffusion coefficient to even higher frequencies. Figures 5.8(c-f) show the far-field scattered sound pressure fields for the different $\Delta_f$ ranges selected. The fact that the diffusion coefficient gets broader along the frequency axis is displayed through a larger and more uniform angular energy band.

In this work, the potential of metadiffusers for displaying quasi-perfect normalized sound diffusion coefficients within deep-subwavelength dimensions has been demonstrated. It has been shown that the slit width and the separation between them is a major factor to account for when aiming for quasi-perfect or broadband sound diffusion due to the directive radiation of individual slits and the emergence of diffraction grating lobes. In addition, using multiple slits rather than a few enhances the flexibility to engineer the complex surface impedance, thus resulting in efficient uniform scattering.

The results presented were obtained considering a normal incidence of sound onto the scattering surfaces. This approach was chosen because (i) it is usually the default incidence for evaluating materials, and (ii) measuring at other angles of incidence would have resulted in a considerable extra amount of time for building the experimental setup and measuring. However, as the above results showed close agreeement at normal incidence, scattering comparisons between analytical, numerical and experimental data at other angles should follow as well to a relative degree, with exceptions potentially arising due to some physical phenomena not being accounted for in the theory that may be more present when considering a grazing incidence of sound, such as transversal slit resonant modes.

The ability to obtain such range of efficient scattered sound distributions within ultra-thin dimensions, instead of larger alternatives, can be welcomed when dealing with environments where space is at a premium, e.g., aerospace applications [103] or orchestra pits [34] (as modelled in the following chapter). The results shown in this work demonstrate the usefulness of metadiffusers to be applied in many practical situations where they can outshine classical solutions due to their versatility.

*Page left intentionally blank*

# LOCAL SCATTERING IN LARGE NUMERICAL VOLUMES

THE appealing nature of metadiffusers as an acoustic treatment can be of great interest as these can significantly impact the acoustics of the space where they are being implemented. As numerical methods allow a great flexibility and foresight in prospective studies, wave-based simulations of metadiffusers in practical environments can be of great value, e.g., helping assess the nature of qualitative factors in a room related to the subjective perception of sound. However, estimating such impact by numerical means requires the modelling of the ultra-thin metadiffuser geometry within a much larger computing environment, which due to meshing constraints would require considerable hardware resources and computational time, both depending on the numerical scheme considered. The Finite Element Method (FEM) applied so far can yield useful results, but only for discrete frequencies, requiring an entire simulation per frequency step. Such method also implies that time-domain information cannot be determined.

Therefore, the aim of this chapter is to present a framework for simulating complex structures with detailed geometries, such as metadiffusers, into large 3D Finite Difference Time-Domain (FDTD) computing environments by reducing them to their equivalent surface impedance through an Resistor-Inductor-Capacitor (RLC) circuit filtering approximation. This reduction helps to simplify the physics involved as well as drastically reduce the meshing load of the model and hence the implicit calculation time. A time-domain scheme is also chosen as not only it can wield broadband frequency information in one simulation, but also enables time-domain insights for the study of temporal dispersion and allows further signal processing operations of the impulse response, such as audio convolution for auralization purposes. Despite the simplification process, the proposed RLC impedance formulation achieves good overall results with respect to the original acoustic metadiffuser whilst ensuring relatively short simulation times over a vast range of frequencies.

## 6.1 NUMERICAL IMPLICATIONS OF SMALL GEOMETRY IN LARGE VOLUMES

The majority of simulations involving metamaterials often require complex physics to be solved through refined meshing grids. However, it can prove challenging to simulate the effect of local physical conditions created by said metamaterials into much wider computing sceneries due to the increased meshing load.

### 6.1.1 *Limitations of Numerical Schemes*

Over the past decades, there has been a lot of progress regarding numerical simulation techniques in the field of wave physics, mostly benefiting from modern hardware and software advances. Yet, computing limits can still be reached in most frequency- or time-domain numerical problems. Both approaches come with their own strategies for approximating the wave equation within a bounded space. Usually, the accuracy and computational time of such schemes are dependent on the minimal size of the meshing grid, on the hardware at hand, the frequency or range of frequencies to be studied, and on the overall size of the numerical environment. To a relative degree, numerical schemes tend to be computationally cheaper for modelling either complex geometries in small spaces or simpler geometries within larger spaces. The suitability of one method over the other generally depends on the scope of the study.

There are cases, however, where simulations of complex geometries in larger sceneries are of specific interest, i.e., sceneries where intricate geometry with fine meshing and non-linear physics (e.g., spatially-dependent viscothermal losses) are required at a local scale, but the physical effect of such geometry has to be studied within a much more global environment. An example of such study can be found in simulations involving metamaterials, which are usually quite compact, where their influence over a bigger 3-dimensional context may be of interest. In the case where the volume of the simulated scenery happens to be very large compared to the metamaterial meshing dimensions, traditional modelling strategies could prove non-viable within realistic means; likely resulting in immense computational

times and memory requirements. This calls for alternative strategies in modelling local wave interactions at boundaries and their respective propagation behaviour in much larger spaces within more reasonable computational requirements.

This problematic has sprung a rising number of research initiatives for many decades. The concept of impedance [104] has helped in establishing a strategy for approximating the physical conditions created by the geometry of an object by a set of Impedance Boundary Conditions (IBCs) [105]. Many of such investigations began to appear in numerical applications linked to electro-magnetic [106, 107], heating [108], and acoustic [109, 110] problems in order to reduce the computational load, particularly so in the early years of scientific computer simulations. Lately, this strategy has seen multiple uses for simplifying intricate subwavelength structures, such as metamaterials [111, 112]. On top of analytical impedance approximations, the Resistor-Inductor-Capacitor (RLC) circuit impedance analogy between electrical and mechanical systems [104] has also allowed for simpler expressions of resonant structures. This becomes notably useful for the description of metamaterials made of locally-resonant elements [113]. The simplification of complex structures, such as metamaterials, opens the way for the computation of wider numerical sceneries that can include the local effects of these refined structures.

The following sections thus propose to look at an acoustic scattering study where compact and locally-resonant acoustic metamaterials, i.e., metadiffusers, are considered too complex to simulate in a 3D FDTD scheme, and thus evaluate the computational and scattering impact of RLC IBCs on the sound diffuse field of a larger space in which they could be installed, such as an orchestra pit. Fig 6.1 illustrates this approach, where the scaled scheme of an $N = 5$ slits Quadratic Residue Metadiffuser (QRM), used here as a reference compact metamaterial, is shown in Fig 6.1(a). The local scattering generated by the metadiffuser can be alternatively reproduced through a simplification of the metamaterial geometry into its surface IBCs. The resulting IBCs can thereafter be reproduced through an RLC circuit optimization routine [114] integrated at the desired boundaries of the 3D FDTD volume, as illustrated in Figs. 6.1(b,c).
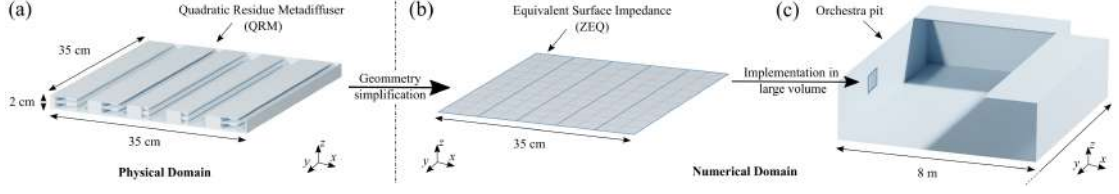
Figure 6.1: Conceptual diagram illustrating (a) a render of a Quadratic Residue Metadiffuser (QRM) with $N = 5$ slits, (b) a numerical equivalent surface impedance (ZEQ) of the metadiffuser identically composed of $N = 5$ slits, and (c) an implementation of the ZEQ into a large computational volume, i.e., an orchestra pit.

### 6.1.2 *Finite-Difference Time-Domain: Scope & Limitations*

In a similar way than FEM, Finite-Difference Time-Domain (FDTD) method discretizes the numerical space and approximates the spatial and temporal derivatives of the PDE of concern, (e.g., scalar wave equation) through a set of forward and backward finite-differences. Mathematically, the central finite-difference approximation for the second order derivative of a univariate scalar function $u(x)$ takes the compact form [115] of

$$\left.\frac{\partial^2 u}{\partial x^2}\right|_{x_i, t_n} \approx \frac{u_{i+1}^n - 2u_i^n + u_{i-1}^n}{(\Delta x)^2} + \mathcal{O}(\Delta x)^2, \tag{6.1}$$

where $\Delta x$ is the space stepping of the grid between two nodal points at the position $x \in [0, i]$ and at a time $t \in [0, n]$. $\mathcal{O}(\cdot)$ denotes the order of truncation for omitting the higher order terms from the subjacent Taylor expansion of $u(x \pm \Delta x)$. Here, this implies that the approximation errors of the finite-difference formulation decay proportionally to $(\Delta x)^2$ as $\Delta x$ decreases [116].

This approach relies on a discritization of space that takes the form of a grid of evenly spaced nodal points. The periodic arrangement of such nodal points, commonly referred to as the stencil (numerical unit cell), thus defines the way the space is being covered by the grid. Figure 6.2 shows a 7 point stencil in a 3D Cartesian coordinate system based on a Standard Rectilinear (SRL) discretization method, i.e., an even spacing of nodal points along the main 3D axes. Other stencils such as the Interpolated Wideband (IWB) or the Interpolated Digital Waveguide Mesh (IDWM)
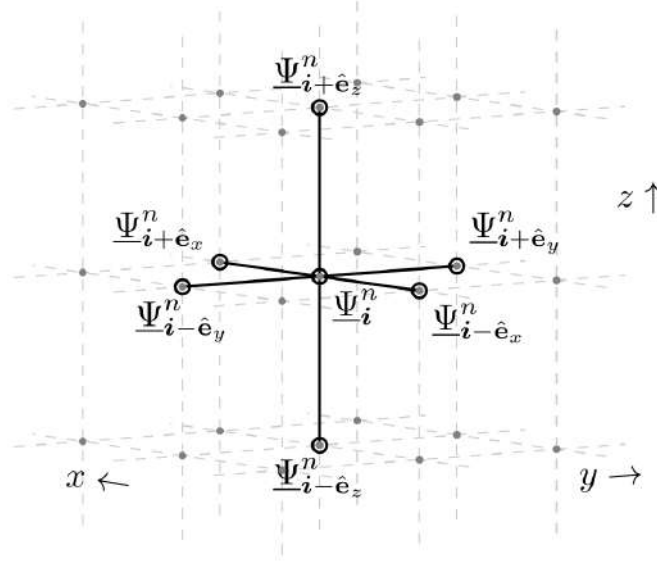
Figure 6.2: Standard Rectiliniear 7 point stencil in 3D Cartesian coordinates [116].

can be found in literature [116–118] for defining the space discretization method of the numerical domain.

The nodal points in the grid contain information about acoustic variables such as acoustic pressure and particle velocity, and their values are iteratively updated through a defined set of time windows when computing the FDTD. This introduces the two major groups of FDTD schemes: the explicit and implicit schemes. The former are generally considered more straightforward to implement due to the stencil values being updated based only on their value during the previous time step. The latter scheme, however, updates the stencil values in function of the values of the neighbouring nodes and thus requires a simultaneous solving of all the nodes.

Unlike FEM, FDTD methods implicitly bring numerical wave dispersion due to the time-space relation in the finite-differences, and can thus limit the bandwidth of the study. In order to reduce the numerical dispersion error that may be introduced in this manner, the Courant or the Courant-Friedrichs-Lewy (CFL) condition is usually applied, in which the duration between discrete time-steps must be less than the time it takes for the wave to travel to adjacent grid points. This can be summarised as

$$C = c\frac{\Delta_t}{\Delta_x} \leq C_{max},\tag{6.2}$$

where $C$ is commonly referred to as the Courant number, $C_{max}$ is the maximum value of the Courant number, $c$ is the propagating speed of the wave, $\Delta_t$ is the time stepping and $\Delta_x$ the space stepping. Generally, for explicit schemes, $C_{max} = 1$ can be taken as a valid condition.

The FDTD method can have many advantages. Being a time-domain technique, the response of the system can be obtained over a wide range of frequencies through a single simulation run. Also, since FDTD can calculate the pressure and velocity fields everywhere in the computational domain, it can provide insightful animated displays of the wave field movement through the model. Another implicit advantage of FDTD is that the numerical algorithm is well suited for parallel-processing computing. Thanks to this efficient scaling on parallel processes, FDTD can thus benefit from the recent developments made in Graphics Processing Unit (GPU)-based accelerated technologies.

However, FDTD also has numerical artefacts and disadvantages that should be remembered. Since FDTD requires a grid over the entire computational domain, and that the spatial grid discretization must be sufficiently fine to resolve both the smallest wavelength of interest and the smallest geometry feature of the model, this can often induce a very large computational domain to be solved for, which can result in extremely long simulation times. Also, as mentioned previously, this computational load can be additionally increased by the CFL condition in order to maintain at least a good numerical stability. Lastly, because FDTD solves for both pressure and velocity everywhere in the computational domain, then values at large distance require large domains to be solved, and therefore can lead to excessively large computational loads. Figure 6.3 illustrates how a trivial domain can be represented in its grid form and volume discritization form.

This chapter addresses the above-mentioned disadvantages of FDTD, as well as presenting a way to bypass them in order to simulate the acoustic influence of metadiffusers within a relatively large 3D FDTD computational volume. This is achieved by reducing the intricate geometrical structures to their equivalent surface impedance.

(a) $\overline{\Omega}$          (b) $\mathbb{G}_h$          (c) $\overline{\Omega}_h$
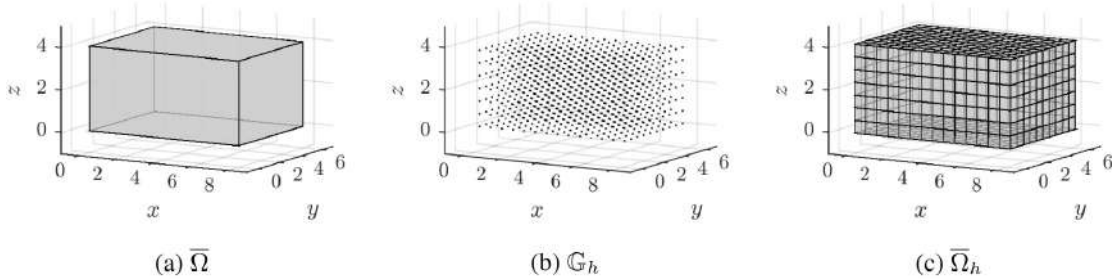
Figure 6.3: (a) An example domain, $\overline{\Omega}$, along (b) a Cartesian grid, $\mathbb{G}_h$, and (c) the associated volume $\overline{\Omega}_h$ [from [116]].

### 6.1.3  *Geometry Reduction via an RLC Circuit Filter*

The magnitude and phase of the surface impedance of a metamaterial are marked by the inherent resonances of the structure. In the case of the QRM, a highly resonant structure is displayed [75] which lends itself to a boundary formulation based on a combination of second-order resonators. One useful passive formulation for a given slit impedance consists of a parallel set of series-RLC circuits (after [114]), each consisting of one resistor (R), one inductor (L) and one capacitor (C), where all RLC parameters are non-negative and real-valued. The admittance of this structure in the Laplace domain is given by

$$Y(s) = \sum_{b=1}^{B} \frac{1}{Z^{(b)}}, \quad Z^{(b)} = L^{(b)}s + R^{(b)} + 1/(sC^{(b)}), \tag{6.3}$$

where, for the current analyses and optimizations, $s$ is limited to $s = j\omega$, and where $B \geq 1$ is the number of RLC branches and $C^{(b)} > 0$. An electrical diagram of such RLC circuit is shown in Fig. 6.4. The associated impedance of the RLC circuit is then simply $Z(j\omega) = 1/Y(j\omega)$. With this impedance boundary formulation, the surface impedance of each slit of the QRM can be fitted with an equivalent circuit made up of set of resonances with non-negative RLC parameters. The passivity of this structure is then preserved in the discrete FDTD setting through the choice of the bilinear transform as a discretisation method [119]. This impedance model can be seen as an extension of various simpler frequency-dependent boundary models presented in the context of FDTD methods for room acoustics [120–122].

127
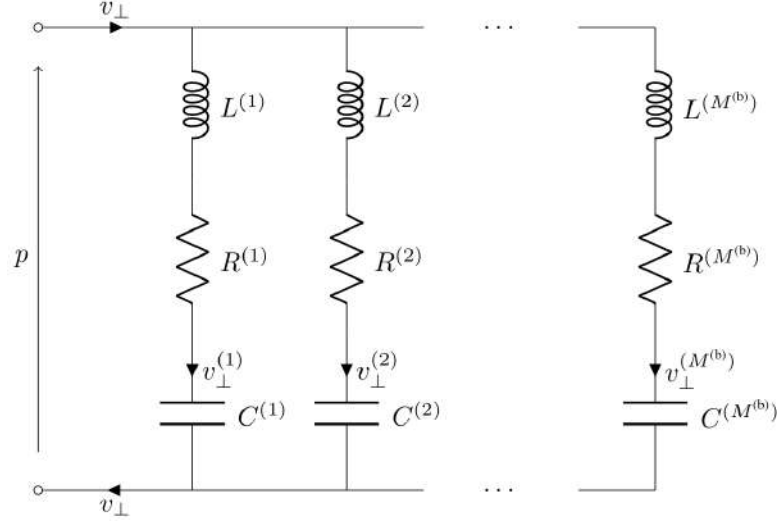
Figure 6.4:    (a) Electric diagram representing a set of $b$ RLC (Resistor-Inductor-Capacitor) circuits joined in parallel (from [116]).

A methodology for fitting RLC parameters is described in Ref. [114], which consists of: (i) identifying resonances in an admittance by their peaks in the admittance magnitude, and (ii) estimating half-power bandwidths for each resonance from admittance magnitude. From those estimates RLC parameters may be identified for each resonance. This is followed by a global optimization over the RLC triplet parameters using a Nelder-Mead optimization [123]. This approach works well when admittance peaks are well-separated, but in general peaks in admittance magnitude data can be difficult to identify, and furthermore half-power bandwidths can be hard to estimate from admittance magnitude data alone. This is especially true in the example admittances shown in Fig. 6.5.

In this study, a novel approach is used, which is based on making use of admittance *phase* information, and derivatives thereof, to identify resonance parameters. It can be observed from Fig. 6.5 that peaks in admittance magnitude are linked to inversions in the phase response. More specifically, we know that the phase response of an individual series-RLC circuit admittance goes to zero at its resonant frequency and also displays a negative slope at that frequency. Additionally, regarding the slope of the phase at the resonant frequency, one can derive:

$$-\left.\frac{\partial \angle Y(j\omega)}{\partial \omega}\right|_{\omega=\omega_0} = \frac{2}{\Delta\omega} = \frac{2L}{R},$$

(6.4)
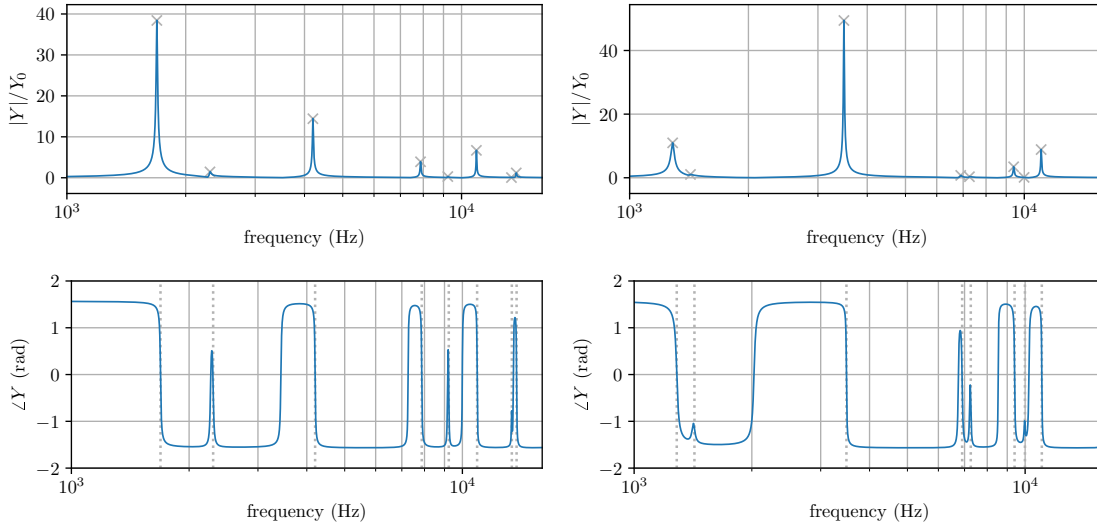
Figure 6.5: Two example surface admittances within two slits of a QRM as a function of frequency in Hz, with identified resonances marked in grey.

where $\omega_0 = 1/\sqrt{LC}$. Thus, after detecting a resonance in the admittance phase from its slope and zero crossings, and after sampling the associated peak in the admittance magnitude, the half-power bandwidth, $\Delta\omega$, follows from Eq. (6.4) (which may be estimated with simple finite differences). This approach is sufficient to obtain RLC parameters for each well-isolated resonance, and can be more robust than peak detection and half-power bandwidth estimation from the admittance magnitude alone. Nevertheless, this approach still has limitations for very-closely spaced resonances (examples can be seen in Fig. 6.5) where the phase response at a resonance may not cross zero (and thus would not be detected with this approach so far). To deal with such issues, the *second derative* of the phase is additionally used to identify resonances, based on the relation:

$$\frac{\partial^2 \angle Y(j\omega)}{\partial \omega^2}\bigg|_{\omega=\omega_0'} = 0\,, \quad \omega_0' = \omega_0\sqrt{\sqrt{4-(\Delta\omega/\omega_0)^2}-1}, \qquad (6.5)$$

where $\omega_0'$ is the angular frequency at which there is a zero crossing in the second-order derivative of the admittance phase. Furthermore $\omega_0' \approx \omega_0$ provided that $(\Delta\omega/\omega_0)^2 \ll 1$, which means that $\omega_0'$ may be used as an initial estimate of $\omega_0$ to seed the subsequent global optimisation. Identified resonances using this phase-derivative zero-crossing method (grey dotted lines) can be seen in Fig. 6.5.
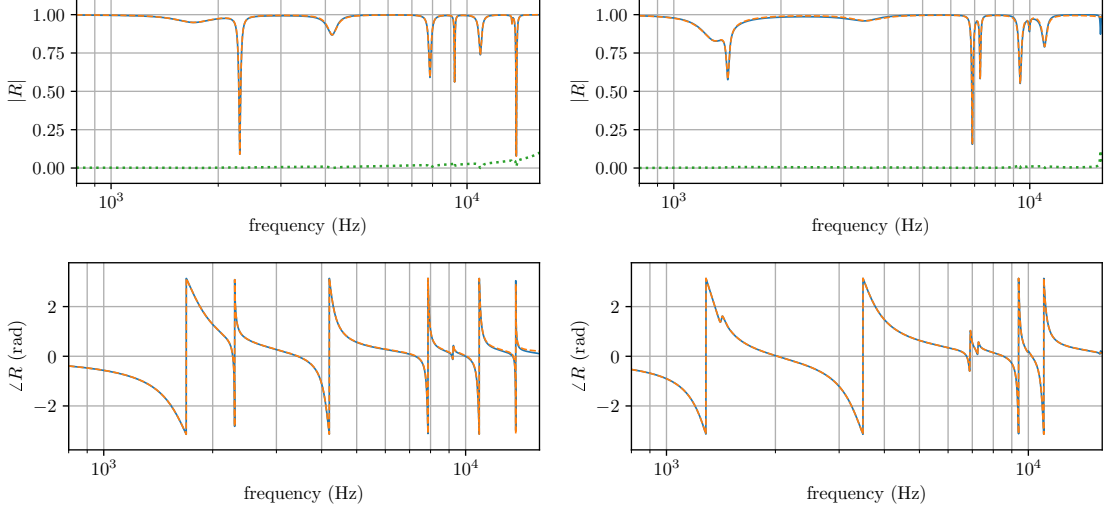
Figure 6.6: Reflection coefficients $R_{TMM}$ (blue, solid) and $R_{RLC}$ (orange, dashed) relating two different surface admittances within QRM ($Y_{TMM}$ and $Y_{RLC}$) along with fitting errors (green, dotted), as a function of frequency in Hz.

Once a set of $3B$ RLC parameters has been identified, a global optimization using the Nelder-Mead method [123] is carried out to minimize $\epsilon = \|Y_{TMM} - Y_{RLC}\|$, where, for a given slit, $Y_{TMM}$ is the target admittance output from the TMM model of the QRM, and $Y_{RLC}$ is the impedance output of the RLC circuit. The fitted reflection coefficients of the previous two slits in the QRM can be seen in Fig. 6.6.

It can be seen in Fig. 6.6 that while discrepancies appear, generally the RLC fit is close to that of the TMM model of the QRM. These discrepancies could be attributed to viscothermal losses in the TMM model which cause deviations from ideal second-order resonances. These discrepancies could be mitigated by using more than one resonance per identified peak in order to compensate such deviations, but this was not pursued as a compromise of accuracy and model complexity. For later comparison purposes, a similar approach for modelling an equivalent surface impedance was adopted in an Finite Element Method (FEM) study in COMSOL Multiphysics 5.3™ where the $N = 5$ impedance patches where modelled using impedance boundary conditions with custom input values. The resulting scattering data is shown in the next section.

### 6.2.1 *Numerical Benchmark: Spatial Dispersion*

Figure 6.7 compares the 3D hemispherical scattered sound pressures of a flat surface, the aforementioned QRM with $N = 5$ slits, and the equivalent RLC surface impedance ZEQ with $N = 5$ slits as well. The scattering distributions have been obtained through three different methods, i.e., (i) the Rayleigh-Sommerfeld (R-S) integral for near-field scattering information, (ii) Finite Element Method (FEM) in COMSOL Multiphysics 5.3™, and (iii) Finite-Difference Time-Domain (FDTD) simulations made with a custom solver. Numerical simulations were computed by installing the surface at the centre of a spherical domain filled with air, surrounded by a concentric perfectly matched layer (PML) with a far-field boundary condition at the boundary of the air domain to simulate the radiation condition. Fig. 6.7 shows the theoretical and numerical solution of the surfaces scattered sound energy integrated over a radius distance of 1 m, so that it can match the finite FDTD and FEM numerical frameworks. In the former, virtual microphones where positioned at 1 m around the surface, which considering its edge dimensions (x,y)[35 cm, 35 cm], should be sufficient to depict correctly the scattered field at a frequency $f = 2$ kHz. FEM results were obtained following a similar approach where the integration was performed over a spherical near-to-far-field boundary condition of 1 m radius.

Overall, the polar plots displayed in Fig. 6.7(a-b) show some variations between the theory and FEM simulations, with normalized diffusion coefficient values varying from $\delta_{n,0} = 0.61$ to $\delta_{n,0} = 0.55$. This small difference can be explained by the divergence of theoretical assumptions with respect to a numerical solving of the wave equation. More specifically, in a theoretical framework, the surface impedance is considered locally homogeneous for each slit, a fact that may not be entirely true in numerical terms due to the potential evanescent coupling between slits; a phenomenon not taken into account in the theory. As the scattered sound field is highly dependent on the distribution of the surface's reflection coefficient, slight variations

in the polar distributions can thus be expected. Nonetheless, it can be seen that the global shapes of the QRM sound scattering distributions are sensibly similar one to another, which can be confirmed by their close autocorrelation values. In addition, Fig. 6.7(b) represents quite well the expected main dip that defines the Quadratic Residue sequence at $\theta \approx -20°$ in the $\phi = [-90° : 90°]$ elevation axis. The main axial and lateral energy lobes are also quite well represented. However, a slightly higher energy lobe can be discerned at $\theta = 20°$ in the FEM case. This is likely due to the finite size of the surface sample in the simulation, resulting in a decrease of the scattered sound energy at grazing angles, thus further enhancing the remaining scattered energy and slightly reducing the intrinsic autocorrelation value. Despite such differences, the FEM model can be estimated to be in good agreement with the theoretical predictions.

The missing scattering distribution under Fig. 6.7(c) is at the core of this work's rationale, as it has proved to be a difficult task to simulate the metadiffuser through a large-scale FDTD solver. The complex physics and the small geometry of the QRM not only would require an extremely fine meshing grid, and thus a very high computational load for conducting the same simulations, but the physics would
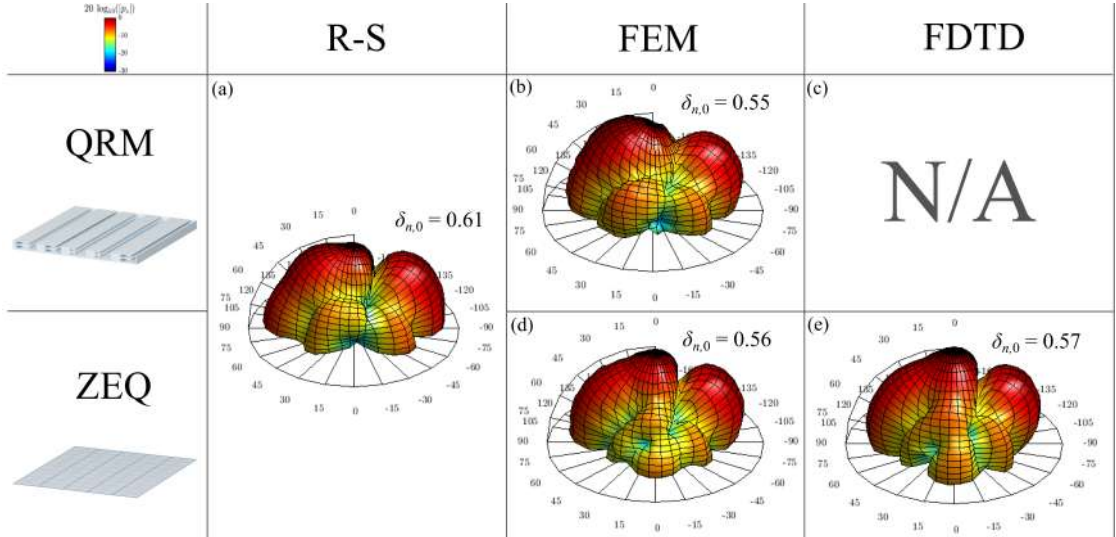


Figure 6.7: Distribution of sound scattered pressure levels at 2 kHz for a Quadratic Residue Metadiffuser (QRM) and the equivalent surface impedance filter (ZEQ) according to Rayleigh-Sommerfeld (R-S) integral, Finite Element Method (FEM), and Finite-Difference Time-Domain (FDTD). $\delta$ insets represent the autocorrelation of the scattered distributions.

also have to be changed to take into account varying bulk modulus and density of air as a function of space; increasing again the computational needs. This is why the aforementioned RLC circuit impedance filtering is herein proposed as a way to bypass the numerical limitations of large scale FDTD simulation techniques for accounting compact metamaterial strategies.

Figure 6.7(d) shows the scattering distribution of the equivalent surface impedance simulated through FEM where the $N = 5$ impedance patches where modelled using IBCs with input values identical to the analytical surface impedance of the QRM. Again, it can be observed that the main dip at $\theta \approx -20°$ is correctly reproduced, and that the main axial lobes are also in good agreement with the theory, leading to a autocorrelation value $\delta_{n,0} = 0.56$ close to that of Fig. 6.7(b). The major differences that can be distinguished compared to the fully modelled QRM are the energy distributions of the lateral lobes in the $[0°:180°]$ plane and the smoothing of the $\theta \approx 20°$ energy lobe. These seems to resemble that of a flat panel scattering. Perhaps this is due to the disappearance of the slit cavities within each impedance patch which may cause variations form the estimated slit impedance values as these are dependent on the free air radiation correction of the slits and on the portion coverage of each slit opening ($h$) within the spatial periodicity of the structure ($a_x$). Also, even though the FDTD supposedly ignores viscothermal losses in its wave propagation model, these are implicitly encoded into the RLC fitting of the theoretical metadiffuser surface impedance, which does take such losses into account. More investigation on the precise origin of these scattering variations is needed.

Fig. 6.7(e) similarly represents the scattered sound distribution of the ZEQ in the FDTD solver. Results are in excellent agreement with the ZEQ FEM data, with a very similar autocorrelation coefficient $\delta_{n,0} = 0.57$. A minor increase in scattered sound energy can however be perceived between FEM and FDTD ZEQ models which also appears in other cross-numerical benchmarks that were conducted for QRDs and flat surfaces. Figures for these can be found in App. C. This slight energy increase in FDTD RLC modelling may then be attributed to energy propagation modelling in each numerical environment (FEM/FDTD), but remains

nonetheless almost negligible with a difference in diffusion coefficient of 1%.

Whilst the equivalent surface impedance method proposed here results in a major simplification of the more intricate geometry of the metamaterial being studied, it can be seen that it is quite efficient for replicating an approximation of its scattered sound field into the surrounding space. Also, it has been previously shown that these FDTD simulations with such RLC circuit boundary conditions are amenable to parallel acceleration [124] for faster calculation times.

### 6.2.2  *Numerical Benchmark: Time Dispersion*

In addition to the previous spatial scattering results, a temporal acoustic scattering study is also presented for evaluating the presence of time dispersion within the above-collected FDTD data. Figure 6.8 thus shows several wavelet transforms of scattered impulse responses corresponding to the previously studied surfaces, viz., a flat panel, an $N = 5$ QRD and the previous ZEQ based on an $N = 5$ QRM. A fully modelled QRD is here presented instead of a QRM due to the difficulty in modelling the latter structure into the FDTD solver. One has to note that these possess different diffusion characteristics overall, which only match around 2 kHz. An alternative for fully modelling a QRM would have been to use a Pseudo-Spectral Time-Domain (PSTD) method which would mixes the aforementioned frequency-domain R-S integral whilst discretizing the study in time steps, allowing to simulate transient acoustic wave propagation in inhomogeneous media; a required ability for modelling the metadiffuser under study. Simulating the QRM in large scale 3D PSTD would however prove hard to compute due to the inherent difficulty for implementing complex geometries at the boundaries, but could be used with confidence under free-field scattering conditions. However, due to time limitations, such alternative could not be explored in this study.

Figure 6.8(a) shows the time-frequency information of the scattered impulse response captured at the top of a flat surface. As expected, only a single hard reflection is obtained in the impulse response, covering the entirety of the frequency
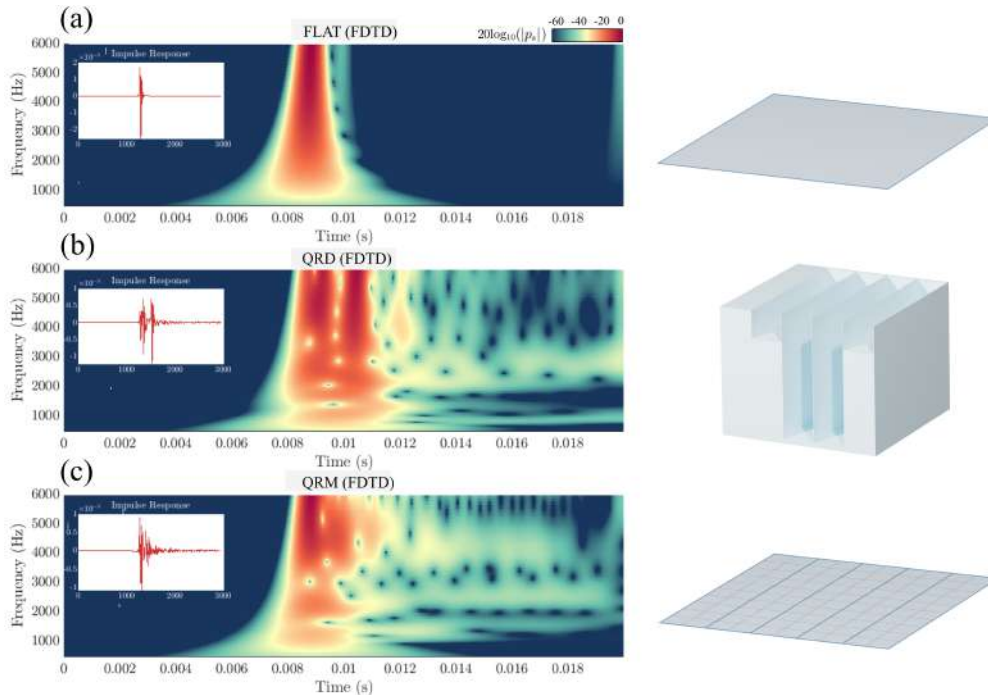
Figure 6.8: Wavelet transforms of scattered impulse responses obtained via 3D FDTD corresponding to (a) a flat panel, (b) an $N = 5$ QRD, and (c) the ZEQ. Insets represent the reconstructed inverse wavelet transform of the original impulse responses.

range of interest. A secondary reflection with much less intensity can also be identified, likely generated from the edge diffraction of the panel coming back to the receiver a couple of milliseconds after the first major reflection. This is supported by the inset displaying the time series of the reconstructed signal by inverse wavelet transform in Fig. 6.8.

The scattering obtained with the QRD via FDTD is illustrated in Fig. 6.8(b), where a strong time dispersion can be distinguished by the spreading of the scattered frequencies through time. In such figure, one can see a major reflection shortly followed by a similarly strong one, after which a series of multiple reflections appear with varying frequency content and continually less energy. This provides with a good illustration of the scattering generated by the frequency-dependent behaviour of a sound diffuser. The blue dots represent the absence of frequency content in very narrow time periods. These are caused by wave interference due to the wavelength delay generated by the phase-grating diffuser, providing with a time-frequency dispersion pattern.

Ultimately, Fig. 6.8(c) displays the scattered impulse response of the ZEQ obtained through RLC circuit filtering. It can be observed that a strong temporal dispersion is also obtained, with a similar pattern than the QRD. Even if the surface of the ZEQ is flat, it reproduces a similar frequency-dependent behaviour than a QRD. Although, as mentioned previously, both temporal dispersions cannot be strictly compared one to the other. Yet, the scattering from the QRD serves as a good reference to observe the added temporal dispersion of the ZEQ.

Although the QRD and ZEQ temporal dispersions cannot be strickly compared, the ZEQ filter (fitted to a QRM) provides a temporal acoustic scattering in par with that of a comparable QRD despite the simplification process regarding its boundary formulation. Now that both the spatial and the temporal scattering properties of the ZEQ have shown good agreement with respect to the original metamaterial, the next section will then emphasize in a case study implementation on a large environment.

## 6.3 SOUND FIELD DIFFUSION IN AUDITORIA WITH RLC FILTERS

### 6.3.1 *Spatio-Temporal Analysis of* 3D *Impulse Responses*

For the purpose of this work, an orchestra pit is chosen for a large scene in which to embed the proposed equivalent surface impedances in a 3D FDTD simulation. The geometry of the orchestra pit is idealized as shown in Fig. 6.11(a), where a sound source $S$ and a receiver $R$ are highlighted. Note here that the pit is isolated from the rest of the opera house. The considered orchestra pit is simulated following two different scattering strategies implemented on the walls. In the first situation, no particular scattering on the boundaries is considered, i.e., the walls are simply assumed perfectly rigid.

The FDTD simulation grid resolution was set to 10.5 PPW at 8 kHz, under which numerical dispersion errors would be less than 1% [116]. The simulations involving flat panels (no scatterers) required 30GB of memory computed in par-
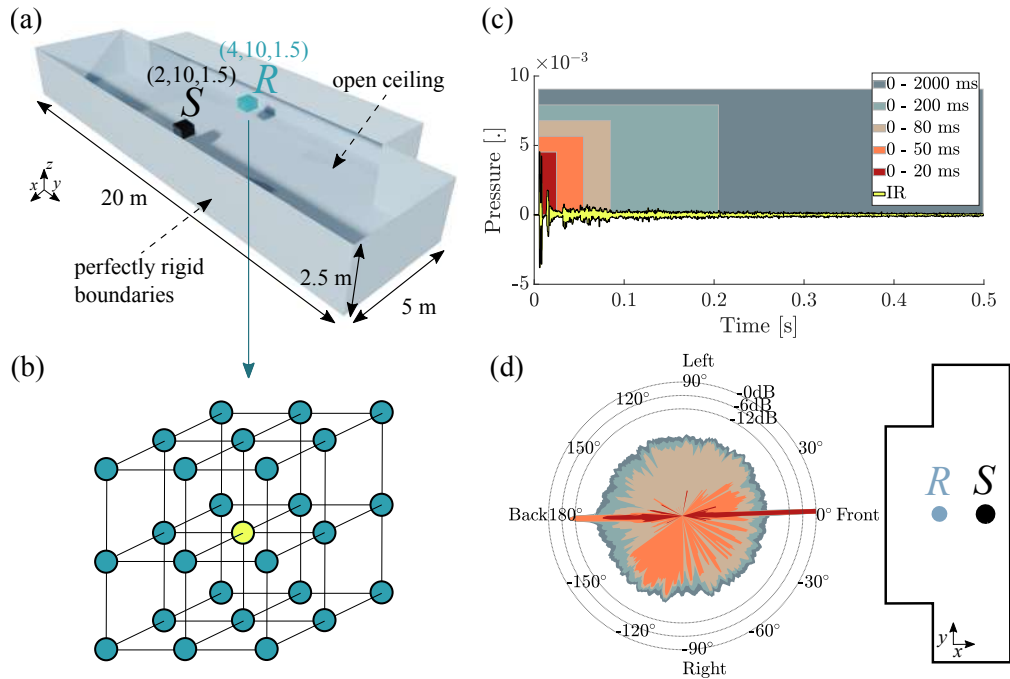
Figure 6.9: (a) Geometry of an ideal orchestra pit used. (b) Configuration of the $3 \times 3$ microphone array. (c) Sample impulse response with different integration times. (d) Spatio-temporal distribution of sound energy received at location $R$ from sound source $S$.

allel using Nvidia CUDA spread over four Nvidia Titan X GPU cards (Maxwell architecture). Simulations times with flat panels were approximately 55 min for 0.5 s of simulated response. Including the more complex RLC boundary conditions, the FDTD simulation took 65 min and required 3% more memory running on the same GPUs. Thus, the equivalent surface impedance incurs some extra minimal simulation costs (as expected [124]), and it is also much smaller relative to the simulation costs expected for a full-fledged multi-physics simulation (taking into account QRM details and physics) in this space up to the chosen frequency resolution.

The impulses responses captured within this environment are analysed by means of a Spatial Decomposition Method (SDM) [125, 126], which allows to determine the direction of arrival (DOA) [127, 128] of sound events in a 3D set of spatial impulse responses. The latter is captured through a microphone array and can be windowed over different integration times in order to show the evolution of the spatial sound field with respect to time. In this case, a $3 \times 3$ virtual microphone array was used for recording the numerical impulse response at the receiver location

$R$, and is displayed in Fig. 6.11(b). For data processing, the Spatial Decomposition Method (SDM) Toolbox [129] made available by the Virtual Acoustics Team at Aalto University, Finland, was used. The impulse responses cover a frequency range $\Delta_f = [20 : 8000]$ Hz and are integrated over several incrementing time windows so that the cumulative energy of the impulse responses can be observed through time. These span from $[0-20]$ ms to $[0-2000]$ ms in order to cover most of the recorded information, as shown in Fig. 6.11(c). Ultimately, the spatial sound field for each time window can be plotted along the 3 orthonormal polar planes, i.e., lateral, transversal and median planes. Fig. 6.9(d) thus shows the lateral ($xy$-plane) spatio-temporal sound field at $R$.

While several methods for characterising the sound diffusion from surfaces have been standardized (see Sec. 3.1.2), the standardization of a similar relationship within a context of sound fields in enclosed spaces is still in progress. Early research on this topic by Thieler, Meyer, Cremer and Abdou [130–132] provides with some insights regarding the description of the isotropy of the sound field at a certain position in space, yielding a quantity called the "directional diffusion" coefficient [133]. In order to avoid confusion with the previously mentioned directional diffusion coefficient in the context of surface scattering – although they are both related to the physical description of isotropy in a sound field – later research seems to prefer the use of the term "diffuseness" in order to refer to the 3D spatial distribution of incoming sound energy at a point [134]. This work will thus also make the same differentiation. The motivation behind the use of the diffuseness equation presented in Ref. [133] and further discussed below comes from a desire to identify differences in field isotropy, either between different windowed spatio-temporal impulse responses or between two different spatio-temporal impulse responses. This, along the Spatial Decomposition Method, allows not only to visualize the spatio-temporal distribution of arriving sound at a point but also to characterize the field isotropy of the responses of interest.

Besides the SDM, some of the latest research in this topic also provides with alternative descriptions of directionally-dependent features of decaying sound fields, with insightful visualization techniques and new quantities. Some are based on

spherical harmonics analysis [135] whereas others focus on the Energy Decay Deviations in order to to show the direction-dependent anisotropic characteristics of sound [136]. The Spatial Decomposition Method was used here for its extensive documented Matlab libraries, as well as its flexibility for variable input microphone array geometries. As in indicated in [125], this method reproduces well the major energy peaks of the sound field but can prove less accurate for minor reflections with small amplitude due to the small-scale interpolation between data points.

At the core of its definition, diffuseness is usually understood as the ratio of the variation of the diffuse sound field intensity averaged on all directions over that obtained in a free-field situation. Mathematically, this notion of diffuseness can be written in the form of a coefficient, or percentage if multiplied by 100, such that

$$\mathcal{D} = \left(1 - \frac{\sigma}{\sigma_0}\right), \tag{6.6}$$

where $\sigma$ is the variation of energy across all directions in the diffuse case and $\sigma_0$ is the value of $\sigma$ in the most non-diffuse case, e.g., single plane wave or free field. The spatial variation $\sigma$ of a given polar distribution can be obtained following various statistical operations, such as standard deviation, absolute average deviations or spatial autocorrelation. For the sake of consistency, the same spatial autocorrelation formulation used for calculating the directional diffusion coefficient in Eq. 3.1 is chosen for determining the variation of the diffuse field. Thus $\sigma \equiv 1/\delta$, where $\delta$ is the spatial autocorrelation coefficient. The ratio of $1/\delta$ aims to conserve the relative sizes of $\sigma$ and $\sigma_0$ in Eq. 6.6. This is to balance the fact that minimal spatial variation (i.e., uniform distribution) has $\sigma \to 0$, whereas the least uniform distribution (i.e., highest spatial variation) has $\sigma_0 \to 1$.

The formulation of diffuseness in Eq. 6.6 results in a good description of the change of isotropy between different sound fields. A particular case of the latter can then be made in order to yield an indicator when relative evaluations between the early and late diffuse sound fields are of interest. In order to make such evaluations, the ratio of early-to-late diffuse energy variation is here proposed which,

by applying the fraction $\sigma \equiv 1/\delta$, allows the early-to-late diffuseness coefficient of a sound field, $\mathcal{D}_{e/l}$, to be determined as

$$\mathcal{D}_{e/l} = \left(1 - \frac{\delta_e}{\delta_l}\right), \tag{6.7}$$

where $\delta_e$ and $\delta_l$ are the early and late spatial autocorrelations of the polar distributions, respectively. In such case, $\mathcal{D}_{e/l} \to 0$ implies that the evolution of the early-to-late diffuseness is non-existent, i.e., that both fields are identical, whereas $\mathcal{D}_{e/l} \to 1$ indicates a maximum increase of diffuseness between early and late diffuse sound fields. The minimal time window used to represent the early diffuse sound field is here chosen as $[0 - \tau_e]$, where $\tau_e = \mathrm{mfp}/c$ represents the average time of early reflections based on the mean-free-path of sound reflections, mfp, and the speed of sound, $c$.

In the context of 360° spatio-temporal distributions, very low values of spatial autocorrelation coefficients can be seen due to the incident sound being much stronger than the later reflections. This can enquire a question regarding the dynamics of the data being handled and if such data can be used. However, Eq. 6.7 shows a ratio of two spatial autocorrelations and gives therefore an insight to the relative difference between the two autocorrelations. Then, although the autocorrelation values are generally quite low, the definition of diffuseness presented above in Eq. 6.7 can be considered as an appropriate tool for characterizing the amount of change in isotropy when the data at hand is alike to spatial variations such as spatial autocorrelation coefficients.

### 6.3.2 *Case Study: Conceptual Orchestra Pit*

The orchestra pit previously mentioned is simulated following two different scattering strategies implemented on the walls. In the first situation, no scattering on the boundaries is considered, i.e., the walls are simply assumed perfectly rigid, as shown in Fig. 6.10(a). In the second case illustrated in Fig. 6.10(b), clusters of repeated equivalent surface impedance panels ($3 \times 6$ panel repetitions of the previously studied 1D ZEQ mimicking a Quadratic Residue Metadiffuser) are sparsely distributed along the walls in order to provide with a relatively homogeneous cover-

age ($\sim$ 10% of total surface, $\sim$ 20% of wall surface), an alternative which according to the previous spatial and temporal scattering study should provide with a more uniform early diffuse sound field. The amount of ZEQ panel coverage was arbitrarily determined as this study only aims to observe the presence of scattering within the orchestra pit in order to validate an practical integration of RLC filter within a large computation domain.
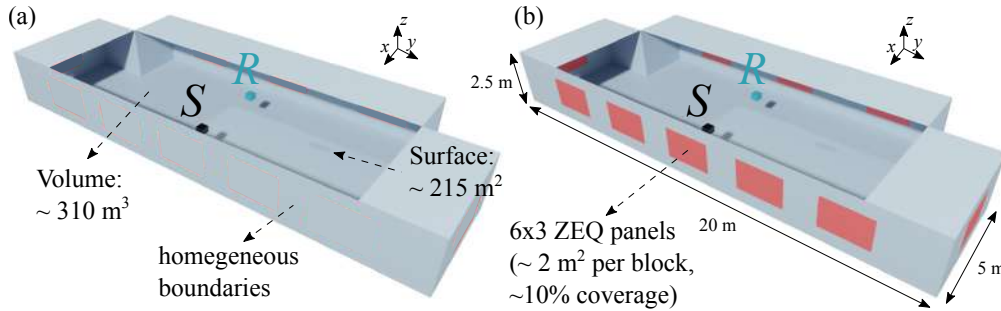


Figure 6.10: Orchestra pits with (a) homogeneous walls, and (b) $6 \times 3$ ZEQ panels.

Fig. 6.11(a) displays the spatio-temporal response at $R$ in the transverse plane ($xy$-plane). It can be observed that early acoustic energy arriving in the first 20 ms (red area), determined by $[0 - \sim \tau_e]$, comes narrowly from the front, where the sound source is located, with a significant contribution from the back as well due to specular wall reflection. Later reflections integrated up to 2 s of the impulse response (orange to blue areas) show an increase of sound energy for many directions of arrival due to a more chaotic state of sound reflections within the environment at those time steps, resulting in a relatively uniform (isotropic) angular sound field distribution at the maximum integration time. Still, in most directions, the energy of the late sound field remains 12 dB or more below the initial energy recorded directly in the front and in the back of the receiver.

In the early $[0 - 20]$ ms window of Fig. 6.11(a), an early autocorrelation coefficient $\delta_e = 0.0056$ can be observed, while for the late time window of $[0 - 2]$ s a value $\delta_l = 0.0223$ is displayed. This corroborates that the early sound field is much less uniform than the overall late sound field with a very narrow energy distribution, which is to be expected in an environment where specular reflections of sound are dominant. This yields an early-to-late diffuseness $\mathcal{D}_{e/l} = 0.75$ describing a great increase (of 75%) of the diffuse field between early and late integration times.
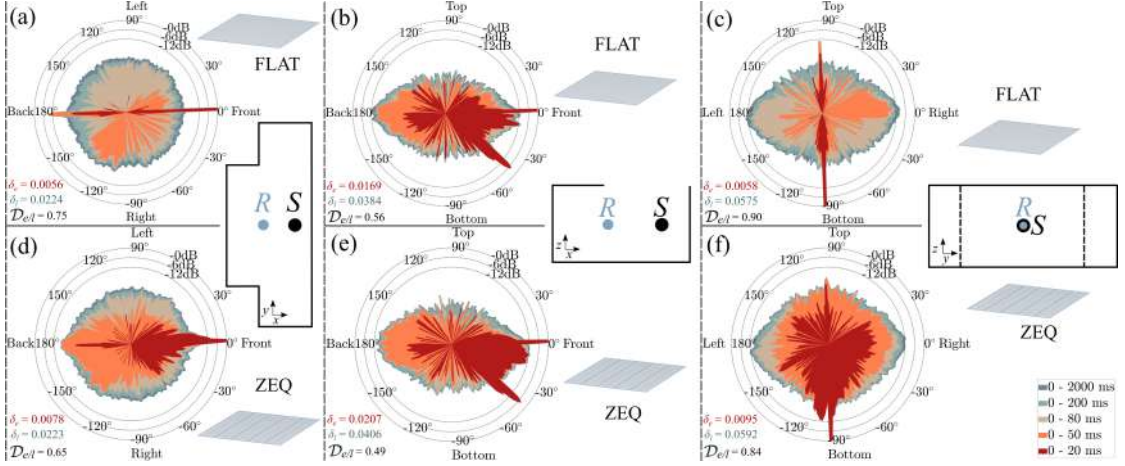
Figure 6.11: Spatio-temporal distributions of sound energy received at location $R$ from sound source $S$ in (a-c) a pit with flat boundaries, and (d-f) a pit with sparsely distributed repetitions of ZEQ patches.

Similar observations can be made for the median ($xz$) and lateral ($yz$) planes in Figs. 6.11(b,c), respectively. In the median plane, a value $\mathcal{D}_{e/l} = 0.56$ is achieved, showing less difference between early and late spatial distributions compared to that of Fig. 6.11(a). This is supported by the axis symmetry and open-air nature of the orchestra pit, where little extra reflection directions are enabled in this particular cross-section. In Fig. 6.11(c), an early-to-late diffuseness $\mathcal{D}_{e/l} = 0.90$ can be identified for the lateral plane, bringing similar features than those encountered in the transverse plane, i.e., very narrow early spatial distribution which significantly widens over late integration times.

In the second pit configuration, an alternative scenario is proposed with clusters of repeated equivalent surface impedance sparsely distributed along the walls in order to provide a relatively homogeneous diffuser coverage. The intention behind this strategy is to distribute more early sound energy in the pit, which incidentally may also help enhance the acoustic conditions for musicians [**cox2009**, 55, 137]. Even if the geometry presented is simply idealised, i.e., without the musicians or chairs which would create additional sound absorption and scattering, this conceptual setup helps distinguish the effect of RLC fitted equivalent impedances within a large volume. The use of equivalent surface impedance is again motivated by the limiting constraints of modelling compact and detailed geometrical structures in a

large 3D FDTD numerical scenery.

The above-mentioned simulations are illustrated in Figs. 6.11(d-f) which show the spatio-temporal plots obtained in the second pit configuration for the transverse, median and lateral planes, respectively. In the transverse plane in Fig. 6.11(d), the early time integration area (red) demonstrates the arrival of strong reflections from broader directions than in the previous configuration with just rigid walls. This is supported by an increased autocorrelation coefficient $\delta_e = 0.0078$, which confirms the presence of sound diffusers at the boundaries of the pit. A second major change in early sound distribution can also be seen in the next $[0 - 50]$ ms time window, displaying a much broader and homogeneous incoming sound field due to the presence of multiple $2^{nd}$ and higher order reflections being more sparsely distributed within the pit thanks to the presence of the ZEQ panels. Additionally, the late time integration area (blue) shows a very similar shape than the previous scenario, with a value $\delta_l = 0.0224$. This implies that the late sound field obtained in both situations tends to a diffuse state of reflections with stochastic directions of arrival quite independently of any local scattering at the boundaries, which is shown to only affects early sound distribution. The difference in early and late sound fields in Fig. 6.11(d) translates in a relative decrease of the early-to-late diffuseness coefficient compared to that of Fig. 6.11(a), with $\mathcal{D}_{e/l} = 0.65$; meaning that the early sound field in the ZEQ configuration is more diffuse. Likewise, a general decrease of early-to-late diffuseness can be observed in Figs. 6.11(e,f), with $\mathcal{D}_{e/l} = 0.49$ and $\mathcal{D}_{e/l} = 0.84$ in the median and lateral planes, respectively. It is worth mentioning that the sound field in Fig. 6.11(e) does not show a significant change compared to the one in Fig. 6.11(b), which is again due to the opening of the pit limiting the potential directions of arrival for reflections in this particular section. A small improvement to the early sound field distribution can however be seen between $0°$ and $-45°$.

In addition to the early-to-late diffuseness, the more general diffuseness coefficient can also be determined between sound fields in both pit configurations, where the ones obtained with homogeneous boundaries are here considered as the least diffuse case of reference mentioned in Eq. 6.6. In this manner, a relative early

diffuseness, $\mathcal{D}_e|_{ZEQ} = 1 - (\delta_e|_{FLAT}/\delta_e|_{ZEQ})$, can be given for the different early sound fields in each cross-section in order to provide a more suitable measure of the impact of sound scattering in the environment. In this sense, $\mathcal{D}_e|_{ZEQ} \to 0$ means that both early sound fields have identical spatial distributions, while $\mathcal{D}_e|_{ZEQ} \to 1$ indicates a transition to a maximal isotropic distribution of the early sound field generated in the ZEQ environment.

In Fig. 6.11(d), the latter results in a relative early diffuseness coefficient $\mathcal{D}_e|_{ZEQ} = 0.28$, meaning that the presence of ZEQ panels helps increase the isotropy of the spatial distribution at $R$ by a factor of 28% compared to that of the pit with homogeneous rigid boundaries. Similarly, relative early diffuseness coefficients $\mathcal{D}_e|_{ZEQ} = 0.18$ and $\mathcal{D}_e|_{ZEQ} = 0.39$ can be observed in Figs. 6.11(e) and 6.11(f), respectively. These values corroborate the analysis made so far in that the median plane in Fig. 6.11(e) shows only a slight increase in early diffuseness between the two configurations, whereas a significant increase between early sound fields is found in the lateral plane illustrated in Fig. 6.11(f).

Overall, Fig. 6.11 shows that equivalent surface impedance filters, approximating the effect of compact metadiffusers, do contribute to the spatio-temporal distribution of sound within the simulated FDTD environment compared to that of a flat and homogeneous orchestra pit. This is illustrated by a broadening of the directions of arrival of the early sound reflections at the position $R$ induced by the presence of local scattering generated by the impedance filters at the boundaries. The amount of the contribution can vary depending on the volume considered as well as on the positioning of the receiver, e.g., close or far from reflective surfaces. Ultimately, the relative early diffuseness obtained in the normalization of the ZEQ configuration to that of the homogeneous orchestra pit allows for a more critical evaluation of the scattering impact of the simplified sound diffusers within the simulated space.

The work presented so far completes the work conducted in this thesis. The research thus presented, linked with the previous analysis of deep-subwavelength sound diffusers, a.k.a, metadiffusers, provides insightful evidence of the importance

of such small compact acoustic metamaterials to be used in critical situations where their traditional counterparts become too limiting, such as in orchestra pits or recording studios.

*Page left intentionally blank*

CONCLUSION

---

THIS final chapter compiles the outcomes of every research investigation topic and finally draws out a summary of the work conducted so far. Additionally, future prospects for each of the research fields explored during this investigation are discussed, outlining the major challenges to overcome should this research be pursued. Lastly, any outstanding remarks around the creation of the present work are ultimately addressed.

## 7.1 SUMMARY, KEY OUTCOMES & CONTRIBUTION TO KNOWLEDGE

### 7.1.1 *Research Summary*

Acoustic scattering is generated when a sound wave interacts with an object or medium in in its path, which causes the impinging sound wave to effectively *scatter*, or break out, in a multitude of wave components. Major works by Kirchhoff, Fresnel, Rayleigh, Sommerfeld and Fraunhofer in the field of wave physics have allowed for approximate, yet efficient ways of characterising the way such acoustic phenomenon occurs.

In acoustics, structures scattering sound waves are termed as acoustic diffusers. Traditionally, most of these devices pioneered by Schröeder make use of series of quarter-wavelength resonators (QWRs) for producing a frequency-dependent spatial distribution of the acoustic impedance at the surface of the wells. However, such way of designing sound diffusing structures can become challenging due to the relatively bulky dimensions and intrinsic mass of such diffusers, limiting their practicality in situations where space and mass are critical.

Metamaterials are engineered composite structures based on locally-reacting resonances which display physical properties that are not found in naturally-occurring materials. In acoustics, metamaterials can be used to slow down the phase velocity of sound into subsonic regimes. This, combined with the subwavelength properties of Helmholtz resonators (HRs), allows to further push down the resonance frequency of the metamaterial into deep-subwavelength extents, resulting in structures dimensions $1/10^{th}$ to $1/80^{th}$ thinner than traditional diffusers. In 2017, such theory was used to design highly efficient and optimizable deep-subwavelength sound diffuser, a.k.a. metadiffusers.

Metadiffusers consist of rigidly-backed slotted panels where each slit is loaded by an array of HRs. This slit arrangement introduces strong dispersion and drastically reduces the effective sound speed in the low frequency regime, thus resulting in a decrease of the structure dimensions. The adaptability rising from the interplay of all the geometrical variables enables to formulate an optimization problem, thus producing a multitude of designs for as many situations needed. Moreover, the optimisation nature of metadiffusers facilitates the design of ambitious sound scattering behaviours, such as narrowband perfect diffusion or highly efficient broadband diffusion over multiple octaves. Hybrid diffusing and sound absorbing metadiffuser designs can also be further optimised for even greater practical challenges.

In large volumes, the numerical implementation of compact structures relying on non-homogeneous physical properties of sound can prove very difficult to perform; mostly due to excessively high computational loads and time that can be required. Due to the highly resonant nature of metadiffusers, an equivalent impedance formulation based on a set of approximated RLC circuit boundaries can greatly help reduce the metamaterial's geometry to a convenient simple form, i.e., flat. The use of optimisation techniques can prove useful in effectively reproducing the surface impedance of the metamaterial. Despite the simplification process, this method achieves good overall results with respect to the original acoustic scattering of metadiffusers whilst ensuring relatively short simulation times over a range of frequencies going from 100 Hz to 8 kHz. This strategy therefore allows to model the

inclusion of compact acoustic metamaterials into much larger numerical domains, such as that of an orchestra pit, and gather further insights regarding the acoustics of the space.

### 7.1.2 *Key Research Outcomes*

The key outcomes of this research can be summarized as follows:

1. Experimental validation of the scattering made by a 3D-printed Quadratic Residue metadiffuser;

2. Analytical design and numerical validation of Quasi-Perfect metadiffusers;

3. Analytical design of highly efficient broadband metadiffusers from Quasi-Perfect diffusion schemes;

4. Analytical design and numerical validation of a framework for reducing complex geometries in 3D FDTD schemes using equivalent RLC circuit filters;

### 7.1.3 *Contribution to Knowledge*

Due to the cross-disciplinary nature of this research, the above key research outcomes contribute to the current state of knowledge in many scientific fields.

*Wave Physics*

In the field of wave physics, the experimental validation of a Quadratic Residue metadiffuser provides a solid reference where the theory behind the design of deep-subwavelength scattering metamaterials is matched by numerical and experimental physical data. This thus strengthens the knowledge of such structures and builds up on top of other experimental validations of the intrinsic wave phenomena related to metadiffusers found in similar metamaterials (e.g., perfect absorption [138] or rainbow-trapping [78]).

Additionally, this work reports the design of Quasi-Perfect metadiffusers which

display higher narrowband scattering properties (almost omnidirectional) than traditional alternatives within structural dimensions much thinner. Similarly, an incremental continuation of such work led to an optimization study on how to change the underlying component architecture of the metasurface in order to broaden the diffusion bandwidth over many octaves, the values of which can be comparable to commercial solutions of thicker architecture. Both works can impact positively on the current manufacturing strategies used in the design of thin and efficient sound diffusers.

Finally, the analytical and numerical validation of a framework for reducing complex geometries in 3D FDTD schemes using equivalent RLC circuit filters can be of great value in the field of wave physics as many other studies involving highly locally-resonant metamaterial strategies over large contextual scenarios can greatly benefit from such strategy, e.g., underwater or seismic contexts.

*Audtiorium Acoustics*

In the narrower field of auditorium acoustics, comprising the acoustical design of auditoria based on objective and subjective criteria, the above-mentioned contributions can significantly impact the way critical listening environments are designed or refurbished. One example illustrated in this work is that of orchestra pits, which posses strong practical constraints regarding the range of acoustical solutions that can be provided to enhance musical conditions, particularly so when considering sound diffusion. The great flexibility and sound diffusion efficiency of metadiffusers could lead to a successful solution in such case, with very limited drawbacks and potentially widely endorsed in the world-wide operatic environment.

*General*

In general, the research presented in this work can help underpin the democratization of state-of-the-art ultra-thin sound diffusers in a similar way the research on the now famous Schröeder diffusers in the 80-90's made it one of the most predominant type of acoustic diffusers for industrial and civil applications.

*Sound Diffusion & Acoustic Metamaterials*

Due to the sensitivity of the data collected in practical measurements, experimental data can be subject to artefacts compared to perfectly controlled situations such as theoretical and numerical predictions (e.g., aberrant reflections in an anechoic chamber). Therefore measurements of sound scattering require great care in the experimental apparatus and signal chain employed. A possible alternative experimental framework for validating the scattering of a surface could take the form of an impedance mapping over said surface using a P/U sensor. Such work could take inspiration from *Kleiner et al.* **??** which used a very similar approach (near-field acoustic holography) for measuring directional scattering coefficients. Such strategy is less susceptible to spurious reflections contaminating a collected impulse response, and thanks to the relation between surface impedance distribution and scattering it can provide an indirect way of validation. Also, this method is less reliant on the need of a perfectly anechoic environment as it measures the acoustic impedance very close to the measured object.

On the topic of acoustic metamaterials, metadiffusers can be further optimized in order to strike a compromise between sound diffusion and sound absorption so as to provide with custom hybrid acoustic treatments. Also, other optimization paradigms of similar structures to metadiffusers taking into account mechanically variable geometries can be designed, which could result in dynamic resonating structures varying in function of the configuration that is required. Resonating cavities could also be filled with porous materials (e.g., foam, aerogel) or membranes for added flexibility in the control of sound.

*Diffuse Sound Fields Evaluation*

Concerning the evaluation of diffuse sound fields, further work regarding standardization of quantifiable parameters for determining the amount of sound dif-

fusion (i.e., diffuseness) at a position could be undertaken. Due to the increasing availability of 3D spatial impulse response technology for both the industry and civilians, such standardized guidance on how to manipulate the raw spatial data (e.g., spatial autocorrelation, standard deviation, etc.) and on how to evaluate the characteristics of the diffuse field (e.g., early, late, early-to-late) is likely to be strongly required.

## 7.3 FINAL THOUGHTS

The research undertaken in this work covers different scientific areas, spanning from wave physics and acoustic metamaterials to subjective evaluations of virtual audio scenarios obtained by state-of-the-art room acoustics numerical simulations. Over these last 3 years and a half, such research has allowed the author to communicate with a great number of scientists from all these various disciplines. It has been a very instructive journey filled with support and genuine interactions, which sparked an even greater thirst for knowledge and motivation in conducting scientific research.

"Somewhere, something incredible is waiting to be known."

— Carl Sagan

# BIBLIOGRAPHY

[1]   L. L. Beranek. *Concert & Opera Halls: How They Sound*. 1996, pp. 2637–2637. DOI: 10.1121/1.414882.

[2]   M. Barron. *Auditorium Acoustics and Architectural Design*. Routledge, 2009.

[3]   R.K. Mackenzie. "The acoustic design of partially enclosed orchestra pits". In: *Proceedings of the Institute of Acoustics, Reproduced Sound, Autumn Conference* (1985), pp. 237–243.

[4]   C.N. Blair. "Listening in the pit". In: *Proceedings of the 16th International Congress on Acoustics, Seattle* 1 (1998), pp. 339–340.

[5]   J. O'Keefe. "Acoustic Conditions in and Propagating from Orchestra Pits". In: *Canadian Acoustics* 22.3 (1994), pp. 55–56.

[6]   A. C. Gade, J. Kapenekas, J. I. Gustafsson, and B. T. Anderson. "Acoustical Problems in Orchestra Pits; Causes and Possibles Solutions". In: *Proceedings of the 17th International Congress on Sound and Vibration, Rome* (2001).

[7]   *American National Standards Institute, "American national psychoacoustical terminology" S3.20, 1973, American Standards Association.*

[8]   H. Fletcher and W. A. Munson. "Loudness, Its Definition, Measurement and Calculation". In: *The Journal of the Acoustical Society of America* 5.2 (1933), pp. 82–108. DOI: 10.1121/1.1915637. eprint: https://doi.org/10.1121/1.1915637. URL: https://doi.org/10.1121/1.1915637.

[9]   S. S. Stevens. "Neural Events and the Psychophysical Law". In: *Science* 170.3962 (1970), pp. 1043–1050. ISSN: 0036-8075. DOI: 10.1126/science.170.3962.1043. eprint: https://science.sciencemag.org/content/170/3962/1043.full.pdf. URL: https://science.sciencemag.org/content/170/3962/1043.

[10]    E Zwicker. "Masking and psychological excitation as consequences of the ear's frequency analysis". In: *Frequency analysis and periodicity detection in hearing* (1970), pp. 376–394.

[11]    J. Roederer. "The Physics and Psychophysics of Music: An Introduction". In: 2007.

[12]    J. Meyer. "Sound fields in orchestra pits". In: *The Journal of the Acoustical Society of America* 103.5 (1998), pp. 2785–2785.

[13]    G.M. Naylor. "Problems and priorities in orchestra pit design". In: *Proceedings of the Institute of Acoustics* 7 (1985), pp. 65–71.

[14]    J Lee, A. Behar, H. Kunov, and W. Wong. "Musicians' noise exposure in orchestra pit". In: *Applied Acoustics* 66 (2005), pp. 919–931.

[15]    Remy Wenmaekers, Constant Hak, and Maarten Hornikx. "How orchestra members influence stage acoustic parameters on five different concert hall stages and orchestra pits". In: *The Journal of the Acoustical Society of America* 140 (Dec. 2016), pp. 4437–4448. DOI: 10.1121/1.4971763.

[16]    Bareld Nicolai, Remy Wenmaekers, Maarten Hornikx, and Armin Kohlrausch. "The influence of stage acoustics on sound exposure of symphony orchestra musicians". PhD thesis. Nov. 2016.

[17]    Julia Doswell Royster, Larry H. Royster, and Mead C. Killion. "Sound exposures and hearing thresholds of symphony orchestra musicians". In: *The Journal of the Acoustical Society of America* 89.6 (1991), pp. 2793–2803. DOI: 10.1121/1.400719. eprint: https://doi.org/10.1121/1.400719. URL: https://doi.org/10.1121/1.400719.

[18]    Jesper Hvass Schmidt, Ellen Raben Pedersen, Peter Møller Juhl, Jakob Christensen-Dalsgaard, Ture Dammann Andersen, Torben Poulsen, and Jesper Bælum. "Sound Exposure of Symphony Orchestra Musicians". In: *The Annals of Occupational Hygiene* 55.8 (2011), pp. 893–905. DOI: 10.1093/annhyg/mer055. eprint: /oup/backfile/content_public/journal/annweh/55/8/10.1093/annhyg/mer055/2/mer055.pdf. URL: http://dx.doi.org/10.1093/annhyg/mer055.

[19]    A C. Gade. "Investigations of musicians' room acoustic conditions in concert halls, Part I: Methods and laboratory experiments". In: *Acta Acustica united with Acustica* 69 (Nov. 1989), pp. 193–203.

[20]    A.C. Gade. "Investigations of musicians' room acoustic conditions in concert halls. II. Field experiments and synthesis of results". In: *Acustica* 69 (Dec. 1989), pp. 249–262.

[21]    R. Wenmaekers, B. Nicolai, M. Hornikx, and A. Kohlrausch. "Why orchestral musicians are bound to wear earplugs: About the ineffectiveness of physical measures to reduce sound exposure". In: *Journal of the Acoustical Society of America* 142.5 (2017). cited By 0, pp. 3154–3164. DOI: 10.1121/ 1.5012689. URL: https://www.scopus.com/inward/record.uri?eid=2- s2.0-85035008790&doi=10.1121%2f1.5012689&partnerID=40&md5= ce2b74490c5a7eda7dbe5f469b9591a7.

[22]    Anders Christian Gade. "Acoustics for Symphony Orchestras; Status after Three Decades of Experimental Research". In: *Building Acoustics* 18.3-4 (2011), pp. 181–206. DOI: 10.1260/1351-010X.18.3-4.181. eprint: https://doi.org/10.1260/1351-010X.18.3-4.181. URL: https: //doi.org/10.1260/1351-010X.18.3-4.181.

[23]    Remy Wenmaekers, bareld nicolai, Maarten Hornikx, and Armin Kohlrausch. "Symphony orchestra musicians: reduction of sound exposure by physical measures". In: vol. 13. EFAS European Federation of Audiology Societies. June 2017.

[24]    T. Hidaka and L. L. Beranek. "Objective and subjective evaluations of twenty-three opera houses in Europe, Japan, and the Americas". In: *The Journal of the Acoustical Society of America* 107.1 (2000), pp. 368–383.

[25]    H. Drotleff, X. Zha, H.V. Fuchs, and M. Leistner. "Acoustic improvements of the working conditions for musicians in orchestra pits". In: *Proceedings CFA/DAGA, Strasbourg* (2004), pp. 525–526.

[26]    T. J. Cox and P. D'antonio. *Acoustic Absorbers and Diffusers: Theory, Design and Application.* Crc Press, 2009.

[27]    P. D'Antonio and T. J. Cox. "Diffusor application in rooms". In: *Applied Acoustics* 60.2 (2000), pp. 113–142.

[28]    T. J. Cox. "Objective and Subjective Evaluation of Reflection and Diffusing Surface in Auditoria". PhD thesis. 1992.

[29]    A. H. Marshall, D. Gottlob, and H. Alrutz. "Acoustical conditions preferred for ensemble". In: *The Journal of the Acoustical Society of America* 64.5 (1978), pp. 1437–1442. DOI: 10.1121/1.382121. eprint: https://doi.org/10.1121/1.382121. URL: https://doi.org/10.1121/1.382121.

[30]    E. L. Harkness. "Performer tuning of stage acoustics". In: *Applied Acoustics* 17.2 (1984), pp. 85–97.

[31]    D. Paoletti, K. Graffy, and L. Tedford. "Some recent experiences with the acoustical design of orchestra pits". In: *The Journal of the Acoustical Society of America* 103.5 (1998), pp. 2824–2824.

[32]    J. J. Dammerud and M. Barron. "Attenuation of direct sound and the contributions of early reflections within symphony orchestras". In: *The Journal of the Acoustical Society of America* 128.4 (2010), pp. 1755–1765.

[33]    Manfred R Schröder. "Diffuse sound reflection by maximum- length sequences". In: *The Journal of the Acoustical Society of America* 57.1 (1975), pp. 149–150.

[34]    Trevor Cox and Peter D'Antonio. "Schroeder diffusers: A review". In: *Building Acoustics* 10.1 (2003), pp. 1–32.

[35]    Trevor J Cox and Peter D'Antonio. "Acoustic phase gratings for reduced specular reflection". In: *Applied Acoustics* 60.2 (2000), pp. 167–186.

[36]    Trevor J Cox and YW Lam. "Prediction and evaluation of the scattering from quadratic residue diffusers". In: *The Journal of the Acoustical Society of America* 95.1 (1994), pp. 297–305.

[37]    Trevor Cox, B.I.L. Dalenback, Peter D'Antonio, J.J. Embrechts, Jin Yong Jeon, E Mommertz, and Michael Vorlaender. "A Tutorial on Scattering and Diffusion Coefficients for Room Acoustic Surfaces". In: *Acta Acustica united with Acustica* 92 (Jan. 2006), pp. 1–15.

[38]  Peter DAntonio. "Planar Binary Amplitude Diffusor". Granted Patent US 5817992 A (United States). Oct. 6, 1998. URL: https://lens.org/109-744-062-388-261.

[39]  A.D. Pierce. *Acoustics: An Introduction to Its Physical Principles and Applications*. McGraw-Hill series in mechanical engineering. McGraw-Hill Book Company, 1981. ISBN: 9780070499614. URL: https://books.google.co.uk/books?id=8IgpAQAAMAAJ.

[40]  R.P. Feynman, R.B. Leighton, and M.L. Sands. *The Feynman Lectures on Physics*. Addison-Wesley world student series. Addison-Wesley Publishing Company, 1963. ISBN: 9780805390490. URL: https://books.google.co.uk/books?id=\_6XvAAAAMAAJ.

[41]  *Fourier Transform*. Wikipedia (online). URL: https://en.wikipedia.org/wiki/Fourier_transform.

[42]  F. V. Hunt. *Origins in Acoustics: The Science of Sound from Antiquity to the Age of Newton*. 1978.

[43]  *Dispersion Relation*. Wikipedia (online). URL: https://en.wikipedia.org/wiki/Dispersion_relation.

[44]  W.C. Elmore, M.A. Heald. *Physics of waves*. Dover, 1969, p. 477.

[45]  *Fundamentals of Physical Acoustics*.

[46]  Michael R Stinson. "The propagation of plane sound waves in narrow and wide circular tubes, and generalization to uniform tubes of arbitrary cross-sectional shape". In: *J. Acoust. Soc. Am.* 89.2 (1991), pp. 550–558.

[47]  C. Zwikker and C.W. Kosten. *Sound Absorbing Materials*. Elsevier Publishing Company, 1949. URL: https://books.google.co.uk/books?id=ezUOnQEACAAJ.

[48]  A. Levis, Y. Y. Schechner, and A. B. Davis. "Multiple-Scattering Microphysics Tomography". In: *2017 IEEE Conference on Computer Vision and Pattern Recognition (CVPR)*. 2017, pp. 5797–5806. DOI: 10.1109/CVPR.2017.614.

[49]   M. Peña, J. Cabrera-Gámez, and A. C. Domínguez-Brito. "Multi-frequency and light-avoiding characteristics of deep acoustic layers in the North Atlantic". In: *Marine Environmental Research* 154 (2020), p. 104842. ISSN: 0141-1136. DOI: https://doi.org/10.1016/j.marenvres.2019.104842. URL: https://www.sciencedirect.com/science/article/pii/S0141113619304623.

[50]   S. Jiménez-Gambín, N. Jiménez, and F. Camarena. "Transcranial Focusing of Ultrasonic Vortices by Acoustic Holograms". In: *Phys. Rev. Applied* 14 (5 2020), p. 054070. DOI: 10.1103/PhysRevApplied.14.054070. URL: https://link.aps.org/doi/10.1103/PhysRevApplied.14.054070.

[51]   O.K. Ersoy. *Wiley Series in Pure and Applied Optics*. John Wiley & Sons, Ltd, 2007, pp. 403–403. ISBN: 9780470085004. DOI: https://doi.org/10.1002/9780470085004.scard. eprint: https://onlinelibrary.wiley.com/doi/pdf/10.1002/9780470085004.scard. URL: https://onlinelibrary.wiley.com/doi/abs/10.1002/9780470085004.scard.

[52]   K. Iizuka. *Wiley Series in Pure and Applied Optics*. John Wiley & Sons, Ltd, 2002. ISBN: 9780471221371. DOI: https://doi.org/10.1002/0471221376. eprint: https://onlinelibrary.wiley.com/doi/abs/10.1002/0471221376. URL: https://onlinelibrary.wiley.com/doi/abs/10.1002/0471221376.

[53]   Trevor Cox and Peter D'Antonio. "Schroeder Diffusers: A Review". In: *Building Acoustics* 10.1 (2003), pp. 1–32. DOI: 10.1260/135101003765184799. eprint: https://doi.org/10.1260/135101003765184799. URL: https://doi.org/10.1260/135101003765184799.

[54]   Tristan J. Hargreaves, Trevor Cox, Yiu Lam, and Peter D'Antonio. "Surface diffusion coefficients for room acoustics: Free-field measures". In: *The Journal of the Acoustical Society of America* 108 (Nov. 2000), pp. 1710–20. DOI: 10.1121/1.1310192.

[55]   Trevor Cox, William Davies, and Yiu Lam. "The Sensitivity of Listeners to Early Sound Field Changes in Auditoria". In: *Acta Acustica united with Acustica* 79 (July 1993), pp. 27–41.

[56]   *Subjective and objective evaluation of the scattered sound in a 1: 10 scale model hall.* 2005.

[57]   Trevor Cox. "The Optimization of Profiled Diffusers". In: *Journal of The Acoustical Society of America - J ACOUST SOC AMER* 97 (May 1995), pp. 2928–2936. DOI: 10.1121/1.412972.

[58]   T Wu, Trevor Cox, and Yiu Lam. "From a profiled diffuser to an optimized absorber". In: *The Journal of the Acoustical Society of America* 108 (Sept. 2000), pp. 643–50. DOI: 10.1121/1.429596.

[59]   Richard J Hughes, Jamie AS Angus, Trevor J Cox, Olga Umnova, Gillian A Gehring, Mark Pogson, and David M Whittaker. "Volumetric diffusers: Pseudorandom cylinder arrays on a periodic lattice". In: *The Journal of the Acoustical Society of America* 128.5 (2010), pp. 2847–2856.

[60]   *Manfred R. Schröeder Bibliography.* Wikipedia (online). URL: https://en.wikipedia.org/wiki/Manfred_R._Schroeder.

[61]   ISO 17497–1:2012. *Acoustics – Sound-scattering properties of surfaces – Part 1: Measurement of the random-incidence scattering coefficient in a reverberation room.* ISO Standard. Geneva, Switzerland: International Organization for Standardization, 2012. URL: https://www.iso.org/standard/31397.html.

[62]   International Standard Organization. *ISO 17497-2:2012 Acoustics – Sound-scattering properties of surfaces – Part 2: Measurement of the directional diffusion coefficient in a free field.* 2012.

[63]   E. Mommertz and M. Vorlander. *Measurement of scattering coefficients of surfaces in the reverberation chamber and in the free field.* Proc. 15th Internat. Congress on Acoustics. 1995.

[64]   AES. *AES-4id-2001 (s2008) AES information document for room acoustics and sound reinforcement systems - Characterization and measurement of surface scattering uniformity.* 2001.

[65] Manfred Schroeder. *Number Theory in Science and Communication: With Applications in Cryptography, Physics, Digital Information, Computing, and Self-Similarity.* 4th. Springer Publishing Company, Incorporated, 1997. ISBN: 3540852972.

[66] D. Chu. "Polyphase codes with good periodic correlation properties (Corresp.)" In: *IEEE Transactions on Information Theory* 18.4 (1972), pp. 531–532. DOI: 10.1109/TIT.1972.1054840.

[67] *The Lean Optimization of Acoustic Diffusers: Design by Artificial Evolution, Time Domain Simulations and Fractals.* Academia (online). URL: https://www.academia.edu/37885028/Acoustic_Diffuser_Optimization_Arqen.

[68] *Barker Code.* Wikipedia (online). URL: https://en.wikipedia.org/wiki/Barker_code.

[69] A. C. Gade and B. Mortensen. "Compromises in orchestra pit design: A ten-year trench war in The Royal Theatre, Copenhagen". In: *Journal of the Acoustical Society of America* 103.5 (1998), pp. 2786–2786. ISSN: 0001-4966. DOI: 10.1121/1.422278.

[70] Ian O'Brien, Wayne Wilson, and Andrew Bradley. "Nature of orchestral noise". In: *The Journal of the Acoustical Society of America* 124 (Sept. 2008), pp. 926–39. DOI: 10.1121/1.2940589.

[71] Jörg Hunecke. "Schallstreuung und Schallabsorption von Oberfl: ahen aus mikroperforierten Streifen". PhD thesis. University of Stuttgart, 1997.

[72] Guancong Ma and Ping Sheng. "Acoustic metamaterials: From local resonances to broad horizons". In: *Science Advances* 2 (Feb. 2016), e1501595. DOI: 10.1126/sciadv.1501595.

[73] Huang, Cheng-Ping and Chan, Che-Ting. "Deep subwavelength Fabry-Perot resonances". In: *EPJ Applied Metamaterials* 1 (2014), p. 2. DOI: 10.1051/epjam/2014003. URL: https://doi.org/10.1051/epjam/2014003.

[74] Yifan Zhu, Xudong Fan, Bin Liang, Jianchun Cheng, and Yun Jing. "Ultra-thin acoustic metasurface-based Schroeder diffuser". In: *Physical Review X* 7.2 (2017), p. 021034.

[75] N. Jimenez, T. J. Cox, V. Romero-Garcia, and J-P. Groby. "Metadiffusers: Deep-subwavelength sound diffusers". In: *Scientific Reports* 7 (2017). ISSN: 2045-2322. DOI: 10.1038/s41598-017-05710-5.

[76] Noé Jiménez, Weichun Huang, V Romero-García, Vincent Pagneux, and Jean-Philippe Groby. "Ultra-thin metamaterial for perfect and omnidirectional sound absorption". In: (June 2016).

[77] Noé Jiménez, V Romero-García, Vincent Pagneux, and Jean-Philippe Groby. "Quasi-perfect absorption by sub-wavelength acoustic panels in transmission using accumulation of resonances due to slow sound". In: *Physical Review B* 95 (Oct. 2016). DOI: 10.1103/PhysRevB.95.014205.

[78] Noé Jiménez, V Romero-García, Vincent Pagneux, and Jean-Philippe Groby. "Rainbow-trapping absorbers for transmission problems: Broadband and perfect sound absorbing panels". In: *Scientific Reports* (July 2017).

[79] E. Ballestero, N. Jiménez, J.-P. Groby, H. Aygun, S. Dance, and V. Romero-García. "Metadiffusers for quasi-perfect and broadband sound diffusion". In: *Applied Physics Letters* 119.4 (2021), p. 044101. DOI: 10.1063/5.0053413. eprint: https://doi.org/10.1063/5.0053413. URL: https://doi.org/10.1063/5.0053413.

[80] J-P. Groby N. Jiménez and V. Romero-García. *Sound Waves in Metamaterials and Porous Media. Chapter 1. The transfer matrix method in acoustics: Modelling one-dimensional acoustic systems, phononic crystals and acoustic metamaterials.* Springer, 2021.

[81] Eli Yablonovitch. "Inhibited spontaneous emission in solid-state physics and electronics". In: *Physical review letters* 58.20 (1987), p. 2059.

[82] Eli Yablonovitch and TJ Gmitter. "Photonic band structure: The face-centered-cubic case". In: *Physical Review Letters* 63.18 (1989), p. 1950.

[83] Michael Sigalas and Eleftherios N Economou. "Band structure of elastic waves in two dimensional systems". In: *Solid state communications* 86.3 (1993), pp. 141–143.

[84] Nobumasa Sugimoto and T. Horioka. "Dispersion characteristics of sound waves in a tunnel with an array of Helmholtz resonators". In: *Journal of the Acoustical Society of America* 97 (1995), pp. 1446–1459.

[85] C. E. Bradley. "Time harmonic acoustic Bloch wave propagation in periodic waveguides. Part I. Theory". In: *The Journal of the Acoustical Society of America* 96.3 (1994), pp. 1844–1853. DOI: 10.1121/1.410196. URL: https://doi.org/10.1121/1.410196.

[86] Rosa Martínez-Sala, J Sancho, Juan V Sánchez, Vicente Gómez, Jaime Llinares, and Francisco Meseguer. "Sound attenuation by sculpture". In: *nature* 378.6554 (1995), pp. 241–241.

[87] Yabin Jin, Daniel Torrent, and B. Djafari-Rouhani. "Robustness of conventional and topologically protected edge states in phononic crystal plates". In: *Physical Review B* 98 (Aug. 2018), p. 054307. DOI: 10.1103/physrevb.98.054307.

[88] unfei Li, Chen Shen, Ana Diaz Rubio, Sergei Tretyakov, and Steven Cummer. "Systematic design and experimental demonstration of bianisotropic metasurfaces for scattering-free manipulation of acoustic wavefronts". English. In: *Nature Communications* 9 (Apr. 2018). ISSN: 2041-1723. DOI: 10.1038/s41467-018-03778-9.

[89] Lucian Zigoneanu, B. Popa, and S. Cummer. "Three-dimensional broadband omnidirectional acoustic ground cloak." In: *Nature materials* 13 4 (2014), pp. 352–5.

[90] Andrea Colombi, Philippe Roux, Marco Miniaci, Richard Craster, Sébastien Guenneau, and Philippe Gueguen. "The role of large scale computing behind the development of seismic (and elastic) metamaterials". In: Aug. 2017, pp. 406–408. DOI: 10.1109/MetaMaterials.2017.8107829.

[91] L. Hoddeson. Cambridge University Press, 1997. DOI: https://doi.org/10.1017/CBO9780511471094.

[92] *Bloch Theorem.* Wikipedia (online). URL: https://en.wikipedia.org/wiki/Bloch%27s_theorem.

[93] *Braggs Law*. Wikipedia (online). URL: https://en.wikipedia.org/wiki/Bragg%27s_law.

[94] JF Bonnans, Jean Charles Gilbert, C Lemaréchal, and Claudia Sagastizabal. *Numerical Optimization – Theoretical and Practical Aspects*. Jan. 2006.

[95] *Constrained Non-Linear Optimization*. Wikipedia (online). URL: https://en.wikipedia.org/wiki/Nonlinear_programming.

[96] *Constrained Non-Linear Optimization Function (fmincon)*. Matlab (online). URL: https://uk.mathworks.com/help/optim/ug/fmincon.html.

[97] V Romero-García, G Theocharis, Olivier Richoux, Aurelien Merkel, Vincent TOURNAT, and Vincent Pagneux. "Perfect and broadband acoustic absorption by critical coupling". In: *Scientific Reports* 6 (Jan. 2016), p. 19519. DOI: 10.1038/srep19519.

[98] Jessica R Piper, Victor Liu, and Shanhui Fan. "Total absorption by degenerate critical coupling". In: *Appl. Phys. Lett.* 104.25 (2014), p. 251110.

[99] V Romero-García, Noé Jiménez, Vincent Pagneux, and Jean-Philippe Groby. "Perfect and broadband acoustic absorption in deep sub-wavelength structures for the reflection and transmission problems". In: *The Journal of the Acoustical Society of America* 141 (May 2017), pp. 3641–3641. DOI: 10.1121/1.4987858.

[100] *COMSOL Multiphysics® v. 5.3, COMSOL AB, Stockholm, Sweden*. Website (online). URL: www.comsol.com.

[101] *Application of Transfer Matrix Method in Acoustics*. COMSOL Conference. Paris, 2010.

[102] *COMSOL Publications, Papers and Presentations*. Website (online). URL: https://www.comsol.com/papers-presentations.

[103] LM Garcia-Raffi, LJ Salmeron-Contreras, I Herrero-Durá, R Picó, J Redondo, VJ Sánchez-Morcillo, K Staliunas, NJE Adkins, A Cebrecos, N Jiménez, et al. "Broadband reduction of the specular reflections by using sonic crystals: A proof of concept for noise mitigation in aerospace applications". In: *Aerospace Science and Technology* 73 (2018), pp. 300–308.

[104]   S. A. Schelkunoff. "The Impedance Concept and Its Application to Problems of Reflection, Refraction, Shielding and Power Absorption". In: *Bell System Technical Journal* 17 (1 Jan. 1938). DOI: 10.1002/j.1538-7305.1938.tb00774.x. URL: http://gen.lib.rus.ec/scimag/index.php?s=10.1002/j.1538-7305.1938.tb00774.x.

[105]   A. Mohsen. "On the impedance boundary condition". In: *Applied Mathematical Modelling* 6 (5 1982). DOI: 10.1016/s0307-904x(82)80109-1. URL: http://gen.lib.rus.ec/scimag/index.php?s=10.1016/s0307-904x(82)80109-1.

[106]   I. D. Mayergoyz and G. Bedrosian. "On finite element implementation of impedance boundary conditions". In: *Journal of Applied Physics* 75 (10 1994). DOI: 10.1063/1.355497. URL: http://gen.lib.rus.ec/scimag/index.php?s=10.1063/1.355497.

[107]   Kyung Suk Oh and J.E. Schutt-Aine. "An efficient implementation of surface impedance boundary conditions for the finite-difference time-domain method". In: *IEEE Transactions on Antennas and Propagation* 43 (7 July 1995). DOI: 10.1109/8.391136. URL: http://gen.lib.rus.ec/scimag/index.php?s=10.1109/8.391136.

[108]   J. Nerg and J. Partanen. "A simplified FEM based calculation model for 3-D induction heating problems using surface impedance formulations". In: *IEEE Transactions on Magnetics* 37 (5 2001). DOI: 10.1109/20.952698. URL: http://gen.lib.rus.ec/scimag/index.php?s=10.1109/20.952698.

[109]   A.E. Karbowiak. "The concept of heterogeneous surface impedance and its application to cylindrical cavity resonators". In: *Proceedings of the IEE Part C Monographs* 105 (7 1958). DOI: 10.1049/pi-c.1958.0003. URL: http://gen.lib.rus.ec/scimag/index.php?s=10.1049/pi-c.1958.0003.

[110]   Ian Drumm. "A Hybrid Finite Element / Finite Difference Time Domain Technique for Modelling the Acoustics of Surfaces Within a Medium". In: *Acta Acustica united with Acustica* 93 (Sept. 2007), pp. 804–809.

[111] Jiangfeng Zhou, Thomas Koschny, and Costas M. Soukoulis. "An efficient way to reduce losses of left-handed metamaterials". In: *Optics Express* 16 (15 2008). DOI: 10.1364/OE.16.011147. URL: http://gen.lib.rus.ec/scimag/index.php?s=10.1364/OE.16.011147.

[112] Matteo Alessandro Francavilla, Enrica Martini, Stefano Maci, and Giuseppe Vecchi. "On the Numerical Simulation of Metasurfaces With Impedance Boundary Condition Integral Equations". In: *IEEE Transactions on Antennas and Propagation* 63 (5 May 2015). DOI: 10.1109/tap.2015.2407372. URL: http://gen.lib.rus.ec/scimag/index.php?s=10.1109/tap.2015.2407372.

[113] Atsushi Sakurai, Bo Zhao, and Zhuomin M. Zhang. "Resonant frequency and bandwidth of metamaterial emitters and absorbers predicted by an RLC circuit model". In: *Journal of Quantitative Spectroscopy and Radiative Transfer* 149 (Dec. 2014). DOI: 10.1016/j.jqsrt.2014.07.024. URL: http://gen.lib.rus.ec/scimag/index.php?s=10.1016/j.jqsrt.2014.07.024.

[114] S. Bilbao, B. Hamilton, J. Botts, and L. Savioja. "Finite Volume Time Domain Room Acoustics Simulation under General Impedance Boundary Conditions". In: 24.1 (2016), pp. 161–173.

[115] K. Kowalczyk. *Boundary and medium modelling using compact finite difference schemes in simulations of room acoustics for audio and architectural design applications*. Dr. Hut, 2011. ISBN: 9783843902731. URL: https://books.google.fr/books?id=RFkgMwEACAAJ.

[116] Brian Hamilton. "Finite Difference and Finite Volume Methods for Wave-based Modelling of Room Acoustics". PhD thesis. Nov. 2016. DOI: 10.13140/RG.2.2.31081.70240.

[117] Jonathan Sheaffer and Bruno Fazenda. "WaveCloud: an Open Source Room Acoustics Simulator using the Finite Difference Time Domain Method". In: Sept. 2014.

[118]    Philip Robinson, Samuel Siltanen, Tapio Lokki, and Lauri Savioja. "Concert hall geometry optimization with parametric modeling tools and wave-based acoustic simulations". English. In: *JOURNAL OF BUILDING ACOUSTICS* 21.1 (2014). VK: Lokki, Savioja, pp. 55–64. ISSN: 1351-010X. DOI: 10.1260/1351-010X.21.1.55.

[119]    Stefan Bilbao and Brian Hamilton. "Passive volumetric time domain simulation for room acoustics applications". In: *The Journal of the Acoustical Society of America* 145.4 (2019), pp. 2613–2624.

[120]    O Chiba, T Kashiwa, H Shimoda, S Kagami, and I Fukai. "Analysis of sound fields in three dimensional space by the time-dependent finite-difference method based on the leap frog algorithm". In: *Journal Acoustical Society of Japan (J)* 49 (1993), pp. 551–562.

[121]    D. Botteldooren. "Finite-difference time-domain simulation of low-frequency room acoustic problems". In: 98 (1995), pp. 3302–3308.

[122]    K. Kowalczyk and M. van Walstijn. "Formulation of locally reacting surfaces in FDTD/K-DWM modelling of acoustic spaces". In: 94.6 (2008), pp. 891–906.

[123]    Pauli Virtanen et al. "SciPy 1.0: Fundamental Algorithms for Scientific Computing in Python". In: *Nature Methods* 17 (2020), pp. 261–272. DOI: https://doi.org/10.1038/s41592-019-0686-2.

[124]    B. Hamilton, C. J. Webb, N. D. Fletcher, and S. Bilbao. "Finite difference room acoustics simulation with general impedance boundaries and viscothermal losses in air: Parallel implementation on multiple GPUs". In: Buenos Aires, Argentina, Sept. 2016.

[125]    Sakari Tervo, Jukka Pätynen, Antti Kuusinen, and Tapio Lokki. "Spatial Decomposition Method for Room Impulse Responses". In: *Journal of the Audio Engineering Society* 61 (Jan. 2013), pp. 16–27.

[126]    S. Tervo, J. Pätynen, and T. Lokki. "Spatial Decomposition Method for Room Impulse Responses". In: *J. Audio Eng. Soc* 61.1 (2013), pp. 1–13.

[127] A. O'Donovan, R. Duraiswami, and D. Zotkin. "Imaging concert hall acoustics using visual and audio cameras". In: *IEEE International Conference on Acoustics, Speech and Signal Processing, 2008.* 2008, pp. 5284 –5287.

[128] D. Khaykin and B. Rafaely. "Acoustic analysis by spherical microphone array processing of room impulse responses". In: *J. Acoust. Soc. Am.* 132.1 (2012), pp. 261–270. DOI: 10.1121/1.4726012. URL: http://link.aip.org/link/?JAS/132/261/1.

[129] *Virtual Acoustics Team at Aalto University, SDM Toolbox v1.0.* https://research.cs.aalto.fi/acoustics/virtual-acoustics/blog/282-sdm-toolbox.html. Accessed: 10.05.2021.

[130] Alban Bassuet. "New Acoustical Parameters and Visualization Techniques to Analyze the Spatial Distribution of Sound in Music Spaces". In: *journal of building acoustics* 18 (Apr. 2011). DOI: 10.1260/1351-010X.18.3-4.329.

[131] L. Cremer, H. A. Müller, and T. Northwood. *Principles and applications of room acoustics.* 2016.

[132] A. Abdou and R. W. Guy. "Spatial information of sound fields for room-acoustics evaluation and diagnosis". In: *The Journal of the Acoustical Society of America* 100.5 (1996), pp. 3215–3226. DOI: 10.1121/1.417205. eprint: https://doi.org/10.1121/1.417205. URL: https://doi.org/10.1121/1.417205.

[133] H. Kuttruff. *Room Acoustics, Fifth Edition.* Taylor & Francis, 2009. ISBN: 9780203876374. URL: https://books.google.fr/books?id=X4BJ9ImKYOsC.

[134] Nicolas Epain and Craig T. Jin. "Spherical Harmonic Signal Covariance and Sound Field Diffuseness". In: *IEEE/ACM Transactions on Audio, Speech, and Language Processing* 24 (10 Oct. 2016). DOI: 10.1109/taslp.2016.2585862. URL: http://gen.lib.rus.ec/scimag/index.php?s=10.1109/taslp.2016.2585862.

[135] Mélanie Nolan, Marco Berzborn, and Efren Fernandez-Grande. "Isotropy in decaying reverberant sound fields". In: *The Journal of the Acoustical*

*Society of America* 148 (2 Aug. 2020). DOI: 10.1121/10.0001769. URL: http://gen.lib.rus.ec/scimag/index.php?s=10.1121/10.0001769.

[136] Benoit Alary, Pierre Massé, Vesa Välimäki, and Markus Noisternig. "Assessing the anisotropic features of spatial impulse responses". In: *EAA Spatial Audio Signal Processing Symposium*. Paris, France, Sept. 2019, pp. 43–48. DOI: 10.25836/sasp.2019.32. URL: https://hal.archives-ouvertes.fr/hal-02275194.

[137] Peter D'Antonio and Trevor J Cox. "Diffusor application in rooms". In: *Applied Acoustics* 60.2 (2000), pp. 113 –142. ISSN: 0003-682X. DOI: https://doi.org/10.1016/S0003-682X(99)00054-7. URL: http://www.sciencedirect.com/science/article/pii/S0003682X99000547.

[138] N. Jiménez, W. Huang, V. Romero-García, V. Pagneux, and J.-P. Groby. "Ultra-thin metamaterial for perfect and quasi-omnidirectional sound absorption". In: *Applied Physics Letters* 109.12 (2016), p. 121902. DOI: 10.1063/1.4962328. eprint: https://doi.org/10.1063/1.4962328. URL: https://doi.org/10.1063/1.4962328.

<div style="text-align: right;">

# A

</div>

## DETAILS ON FLUID VISCOSITY & HEAT CONDUCTION

---

Many dissipative effects are responsible for dampening the energy waves convey through different fluid media, e.g., fluid viscosity, heat conduction and molecular relaxation. Out of the three, the latter will have the least impact (if any) on this work and will be briefly mentioned. The two others, however, are quite critical for explaining the nature of certain mechanisms introduced later on.

Molecular relaxation involves the return of a perturbed system into equilibrium. One of the assumptions made heretofore has been that the considered fluid was in local thermodynamic equilibrium. That means that an equation of state such as $P = P(\rho, T)$ is used, where the pressure at any given time and position in the fluid only depends on the local, instantaneous values of density and temperature, disregarding the rate at which these vary. However, when the fluid is being composed of different constituents, say molecules A and B in different proportions, there is a rate dependence between the variation of the quantity ($\rho$ or $T$) and the thermodynamic equilibrium state that is being disrupted by the compressions or rarefactions left after a disturbance. When the equilibrium is disturbed, the vibration modes acted upon the molecules by the energy of the wave require different relaxation times to readjust themselves to new equilibrium values. Such is the case for the air that permeates the atmosphere which is mostly composed of dioxygen ($O_2$) and nitrogen ($N_2$) molecules, forming approximatively 99% of Earth's atmospheric composition (78% $N_2$ + 21% $O_2$). The relaxation times of diogygen vibration ($\approx 10^{-5}s$) and nitrogen vibration ($\approx 10^{-3}s$) cause the transformation of mechanical energy into heat, making them quite important for determining sound absorption in air at audio and low ultrasonic frequencies. Yet, the amount of sound absorption generated that way can be considered negligible with respect to other sound absorption mechanisms, such as porous absorption or thermoviscous boundary layer absorption.

FLUID VISCOSITY & DISPERSION RELATION

Whereas molecular relaxation is predominant in relatively low frequencies, dissipation at higher frequencies mostly comes from the thermal and viscous properties of the fluid. Regarding viscous processes, these depict the resistance a travelling wave can encounter in a medium due to frictional forces arising either within the medium or at the adjacency of boundaries. Viscous fluids are said to be *viscid,* in opposition to *inviscid* fluids with no stress resistance or viscosity, such as the one that has been assumed so far in this chapter. In order to take viscous processes into account in a fluid, the linearised conservation equations need to be rewritten, where the continuity and state equations remain the same but the momentum equation now includes viscous parameters, such as:

$$\text{Continuity}: \quad \frac{\partial \delta \rho}{\partial t} + \frac{\partial}{\partial x}(\rho_0 v) = 0, \tag{A.1}$$

$$\text{Momentum}: \quad \rho_0 \frac{\partial v}{\partial t} + \frac{\partial p}{\partial x} = (\lambda + 2\mu)\frac{\partial^2 v}{\partial x^2}, \tag{A.2}$$

$$\text{State}: \quad p = c_0^2 \delta \rho, \tag{A.3}$$

where $\lambda$ and $\mu$ are the dilatation and shear viscosity coefficients, respectively. Eq. A.1 and A.3 remain the same as those for a lossless fluid due to the small signal approximation. This can seem strange as entropy is not constant for fluid in motion in a viscous medium but the entropy variation is, however, described by a second order non-linear term in the resulting energy equation and since all non-linear terms become negligible in small signal approximations, the latter is here ignored.

Attention can now be given to the viscous momentum equation. For simplicity, it is assumed here that the flow in the fluid goes along one dimension (plane wave propagation) and that it is irrotational, i.e., that the vorticity of the particle velocity close to the duct boundaries is zero. As a result, the velocity can simply be expressed as a gradient of a scalar field. In contrast, rotational flows become important when considering flow very close to boundaries – where fluid shear and vorticity become significant – or with non-uniform flow, and can lead to more complex mathematical developments.

The dilatation coefficient, $\lambda$, used in the right term of Eq. A.2 can be very difficult to measure. This issue can be bypassed through the use of Stoke's assumption, in that $\lambda$ should be equal to $-\frac{2}{3}\mu$, which holds true for very simple fluids such as noble and monoatomic gases. For fluids that do not follow Stoke's assumption, the dilation coefficient can be extended to $\lambda = -\frac{2}{3}\mu + \mu_B$, where $\mu_B$ is called the bulk viscosity coefficient. The sum $\lambda + 2\mu$ thus becomes

$$\lambda + 2\mu = \frac{4}{3}\mu + \mu_B = \mu\tilde{V}, \tag{A.4}$$

where $\tilde{V} = \frac{4}{3} + \frac{\mu_B}{\mu}$ is the viscosity number. Although no significant ease of measurement has been added this way, this process allows to adjust the expression of viscosity for non-ideal gases. Eq. A.2 can therefore be rewritten as follows:

$$\rho_0 \frac{\partial v}{\partial t} + \frac{\partial p}{\partial x} = \mu\tilde{V}\frac{\partial^2 v}{\partial x^2} \tag{A.5}$$

The equations of motion can now be combined to form a viscous wave equation, where $\delta_\rho$ is eliminated between Eq. A.1 and Eq. A.3, and $p$ is taken out from the resultant expression, yielding

$$\frac{\nu\tilde{V}}{c_0^2}\frac{\partial^2}{\partial x^2}\frac{\partial}{\partial t}v + \frac{\partial^2 v}{\partial x^2} - \frac{1}{c_0^2}\frac{\partial^2 v}{\partial t^2} = 0, \tag{A.6}$$

where $\nu = \mu/\rho_0$ is the kinematic viscosity coefficient.

The absorption and dispersion properties can be found by substituting a time-harmonic wave travelling solution into the previous wave equation. The resulting dispersion relation is

$$\frac{\omega^2}{c_0^2} = (1 + i\frac{\omega\nu\tilde{V}}{c_0^2})k^2, \tag{A.7}$$

with the wavenumber $k$ thus defined as

$$k = \pm\frac{\omega/c_0}{\sqrt{1 + i\tilde{V}\delta_v}}, \tag{A.8}$$

where $\delta_v = \omega\nu/c_0^2$ is the dimensionless viscosity coefficient. The plus or minus sign in Eq. A.8 applies to outgoing or incoming waves, respectively. In order to find the absorption and phase speed of the medium due to viscous effects, $k$ must be split into real and imaginary parts. However, the denominator needs to be further broken down in order to better dissociate one part from the other. In order

to accomplish such endeavour, one must consider that $\delta_v$ is ordinarily very, very small, even for very high ultrasonic frequencies, e.g., $\delta_v^{air} \approx 8 \times 10^{-10} f$ where $f$ is the frequency in Hertz. Consequently, a simple second order binomial expansion of $(1 + i\widetilde{V}\delta_v)^{\frac{1}{2}}$ in Eq. A.8 can be considered sufficient for separating the real and imaginary parts, yielding (in the case of a outcoming wave)

$$k \doteq \frac{\omega}{c_0(1 - i\widetilde{V}\delta_v/2)} = \frac{\omega}{c_0} - i\frac{\widetilde{V}\delta_v\omega}{2c_0}. \tag{A.9}$$

With the relation stated in Eq. 2.22, the absorption due to viscosity, $\alpha_v$, can be written as

$$\alpha_v = \frac{\widetilde{V}\nu\omega^2}{2c_0^3}, \tag{A.10}$$

whereas the phase speed of sound is simply

$$c_{p,v} = c_0. \tag{A.11}$$

Therefore, in a viscous fluid, sound seems to propagate without dispersion but is attenuated. However, if the third term of the binomial expansion was taken into account, the phase speed of sound would change to

$$c_{p,v} = \frac{c_0}{1 - \frac{3}{8}\widetilde{V}^2\delta_v^2}, \tag{A.12}$$

which shows that, in reality, the phase velocity does actually depend on frequency, but is generally considered too weak due to the smallness of $\delta_v$.

## HEAT CONDUCTION & DISPERSION RELATION

In the previous example, sound propagation was assumed to be adiabatic, meaning that the compressions and rarefactions in the fluid do not involve thermal transfer, or heat flow. However, all media conduct heat to some extent, as the local condensations or expansions of the air particles generate higher or lower molecular collision rates. Therefore, compression zones are generally a little hotter whereas rarefaction zones are a little colder. In a context of heat conduction, where a medium tries to establish a temperature equilibrium between hot and cold bodies, these temperature variations are likely to give rise to a transfer of heat. Consequently, this heat flow reduces the amount of energy available for the sound

wave to travel and thus represents a loss of acoustic energy.

In order to account for heat flow for a sound wave propagating in a fluid, the conservation equations need to be rewritten. An inviscid fluid is here assumed, where a combined case of thermal conduction in an viscous fluid will later be made. For simplicity and ease of read, the derivation process needed to achieve the final form of the energy equation will here be neglected. Thus, the following energy equation can be stated for an ideal gas:

$$\frac{\partial}{\partial t}(p - c_0^2 \delta\rho) = \frac{\vartheta}{\rho_0 C_v} \frac{\partial^2}{\partial x^2}\left(p - \frac{c_0^2}{\gamma}\delta\rho\right), \tag{A.13}$$

where $\vartheta$ is the heat conduction coefficient, $\gamma = C_p/C_v$ is the ratio of specific heats, $C_p$ is the specific heat at constant pressure, and $C_v$ the specific heat at constant volume. Although derived for an ideal gas, holding to the ideal gas law equation of state $PV = nRT$, this equation can also be valid for an inert fluid of arbitrary equation of state. Combining the latter with the equation of continuity in Eq. A.1 and the linear momentum equation for an inviscid fluid in Eq. 2.5 results in the following thermally conducting wave equation:

$$\frac{\vartheta}{\rho_0 C_p} \frac{\partial^2}{\partial x^2}\left[\frac{\partial^2 v}{\partial x^2} - \frac{\gamma}{c_0^2}\frac{\partial^2 v}{\partial t^2}\right] - \frac{\partial}{\partial t}\left[\frac{\partial^2 v}{\partial x^2} - \frac{1}{c_0^2}\frac{\partial^2 v}{\partial t^2}\right] = 0. \tag{A.14}$$

It can be observed that the first bracket term is highly dependent of the magnitude of the heat conduction coefficient $\vartheta$. For further clarity in the equations to come, the first factor of the equation is reduced to a dimensionless coefficient, thus taking dimensionless time and space variables $t^* = \omega t$ and $x^* = \omega x/c_0$, respectively. This results in the dimensionless thermal conduction coefficient in front of the first bracket term,

$$\delta_{th} = \frac{\vartheta\omega}{\rho_0 C_p c_0}, \tag{A.15}$$

which plays an analogous role to the viscosity coefficient, $\delta_v$, previously mentioned, and has similarly very small values, e.g., $\delta_{th}^{air} \approx 1 \times 10^{-9} f$.

The dispersion relation for a heat-conducting fluid can be found by substituting a time-harmonic solution into Eq. A.14, leading to

$$i\delta_{th}K^4 - (1 + i\delta_{th}\gamma)K^2 + 1 = 0, \tag{A.16}$$

where $K = kc_0/\omega$ is the dimensionless wavenumber. The resulting quartic equation has two roots, $K_1$ and $K_2$, where both have positive and negative roots accounting for outgoing and incoming waves. $K_1$ root is associated with ordinary sound waves whereas $K_2$ describes thermal waves which are wavelike solutions for heat flow. The latter type of waves are usually quite insignificant at ordinary frequencies in ordinary fluids, and will be ignored. Focusing on an outgoing ordinary sound wave, $K_1^+$ can be expressed as

$$K_1^+ = \sqrt{\frac{(1 + i\gamma\delta_{th}) - \sqrt{(1 + i\gamma\delta_{th})^2 - 4\delta_{th}}}{i2\delta_{th}}}. \tag{A.17}$$

For very small values of $\delta_{th}$ or for low frequencies, the expression above can be be expanded into

$$K_1^+ = 1 - i\frac{1}{2}(\gamma - 1)\delta_{th} + \mathcal{O}(\delta_{th}^2), \tag{A.18}$$

where $\mathcal{O}(\delta_{th}^2)$ means "terms of order $\delta_{th}^2$ and higher". If those high order terms are dropped, due to the smallness of $\delta_{th}$, then the expression of the wavenumber becomes

$$k_1^+ = \frac{\omega}{c_0} - i\frac{\gamma - 1}{\mathrm{Pr}}\frac{\omega^2\nu}{2c_0^3}, \tag{A.19}$$

where $\mathrm{Pr} = \mu C_p/\kappa$ is the dimensionless Prandtl number used to characterize the importance of viscosity with respect to heat conduction, i.e. $\delta_{th} = \delta_v/\mathrm{Pr}$.

Following a similar analysis to viscosity, the phase speed of sound in a thermally conducting fluid is $c_{p,th} = c_0$ and the absorption equates to the imaginary part of the said wavenumber. For most gases, $\mathrm{Pr}$, $\widetilde{V}$ and $\gamma - 1$ are almost of order of unity, making the absorption due to heat conduction and viscosity comparable. For most liquids, where $\mathrm{Pr}$ is large and $\gamma$ close to unity, the absorption due to heat conduction is generally much less important than viscous absorption.

## FLUID VISCOSITY + HEAT CONDUCTION & DISPERSION RELATION

Now that the mechanisms of fluid viscosity and heat conduction have been separately described, a case can be made for their simultaneous combination. In such case, the wave equation for a viscothermal fluid can be obtained by combining

the continuity and momentum equations of a viscous fluid (Eq. A.1 and A.2) with the energy equation of a thermally conducting fluid (Eq. A.13), resulting in

$$\frac{\gamma \nu^2 \widetilde{V}}{\mathrm{Pr} c_0^2} \left( \frac{\partial^4}{\partial x^4} \frac{\partial}{\partial t} \upsilon \right) + \nu \frac{\partial^2}{\partial x^2} \left[ \frac{\partial^2 \upsilon / \partial x^2}{\mathrm{Pr}} - \left( \frac{\widetilde{V} + \gamma}{\mathrm{Pr}} \right) \frac{\partial^2 \upsilon / \partial t^2}{c_0^2} \right] - \left[ \frac{\partial^2 \upsilon}{\partial x^2} - \frac{\partial^2 \upsilon / \partial t^2}{c_0^2} \right] = 0. \tag{A.20}$$

The $\nu^2/\mathrm{Pr}$ factor of the first term of the equation implies that the relative order of this term is of $\delta_v \delta_{th}$. Additionally, the factor $\nu$ in front of the first square bracket term implies that the terms inside the bracket are of relative order $\delta_v$ or $\delta_{th}$. The remaining bracket term can be considered of relative order of unity due to the absence of any coefficient. Therefore, the above equation can be physically interpreted as follows: the first term represents the interaction of viscous and thermal effects, while the first bracketed pair of terms represent their superposition. Since both $\delta_v$ and $\delta_{th}$ are usually very small, their product can also be considered small and may be dropped. With such statement, a zeroth-order approximation can be made where the last bracket term remains, resulting in

$$\frac{\nu}{c_0^2} \left[ \widetilde{V} + \frac{\gamma - 1}{\mathrm{Pr}} \right] \frac{\partial^2}{\partial x^2} \frac{\partial}{\partial t} \upsilon + \frac{\partial^2 \upsilon}{\partial x^2} - \frac{1}{c_0^2} \frac{\partial^2 \upsilon}{\partial t^2} = 0. \tag{A.21}$$

Again, the wavenumber of the latter equation can be obtained following the same logic as before, yielding

$$k_{v,th} = \frac{\omega \delta_v}{c_0^2} - i \frac{\omega \delta_v}{2 c_0} \left[ \widetilde{V} + \frac{\gamma - 1}{\mathrm{Pr}} \right] \frac{\partial^3 \upsilon}{\partial x^2 \partial t}. \tag{A.22}$$

It can be concluded that the dispersion is negligible (at least of order $\delta_v$) whereas the absorption $\alpha_{v,th}$ is dependent on both viscous and thermal mechanisms. Although approximated, the effects of viscosity and heat conduction can be considered to be additive in the absorption of sound, i.e., $\alpha_{v,th} = \alpha_v + \alpha_{th}$.

## VISCOTHERMAL ACOUSTIC BOUNDARY LAYERS & DISPERSION RELATION

The two types of acoustic boundary layers can be combined in order to account for both processes. Deriving from the momentum and energy equations for both models, the 1D viscothermal wave equation for sound propagating in a duct

of arbitrary shape, and taking into account viscothermal acoustic effects at the boundaries, can be written as

$$\frac{\partial^2 \upsilon}{\partial x^2} - \frac{1}{c_0^2}\frac{\partial^2 \upsilon}{\partial t^2} = B \int_0^\infty \frac{\partial^2 \upsilon(x, t-\tau)}{\partial t^2}\frac{d\tau}{\sqrt{\tau}}, \tag{A.23}$$

where

$$B = \frac{4}{\text{HD}}\sqrt{\frac{\mu}{\pi\rho_0}}\left(1 + \frac{\gamma-1}{\sqrt{\text{Pr}}}\right). \tag{A.24}$$

Here $\text{HD} = 4S/C$ is the hydraulic diameter, and $S$ and $C$ are the area and perimeter of the cross section, respectively. The derivation of Eq. A.23 is based on the assumption that the boundary layer is (i) small compared to the effective radius of the duct (HD/2), but (ii) not so small that mainstream viscothermal losses are important. This restriction can be expressed in the following form

$$\delta_{visc}^{BL} \ll \frac{\text{HD}}{2} \ll \frac{c_0^2}{\omega^2 \delta_{visc}^{BL}}. \tag{A.25}$$

Substituting a time-harmonic solution into Eq. A.23 leads to the following dispersion relation:

$$(-ik)^2 + \frac{\omega^2}{c_0^2} = B(-ik)^2 \int_0^\infty e^{-i\omega\tau}\frac{d\tau}{\sqrt{\tau}}, \tag{A.26}$$

which when solved for $k$ gives

$$k = \pm\frac{\omega/c_0}{\sqrt{1 - B\sqrt{\pi/i\omega}}}. \tag{A.27}$$

Expanding this equation for a outgoing wave in a round tube of radius $a$ (with $\text{HD} = 2a$), the expression of $k$ can be reduced to

$$k \doteq \frac{\omega}{c_0}\left[1 + (1-i)\frac{1}{a}\sqrt{\frac{\mu}{2\rho_0\omega}}\left(1 + \frac{\gamma-1}{\sqrt{\text{Pr}}}\right)\right], \tag{A.28}$$

from which can be deduced

$$\alpha_{v,th}^{BL} = \frac{1}{a}\sqrt{\frac{\mu}{2\rho_0\omega}}\left(1 + \frac{\gamma-1}{\sqrt{\text{Pr}}}\right), \tag{A.29}$$

and

$$c_p = \frac{\omega}{\beta} = \frac{c_0}{1 + \alpha_{v,th}^{BL}c_0/\omega} \doteq c_0\left(1 - \frac{\alpha_{v,th}^{BL}c_0}{\omega}\right). \tag{A.30}$$

Thus, a sound wave travelling in a viscothermal fluid bounded within a round tube has $\alpha_{v,th}^{BL}$ vary as $\sqrt{\omega}$ and $c_p \to c_0$ at high frequency, but is less than $c_0$ at low frequencies. This subsonic phenomenon is clearly demonstrated in Sec. 4.2.3 where acoustic boundary layers help create highly dispersive acoustic metamaterials.

# GEOMETRY DIMENSIONS OF QPD-METADIFFUSER

THIS appendix details the geometrical parameters of the $N = 11$ Quasi-Perfect Diffusion metadiffuser illustrated in Sec. 5.3.

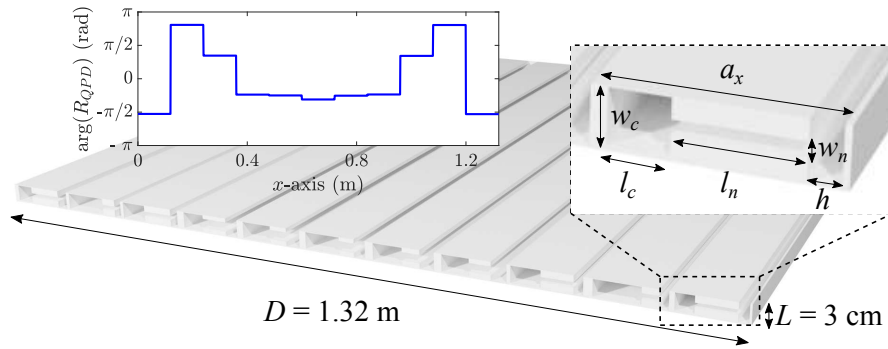

Figure B.1: Geometry of the $N = 11$ slits QPD-metadiffuser design. (See Fig. 5.6)

Table B.1: Geometrical parameters for the $n$-th well of the $N = 11$ QPD-metadiffuser.

| $n$ | $L$ (mm) | $h$ (mm) | $l_n$ (mm) | $l_c$ (mm) | $w_n$ (mm) | $w_c$ (mm) |
|---|---|---|---|---|---|---|
| 1 | 30 | 15.5 | 60.7 | 29.1 | 7.2 | 28 |
| 2 | 30 | 14.2 | 25.7 | 73.2 | 9.2 | 28 |
| 3 | 30 | 14.9 | 50.9 | 48.5 | 7.5 | 28 |
| 4 | 30 | 26.0 | 35.4 | 46.3 | 14.4 | 28 |
| 5 | 30 | 24.8 | 30.1 | 51.4 | 13.9 | 28 |
| 6 | 30 | 20.0 | 26.4 | 62.0 | 16.1 | 28 |
| 7 | 30 | 25.1 | 30.2 | 52.8 | 15.3 | 28 |
| 8 | 30 | 22.7 | 44.7 | 39.2 | 14.3 | 28 |
| 9 | 30 | 14.8 | 53.9 | 45.6 | 7.4 | 28 |
| 10 | 30 | 13.7 | 25.6 | 74.5 | 9.6 | 28 |
| 11 | 30 | 19.6 | 59.4 | 30.7 | 7.2 | 28 |

# FDTD SOUND SCATTERING FOR FLAT & QRD SURFACES

THIS appendix displays the sound scattering distributions obtained via 3D FDTD for a flat surface and $N = 5$ QRD as illustrated in Sec. 3.2.2. It can be observed in Fig. C.1 that a very good agreement in found between 3D FEM and 3D FDTD simulations for flat and QRD surfaces. It can be seen however that FDTD distributions seem to be smoother, or more averaged, than FEM data, which may result in a slight increase in sound intensity distribution.

It is worth noting that there is an increase of distributed energy between far-field and near-field sound scattering distributions, which can be seen between F-F and R-S figures. This is expected due to the closer integration of acoustic energy relative to the surface.
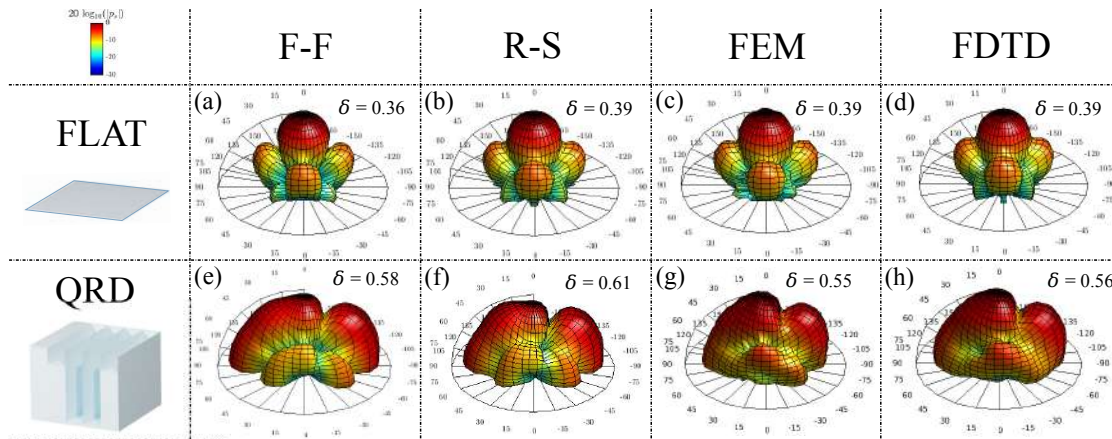


Figure C.1: Distribution of sound scattered pressure levels at 2 kHz for a flat panel and an $N = 5$ Quadratic Residue Diffuser (QRD) according to Fraunhofer-Fourier (F-F) integral, Rayleigh-Sommerfeld (R-S) integral, Finite Element Method (FEM), and Finite-Difference Time-Domain (FDTD). $\delta$ insets represent the autocorrelation of the scattered distributions. (See Fig. 6.7)

*Page left intentionally blank*